Computational microporomechanics for phase-changing geological materials

Hyoung Suk Suh

Submitted in partial fulfillment of the
requirements for the degree of
Doctor of Philosophy
under the Executive Committee
of the Graduate School of Arts and Sciences

COLUMBIA UNIVERSITY

2022

Abstract

Computational microporomechanics for phase-changing geological materials

Hyoung Suk Suh

Global challenges associated with extreme climate events and increasing energy demand require significant advances in our understanding and predictive capability of coupled multi-physical processes across spatial and temporal scales. While classical approaches based on the mixture theory may shed light on the macroscopic poromechanics simulations, accurate forward predictions of the complex behavior of phase-changing geomaterials cannot be made without understanding the underlying coupling mechanisms among constituents at the microstructural scale. To precisely predict the multi-physical behaviors originated by smaller scales, fundamental understandings of the micromechanical interactions among phase constituents are crucial. Hence, this dissertation discusses mathematical and computational frameworks designed to capture coupled thermo-hydro-mechanical-fracture processes in phase-changing porous media that incorporate necessary microscopic details. To achieve this goal, this dissertation aims to introduce a practical way to investigate how phase transition and evolving microstructural attributes at small scales affect the applicability of meso- or macroscopic finite element simulations, by leveraging the phase field method to represent the regularized interfaces of phase constituents.

Firstly, a multi-phase-field microporomechanics model is presented to model the growth and thaw of ice lenses. In specific, we extend the field theory for ice lens that is not restricted to one-dimensional space. The key idea is to represent the state of the pore fluid and the evolution of freezing-induced fracture via two distinct phase field variables coupled with balance laws, which leads to an immersed approach where both the homogeneous freezing and ice lensing are distinctively captured. Secondly, a thermo-hydro-mechanical theory for geological media with thermally non-equilibrated constituents is presented, where we develop an operator-split framework that updates the temperature of each constituent in an asynchronous manner. Here, the existence of an effective medium is hypothesized, in which

the constituents exhibit different temperatures while heat exchange among the phases is captured via Newton's law of cooling. Thirdly, an immersed phase field model is introduced to predict fluid flow in fracturing vuggy porous media, where crack growth may connect previously isolated voids and form flow conduits. In this approach, we present a framework where the phase field is not only used as a damage parameter for the solid skeleton but also as an indicator of the pore space, which enables us to analyze how crack growth in vuggy porous matrix affects the flow mechanism differently compared to the homogenized effective medium while bypassing the needs of partitioning the domain and tracking the moving interface. Finally, we present a new phase field fracture theory for higher-order continuum that can capture physically justified size effects for both the path-independent elastic responses and the path-dependent fracture. Specifically, we adopt quasi-quadratic degradation function and linear local dissipation function such that the physical size dependence are insensitive to the fictitious length scale for the regularized interface, which addresses the numerical needs to employ sufficiently large phase field length scale parameter without comprising the correct physical size effect.

Table of Contents

List of Figures

List of Tables

Acknowledgements

First and foremost, I would like to express my deepest gratitude to my advisor Prof. Steve WaiChing Sun who shared the excitement of four years of discovery. His continuous academic enthusiasm, invaluable guidance, and generous support kept me constantly engaged with my research. It has been a great pleasure to have spent these years with him, both personally and professionally.

Additionally, I would like to give my sincere appreciation to my candidacy examination and defense committee members: Prof. George Deodatis, Prof. Haim Waisman, Prof. Ronaldo Borja, Prof. Majid Manzari, and Prof. Kristin Myers for their valuable comments, remarks, and suggestions in completion of my dissertation.

I have been lucky to have shared my time in Theoretical and Computational Poromechanics Laboratory at Columbia, and would like to thank my colleagues: Prof. Jinhyun Choo, Prof. Chuanqi Liu, Dr. Yousef Heider, Dr. Ran Ma, Dr. Qing Yin, Dr. Camilo Duarte-Cordon, Prof. SeonHong Na, Dr. Kun Wang, Dr. Eric Bryant, Dr. Nikolaos Vlassis, Bahador Bahmani, Jarett Poliner, Zeyu Xiong, Mian Xiao, Nhon Phan, and Chulmin Kweon, for making this group an exciting and productive place to be.

I also gratefully acknowledge the primary funding supports through the Columbia University Presidential Fellowship and the Earth Materials and Processes program from the US Army Research Office under grant contract W911NF-18-2-0306, and the additional supports by the NSF CAREER grant from Mechanics of Materials and Structures program at National Science Foundation under grant contract CMMI-1846875, and the Dynamic Materials and Interactions Program from the Air Force Office of Scientific Research under

grant contracts FA9550-17-1-0169 and FA9550-19-1-0318.

My special thanks go to my parents in South Korea for unconditional love and trust during my pursuit. I would also like to thank my family in New York City: Karen, Justin, Isabella, Christina, and Jaewoo. This dissertation would not have been possible without their support and encouragement.

Finally, to my wife Nayoung, thank you for being the love of my life, for believing in me long after I'd lost belief in myself, for enduring this entire process, and for making countless sacrifices to help me get to this point. I will remain indebted to you for everything you have done for me. Love you till the very end.

Dedicated to my beloved wife, Nayoung

This page intentionally left blank.

Chapter 1: Introduction

1.1 Motivation and objective

Climate change has been observed for more than several decades, and has caused substantial impacts on the Earth's environment. In particular, the Intergovernmental Panel on Climate Change (IPCC)'s Sixth Assessment Report (AR6) [1] indicates that the global surface temperature has risen 1.1°C since early 20th century (Figure 1.1), causing changes in atmospheric circulation and precipitation patterns [2–5], which in turn affects underground moisture content and thermal cycles [6–8]. Combination of such changes are considered

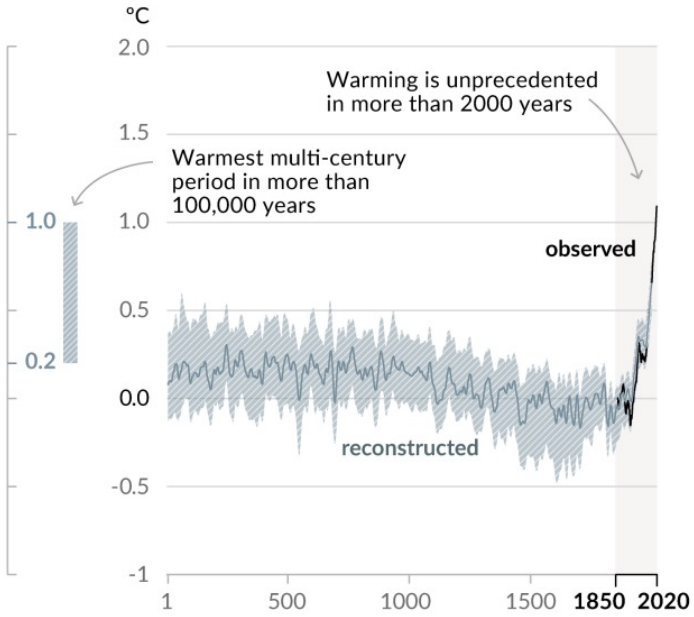

Figure 1.1: Changes in global surface temperature (from the IPCC Climate Change 2021: The Physical Science Basis Summary for Policymakers [9]).

as external factors of geo-hazards such as landslides, rockfalls, and snow avalanches [10–13], while the key internal factors are the coupled thermo-hydro-mechanical properties of geomaterials governed by the phase transition of the pore fluid [14, 15]. These changes have also brought increasing attention to the freeze-thaw action of phase-changing geological media, not only because it contributes to a positive feedback loop in climate change due to the fact that the permafrost region contains twice as much carbon in the atmosphere [16–18], but also results in abrupt frost heaving or thawing settlement that cause damages to the infrastructures [19, 20].

The IPCC AR6 [1] also states that human influence through greenhouse gas emissions on the climate is unequivocal. Although world population growth rate between 2010 and 2020 remained almost identical to the previous five decades [21], nevertheless, global urbanization has been accelerating as a consequence of sharp economic growth, which led to significantly increased energy demands (Figure 1.2). Since energy production that involves

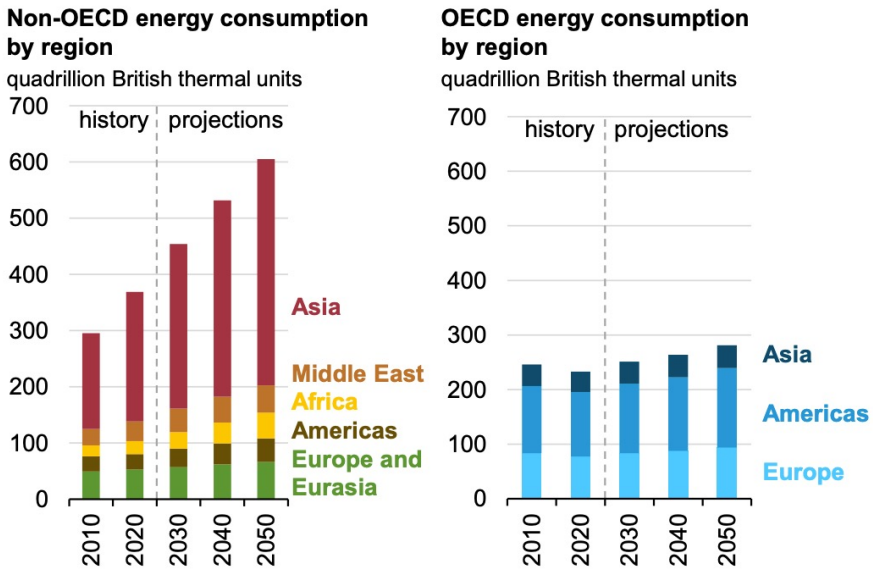

Figure 1.2: Energy consumption by region: history and projections (from the International Energy Outlook 2021 (IEO2021), U.S. Energy Information Administration [22]).

greenhouse gas emissions from fossil fuel combustion is by far the largest contributor of human-caused greenhouse gas emissions [1, 23, 24], clean and renewable energy, such as geothermal energy, has been emerging as an effective alternative technology [25, 26], while

carbon capture and storage (CCS) technology has gained attention since it allows the continued use of fossil fuels and at the same time reduces the amount of CO_2 in the atmosphere [27, 28].

Due to the emerging global challenges associated with climate change and increasing energy demand, geotechnical engineering has expanded its area into the fields of energy and environmental geotechnics, where computer models are indispensable since they require accurate forward predictions. While traditional geomechanics approach dedicated to constitutive models enjoyed partial success in replicating the behavior of fluid-infiltrating deformable porous media [29–31], precisely capturing multi-physical coupled processes remains a great challenge due to the complex interplay between solid deformation, fluid diffusion, heat transfer, phase transition, and evolution of the defects [32–34]. Since proposing a phenomenological constitutive model alone may not be sufficient to meet the current and future technological needs in geo-energy applications and climate change adaptations, incorporating multi-physics components into a computer simulation has become a necessary which requires fundamental understanding of the micromechanical interactions among phase constituents, in addition to the macroscopic poromechanics theory.

Given this background, this dissertation aims to present mathematical and computational frameworks designed to capture coupled thermo-hydro-mechanical-fracture processes in phase-changing porous media that incorporate necessary microscopic details. By leveraging continuous phase fields to represent interfaces of constituents, this study attempts to provide a practical way to analyze how phase transition and evolving microstructures at the small scales affect the applicability of mixture theory and effective stress principle at the macroscopic scale that is relevant to engineering designs. Evolution of the phase fields are coupled with balance principles such that the coupling among solid and fluid motions, heat transfer, phase transition, and crack growth can be observed numerically. Numerical techniques and solution schemes are also explored to handle the different growth rates of the boundary layers in a stable and computationally efficient manner. Numerical

examples including verification and validation exercises are provided to demonstrate the predictive capabilities of the proposed model.

1.2 Outline of dissertation

This dissertation focuses on studying coupled thermo-hydro-mechanical-fracture processes in phase-changing geomaterials, and at the same time, exploring the necessary microporomechanical approaches to capture their details. The outline of this dissertation is summarized as follows.

In Chapter 2, a multi-phase-field microporomechanics model is introduced to simulate the growth and thaw of ice lenses and the resultant frost heave and thawing settlement in multi-constituent frozen porous media. In this model, the growth of segregated ice inside the freezing-induced fracture is implicitly represented by the evolution of two phase fields that indicate the locations of ice and the damaged zone, respectively. The evolution of two phase fields is induced by their own driving forces that capture the physical mechanisms of ice and crack growths, respectively, while the phase field governing equations are coupled with the balance laws for the microporomechanical problem. Unlike phenomenological approaches that indirectly captures the freezing influence on the shear strength, this chapter introduces an immersed approach where both the homogeneous freezing and the ice lens growth are distinctively captured by the freezing retention function and the driving force accordingly.

Chapter 3 presents the mathematical framework and the asynchronous finite element solver that captures the brittle fractures in multi-phase fluid-infiltrating porous media at the mesoscale where the constituents are not necessarily in a thermal equilibrium state. Specifically, this model incorporates a dual-temperature effective medium theory in which the distinct constituent temperatures are homogenized independently whereas the heat exchange among the constituents is captured via Newton's law of cooling in analog to the

dual-permeability theory. In addition, a computationally efficient time integrator is proposed and implemented in an operator-split algorithm that updates the displacement, pore pressure, phase field, and temperature of each constituent in an asynchronous manner.

In Chapter 4, an immersed phase field fracture model is introduced to predict the fracture-induced fluid flow due to the brittle fracture in vuggy porous media. Due to the multiscale nature of pores in the vuggy porous material, crack growth may connect previously isolated pores, which leads to flow conduits. To understand the detailed microporomechanics that causes fracture-induced flow, this chapter introduces a new phase field framework where the phase field is not only used as an indicator function for damage of the solid skeleton but also used as an indicator of the pore space. By coupling the Stokes equation that governs the fluid transport in the voids, cavities, and cracks, and the Darcy's flow in the deformable porous media, this model enables us to capture the fluid-solid interaction of the pore fluid and solid constituents during crack growth.

Chapter 5 presents a phase field fracture model for higher order continuum, which intends to introduce a unified treatment that correctly captures the size effect of the materials in both elastic and damaged regimes. By introducing a cohesive micropolar phase field fracture theory, this chapter explores the interacting size-dependent elastic deformation and fracture mechanisms exhibits in materials of complex microstructures. To achieve this goal, this chapter introduces the distinctive degradation functions of the force-stress-strain and couple-stress-micro-rotation energy-conjugated pairs for a given regularization profile such that the macroscopic size-dependent responses of the micropolar continua are insensitive to the length scale parameter of the regularized interface. Here, the governing equations are derived based on the variational principle, from the micropolar stored energy and dissipative functionals.

Finally, in Chapter 6, a summary of contributions and concluding remarks are provided, and potential future research directions are discussed as well.

1.3 Notations and symbols

As for notations and symbols, bold-faced and blackboard bold-faced letters denote tensors (including vectors which are rank-one tensors); the symbol '$\cdot$' denotes a single contraction of adjacent indices of two tensors (e.g., $\boldsymbol{a} \cdot \boldsymbol{b} = a_i b_i$ or $\boldsymbol{c} \cdot \boldsymbol{d} = c_{ij} d_{jk}$); the symbol ':' denotes a double contraction of adjacent indices of tensor of rank two or higher (e.g., $\mathbb{C} : \boldsymbol{\varepsilon} = C_{ijkl} \varepsilon_{kl}$); the symbol '$\otimes$' denotes a juxtaposition of two vectors (e.g., $\boldsymbol{a} \otimes \boldsymbol{b} = a_i b_j$) or two symmetric second-order tensors [e.g., $(\boldsymbol{\alpha} \otimes \boldsymbol{\beta})_{ijkl} = \alpha_{ij} \beta_{kl}$]. We also define identity tensors: $\boldsymbol{I} = \delta_{ij}$, $\mathbb{I} = \delta_{ik} \delta_{jl}$, and $\bar{\mathbb{I}} = \delta_{il} \delta_{jk}$, where δ_{ij} is the Kronecker delta. As for sign conventions, unless specified, the directions of the tensile stress and dilative pressure are considered as positive.

Chapter 2: Multi-phase-field microporomechanics model for ice lens growth and thaw in frozen porous media

This chapter is under review as: H.S. Suh, W.C. Sun, Multi-phase-field microporomechanics model for simulating ice lens growth and thaw in frozen soil.

2.1 Introduction

Ice lens formation at the microscopic scale is a physical phenomenon critical for understanding the physics of frost heave and thawing settlement occurred at the field scale under the thermal cycles. Since ice lens may affect the freeze-thaw action and cause frost heave and thawing settlement sensitive to the changing climate and environment conditions, knowledge on the mechanism for the ice lens growth is of practical value for many civil engineering applications in cold regions [35–39]. For example, substantial heaving and settlement caused by the sequential formations and thawing of ice lenses lead to uneven deformation of the road which also damages the tires, suspension, and ball joints of vehicles. In the United States alone, it was estimated that two billion dollars had been spent annually to repair frost damage of roads [40]. Moreover, extreme climate change over the last few decades has brought increasing attention to permafrost degradation, since unusual heat waves may cause weakening of foundations and increase the likelihood of landslides triggered by the abrupt melting of the ice lens [41–45]. Under these circumstances, both the fundamental understanding of the ice lens growth mechanisms and the capacity to predict and simulate

the effect beyond the one-dimensional models becomes increasingly important.

Since the pioneering work on the ice lens by Stephan Taber in the early 20th century [46, 47], there has been a considerable amount of progress in the geophysics and fluid mechanics community to elucidate the mechanisms in the ice segregation process (e.g., [48] and references cited therein). During the freezing phase, it is now known that the crystallized pore ice surrounded by a thin pre-melted water film develops a suction pressure (i.e., cryo-suction) that attracts the unfrozen water towards the freezing front [49–51]. These films remain unfrozen below the freezing temperature and form an interconnected flow network that supplies water to promote ice crystal growth. Accumulation of pore ice crystals accompanies the void expansion and micro-cracking of the host matrix, which may result in the formation of a horizontal lens of segregated ice. However, despite these substantial amounts of work, the criterion for the ice lens initiation and its detailed mechanism still remains unclear. Based on the thermo-hydraulic model proposed by Harlan [52], Miller [53–55] introduces a concept of stress partitioning and assumed that an ice lens starts to form if the solid skeleton experiences tensile stress. This idea has been further adopted and further generalized in [56, 57] via an asymptotic method. Gilpin [58] suggests that the ice lens formation takes place when the ice pressure reaches the particle separation pressure depending on the particle size and the interfacial tension between the water and ice, whereas Zhou and Li [59] propose the idea of separation void ratio as a criterion for the ice lensing. Konrad and Morgenstern [60] present an alternative approach that can describe the formation and growth of a single ice lens based on segregation potential, of which the applicability has been demonstrated in [61–63]. On the other hand, Rempel [64, 65] develops regime diagrams that delineate the growth of a single lens, multiple lenses, and homogeneous freezing. In this line of work, the one-dimensional momentum and mass equilibrium equations are coupled with the heat flow in a step-freezing Stefan configuration to calculate the intermolecular force that drives the premelted fluid to the growing ice lenses. While the proposed method is helpful for estimating the lens thickness and spacing,

the one-dimensional setting is understandably insufficient for the geo-engineering applications that require understanding of the implication of ice lenses on the shear strength. More recently, Style et al. [66] propose a new theory on the ice lens nucleation by considering the cohesion of soil and the geometric supercooling of the unfrozen water in the pore space. Although the aforementioned studies formed the basis to shed light on explaining the ice lens formation, they are limited to the idealized one-dimensional problems and often idealized soil as a linear elastic material and hence not sufficient for applications that require a more precise understanding of the constitutive responses of the ice-rich soil.

Meanwhile, within the geomechanics and geotechnical engineering community, a number of theories and numerical modeling frameworks have been proposed based on the mixture theory and thermodynamics principles [67–70] with a variety of complexities and details. By adopting the premelting theory and considering the frozen soil as a continuum mixture of the solid, unfrozen water, and ice constituents, the freezing retention behavior of frozen soil can be modeled in a manner similar to those for the unsaturated soil. The resultant finite element implementation of these models enables us to simulate freeze-thaw effects in two- or three-dimensional spaces often with more realistic predictions on the solid constitutive responses. Nevertheless, the presence of crystal ices in the pores and that inside the expanded ice lens are often represented via phenomenological laws [70, 71]. Since the morphology, physics, and the mechanisms as well as the resultant mechanical characteristics of the ice lens and ice crystals in pores are profoundly different, it remains difficult to develop a predictive phenomenological constitutive law for an effective medium that represents the multi-constituent frozen soil with ice lenses [72].

This study is an attempt to reconcile the fluid mechanics and geotechnical engineering modeling efforts on modeling the frozen soil under changing climates. Our goal is to (1) extend the field theory for ice lens such that it is not restricted to one-dimensional problems and (2) introduce a framework that may incorporate more realistic path-dependent constitutive laws. As such, the coupling mechanism among phase transition, fluid diffusion,

heat transfer, and solid mechanics can be captured without solely relying on phenomenological material laws. In particular, we introduce a mathematical framework and a corresponding finite element solver that may distinctively capture the physics of ice lens and freezing/thawing. We leverage the implicit representation of complex geometry afforded by a multi-phase-field framework to first overcome the difficulty of capturing the evolving geometry of the ice lens. By considering the ice lens as segregated bulk ice inside the freezing-induced fracture, we adopt two phase field variables that represent the state of the fluid phase constituent and the regularized crack topology, respectively. This treatment enables us to take account of the brittle fracture that may occur during ice lens growth and explicitly incorporate the addition and vanishing shear strength and bearing capacity of the ice lens under different environmental conditions. The phase transition of the fluid is modeled via the Allen-Cahn equation [73, 74], while we adopt the phase field fracture framework to model brittle cracking in a solid matrix [75–77]. The resultant framework may provide a fuller picture to analyzing the growth of the ice lens in the frozen soil, while verification exercises also confirm that the model may reduce to a classical thermo-hydro-mechanical model and isothermal poromechanics model under limited conditions.

The rest of the paper is organized as follows. Section 2.2 summarizes the necessary ingredients for the mathematical framework, while we present the multi-phase-field microporomechanics model that describes the coupled behavior of a fluid-saturated phase-changing porous media in Section 2.3. For completeness, the details of the finite element formulation and the operator splitting solution strategy are discussed in Section 2.4. Finally, numerical examples are given in Section 2.5 to verify, validate, and showcase the model capacity, which highlights its potential by simulating the growth and melting of multiple ice lenses.

2.2 Kinematics and effective stress principle for frozen soil with ice lens

In this section, we introduce the ingredients necessary to derive the field theory for the phase field modeling of frozen soil presented later in Section 2.3. Similar to the treatments in [67], [68], and [69], we first assume that the frozen soil is fully saturated with either water or ice and therefore idealize the frozen soil as a three-phase continuum mixture that consists of solid, water, and ice phase constituents whereas the ice lens is a special case in which the solid skeleton no longer holds bearing capacity. This treatment enables us to formulate a multi-phase-field approach to employ two phase field variables as indicator functions for the state of the pore fluid (in ice or water form) [74, 78, 79] and that of the solid skeleton (in damage or intact form) [75–77]. We then extend the effective stress theory originated from damage mechanics [80] to incorporate the internal stress of ice lenses caused by the deformation of the effective medium into the Bishop's effective stress principle for frozen soil where the introduction of phase field provide smooth transition of the material states for both the pore fluid and the solid skeleton. This procedure allows us to incorporate both the capillary pressure of the ice crystal surrounded by the water thin film as well as the volumetric and deviatoric stresses triggered by the deformation of the ice lens.

2.2.1 Continuum representation and kinematics

Based on the mixture theory, we idealize our target material as a multiphase continuum where the solid, water, and ice phase constituents are overlapped. For simplicity, this study assumes that there is no gas phase inside the pore such that the pore space is either occupied by water or ice. The volume fractions of each phase constituent are defined as,

$$\phi^s = \frac{dV_s}{dV} \;;\; \phi^w = \frac{dV_w}{dV} \;;\; \phi^i = \frac{dV_i}{dV} \;;\; \phi^s + \sum_{\alpha=\{w,i\}} \phi^\alpha = 1, \tag{2.1}$$

where the indices s, w, and i refer to the solid, water, and ice phase constituents, respectively, while $dV = dV_s + dV_w + dV_i$ denote the total elementary volume of the mixture. Note that an index used as a subscript indicates the intrinsic property of a phase constituent, while it is used as a superscript when referring to a partial property of the entire mixture. By letting ρ_s, ρ_w, and ρ_i denote the intrinsic mass densities of the solid, water, and ice, respectively, the partial mass densities of each phase constituent are given by,

$$\rho^s = \phi^s \rho_s \;\; ; \;\; \rho^w = \phi^w \rho_w \;\; ; \;\; \rho^i = \phi^i \rho_i \;\; ; \;\; \rho^s + \sum_{\alpha=\{w,i\}} \rho^\alpha = \rho, \tag{2.2}$$

where ρ is the total mass density of the entire mixture. We also define the saturation ratios for the fluid phase constituents $\alpha = \{w, i\}$ as:

$$S^w = \frac{\phi^w}{\phi} \;\; ; \;\; S^i = \frac{\phi^i}{\phi} \;\; ; \;\; \sum_{\alpha=\{w,i\}} S^\alpha = 1, \tag{2.3}$$

where $\phi = 1 - \phi^s$ is the porosity.

Since the solid (s), water (w), and ice (i) phases do not necessarily follow the same trajectory, each constituent possesses its own Lagrangian motion function that maps the position vector of the current configuration $\boldsymbol{x}$ at time t to their reference configurations. In this study, we adopt a kinematic description that traces the motion of the solid matrix by following the classical theory of porous media [81–84]. Hence, the motion of the solid phase is described by using the Lagrangian approach via its displacement vector $\boldsymbol{u}(\boldsymbol{x}, t)$, whereas the fluid phase ($\alpha = \{w, i\}$) motions are described by the modified Eulerian approach via relative velocities $\tilde{\boldsymbol{v}}_w$ and $\tilde{\boldsymbol{v}}_i$, instead of their own velocity fields $\boldsymbol{v}_w$ and $\boldsymbol{v}_i$, i.e.,

$$\tilde{\boldsymbol{v}}_\alpha = \boldsymbol{v}_\alpha - \boldsymbol{v}, \tag{2.4}$$

where $\boldsymbol{v} = \dot{\boldsymbol{u}}$ is the solid velocity, while $\dot{(\bullet)} = \mathrm{d}(\bullet)/\mathrm{d}t$ is the total time derivative following the solid matrix.

2.2.2 Multi-phase-field approximation of freezing-induced crack

In this current study, we assume that the path-dependent constitutive responses of the frozen soil is due to the fracture in the brittle regime and the growth/thaw of the ice lens in the void space that could be opened by the expanded ice. While plasticity of the solid skeleton as well as the damage and creeping of the segregated ice may also play important roles on the mechanisms of the frost heave and thaw settlement, they are out of the scope of this study. As such, this study follows Miller's theory which assumes that a new ice lens may only form if and only if the compressive effective stress becomes zero or negative [53–55, 85]. Since opening up the void space is a necessary condition for the ice lens to grow inside, we introduce a phase field model that captures the crack growth potentially caused by the ice lenses growth. In this work, our strategy is to adopt diffuse approximations for both the phase transition of the pore fluid and the crack topology, where each requires a distinct phase field variable. As illustrated in Fig. 2.1, introducing two phase fields not only enables us to distinguish the homogeneous freezing from the ice lens growth but also leads to a framework that can be considered as a generalization of a thermo-hydro-mechanical model.

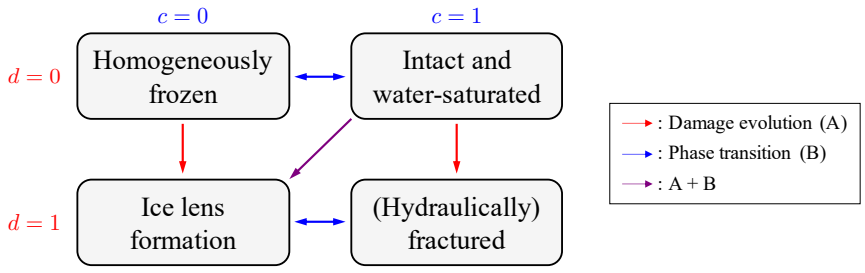

Figure 2.1: Schematic of multi-phase-field approach coupled with a thermo-hydro-mechanical model.

The first phase field variable $c \in [0, 1]$ used in this study is an order parameter that models the freezing of water (melting of ice) in a regularized manner [78, 79]. In other words, we employ a diffuse representation of the ice-water interface using variable c that is

a function of $\boldsymbol{x}$ and t:

$$c = c(\boldsymbol{x}, t) \text{ with } \begin{cases} c = 0 & : \text{completely frozen,} \\ c = 1 & : \text{completely unfrozen,} \\ c \in (0,1) & : \text{diffuse ice-water interface,} \end{cases} \tag{2.5}$$

which is the solution of the Allen-Cahn phase field equation [73, 74] that will be presented later in Section 2.3.1. Based on this setting, we consider the degree of saturation of water as an interpolation function of the phase field c, i.e., $S^w = S^w(c)$, that monotonically increases from 0 to 1 as,

$$S^w(c) = c^3(10 - 15c + 6c^2), \tag{2.6}$$

which guarantees smooth variation of different material properties between ice and water and at the same time enables us to properly include the latent heat effect in the energy balance equation in Section 2.3.1. Note that the evolution of the phase field variable c itself does not necessarily imply the ice lens growth since both the homogeneously frozen region and segregated ice can reach $c = 0$, regardless of the level of the effective stress or stored energy that drives the crack growth (Fig. 2.1).

The second phase field variable $d \in [0, 1]$ adopted in this study is a damage parameter that treats the sharp discontinuity as a diffusive crack via implicit function [75–77, 86]. In particular, we have:

$$d = d(\boldsymbol{x}, t) \text{ with } \begin{cases} d = 0 & : \text{intact,} \\ d = 1 & : \text{damaged,} \\ d \in (0,1) & : \text{transition zone,} \end{cases} \tag{2.7}$$

to approximate the fracture surface area A_Γ as A_{Γ_d}, which is the volume integration of crack

surface density $\Gamma_d(d, \nabla d)$ over a body $\mathcal{B}$, i.e.,

$$A_\Gamma \approx A_{\Gamma_d} = \int_{\mathcal{B}} \Gamma_d(d, \nabla d)\, dV \;\; ; \;\; \Gamma_d(d, \nabla d) = \frac{d^2}{2l_d} + \frac{l_d}{2}(\nabla d \cdot \nabla d), \tag{2.8}$$

where l_d is the length scale parameter that controls the size of the transition zone. In this case, the crack resistance force $\mathcal{R}_d$ can be expressed as,

$$\mathcal{R}_d = \frac{\partial W_d}{\partial d} - \nabla \cdot \left(\frac{\partial W_d}{\partial \nabla d} \right) \;\; ; \;\; W_d = \mathcal{G}_d \Gamma_d \left(d, \nabla d \right), \tag{2.9}$$

where $\mathcal{G}_d$ is the critical energy release rate that quantifies the resistance to cracking. As hinted in Fig. 2.1, in order to guarantee crack irreversibility, the thermodynamic restriction $\dot{\Gamma}_d \geq 0$ must be satisfied [76, 87–89] unlike the reversible freezing and thawing process. In other words, we require non-negative crack driving force $\mathcal{F}_d$ based on the microforce balance. Among multiple options, this study adopts the most widely used quadratic degradation function $g_d(d) = (1-d)^2$ following [87], that reduces the thermodynamic restriction into $\dot{d} \geq 0$ [34, 90] and satisfies the following conditions:

$$g_d(0) = 1 \;\; ; \;\; g_d(1) = 0 \;\; ; \;\; \frac{\partial g_d(1)}{\partial d} = 0 \;\; ; \;\; \frac{\partial g_d(d)}{\partial d} \leq 0 \text{ for } d \in [0, 1]. \tag{2.10}$$

Based on this setting, we define an indicator function $\chi^i \in [0, 1]$ for the segregated ice inside the freezing-induced fracture as follows:

$$\chi^i(c, d) = [1 - S^w(c)][1 - g_d(d)], \tag{2.11}$$

such that $\chi^i = 1$ implies the formation of the ice lens, which is different from the in-pore crystallization of the ice phase constituent.

2.2.3 Effective stress principle

Leveraging the similarities between freezing/thawing and drying/wetting processes, Miller and co-workers [53–55, 85] proposed the concept of neutral stress that partitions the net pore pressure $\bar{p}$ into the pore water and pore ice pressures (p_w and p_i), respectively:

$$\bar{p} = S^w(c)p_w + [1 - S^w(c)]p_i. \tag{2.12}$$

Clearly, Eq. (2.12) alone cannot capture the deviatoric stress induced by the deformation of the ice lens. Previous efforts on modeling frozen soil often relies on an extension of critical state theory that evolves the yield function according to the degree of saturation of ice (and therefore introduces the dependence of the tensile and shear strength on the presence of ice) [67, 69]. However, this treatment is not sufficient to consider the soil that may become brittle at low temperature due to the low moisture content and the influence of ice lens on the elasticity. Hence, this study extends Miller's approach into a phase field framework by decomposing the effective stress tensor $\bar{\boldsymbol{\sigma}}'$ into two partial stresses for the solid and ice lens via the damage phase field doubled as a weighting function, i.e.,

$$\bar{\boldsymbol{\sigma}}' = g_d(d)\boldsymbol{\sigma}'_{\text{int}} + [1 - g_d(d)]\boldsymbol{\sigma}'_{\text{dam}}. \tag{2.13}$$

where the second term on the right hand side of Eq. (2.13) depends on the saturation $S^w(c)$. Specifically, the effective stress contribution from the solid skeleton $\boldsymbol{\sigma}'_{\text{int}}$ degrades due to the damage when the ice lens grows, but may also evolve by the change of $\boldsymbol{\sigma}'_{\text{dam}}$ in the presence of ice lens [for instance, see Eq. (2.29) in Section 2.3.2]. From a physical point of view, we propose Eq. (2.13) based on the assumption that there is no relative motion between the solid skeleton and the ice lens in the sense that the ice lenses cannot be squeezed out from the host matrix, which also has a benefit of ensuring continuous displacement field. Similar models that capture the constituent responses of porous media consisting of multiple solid

constituents can also be found in [91]. In addition, this study also considers the volumetric expansion due to the phase transition from water to ice while neglecting the thermal expansion or contraction of each phase constituent. Specifically, we incorporate an additional term for the total Cauchy stress tensor $\boldsymbol{\sigma}$ that describes phase-transition-induced volumetric expansion, which stems from the Helmholtz free energy functions of the solid and ice phase constituents postulated in [92, 93]. Hence, similar to [67, 69], as a modification of the Bishop's equation, the total Cauchy stress tensor can be expressed as follows:

$$\boldsymbol{\sigma} = \bar{\boldsymbol{\sigma}}' - \bar{p}\boldsymbol{I} - \phi[1 - S^w(c)]\bar{\alpha}_v K_i \boldsymbol{I}, \tag{2.14}$$

where $\bar{\alpha}_v = g_d(d)\alpha_{v,\text{int}} + [1 - g_d(d)]\alpha_{v,\text{dam}}$ is the net volumetric expansion coefficient which is influenced by the evolution of the fracture. In particular, we assume that the volumetric expansion coefficient of the ice lens $\alpha_{v,\text{dam}}$ is greater than that of the pore ice crystal $\alpha_{v,\text{int}}$ due to the degradation of the solid skeleton.

2.3 Multi-phase-field microporomechanics model for phase-changing porous media

This section presents the balance principles and constitutive laws that capture the thermo-hydro-mechanical behavior of the phase-changing porous media. We first introduce the coupled field equations that govern the heat transfer and the ice-water phase transition processes which involve the latent heat effect. Unlike previous studies that model the phase transition of the pore fluid by using the semi-empirical approach which links either the Gibbs-Thomson equation [68] or the Clausius-Clapeyron equation [67, 69] with the van Genuchten curve [94], we adopt the Allen-Cahn type phase field model [73, 74] with a driving force that depends both on the temperature and the damage. We then present microporomechanics and phase field fracture models that complete the set of governing equations,

which is not only capable of simulating freeze-thaw action but also the freezing-induced or hydraulically-driven fractures. The implications of our model will be examined via numerical examples in Section 2.5.

2.3.1 Thermally induced phase transition

Heat transfer

Since underground freezing and thawing processes may span over long temporal scales, this study employs a single temperature field θ by assuming that all the phase constituents reach a local thermal equilibrium instantly [34]. We also neglect thermal convection by considering the case where the target material possesses low permeability. Let e denote the internal energy per unit volume and $\boldsymbol{q}$ the heat flux. Then, the energy balance of the entire mixture can be expressed as [34, 95],

$$\dot{e} = -\nabla\cdot\boldsymbol{q} + \hat{r}, \;\; ; \;\; e = e^s + \sum_{\alpha=\{w,i\}} e^\alpha, \tag{2.15}$$

where $\hat{r}$ indicates the heat source/sink, $e^s = \rho^s c_s \theta$ and $e^\alpha = \rho^\alpha c_\alpha \theta$ are the partial energies for the solid and fluid phase constituents, respectively, while c_s and c_α are their heat capacities. Although the freezing temperature of water (melting temperature of ice) depends on the curved phase boundaries due to the intermolecular forces, i.e., freezing point depression [96], for simplicity, we assume that the freezing temperature of water remains constant $\theta_m = 273.15$ K, so that the internal energy of the entire mixture e in Eq. (2.15) can be rewritten as,

$$e = \rho^s c_s \theta + (\rho^w c_w + \rho^i c_i)(\theta - \theta_m) + (\rho^w c_w + \rho^i c_i)\theta_m. \tag{2.16}$$

From the relations shown in Eqs. (2.1)-(2.3), substituting Eq. (2.16) into Eq. (2.15) yields the following:

$$(\rho^s c_s + \rho^w c_w + \rho^i c_i)\dot{\theta} + \phi\left[(\rho_w c_w - \rho_i c_i)(\theta - \theta_m) + \rho_i L_\theta\right]\dot{S}^w(c) + \nabla\cdot\boldsymbol{q} = \hat{r}, \quad (2.17)$$

where:

$$L_\theta = \left(\frac{\rho_w}{\rho_i}c_w - c_i\right)\theta_m \quad (2.18)$$

is the latent heat of fusion which is set to be $L_\theta = 334$ kJ/kg for pure water [67, 78, 97, 98]. Notice that the second term on the left-hand side of Eq. (2.17) describes the energy associated with the phase change of the fluid phase constituent $\alpha = \{w, i\}$, which is responsible for the constant temperature during the transformation processes, i.e., where c is changing with time since $\dot{S}^w(c) = \{\partial S^w(c)/\partial c\}\dot{c}$. For the constitutive model that describes the heat conduction, this study adopts Fourier's law where the heat flux can be written as the dot product between the effective thermal conductivity and the temperature gradient, i.e.,

$$\boldsymbol{q} = -\left(\phi^s\kappa_s + \sum_{\alpha=\{w,i\}}\phi^\alpha\kappa_\alpha\right)\cdot\nabla\,\theta, \quad (2.19)$$

where κ_s and κ_α denote the intrinsic thermal conductivities of the solid and fluid phase constituents, respectively. This volume-averaged approach, however, is only valid for the case where all the phase constituents are connected in parallel. Although there exists alternative homogenization approaches such as Eshelby's equivalent inclusion method [99–101], determination of correct effective thermal conductivity often requires knowledge of the pore geometry and topology [100, 102, 103]. Since the information is not always readily approachable, this extension will be considered in the future.

Phase transition

By using the phase field variable c defined in Eq. (2.5), we adopt the Allen-Cahn model that is often used to simulate dendrite growth or multi-phase flow [73, 104, 105]. Following [74], we consider one of the simplest forms of the Gibbs free energy functional Ψ_c:

$$\Psi_c = \int_{\mathcal{B}} \psi_c \, dV = \int_{\mathcal{B}} f_c(\theta, c) + \frac{\epsilon_c^2}{2} |\nabla c|^2 \, dV, \tag{2.20}$$

where $f_c(\theta, c)$ is the free energy density that couples the heat transport with the phase transition, while ϵ_c is the gradient energy coefficient. From Eq. (2.20), we consider the evolution of the phase field c over time, which yields the well-known Allen-Cahn equation or time-dependent Ginzburg-Landau equation, i.e.,

$$-\frac{1}{M_c}\dot{c} = \frac{\partial \psi_c}{\partial c} - \nabla \cdot \left(\frac{\partial \psi_c}{\partial \nabla c} \right) = \frac{\partial f_c}{\partial c} - \epsilon_c^2 \nabla^2 c, \tag{2.21}$$

where $\nabla^2(\bullet) = \nabla \cdot \nabla (\bullet)$ is the Laplacian operator and M_c is the mobility parameter. Since this study does not consider solute transport or any other chemical effects, we focus on the pure water-ice phase transition such that the free energy density $f_c(\theta, c)$ can be written as,

$$f_c = W_c g_c(c) + \mathcal{F}_c(\theta) p_c(c), \tag{2.22}$$

where $g_c(c) = c^2(1-c)^2$ is the double well potential [Fig. 2.2(a)] that can be regarded as an energy barrier at the ice-water interface with the height of W_c, and $p_c(c) = S^w(c) = c^3(6c^2 - 15c + 10)$ is the interpolation function [Fig. 2.2(b)] that ensures minima of the free energy density f_c at $c = 0$ and $c = 1$, respectively. The driving force $\mathcal{F}_c(\theta)$ that induces ice-water phase transition should describe the thermodynamically equilibrated state of water and ice phase constituents, which can be derived from the following relation [106]:

$$dp_i = \frac{\rho_i}{\rho_w} dp_w - \rho_i L_\theta \frac{d\theta}{\theta}. \tag{2.23}$$

Then, integrating Eq. (2.23) yields the Clausius-Clapeyron equation:

$$p_i - p_w = \left(\frac{\rho_i}{\rho_w} - 1\right) p_w - \rho_i L_\theta \ln \frac{\theta}{\theta_m}. \tag{2.24}$$

Eq. (2.24) suggests that the surface tension develops along the ice-water interface, establishing the relation among water pressure (p_w), ice pressure (p_i), and temperature (θ). However, as pointed out in [67], the ice-water phase transition is mainly governed by the temperature while the influence of pressure on the ice saturation S^i is relatively minor. Hence, for simplicity, we define the driving force $\mathcal{F}_c(\theta)$ as an approximation of the pressure difference, by neglecting the effect of pore water pressure and adopt its first-order Taylor approximation following [74] as follows:

$$p_i - p_w \approx \mathcal{F}_c(\theta) = \rho_i L_\theta \left(1 - \frac{\theta}{\theta_m}\right). \tag{2.25}$$

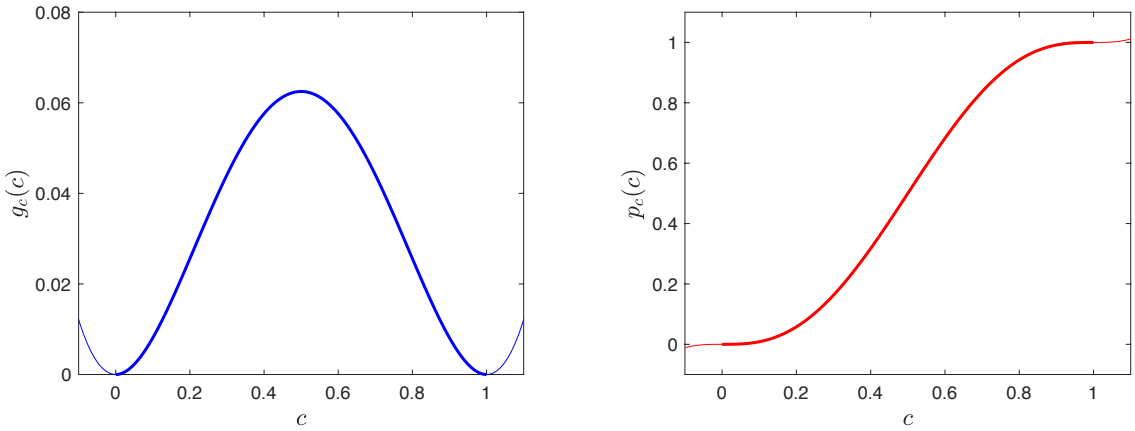

(a) (b)

Figure 2.2: (a) The double well potential $g_c(c)$, and (b) the interpolation $p_c(c)$ functions. Thin colored curves correspond to the values outside the range of the phase field c.

As pointed out in [74, 78], since Eq. (2.21) captures the evolution of the regularized ice-water interface, numerical parameters ϵ_c, W_c, and M_c can be related to the ice-water surface

tension γ_{iw}, the interface thickness δ_c, and the kinetic coefficient ν_c as,

$$\epsilon_c = \sqrt{6\gamma_{iw}\delta_c} \;;\; W_c = \frac{3\gamma_{iw}}{\delta_c} \;;\; M_c = \frac{\nu_c \theta_m}{6\rho_i L_\theta \delta_c}. \tag{2.26}$$

However, physical range of the width of the ice-water interface is at the atomic scale, i.e., 10^{-10} m, which makes macro-scale simulations unfeasible [79, 107]. In addition to the interfacial tension γ_{iw}, this study therefore treats the interface thickness δ_c and the gradient energy coefficient ϵ_c as input material parameters, since they could be increased according to the mesh size without significantly influencing the interface evolution [78, 108, 109].

Furthermore, since the existence of segregated ice governs the heave rate of frozen soil [70, 110], this study considers different rates between homogeneous freezing and ice lens growth. Specifically, while employing different volumetric expansion coefficients for the in-pore crystallization and the formation of ice lens [Eq. (2.14)], we replace the driving force $\mathcal{F}_c(\theta)$ with $\mathcal{F}_c^*(\theta, d)$ that contains an additional term that describes the intense growth of ice lenses similar to the kinetic equation proposed by Espinosa et al. [111], which is often used to model salt crystallization in porous media [88, 112, 113]:

$$\mathcal{F}_c^*(\theta, d) = \rho_i L_\theta \left(1 - \frac{\theta}{\theta_m}\right) + [1 - g_d(d)] K_c^* \left(1 - \frac{\theta}{\theta_m}\right)^{g_c^*}, \tag{2.27}$$

where $K_c^* > 0$ and $g_c^* > 0$ are the kinetic parameters. The effect of the additional term in Eq. (2.27) is illustrated in Fig. 2.3, where we simulate the water-ice phase transition by placing a heat sink at the center while the kinetic parameters are set to be $K_c^* = 5.0$ GPa and $g_c^* = 1.2$. By considering two different cases where the entire 1 mm^2 large water-saturated square domain remains intact and is completely damaged, Fig. 2.3 shows that the modified driving force $\mathcal{F}_c^*$ is capable of capturing different growth rates depending on the damage parameter d.

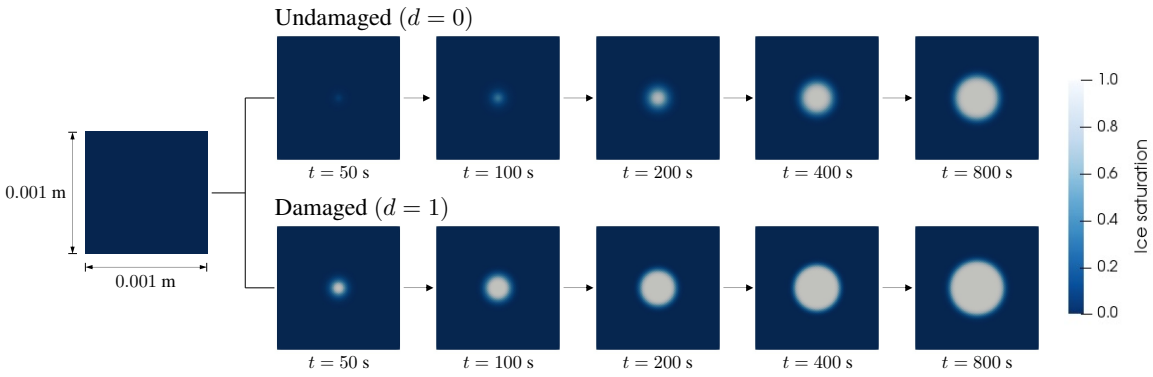

Figure 2.3: Different growth rates of the ice phases when a heat sink of $\hat{r} = -10^9$ W/m^3 is placed at a small region at the center with the area of $A_c = 10^{-10}$ m^2.

2.3.2 Freezing-induced fracture in microporoelastic medium

Microporomechanics of the phase-changing porous medium

Focusing on the ice lens formation that involves a long period of time up to annual scales [114, 115], this study neglects the inertial effects such that the balance of linear momentum for the three-phase mixture can be written as,

$$\nabla \cdot \boldsymbol{\sigma} + \rho \boldsymbol{g} = \boldsymbol{0}. \tag{2.28}$$

Based on the observation that geological materials remain brittle at a low temperature [116, 117], we assume that the evolution of the damage parameter d replicates the mechanism of brittle fracture. In this case, undamaged effective stress $\boldsymbol{\sigma}'_{\text{int}}$ can be considered linear elastic, while the stress tensor inside the damaged zone should remain $\boldsymbol{\sigma}'_{\text{dam}} = \boldsymbol{0}$ unless the temperature is below θ_m to form bulk ice. Moreover, since the ice flow with respect to the solid phase is negligible compared to that of water [68, 69], both $\boldsymbol{\sigma}'_{\text{int}}$ and $\boldsymbol{\sigma}'_{\text{dam}}$ can be related to the strain measure $\boldsymbol{\varepsilon} = (\nabla \boldsymbol{u} + \nabla \boldsymbol{u}^{\text{T}})/2$ by approximating $\tilde{\boldsymbol{v}}_i \approx \boldsymbol{0}$. Given these considerations, we define the constitutive relations for $\boldsymbol{\sigma}'_{\text{int}}$ and $\boldsymbol{\sigma}'_{\text{dam}}$ as,

$$\boldsymbol{\sigma}'_{\text{int}} = K\varepsilon^{\text{vol}}\boldsymbol{I} + 2G\boldsymbol{\varepsilon}^{\text{dev}} \;\; ; \;\; \boldsymbol{\sigma}'_{\text{dam}} = [1 - S^w(c)](K_i\varepsilon^{\text{vol}}\boldsymbol{I} + 2G_i\boldsymbol{\varepsilon}^{\text{dev}}), \tag{2.29}$$

where $\varepsilon^{\text{vol}} = \text{tr}\,(\boldsymbol{\varepsilon})$ and $\boldsymbol{\varepsilon}^{\text{dev}} = \boldsymbol{\varepsilon} - (\varepsilon^{\text{vol}}/3)\boldsymbol{I}$, while K and K_i are the bulk moduli; and G and G_i are the shear moduli for the solid skeleton and the ice, respectively. Based on this approach, $\boldsymbol{\sigma}'_{\text{dam}}$ can be interpreted as a developed stress due to the ice lens growth, since it not only depends on the fracturing process but also on the state of the fluid phase.

Remark 1. Since we consider the phase field model for brittle fracture, this approach may not fully capture the realistic thawing soil behavior. One possible approach would be to consider both the constitutive model and finite strain theory that can capture subsequent settlement which involves the drainage of large amount of pore water [19, 69, 118], but this extension is out of scope of this study and will be considered in the future.

The net pore pressure $\bar{p}$, on the other hand, is a driver of deformation and fracture due to the formation of ice crystal that exerts significant excess pressure on the premelted water film. This pressure is referred to as cryo-suction s_{cryo} that induces the ice pressure p_i to be far greater than the water pressure p_w. As shown in Eqs. (2.12) and (2.24), the net pore pressure can be rewritten as $\bar{p} = [1 - S^w(c)]s_{\text{cryo}} - p_w$, while $s_{\text{cryo}} = p_i - p_w$ can be determined based upon the Clausius-Clapeyron equation. In practice, however, the Clausius-Clapeyron equation is typically replaced by an empirical model, such as the exponential [119] or the van Genuchten [94] curves, which is considered to be more accurate, since freezing retention characteristics are affected by both the pore size distribution and the ice-water interfacial tension [120–123]:

$$S^{w*} = \exp\left(b_B \langle \theta - \theta_m \rangle_-\right) \;\; ; \;\; s^*_{\text{cryo}} = p_{\text{ref}} \left[\left\{ S^w(c) \right\}^{-\frac{1}{m_{vG}}} - 1 \right]^{\frac{1}{n_{vG}}}, \tag{2.30}$$

where b_B, p_{ref}, m_{vG}, and n_{vG} are empirical parameters while $\langle \bullet \rangle_\pm = (\bullet \pm |\bullet|)/2$ is the Macaulay bracket. Note that we use a superscripted symbol $*$ to indicate that the corresponding variables are empirically determined. Yet, these empirical models still yield unrealistic results in some cases. For example, the derivative of the exponential model possesses a discontinuity at the freezing temperature θ_m, while s^*_{cryo} approaches infinity if $S^w(c) \to 0$

if adopting the van Genuchten model. Hence, in this study, we combine the two models to obtain the freezing retention curve that bypasses such issues (Fig. 2.4):

$$s^*_{\text{cryo}} = p_{\text{ref}} \left\{ \left[\{ \exp\left(b_B \langle \theta - \theta_m \rangle_- \right) \} \right]^{-\frac{1}{m_{vG}}} - 1 \right\}^{\frac{1}{n_{vG}}}, \tag{2.31}$$

and we replace s_{cryo} with s^*_{cryo} for the net pore pressure such that: $\bar{p} = [1 - S^w(c)] s^*_{\text{cryo}} - p_w$. For all the numerical examples presented in Section 2.5, we adopt the same values used in [69, 123]: $b_B = 0.55$ K^{-1}, $p_{\text{ref}} = 200$ kPa, $m_{vG} = 0.8$, and $n_{vG} = 2.0$.

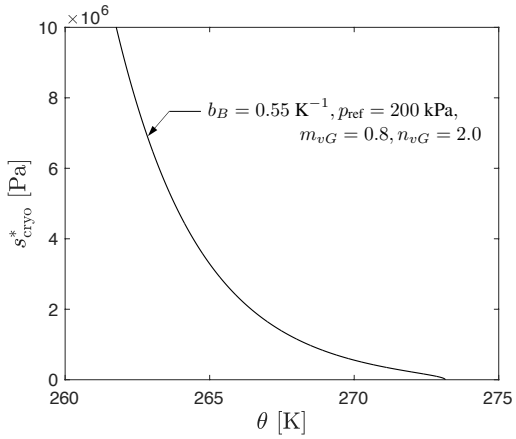

Figure 2.4: Freezing characteristic function [Eq. (2.31)] used in this study.

Recall Section 2.2 that our material of interest is a fluid-saturated phase-changing porous media. Thus, this study considers the balance of mass for three phase constituents (i.e., solid, water and ice) as follows:

$$\dot{\rho}^s + \rho^s \nabla \cdot \boldsymbol{v} = \dot{m}_s, \tag{2.32}$$

$$\dot{\rho}^w + \rho^w \nabla \cdot \boldsymbol{v} + \nabla \cdot \rho^w \tilde{\boldsymbol{v}}_w = \dot{m}_w, \tag{2.33}$$

$$\dot{\rho}^i + \rho^i \nabla \cdot \boldsymbol{v} + \nabla \cdot \rho^i \tilde{\boldsymbol{v}}_i = \dot{m}_i, \tag{2.34}$$

where $\dot{m}_s$, $\dot{m}_w$, and $\dot{m}_i$ indicate the mass production rate for each phase constituent [68, 69, 88]. Here, we assume that only the water and ice phase constituents exchange mass among constituents (i.e., $\dot{m}_s = 0$ and $\dot{m}_w = -\dot{m}_i$). Hence, summation of Eqs. (2.33) and (2.34)

yields:

$$\begin{aligned}&\dot{\phi}\left\{S^w(c)\rho_w+[1-S^w(c)]\rho_i\right\}+\phi\dot{S}^w(c)(\rho_w-\rho_i)\\&+\phi\left\{S^w(c)\rho_w+[1-S^w(c)]\rho_i\right\}\nabla\cdot\boldsymbol{v}+\nabla\cdot\rho^w\tilde{\boldsymbol{v}}_w=0,\end{aligned}\tag{2.35}$$

since $\tilde{\boldsymbol{v}}_i\approx\mathbf{0}$, while Eq. (2.32) can be rewritten as,

$$\dot{\phi}=(1-\phi)\nabla\cdot\boldsymbol{v}.\tag{2.36}$$

Substituting Eq. (2.36) into (2.35) yields the mass balance equation for the three-phase mixture:

$$\phi\dot{S}^w(c)(\rho_w-\rho_i)+\left\{S^w(c)\rho_w+[1-S^w(c)]\rho_i\right\}\nabla\cdot\boldsymbol{v}+\nabla\cdot\rho^w\tilde{\boldsymbol{v}}_w=0.\tag{2.37}$$

In this study, we focus on the case where the water flow inside both the porous matrix and the fracture obeys the generalized Darcy's law while considering the pore blockage due to the water-ice phase transition [124–126]. In other words, we adopt the following constitutive relation between $\tilde{\boldsymbol{v}}_w$ and p_w:

$$\boldsymbol{w}_w=-\frac{k_r\boldsymbol{k}}{\mu_w}(\nabla p_w-\rho_w\boldsymbol{g}),\tag{2.38}$$

where $\boldsymbol{w}_w=\phi\tilde{\boldsymbol{v}}_w$ is Darcy's velocity, $\boldsymbol{k}$ is the permeability tensor, μ_w is the water viscosity, and k_r is the saturation dependent relative permeability:

$$k_r=S^w(c)^{1/2}\left\{1-\left[1-S^w(c)^{1/m_{vG}}\right]^{m_{vG}}\right\}^2.\tag{2.39}$$

Damage evolution

Following [34], this study interprets cracking as the fracture of the solid skeleton. In other words, we define the crack driving force $\mathcal{F}_d \geq 0$ as,

$$\mathcal{F}_d = -\frac{\partial g_d(d)}{\partial d}\psi'_{\text{int}} \ ; \ \psi'_{\text{int}} = \frac{1}{2}K(\varepsilon^{\text{vol}})^2 + G(\boldsymbol{\varepsilon}^{\text{dev}} : \boldsymbol{\varepsilon}^{\text{dev}}), \tag{2.40}$$

such that the damage evolution equation can be obtained from the balance between the crack driving force $\mathcal{F}_d$ and the crack resistance $\mathcal{R}_d$ [34, 127, 128]:

$$\mathcal{R}_d - \mathcal{F}_d = \frac{\partial g_d(d)}{\partial d}\psi'_{\text{int}} + \frac{\mathcal{G}_d}{l_d}(d - l_d^2\nabla^2 d) = 0. \tag{2.41}$$

Recall Section 2.2.2 that our choice of degradation function $g_d(d)$ reduces the thermodynamic restriction into $\dot{d} \geq 0$, which requires additional treatment to ensure monotonic crack growth. In this study, we adopt the same treatment used in [90, 129]. By considering the homogeneity $\nabla\, d = \mathbf{0}$, Eq. (2.41) yields the following expression:

$$\dot{d} = \frac{2}{(1+2\mathcal{H})^2}\dot{\mathcal{H}} \geq 0 \ ; \ \mathcal{H} = \frac{\psi'^{+}_{\text{int}}}{\mathcal{G}_d/l_d}, \tag{2.42}$$

implying that non-negative $\dot{d}$ is guaranteed if $\dot{\mathcal{H}} \geq 0$. Here, notice that we adopt the volumetric-deviatoric splitting scheme proposed by Amor et al. [130] to avoid crack growth under compression. Specifically, we decompose the elastic strain energy into two parts, i.e., $\psi'_{\text{int}} = \psi'^{+}_{\text{int}} + \psi'^{-}_{\text{int}}$,

$$\psi'_{\text{int}} = \frac{1}{2}K\langle\varepsilon^{\text{vol}}\rangle_+^2 + G(\boldsymbol{\varepsilon}^{\text{dev}} : \boldsymbol{\varepsilon}^{\text{dev}}) \ ; \ \psi'_{\text{int}} = \frac{1}{2}K\langle\varepsilon^{\text{vol}}\rangle_-^2, \tag{2.43}$$

and only degrade the expansive volumetric and deviatoric parts, while $\langle\bullet\rangle_\pm = (\bullet + |\bullet|)/2$. To ensure $\dot{\mathcal{H}} \geq 0$, as a simple remedy, we replace $\mathcal{H}$ with $\mathcal{H}^*$ which is defined as the pseudo-temporal maximum of normalized strain energy, while considering a critical value

$\mathcal{H}_{\text{crit}}$ that restricts the crack to initiate above a threshold strain energy [90, 131–133]:

$$\mathcal{H}^* = \max_{\tau \in [0,t]} \langle \mathcal{H} - \mathcal{H}_{\text{crit}} \rangle_+ , \tag{2.44}$$

such that Eq. (2.41) accordingly becomes:

$$\frac{\partial g_d(d)}{\partial d} \mathcal{H}^* + (d - l_d^2 \nabla^2 d) = 0. \tag{2.45}$$

For either partially or fully saturated soils, crack healing may occur during the thawing process. In specific, when ice lenses melt in a highly plastic clayey soil, cracks may heal due to the interactions between water molecules, whereas in a less cohesive soil, relocation of eroded particles result in the clogging of cracks or cavities [134–136]. One possible approach to model the crack healing process is to allow crack driving force to decrease and incorporate constitutive model that can capture the thaw-weakening process properly. For example, Ma and Sun [137] assumed that the healing process is activated when the material experiences volumetric compression, while the stiffness recovery rate becomes slower along the healing process. This extension is out of scope of this study, and hence, we assume that cracking is irreversible.

In order to model the fracture flow in a fluid-infiltrating porous media, we adopt the permeability enhancement approach that approximates the water flow inside the fracture as the flow between two parallel plates [138–141]:

$$\boldsymbol{k} = \boldsymbol{k}_{\text{mat}} + \boldsymbol{k}_d = k_{\text{mat}} \boldsymbol{I} + d^2 k_d (\boldsymbol{I} - \boldsymbol{n}_d \otimes \boldsymbol{n}_d), \tag{2.46}$$

where k_{mat} is the effective permeability of the undamaged matrix, $\boldsymbol{n}_d = \nabla d / \| \nabla d \|$ is the unit normal of crack surface, and $k_d = w_d^2/12$ describes the permeability enhancement due to the crack opening which depends on the hydraulic aperture w_d based on the cubic law. However, freezing-induced fracture involves different situations where the pore ice crystal

growth drives fracture but at the same time blocks the pore that may hinder the water flow therein. Hence, we adopt the approach used in [88] which assumes a linear relationship between the hydraulic aperture w_d and the water saturation $S^w(c)$:

$$w_d = S^w(c) l_\perp (\boldsymbol{n}_d \cdot \boldsymbol{\varepsilon} \cdot \boldsymbol{n}_d), \tag{2.47}$$

where $l_\perp$ is the characteristic length of a line element perpendicular to the fracture which is often assumed to be equivalent to the mesh size [138, 142]. Furthermore, by assuming that the crack opening leads to complete fragmentation of the solid matrix, we adopt the following relation for the porosity [34, 143]:

$$\phi = 1 - g_d(d)(1 - \phi_0)(1 - \nabla \cdot \boldsymbol{u}), \tag{2.48}$$

such that the porosity approaches 1 if the solid skeleton is completely damaged.

2.4 Finite element implementation

This section presents a finite element discretization of the set of governing equations described in Section 2.3, and the solution strategy for the resulting discrete system. We first formulate the weak form of the field equations by following the standard weighted residual procedure. In specific, we adopt the Taylor-Hood element for the displacement and pore water pressure fields, while employing linear interpolation functions for all other variables in order to remove spurious oscillations. We then describe the operator split solution scheme that separately updates $\{\theta, c\}$ and $\{\boldsymbol{u}, p_w\}$, while the damage parameter d is updated in a staggered manner for numerical robustness.

2.4.1 Galerkin form

Let domain $\mathcal{B}$ possesses boundary surface $\partial\mathcal{B}$ composed of Dirichlet boundaries (displacement $\partial\mathcal{B}_u$, pore water pressure $\partial\mathcal{B}_p$, and temperature $\partial\mathcal{B}_\theta$) and Neumann boundaries (traction $\partial\mathcal{B}_t$, water mass flux $\partial\mathcal{B}_w$, and heat flux $\partial\mathcal{B}_q$) that satisfies:

$$\begin{aligned} \partial\mathcal{B} &= \overline{\partial\mathcal{B}_u \cup \partial\mathcal{B}_t} = \overline{\partial\mathcal{B}_p \cup \partial\mathcal{B}_w} = \overline{\partial\mathcal{B}_\theta \cup \partial\mathcal{B}_q}, \\ \emptyset &= \partial\mathcal{B}_u \cap \partial\mathcal{B}_t = \partial\mathcal{B}_p \cap \partial\mathcal{B}_w = \partial\mathcal{B}_\theta \cap \partial\mathcal{B}_q. \end{aligned} \tag{2.49}$$

Then, the prescribed boundary conditions can be specified as,

$$\begin{cases} \boldsymbol{u} = \hat{\boldsymbol{u}} & \text{on } \partial\mathcal{B}_u, \\ p_w = \hat{p}_w & \text{on } \partial\mathcal{B}_p, \\ \theta = \hat{\theta} & \text{on } \partial\mathcal{B}_\theta, \end{cases} \; ; \; \begin{cases} \boldsymbol{\sigma}\cdot\boldsymbol{n} = \hat{\boldsymbol{t}} & \text{on } \partial\mathcal{B}_t, \\ -\boldsymbol{w}_w\cdot\boldsymbol{n} = \hat{w}_w & \text{on } \partial\mathcal{B}_w, \\ -\boldsymbol{q}\cdot\boldsymbol{n} = \hat{q} & \text{on } \partial\mathcal{B}_q, \end{cases} \tag{2.50}$$

where $\boldsymbol{n}$ is the outward-oriented unit normal on the boundary surface $\partial\mathcal{B}$. Meanwhile, the following boundary conditions on $\partial\mathcal{B}$ are prescribed for the phase fields c and d:

$$\nabla c\cdot\boldsymbol{n} = 0 \;\; ; \;\; \nabla d\cdot\boldsymbol{n} = 0. \tag{2.51}$$

For model closure, the initial conditions for the primary unknowns $\{\boldsymbol{u}, p_w, \theta, c, d\}$ are imposed as:

$$\boldsymbol{u} = \boldsymbol{u}_0 \;\; ; \;\; p_w = p_{w0} \;\; ; \;\; \theta = \theta_0 \;\; ; \;\; c = c_0 \;\; ; \;\; d = d_0, \tag{2.52}$$

at time $t = 0$. We also define the trial spaces V_u, V_p, V_θ, V_c, and V_d for the solution variables as,

$$\begin{aligned}
V_u &= \left\{ \boldsymbol{u} : \mathcal{B} \to \mathbb{R}^3 \mid \boldsymbol{u} \in [H^1(\mathcal{B})]^3,\ \boldsymbol{u}|_{\partial\mathcal{B}_u} = \hat{\boldsymbol{u}} \right\}, \\
V_p &= \left\{ p_w : \mathcal{B} \to \mathbb{R} \mid p_w \in H^1(\mathcal{B}),\ p_w|_{\partial\mathcal{B}_p} = \hat{p}_w \right\}, \\
V_\theta &= \left\{ \theta : \mathcal{B} \to \mathbb{R} \mid \theta \in H^1(\mathcal{B}),\ \theta|_{\partial\mathcal{B}_\theta} = \hat{\theta} \right\}, \\
V_c &= \left\{ c : \mathcal{B} \to \mathbb{R} \mid c \in H^1(\mathcal{B}) \right\}, \\
V_d &= \left\{ d : \mathcal{B} \to \mathbb{R} \mid d \in H^1(\mathcal{B}) \right\},
\end{aligned} \tag{2.53}$$

which is complimented by the admissible spaces:

$$\begin{aligned}
V_\eta &= \left\{ \boldsymbol{\eta} : \mathcal{B} \to \mathbb{R}^3 \mid \boldsymbol{\eta} \in [H^1(\mathcal{B})]^3,\ \boldsymbol{\eta}|_{\partial\mathcal{B}_u} = \boldsymbol{0} \right\}, \\
V_\xi &= \left\{ \xi : \mathcal{B} \to \mathbb{R} \mid \xi \in H^1(\mathcal{B}),\ \xi|_{\partial\mathcal{B}_p} = 0 \right\}, \\
V_\zeta &= \left\{ \zeta : \mathcal{B} \to \mathbb{R} \mid \zeta \in H^1(\mathcal{B}),\ \zeta|_{\partial\mathcal{B}_\theta} = 0 \right\}, \\
V_\gamma &= \left\{ \gamma : \mathcal{B} \to \mathbb{R} \mid \gamma \in H^1(\mathcal{B}) \right\}, \\
V_\omega &= \left\{ \omega : \mathcal{B} \to \mathbb{R} \mid \omega \in H^1(\mathcal{B}) \right\},
\end{aligned} \tag{2.54}$$

where H^1 indicates the Sobolev space of order 1. By applying the standard weighted residual procedure, the weak statements for Eqs. (2.17), (2.21), (2.28), (2.37), and (2.45) are to: find $\{\boldsymbol{u}, p_w, \theta, c, d\} \in V_u \times V_p \times V_\theta \times V_c \times V_d$ such that for all $\{\boldsymbol{\eta}, \xi, \zeta, \gamma, \omega\} \in V_\eta \times V_\xi \times V_\zeta \times V_\gamma \times V_\omega$,

$$G_u = G_p = G_\theta = G_c = G_d = 0, \tag{2.55}$$

where:

$$\begin{aligned}
G_u &= \int_{\mathcal{B}} \nabla \boldsymbol{\eta} : \boldsymbol{\sigma}\, dV - \int_{\mathcal{B}} \boldsymbol{\eta} \cdot \rho \boldsymbol{g}\, dV - \int_{\partial\mathcal{B}_t} \boldsymbol{\eta} \cdot \hat{\boldsymbol{t}}\, d\Gamma = 0, \\
G_p &= \int_{\mathcal{B}} \xi \left[\phi \dot{S}^w(c)(\rho_w - \rho_i) \right] dV + \int_{\mathcal{B}} \xi \left\{ S^w(c)\rho_w + [1 - S^w(c)]\rho_i \right\} \nabla \cdot \boldsymbol{v}\, dV
\end{aligned} \tag{2.56}$$

$$- \int_{\mathcal{B}} \nabla \xi \cdot (\rho_w \boldsymbol{w}_w)\, dV - \int_{\partial \mathcal{B}_w} \xi (\rho_w \hat{\boldsymbol{w}}_w)\, d\Gamma = 0, \tag{2.57}$$

$$G_\theta = \int_{\mathcal{B}} \zeta (\rho^s c_s + \rho^w c_w + \rho^i c_i) \dot{\theta}\, dV + \int_{\mathcal{B}} \zeta \left\{ \phi \left[(\rho_w c_w - \rho_i c_i)(\theta - \theta_m) + \rho_i L_\theta \right] \dot{S}^w(c) \right\} dV$$
$$- \int_{\mathcal{B}} \nabla \zeta \cdot \boldsymbol{q}\, dV - \int_{\mathcal{B}} \zeta \hat{r}\, dV - \int_{\partial \mathcal{B}_q} \zeta \hat{q}\, d\Gamma = 0, \tag{2.58}$$

$$G_c = \int_{\mathcal{B}} \gamma \frac{1}{M_c} \dot{c}\, dV + \int_{\mathcal{B}} \gamma \frac{\partial f_c}{\partial c}\, dV + \int_{\mathcal{B}} \nabla \gamma \cdot (\epsilon_c^2 \nabla c)\, dV = 0, \tag{2.59}$$

$$G_d = \int_{\mathcal{B}} \omega \frac{\partial g_d(d)}{\partial d} \mathcal{H}^*\, dV + \int_{\mathcal{B}} \omega d\, dV + \int_{\mathcal{B}} \nabla \omega \cdot (l_d^2 \nabla d)\, dV = 0. \tag{2.60}$$

2.4.2 Operator-split solution strategy

Although one may consider different strategies to solve the coupled system of equations [Eqs. (2.56)-(2.60)], the solution strategy adopted in this study combines the staggered scheme [76] and the isothermal operator splitting scheme [144, 145]. Specifically, we first update the damage field d via linear solver while the variables $\{\boldsymbol{u}, p_w, \theta, c\}$ are held fixed. We then apply the isothermal splitting solution scheme that iteratively solves the thermally-induced phase transition problem to advance $\{\theta, c\}$, followed by a linear solver that updates $\{\boldsymbol{u}, p_w\}$ by solving an isothermal poromechanics problem [34], i.e.,

$$\overbrace{\begin{bmatrix} \boldsymbol{u}_{\mathrm{n}} \\ p_{w,\mathrm{n}} \\ \theta_{\mathrm{n}} \\ c_{\mathrm{n}} \\ d_{\mathrm{n}} \end{bmatrix} \xrightarrow[\delta\boldsymbol{u}=\boldsymbol{0},\, \delta p_w=0,\, \delta\theta=0,\, \delta c=0]{G_d=0} \begin{bmatrix} \boldsymbol{u}_{\mathrm{n}} \\ p_{w,\mathrm{n}} \\ \theta_{\mathrm{n}} \\ c_{\mathrm{n}} \\ d_{\mathrm{n+1}} \end{bmatrix}}^{\text{Linear solver}} \overbrace{\xrightarrow[\delta\boldsymbol{u}=\boldsymbol{0},\, \delta p_w=0,\, \delta d=0]{G_\theta=G_c=0} \begin{bmatrix} \boldsymbol{u}_{\mathrm{n}} \\ p_{w,\mathrm{n}} \\ \theta_{\mathrm{n+1}} \\ c_{\mathrm{n+1}} \\ d_{\mathrm{n+1}} \end{bmatrix}}^{\text{Iterative solver}} \overbrace{\xrightarrow[\delta\theta=0,\, \delta c=0,\, \delta d=0]{G_u=G_p=0} \begin{bmatrix} \boldsymbol{u}_{\mathrm{n+1}} \\ p_{w,\mathrm{n+1}} \\ \theta_{\mathrm{n+1}} \\ c_{\mathrm{n+1}} \\ d_{\mathrm{n+1}} \end{bmatrix}}^{\text{Linear solver}}, \tag{2.61}$$

where we adopt an implicit backward Euler time integration scheme. The implementation of the model including the finite element discretization and the solution scheme relies on the finite element package `FEniCS` [146–148] with `PETSc` scientific computational toolkit

[149].

2.5 Numerical examples

This section presents three sets of numerical examples to verify (Section 2.5.1), validate (Section 2.5.2), and showcase (Sections 2.5.3 and 2.5.4) the capacity of the proposed model. Since the evolution of two phase fields c and d requires a fine mesh to capture their sharp gradients, we limit our attention to one- or two-dimensional simulations while considering the diffusion coefficient ϵ_c as an individual input parameter independent to the interface thickness δ_c which may additionally reduce the computational cost [79, 150]. We first present two examples that simulate the latent heat effect and 1d consolidation to verify the implementation of our proposed model. As a validation exercise, we perform numerical experiments that replicate the physical experiments conducted by Feng et al. [151], which studies the homogeneous freezing of a phase change material (PCM) embedded in metal foams. We then showcase the performance of the computational model for simulating the ice lens formation and the thermo-hydro-mechanical processes in geomaterials undergoing freeze-thaw cycle, and also its capacity to simulate non-planar ice lens growth that follows the crack trajectory.

2.5.1 Verification exercises: latent heat effect and 1d consolidation

Our first example simulates one-dimensional freezing of water-saturated porous media to investigate the phase transition of the fluid phase $\alpha = \{w, i\}$ and the involved latent heat effect. By comparing the results against the models presented by Lackner et al. [152] and Sweidan et al. [79], this example serves as a verification exercise that ensures the robust implementation of the heat transfer model involving phase transition [i.e., Eqs. (2.58) and (2.59)]. Hence, this example considers a rigid solid matrix while neglecting the fluid flow, following [152]. As illustrated in Fig. 2.5(a), the problem domain is a fully saturated

rectangular specimen with a height of 0.09 m and a width of 0.41 m. While the initial temperature of the entire specimen is set to be $\theta_0 = 283.15$ K, the specimen is subjected to freezing with a constant heat flux of $\hat{q} = 100$ W/m^2 on the top surface, whereas all other boundaries are thermally insulated. Here, we choose the same material properties used in [152] and [79] as follows: $\phi_0 = 0.42$, $\rho_s = 2650$ kg/m^3, $\rho_w = 1000$ kg/m^3, $\rho_i = 913$ kg/m^3, $c_s = 740$ J/kg/K, $c_w = 4200$ J/kg/K, $c_i = 1900$ J/kg/K, $\kappa_s = 7.694$ W/m/K, $\kappa_w = 0.611$ W/m/K, and $\kappa_i = 2.222$ W/m/K. In addition, we set $\nu_c = 0.001$ m/s, $\gamma_c = 0.03$ J/m^2, $\delta_c = 0.005$ m, and $\epsilon_c = 1.25$ (J/m)$^{1/2}$ for the Allen-Cahn phase field model, while we use the structured mesh with element size of $h_e = 0.6$ mm and choose the time step size of $\Delta t = 100$ sec.

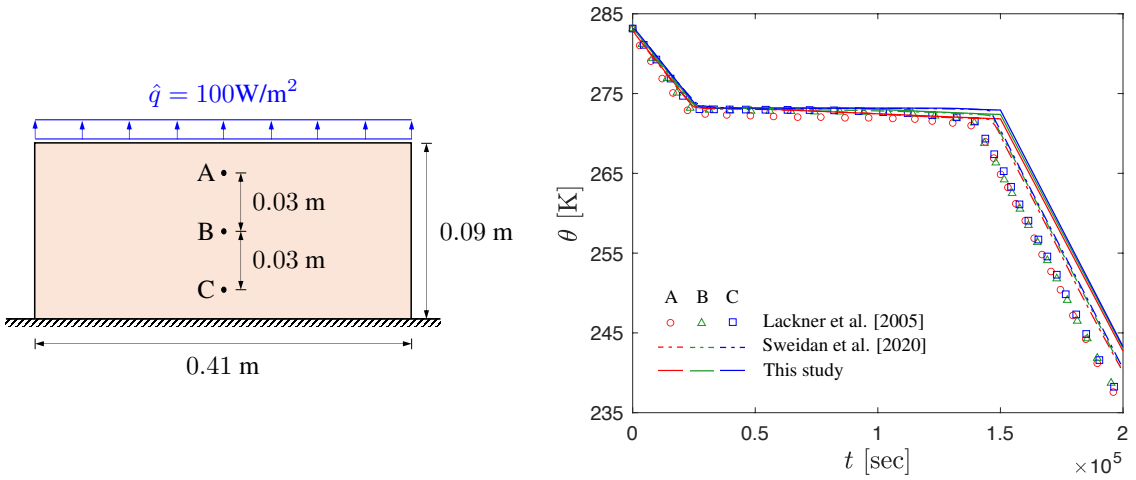

(a) (b)

Figure 2.5: (a) Schematic of geometry and boundary conditions for the 1d freezing example; (b) Temperature evolution at points A, B, and C.

As shown in Figure 2.5(b), measured temperatures at points A, B, and C during the simulation first linearly decrease due to the applied heat flux $\hat{q}$ until they reach the freezing temperature of $\theta_m = 273.15$ K. As soon as the phase transition starts, the freezing front propagates through the specimen while the release of the energy associated with the phase transition prevents the temperature decrease (i.e., latent heat effect). Once the phase change is complete, the temperature linearly decreases over time again since the heat transfer pro-

cess is no longer affected by the latent heat. More importantly, a good agreement with the results reported in [79, 152] verifies that our proposed model is capable of capturing the thermal behavior of the phase-changing porous media.

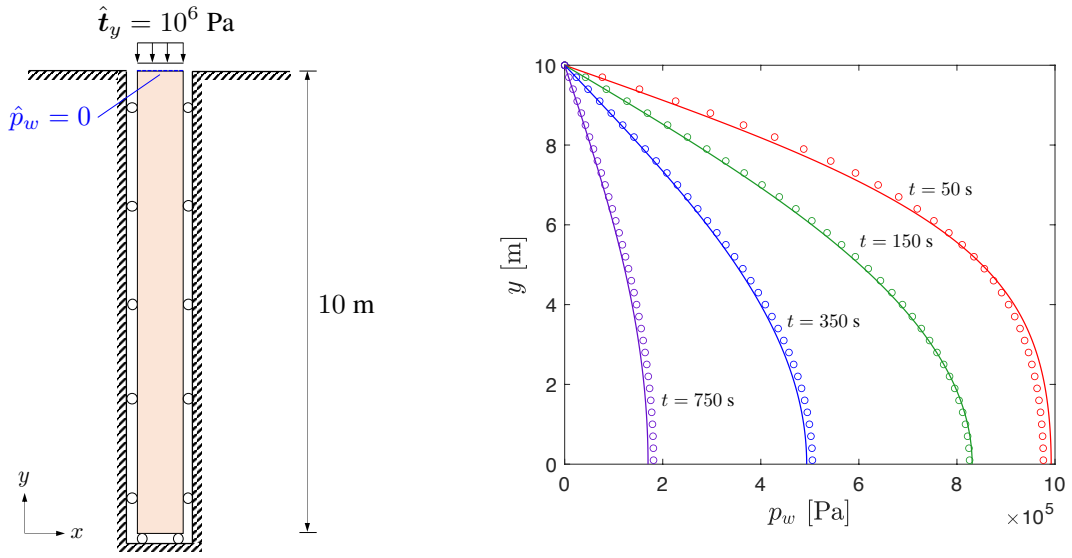

Figure 2.6: (a) Schematic of geometry and boundary conditions for Terzaghi's problem; (b) Time-dependent pore water pressures along the height of the specimen.

For the second verification exercise, we choose the classical Terzaghi's 1d consolidation problem since it possesses an analytical solution [153], which can directly be compared with the results obtained via poromechanics model [Eqs. (2.56) and (2.57)]. Our problem domain shown in Fig. 2.6(a) consists of a 10 m high water-saturated linear elastic soil mass. While a 1 MPa compressive load $\boldsymbol{t}_y$ is imposed on the top surface, we replicate the single-drained condition by prescribing zero pore water pressure at the top ($\hat{p}_w = 0$) and a no-slip condition at the bottom. By assuming that the temperature of the soil column remains constant during the simulation ($\theta = 293.15$ K), we only focus on its hydro-mechanically coupled response while the material parameters are chosen as follows: $\phi_0 = 0.4$, $\rho_s = 2650$ kg/m^3, $\rho_w = 1000$ kg/m^3, $K = 66.67$ MPa, $G = 40$ MPa, $k_{\text{mat}} = 10^{-12}$ m^2, and $\mu_w = 10^{-3}$ Pa·s. Here, we choose $h_e = 0.1$ m and $\Delta t = 20$ sec.

Fig. 2.6(b) illustrates the pore water pressure profile during the simulation at $t = 50$,

150, 350, and 750 s. The results show that the applied mechanical load $\boldsymbol{t}_y$ builds up the pore water pressure, affecting the pore water to migrate towards the top surface, which leads to the dissipation of the excess pressure over time (i.e., consolidation). By comparing the simulation results (circular symbols) to the analytical solution (solid curves), Fig. 2.6(b) verifies the reliability of our model to capture the hydro-mechanically coupled responses.

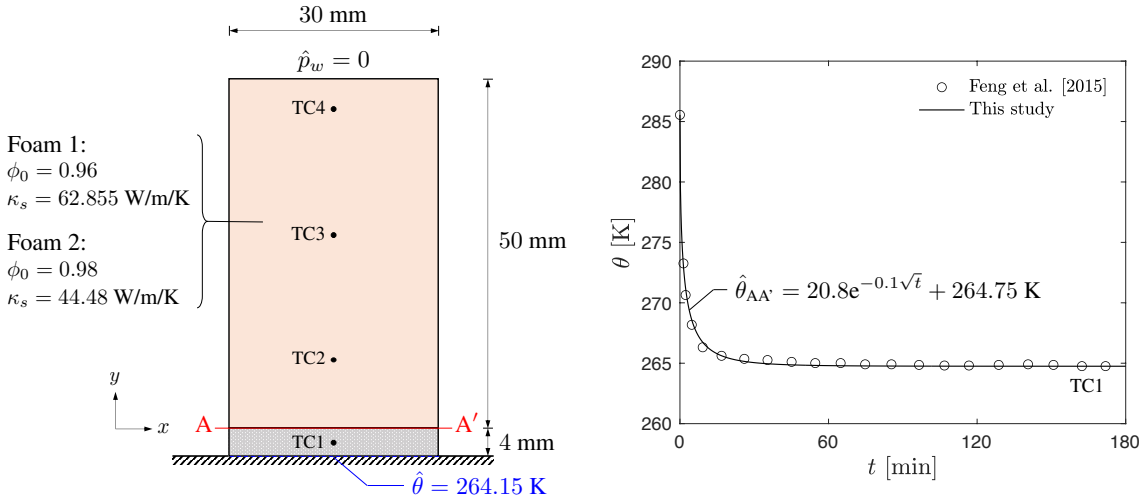

Figure 2.7: (a) Schematic of the experimental setup for the unidirectional freezing test conducted in [151]; (b) Temperature boundary condition applied at the bottom surface of the copper foam (AA') for the numerical simulation.

2.5.2 Validation example: homogeneous freezing

This section compares the results obtained from the numerical simulation against the physical experiment conducted by Feng et al. [151]. This experiment is used as a benchmark since it considers the unidirectional freezing of distilled water filled in porous copper foams, which does not involve a fracturing process and yields a clear water-ice boundary layer due to the microstructural attributes of the host matrix. As schematically shown in Fig. 2.7(a), a 30 mm wide, 50 mm long water-saturated copper foam is mounted on a 4 mm thick copper block. While the initial temperature is measured to be $\theta_0 = 285.55$ K, the experiment is performed by applying a constant temperature of $\hat{\theta} = 264.15$ K at the bottom part of

the copper block at $t = 0$. Temperature measurements during the experiment are made by three thermocouples (TC2-TC4) located at 10 mm, 28 mm, and 46 mm from the bottom of the foam (AA'), whereas TC1 records the temperature of the block. For the numerical simulation, instead of considering the problem domain as a layered material, we only focus on the water-saturated copper foam and apply time-dependent Dirichlet boundary condition on AA' by using the temperature measured by TC1 [Fig. 2.7(b)]. We also assume an unlimited water supply from the top surface by imposing $\hat{p}_w = 0$ and applying a fixed boundary condition at the bottom part of the foam. Moreover, we consider two different types of copper foams (Foam 1 and Foam 2) with different initial porosity and thermal conductivity [Fig. 2.7(a)]. As summarized in Table 2.1, our numerical simulation directly adopts the same thermal properties compared to the physical experiment whereas the solid phase thermal conductivities of the foams are computed based upon the effective properties reported in [151]. For all other material parameters that are not specified in [151], we choose the properties that resemble those of the water-saturated copper foam. In this section, the Allen-Cahn parameters are chosen as: $\nu_c = 0.0001$ m/s, $\gamma_c = 0.065$ J/m^2, $\delta_c = 0.0001$ m, and $\epsilon_c = 0.75$ (J/m)$^{1/2}$, while adopting a structured mesh with $h_e = 2.5$ mm and $\Delta t = 60$ sec.

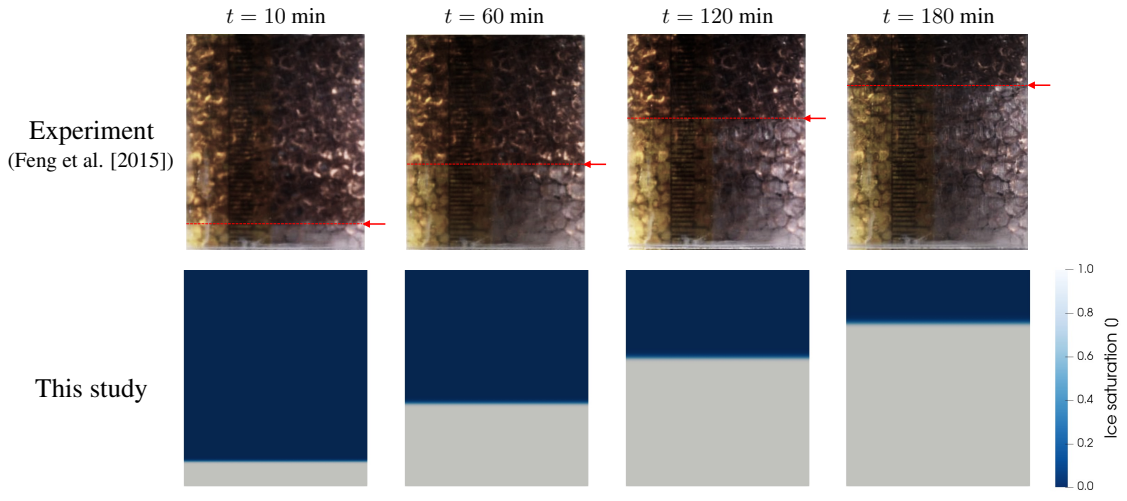

Figure 2.8: Comparison between the physical and numerical experiments on the evolution of the water-ice interface.

Table 2.1: Material parameters for the validation exercise.

Parameter	Description [Unit]	Value	Reference
ρ_s	Intrinsic solid mass density [kg/m^3]	7800.0	-
ρ_w	Intrinsic water mass density [kg/m^3]	1000.0	[151]
ρ_i	Intrinsic ice mass density [kg/m^3]	920.0	[151]
c_s	Specific heat of solid [J/kg/K]	0.385×10^3	-
c_w	Specific heat of water [J/kg/K]	4.216×10^3	[151]
c_i	Specific heat of ice [J/kg/K]	2.040×10^3	[151]
κ_s	Thermal conductivity of solid [W/m/K]	62.855, 44.48	[151]
κ_w	Thermal conductivity of water [W/m/K]	0.56	[151]
κ_i	Thermal conductivity of ice [W/m/K]	1.90	[151]
K	Bulk modulus of solid skeleton [Pa]	93.75×10^9	-
K_i	Bulk modulus of ice [Pa]	5.56×10^9	-
G	Shear modulus of solid skeleton [Pa]	33.58×10^9	-
G_i	Shear modulus of ice [Pa]	4.20×10^9	-
ϕ_0	Initial porosity [-]	0.96, 0.98	[151]
k_{mat}	Matrix permeability [m^2]	3.25×10^{-7}	-
μ_w	Viscosity of water [Pa·s]	1.0×10^{-3}	-
$\alpha_{v,\text{int}}$	Volumetric expansion coefficient [-]	5.0×10^{-3}	-

Fig. 2.8 illustrates the evolution of the freezing front within a water-saturated copper foam (Foam 2). In both the physical and numerical experiments, water freezing starts from the bottom (AA') and migrates towards the upper part of the foam over time, depending on the conductive heat transfer process. While it shows a qualitative agreement between the two, Fig. 2.9 quantitatively confirms the validity of our model, where we use the circular symbols to indicate the experimental measurements whereas the solid curves denote the numerical results. As shown in Fig. 2.9(a), since Foam 1 possesses higher solidity (lower porosity) compared to Foam 2, the water-ice interface tends to grow relatively faster because it exhibits higher effective thermal conductivity. In addition, temperature variations illustrated in Fig. 2.9(b) clearly show the interplay between the thermal boundary layer growth and the latent heat, resulting in a nonlinear evolution of the freezing front. Although has not been measured experimentally, we further investigate the time-dependent hydro-mechanical response of the specimen from the simulation results shown in Fig. 2.10.

Based on the freezing retention curve [Eq. (2.31)] adopted in this study, positive suction starts to develop if $\theta < \theta_m$ while the region where $s^*_{\text{cryo}} > 0$ evolves over time following the same trajectory of that of the freezing front [Fig. 2.10(a)]. This process also involves a volumetric expansion of the specimen that leads to an increase of the vertical displacement as shown in Fig. 2.10(b), due to the difference between water (ρ_w) and ice densities (ρ_i). Since our framework idealizes the material as a multiphase mixture of the solid, water, and ice phase constituents, notice that relatively small displacement compared to the volume expansion due to the ice-water phase transition is because of the mechanical properties of the host matrix, which is less compressible compared to geological materials. It should be also noted that the freezing front always exhibits the largest vertical displacement, implying that the water migration towards the freezing front induced by the suction triggers the consolidation process above the frozen area, resulting in a small volumetric compression therein. This observation agrees with the explanation in [154] where the consolidation front of a frozen soil has been observed experimentally, which corroborates the applicability of our proposed model.

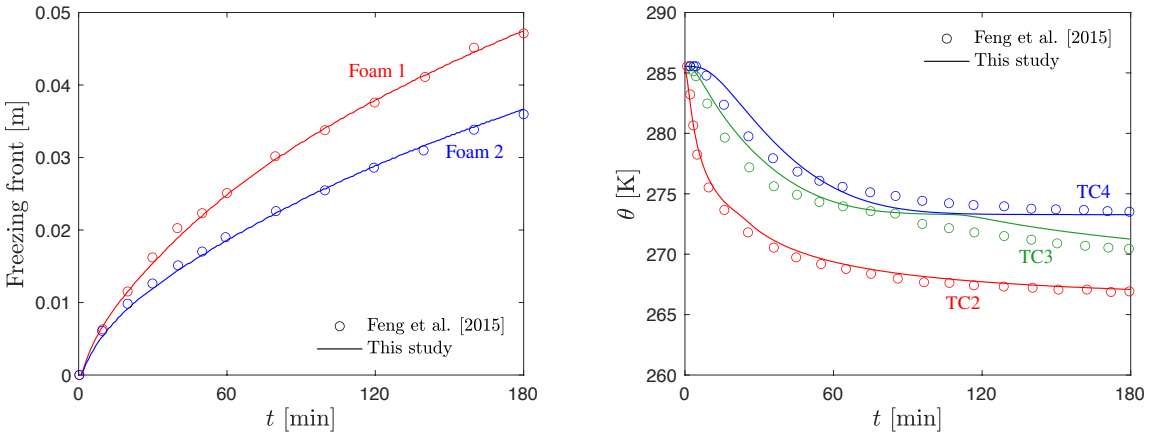

Figure 2.9: (a) Evolution of the freezing front over time; (b) Temperature variation within Foam 2 measured from TC2, TC3, and TC4.

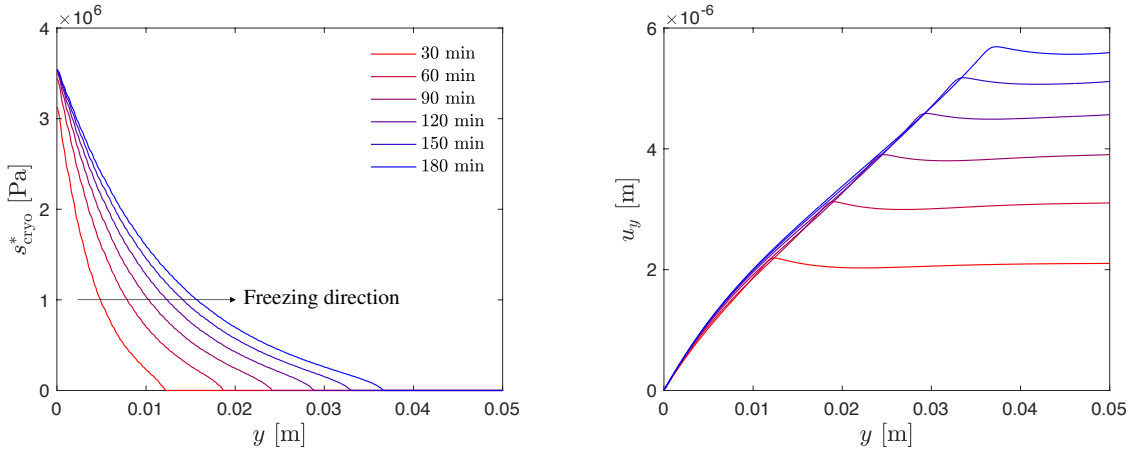

Figure 2.10: Hydro-mechanical response of Foam 2 subjected to freezing: (a) cryo-suction (s^*_{cryo}) and (b) vertical displacement (u_y) profiles.

2.5.3 Freeze-thaw action: multiple ice lens growth and thawing in heterogeneous soil

In this section, we showcase the capability of our proposed model by simulating the formation and melting of multiple ice lenses inside a heterogeneous clayey soil specimen. As illustrated in Fig. 2.11(a), the problem domain is 0.04 m wide and 0.1 m long soil column that possesses a random porosity profile along the vertical axis with a mean value of $\phi_{\text{ref}} = 0.4$ such that the specimen possesses layered microstructure. In addition, we introduce a set of heterogeneous material properties that solely depends on the spatial distribution of initial porosity ϕ_0. Specifically, we adopt a phenomenological model proposed by [155] for the shear modulus G, while we use a power law for the critical energy release rate $\mathcal{G}_d$ similar to [140, 156]:

$$G = \frac{3}{2}\left(\frac{1-2\nu}{1+\nu}\right)\exp\left[10(1-\phi_0)\right]\,[\text{MPa}]\;\;;\;\;\mathcal{G}_d = \mathcal{G}_{d,\text{ref}}\left(\frac{1-\phi_0}{1-\phi_{\text{ref}}}\right)^{n_\phi}. \tag{2.62}$$

Here, we assume that the Poisson's ratio remains constant $\nu = 0.25$ throughout the entire domain while we set $\mathcal{G}_{d,\text{ref}} = 1.5$ N/m and $n_\phi = 50$. Based on this setting, we attempt to

incorporate ice lens initiation criterion proposed by Zhou and Li [59], where a separation void ratio determines the positions of the ice lenses. For all other material properties that are homogeneous, as summarized in Table 2.2, we choose values similar to those of the clayey soil. It should be noted that we adopt $\alpha_{v,\text{dam}} = 0.08$ which is identical to the theoretical value of $1-\rho_i/\rho_w$ for the expansion coefficient, whereas we set $\alpha_{v,\text{int}} = 0.005$ due to the existence of thin water film between the intact solid and the pore ice. Meanwhile, the parameters for the Allen-Cahn phase field equation are chosen as: $\nu_c = 0.0001$ m/s, $\gamma_c = 0.065$ J/m^2, $\delta_c = 0.0001$ m, and $\epsilon_c = 1.0$ (J/m)$^{1/2}$, whereas we set $h_e = 0.5$ mm and $\Delta t = 60$ sec.

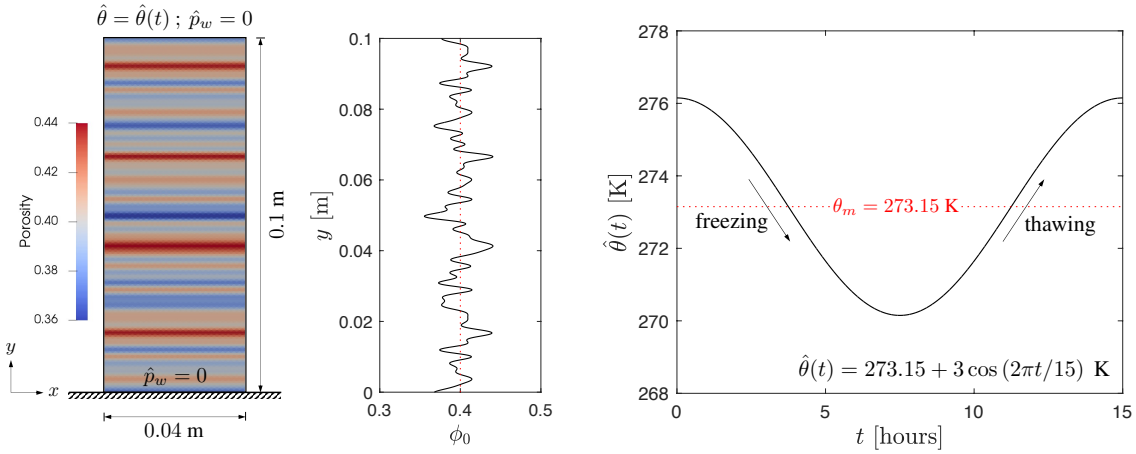

Figure 2.11: (a) Schematic of geometry and boundary conditions for the numerical freeze-thaw test; (b) Temperature boundary condition applied at the top surface.

While we set the initial temperature as $\theta_0 = 276.15$ K, the numerical freeze-thaw test is performed by applying a time-dependent temperature boundary condition at the top, represented by a sinusoidal function. As shown in Fig. 2.11(b), the freezing process starts at $t = 3.75$ hr and continues until the top surface temperature reaches the melting temperature of $\theta_m = 273.15$ K at $t = 11.25$ hr, where the frozen soil begins to thaw. During the simulation, the bottom part of the specimen is held fixed while we prescribe zero pore water pressure boundaries ($\hat{p}_w = 0$) at both the top and the bottom surfaces. The left and right boundaries, on the other hand, are subjected to zero water mass flux and heat flux conditions. Based on this setting, the water is supplied from the bottom during the freezing

Table 2.2: Material parameters for the numerical freeze-thaw test.

Parameter	Description [Unit]	Value
ρ_s	Intrinsic solid mass density [kg/m^3]	2650.0
ρ_w	Intrinsic water mass density [kg/m^3]	1000.0
ρ_i	Intrinsic ice mass density [kg/m^3]	920.0
c_s	Specific heat of solid [J/kg/K]	0.75×10^3
c_w	Specific heat of water [J/kg/K]	4.20×10^3
c_i	Specific heat of ice [J/kg/K]	1.90×10^3
κ_s	Thermal conductivity of solid [W/m/K]	7.69
κ_w	Thermal conductivity of water [W/m/K]	0.56
κ_i	Thermal conductivity of ice [W/m/K]	2.25
K_i	Bulk modulus of ice [Pa]	5.56×10^9
G_i	Shear modulus of ice [Pa]	4.20×10^9
ϕ_{ref}	Reference porosity [-]	0.4
k_{mat}	Matrix permeability [m^2]	1.0×10^{-13}
μ_w	Viscosity of water [Pa·s]	1.0×10^{-3}
$\mathcal{G}_{d,\text{ref}}$	Reference critical energy release rate [N/m]	1.5
l_d	Regularization length scale parameter [m]	1.0×10^{-3}
$\mathcal{H}_{\text{crit}}$	Normalized threshold strain energy [-]	0.05
$\alpha_{v,\text{int}}$	Volumetric expansion coefficient (intact) [-]	5.0×10^{-3}
$\alpha_{v,\text{dam}}$	Volumetric expansion coefficient (damaged) [-]	80.0×10^{-3}
K_c^*	Kinetic parameter [Pa]	5.0×10^9
g_c^*	Kinetic parameter [-]	1.25

phase, while the water expulsion towards the top surface during the melting phase leads to a thawing settlement of the specimen.

Fig. 2.12 shows the formation and melting of multiple ice lenses and the evolution of the fracture phase field during the numerical freeze-thaw test. Here, we use a scaling factor of 5 while the color bar illustrated in Fig. 2.12(a) represents the value of the indicator function χ^i defined in Eq. (2.11). As illustrated in Fig. 2.13, the water freezes from the top to the bottom during the freezing phase (3.75 hr $\leq t \leq 11.25$ hr), which leads to the development of the cryo-suction and a volumetric expansion due to the phase transition. Since the applied temperature at the top starts to increase after reaching its minimum, s^*_{cryo} tends to decrease after $t = 7.5$ hr due to the freezing characteristic function in Eq. (2.31) although the freezing front still propagates towards the bottom. Also, during the freezing phase, soil specimen

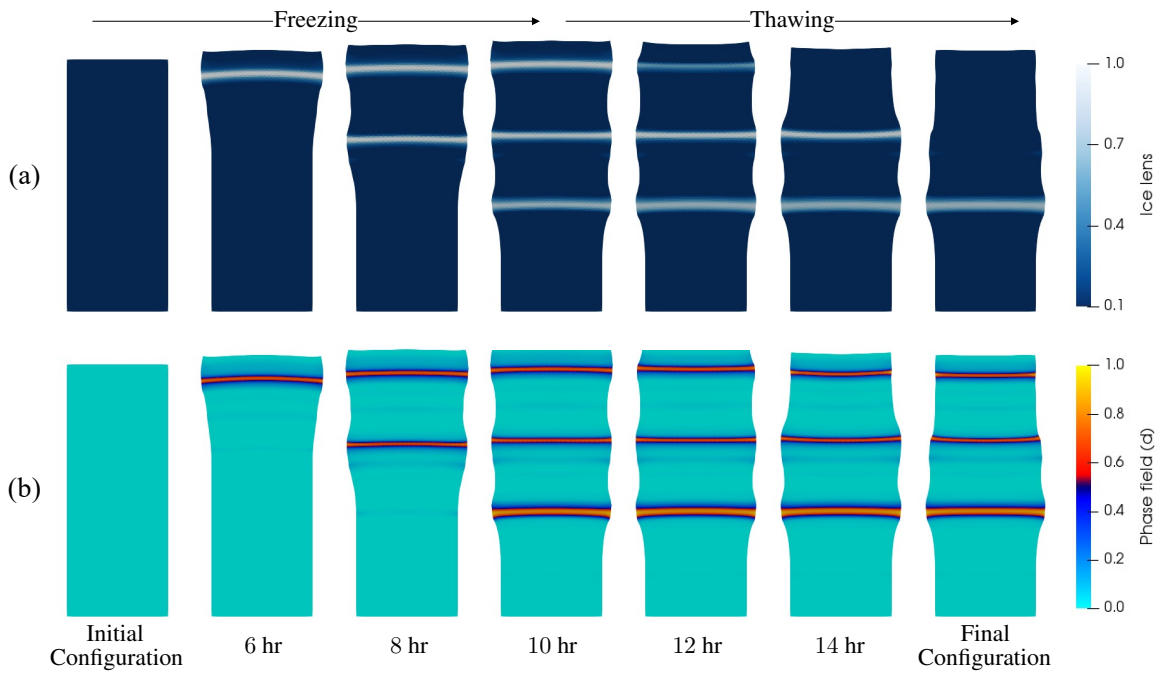

Figure 2.12: (a) Formation and melting of multiple ice lenses and (b) evolution of the fracture phase field d during the numerical freeze-thaw test.

tends to exhibit a constant temperature distribution at the region below the freezing front due to the latent heat effect, similar to our previous example shown in Section 2.5.2. More importantly, we observe a sequential development of the ice lenses at $y = 0.092$ m, $y = 0.066$ m, and $y = 0.042$ m, respectively, which implies that separation void ratio (e_{sep}) can be approximated as $\sim$0.75 [59]. This result is expected, since those regions possess relatively high initial porosity compared to the other regions [Fig. 2.11(a)]. If the freezing front reaches the porous zone where the critical energy release rate is relatively low, both the cryo-suction and the exerted stress due to the phase transition initiate the horizontal crack.

Once the freezing-induced fracture is developed, segregated bulk ice tends to form inside the opened crack at higher growth rates that lead to an abrupt volume expansion therein (Fig. 2.12). As illustrated in Fig. 2.14, we observe the opposite response during the thawing phase (11.25 hr $\leq t \leq 15$ hr). At $t = 11.25$ hr, once the applied temperature at the top again reaches the melting temperature $\theta_m = 273.15$ K, the soil specimen stops freezing and

begins to thaw from the top to the bottom. During the thawing process, the melting front tends to move downwards whereas the freezing front remains unchanged since the bottom surface is thermally insulated. As the melted region where $\theta > \theta_m$ evolves, the vertical displacement tends to decrease over time due to both the volume contraction during the phase transition and the water expulsion towards the top surface.

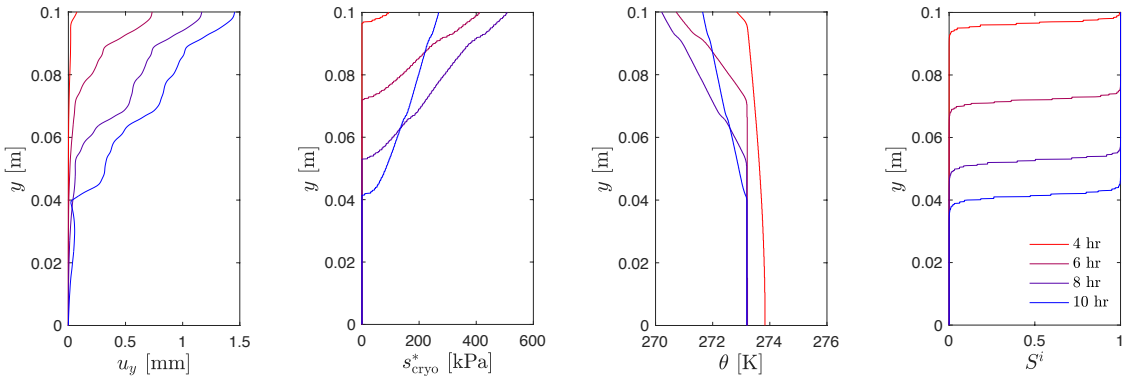

Figure 2.13: Thermo-hydro-mechanical response of the specimen during the freezing phase: (a) vertical displacement (u_y), (b) cryo-suction (s^*_{cryo}), (c) temperature (θ), and (d) ice saturation (S^i) profiles along the central axis.

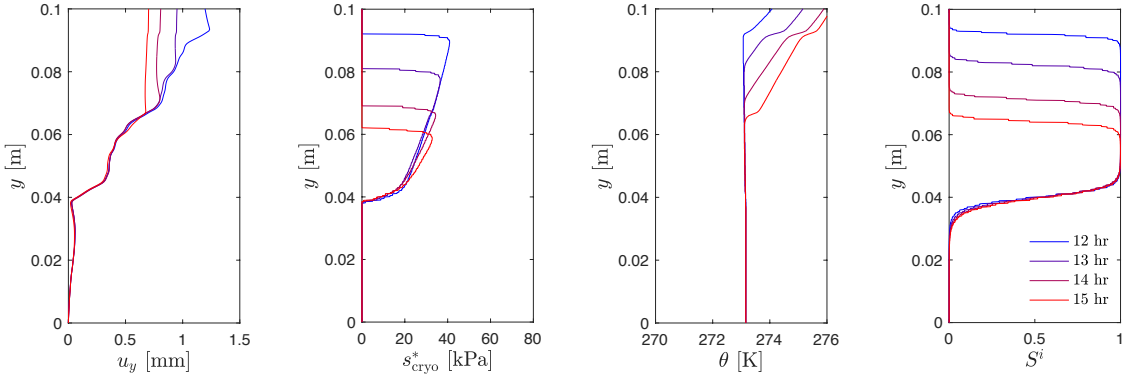

Figure 2.14: Thermo-hydro-mechanical response of the specimen during the thawing phase: (a) vertical displacement (u_y), (b) cryo-suction (s^*_{cryo}), (c) temperature (θ), and (d) ice saturation (S^i) profiles along the central axis.

Fig. 2.15 shows the evolution of the vertical displacement of the top surface during the freeze-thaw test (black curve). For comparison, we introduce a control experiment

where the phase field solvers for both ice lens and damage are disabled but otherwise the material parameters are identical (blue curve). Hence, the numerical specimen in the control experiment may exhibit homogeneous freezing and thawing but not ice lens formation and melting. The frost heave and thawing settlement for both experiments are compared to assess the impact of the ice lenses on the material responses.

In the prime numerical experiment, ice lenses sequentially develop at $y = 0.092$ m, $y = 0.066$ m, and $y = 0.042$ m (see Fig. 2.12), respectively. Each time the ice lens begins to form, the soil expands more rapidly and hence the steeper slope of the black curve, which indicates the rapid expansion of the numerical specimen, at $t = 4.2$ hr, $t = 6.2$ hr, and $t = 8.8$ hr. During the thawing phase, the prescribed temperature of the top surface increase. This temperature increase leads to abrupt settlement within the first 2 hours of the thawing phase. As the ice lenses melt and subsequently drain out from the domain, the numerical specimen shrinks (black curve). In contrast, homogeneous freezing and thawing result in considerably less amount of frost heaving and thawing settlement, due to the absence of cracks where ice lenses may form.

The significant difference between the two simulations has important practical implications. It is presumably possible to use an optimization algorithm to identify the material parameters such that the control experiment may match better with the observed frost heave and thawing settlements of soil vulnerable to ice lens formation. However, the apparent match obtained from such an excessive calibration is fruitless as it may lead to material parameters that are not physics and therefore lead to a model weak at forward predictions. Results of these numerical experiments again suggest that the ice lenses play a key role in frost heaving and the subsequent settlement of soils. This example also highlights that our proposed model is capable of simulating the ice lens growth and thaw in a fluid-saturated porous media, which may not be easily captured via a classical thermo-hydro-mechanical model.

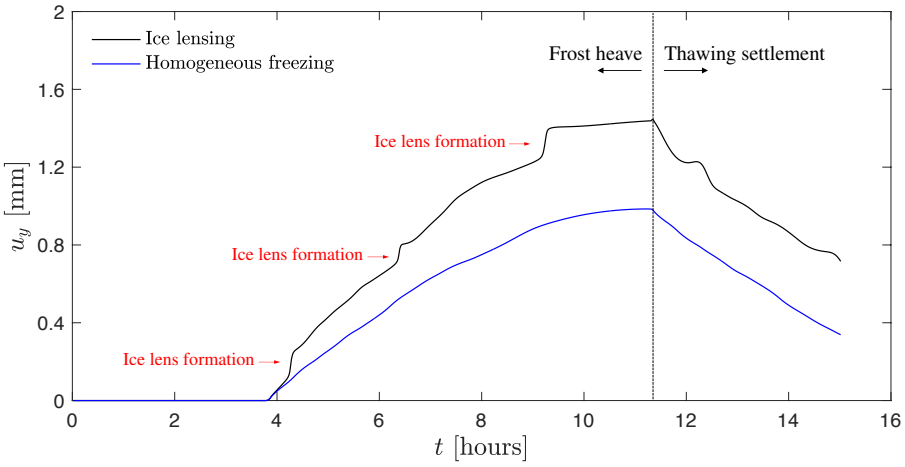

Figure 2.15: Vertical displacement (u_y) evolution of the top surface during the numerical freeze-thaw test. The black curve is obtained from a thermo-hydro-mechanical simulation that enables ice lensing; the blue curve is obtained from the control experiment that takes out the ice lensing capacity.

2.5.4 Vertical ice lens growth in edge notched specimen

While numerical example presented in Section 2.5.3 demonstrated horizontal ice lens formation perpendicular to the freezing direction, in this section, we simulate vertical ice lens growth which is parallel to the freezing direction, by leveraging the proposed driving force [Eq. (2.27)] for the Allen-Cahn equation. Specifically, our objective is to demonstrate the formation of an ice lens that follows the crack trajectory that leads to a non-planar ice growth. Hence, as shown in Fig. 2.16, the problem domain is a 0.06 m wide and 0.02 m long rectangular globally undrained porous specimen that contains a 0.005 m long initial vertical edge notch along the central axis, while considering an ideal case where $\boldsymbol{\sigma}'_{\text{dam}} = \mathbf{0}$ and $\bar{\alpha}_v = 0$ to focus on the ice lens growth along the crack by decoupling the interactions between the two. By setting the initial temperature as $\theta_0 = 274.15$ K, the numerical experiment is performed by applying a constant heat flux of $\hat{q} = 25$ W/m^2 that induces conductive vertical cooling from the top surface, with prescribed vertical displacement $\hat{\boldsymbol{u}}$ at a rate of -10^{-6} mm/s to promote crack growth from the notch tip. Here, we assume that the material is homogeneous while the material parameters are chosen as follows: $\phi_0 = 0.2$, $\rho_s = 2500$

kg/m^3, $\rho_w = 1000$ kg/m^3, $\rho_i = 920$ kg/m^3, $E = 2.5$ GPa, $\nu = 0.3$, $k_{\text{mat}} = 10^{-15}$ m^2, $\mu_w = 10^{-3}$ Pa·s, $c_s = 0.9 \times 10^3$ J/kg/K, $c_w = 4.2 \times 10^3$ J/kg/K, $c_i = 1.9 \times 10^3$ J/kg/K, $\kappa_s = 7.55$ W/m/K, $\kappa_w = 0.5$ W/m/K, $\kappa_i = 2.25$ W/m/K, $\mathcal{G}_d = 2.25$ N/m, $l_d = 1.0 \times 10^{-3}$ m, $K_c^* = 5.0 \times 10^9$ Pa, and $g_c^* = 1.25$. In addition, we set $\nu_c = 0.0001$, $\gamma_c = 0.05$ J/m^2, $\delta_c = 0.0001$ m, and $\epsilon_c = 0.5$ (J/m)$^{1/2}$ for the Allen-Cahn phase field model while adopting the structured mesh with element size of $h_e = 0.25$ mm and the time step size of $\Delta t = 1$ min.

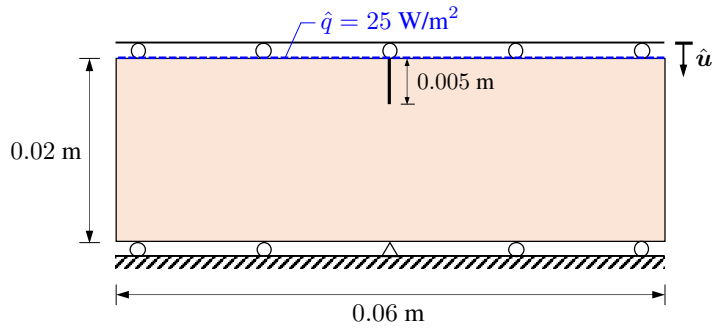

Figure 2.16: Schematic of geometry and boundary conditions for the single edge notched test.

Based on this setting, as shown in Fig. 2.17, prescribed compression results in tensile stresses perpendicular to the loading direction that stimulates crack growth, while permeability enhancement [Eq. (2.46)] and relative permeability [Eq. (2.39)] yield relatively low pore water pressure inside the notch similar to the results shown in [141]. The phase transition process of pore water begins once the temperature at the top surface reaches the freezing temperature θ_m in both the damaged and undamaged regions, however, since the proposed driving force for the Allen-Cahn equation in Eq. (2.27) leads to an intense growth of ice inside the fracture (i.e., ice lens) such that the phase field c tends to evolve faster inside the damaged region [Fig. 2.17(a) and Fig. 2.17(d)].

As evidenced in Fig. 2.17(d), ice phase tends to continuously grow along the pre-existing notch until crack initiates from the tip. Then, as illustrated in Fig. 2.18, once crack starts to propagate due to the combined effect of ice-water phase transition and the applied load, ice lens tends to follow the crack trajectory. We can also see from Fig. 2.18

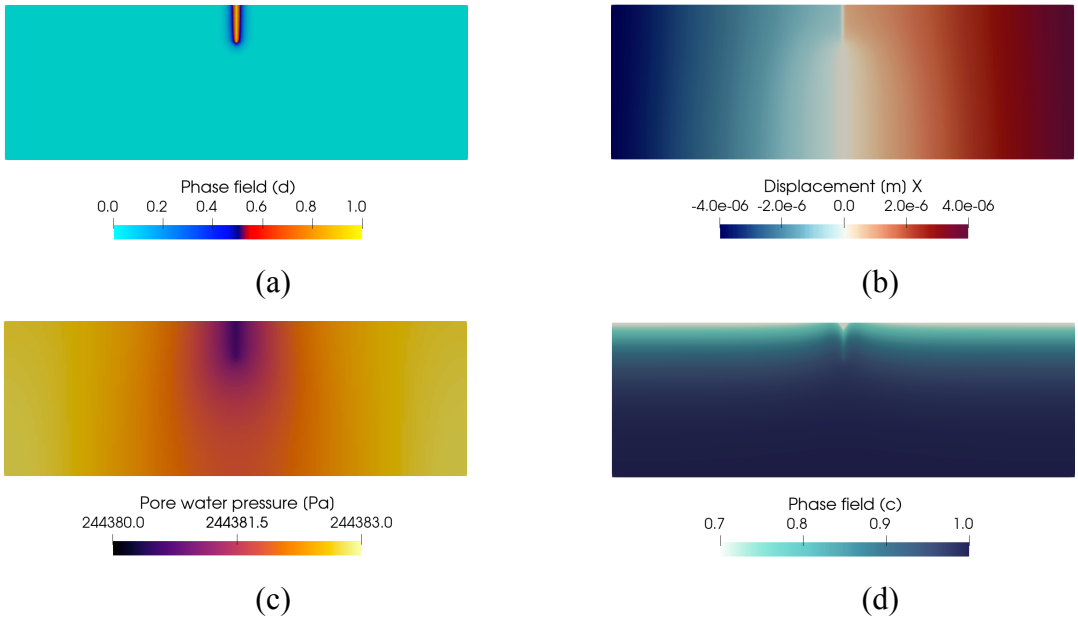

Figure 2.17: Transient response of porous specimen at $t = 45$ min. (a) fracture phase field d; (b) x-displacement u_x; (c) pore water pressure p_w; and (d) Allen-Cahn phase field c.

that crack opening leads to complete fragmentation of the solid matrix due to the relation shown in Eq. (2.48), which results in more realistic ice lens simulations since it possesses zero solidity, i.e., $1-\phi$. More importantly, the results indicate that our proposed framework is not only restricted to simulating planar ice lenses but also capable of modeling non-planar ice lenses that are not necessarily perpendicular to the freezing direction, which may have a more profound impact on microporomechanical problems that involve water adsorption processes which can affect microscopic fluid motion inside the heterogeneous matrix and hence the freezing patterns.

2.6 Conclusion

In this work, we introduce a multi-phase-field microporomechanics theory and the corresponding finite element solver to capture the freeze-thaw action in a frozen/freezing/thawing porous medium that may form ice lenses. By introducing two phase field variables that indicate the phase of the ice/water and damaged/undamaged material state, the pro-

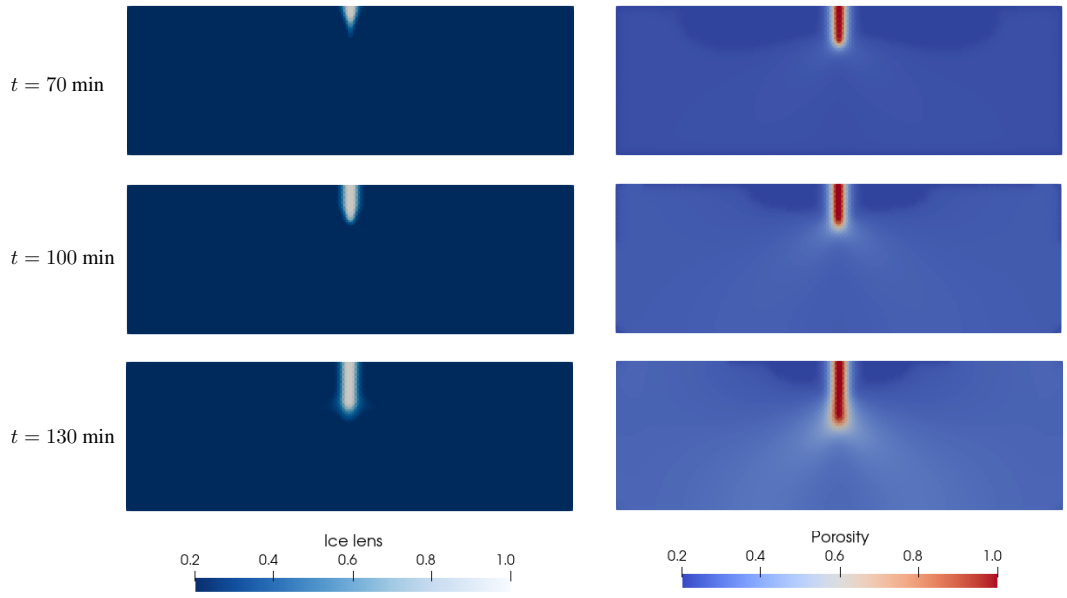

Figure 2.18: Evolution of ice lens (χ^i) and porosity (ϕ) during vertical freezing of edge notched specimen.

posed thermo-hydro-mechanical model is capable of simulating the freezing-induced fracture caused by the growth of the ice lens as segregated ice. We also extend the Bishop's effective stress principle for frozen soil to incorporate the effects of damage and ice growth and distinguish them from those of the freezing retention responses. This treatment enables us to take into account the shear strength of the ice lenses and analyzes how the homogeneous freezing process and the ice lens growth affect the thermo-hydro-mechanical coupling effects in the transient regime. The model is validated against published freezing experiments. To investigate how the formation and thawing of ice lens affect the frost heave and thaw settlement, we conduct numerical experiments that simulate the climate-induced frozen heave and thaw settlement in one thermal cycle and compare the simulation results with those obtained from a thermo-hydro-mechanical model that does not explicitly capture the ice lens. The simulation results suggest that explicitly capturing the growth and thaw of ice lens may provide more precise predictions and analyses on the multi-physical coupling effects of frozen soil at different time scales. Accurate and precise predictions on the frozen heave and thaw settlement are crucial for many modern engineering applications,

from estimating the durability of pavement systems to the exploration of ice-rich portions of Mars. This work provides a foundation for a more precise depiction of frozen soil by incorporating freezing retention, heat transfer, fluid diffusion, fracture mechanics, and ice lens growth in a single model. More accurate predictions nevertheless may require sufficient data to solve the inverse problems and quantify uncertainties as well as optimization techniques to identify material parameters from different experiments. Such endeavors are important and will be considered in the future studies.

Chapter 3: Asynchronous phase field fracture model for porous media with thermally non-equilibrated constituents

This chapter is published as: H.S. Suh, W.C. Sun, Asynchronous phase field fracture model for porous media with thermally non-equilibrated constituents, Computer Methods in Applied Mechanics and Engineering, Volume 387, 2021, doi.org/10.1016/j.cma.2021.114182.

3.1 Introduction

The thermo-hydro-mechanical responses of porous media are critical for many geothermal and geomechanics applications such as underground radioactive waste disposal, geothermal energy recovery, oil production, and CO_2 geological storage [157–165]. For instance, frictional heating may lead to the temperature increase of both the solid skeleton and the pore fluid through heat exchanges [133]. Geological storage of CO_2 and oil recovery often require the injection of the pore fluid in a supercritical state such that the thermal convection may play an important role both for the fluid transport and the fluid-driven fracture. The combination of temperature, pressure, and loading rate are also critical for the brittle-ductile transition of geological materials [166–168]. Heat exchange is an important mechanism for selecting the candidate materials for the nuclear waste geological disposal such as clay and salt. Long-term disposal such as the Yucca Mountain Project in New Mexico, for instance, relies on the combination of low permeability, high thermal conductivity, and self-healing mechanisms to ensure the isolation of the radioactive wastes [137, 169, 170].

Traditionally, large-scale reservoir simulators that simulate thermo-hydro-mechanical responses of porous media, such as TOUGH-FLAC [171] and OpenGeoSys [172], often assume that different constituents of the porous media share the same temperature. This assumption could be valid when (1) the representative elementary volume is sufficiently large for the macroscopic porous continua to function as an effective medium for the multiphase materials, and (2) when the time scale considered in the simulations is much larger than the time it takes for the constituents to reach equilibrium locally. This assumption may lead to discrepancy to experimental observation when the constituents have significant difference in specific heat capacity and thermal conductivity, and when the temporal and spatial scales of interest are sufficiently small such that the homogenized temperature may yield erroneous results that violates the thermodynamic principle [69, 101, 173–180].

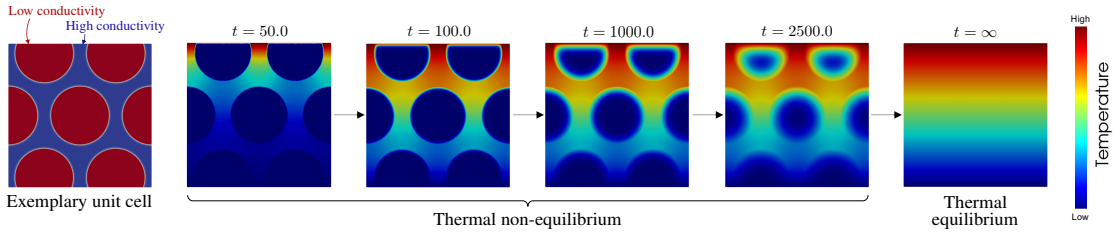

Figure 3.1: Longitudinal heat transfer on an exemplary unit cell that consists of two different materials with different thermal conductivities.

As a thought experiment, we construct a heat conduction problem of which the domain is occupied by a two-phase material where the host matrix exhibits four orders higher thermal conductivity than that of the inclusion. As demonstrated in Fig. 3.1, this leads to a period of transition in which the heat transfer among the constituents dominates the overall thermal responses. While it is possible to obtain effective thermal conductivity through homogenization, doing so may not be suitable to capture the thermo-hydro-mechanical responses where the difference in the thermal expansion among the constituents and the thermal-softening of the solid skeleton may both affect the residual stress of the constituents. This issue has also been captured in experiments. For example, Truong and Zinsmeister [181] showed that the one-temperature approach may not yield physically consistent re-

sults if thermal conductivities of the constituent differ significantly, which corroborates our simulation in Fig. 3.1, while He, Jin, and Zhang [182] pointed out that the local thermal equilibrium assumption is only valid when the interstitial heat transfer coefficient between the constituents is sufficiently large or the specific surface area of the porous medium is high enough. Furthermore, Jiang et al. [183] showed that the effect of local thermal non-equilibrium becomes more significant in fractured media where the convective heat flow inside the fracture plays a crucial role in its coupled behavior. Accordingly, it has been widely recognized that the thermo-hydro-mechanical responses of the porous media can be captured more precisely for the problems at the temporal and spatial scales if the heat transfer among the constituents can be explicitly captured [184–190]. This is particularly important for strain localization and fracture simulations where small perturbations in temperature may lead to significantly different path-dependent behaviors.

Solving the thermo-hydro-mechanical problems with non-equilibrated constituents is nevertheless not trivial. Thermal convection, Soret diffusion, and the orders of difference in thermal diffusivities all require complicated and sophisticated treatments in designing the algorithm. While stabilization procedures such as streamline upwind Petrov-Galerkin (SUPG) scheme may help resolving the numerical issues related to the sharp gradient of temperature and/or pore pressure, capturing the boundary layers of multiple constituent temperature fields remain a great numerical challenge [69, 88, 191, 192] and yet may have a profound impact on the brittle or quasi-brittle fracture of porous media [76, 77, 86].

The goal of this study is to fill this knowledge gap by (1) proposing a thermo-hydro-mechanical theory for deformable porous media with non-equilibrated constituents and (2) introducing an asynchronous operator-split framework that enables us to capture the coupling mechanisms among the constituents without spurious numerical oscillations or over-diffusion. To achieve the first goal, we hypothesize that the existence of an effective medium where constituents may exhibit different temperature while the heat transfer among different constituents are captured by an interface constitutive law in analog with the dual-

permeability theory. Meanwhile, we assume that the material may exhibit fracture and this fracture is captured by a phase field that provides a diffusive representation of the crack location and therefore does not require embedded discontinuities. The governing equations derived from the balance principles of the solid and fluid constituents are then discretized in both spatial and time domains to establish numerical algorithm for computer simulations. In particular, we adopt the staggered scheme for the phase field fracture while enabling an asynchronous dual-temperature isothermal splitting scheme that updates the displacement, the pore pressure, the constituent temperature, and the phase field sequentially and asynchronously.

The rest of the chapter is organized as follows. In Section 3.2, we introduce the theoretical framework that enables us to consider the heat transfer among constituents in a two-phase effective medium or mixture. We present the balance principles (Section 3.3) and constitutive relations (Section 3.4) that describe the thermo-hydro-mechanically coupled behavior of fluid-saturated porous media undergoing brittle fracture. We then propose a special time integration scheme that updates the field variables in an asynchronous manner in Section 3.6. Finally, numerical examples are given in Section 3.7 to highlight the computational efficiency of the proposed scheme, and to showcase the model capacity by simulating the mechanically driven and hydraulically induced fracture propagation during the transient period where the solid and fluid constituents are thermally non-equilibrated.

3.2 Modeling approaches

In this section, we introduce the necessary ingredients for the conservation laws and the constitutive relations that will be presented later in Sections 3.3 and 3.4. We first present the homogenization strategy for the solid and fluid temperatures that allows us to consider non-isothermal effects in a two-phase porous medium with thermally non-equilibrated constituents. Kinematic assumptions based on the mixture theory are also stated, where ther-

mal expansion of the solid skeleton is considered to be isotropic and solely depends on the solid temperature. We then summarize the smooth approximation of crack topology that adopts an implicit function, in which the phase field variable serves as a damage parameter while the regularization length scale parameter controls the size of the diffusive crack zone. Based on this setting, we define the effective stress by following the scenario from Miehe and Mauthe [138], which decomposes the free energy functional into multiple parts including the effective strain energy stored in the solid skeleton and the energy stored in the pore fluid.

3.2.1 Kinematics and homogenization strategy

Consider a fully saturated porous element Ω composed of solid (s) and fluid (f) constituents, i.e., $\Omega = \overline{\Omega_s \cup \Omega_f}$. In small scale, the spatial distribution of each constituent in Ω can be represented by indicator functions $r^s(\boldsymbol{y})$ and $r^f(\boldsymbol{y})$:

$$r^s(\boldsymbol{y}) = \begin{cases} 1 & \text{if } \boldsymbol{y} \in \Omega_s, \\ 0 & \text{otherwise,} \end{cases} \;;\; r^f(\boldsymbol{y}) = \begin{cases} 1 & \text{if } \boldsymbol{y} \in \Omega_f, \\ 0 & \text{otherwise,} \end{cases} \tag{3.1}$$

where $\boldsymbol{y}$ denotes the position vector associated with small-scale configuration. By assuming that Ω can be regarded as a representative volume element (RVE), the mixture theory states that the material of interest can be idealized as a homogenized continuum mixture $\mathcal{B}$ in which the solid and fluid constituents occupies a fraction of volume at the same material point $\mathcal{P}$ [32, 193, 194]. In this case, the volume fractions of each phase constituent are defined as,

$$\phi^s = \frac{dV_s}{dV} = \frac{1}{dV}\int_\Omega r^s(\boldsymbol{y})\, d\Omega \;;\; \phi^f = \frac{dV_f}{dV} = \frac{1}{dV}\int_\Omega r^f(\boldsymbol{y})\, d\Omega, \tag{3.2}$$

where $dV = \int_\Omega [r^s(\boldsymbol{y}) + r^f(\boldsymbol{y})]\, d\Omega$ indicates the total elementary volume of the mixture, such that $\phi^s + \phi^f = 1$. Similarly, the total mass of the mixture at $\mathcal{P}$ is defined by the mass

from each constituent, i.e., $dM = dM_s + dM_f$, and the intrinsic mass densities for the i-phase is given by $\rho_i = dM_i/dV_i$. Hence, the total mass density of the mixture reads,

$$\rho = \rho^s + \rho^f = \phi^s \rho_s + \phi^f \rho_f, \tag{3.3}$$

where $\rho^i = dM_i/dV$ is the partial mass density for the i-phase constituent.

While previous studies on thermo-hydro-mechanics often employ a single temperature field at meso- or macro-scales (θ_m) [69, 101, 177–180], this study adopts a different homogenization strategy for each constituent. This approach not only allows us to model detailed non-isothermal processes in porous media but also to avoid the need to construct the mapping between small- and large-scale temperature fields. Having defined the indicator functions in Eq. (3.1), we define the intrinsic large-scale solid and fluid temperatures (θ_s and θ_f, respectively) as follows:

$$\theta_s = \frac{1}{dV_s} \int_\Omega r^s(\boldsymbol{y}) \theta(\boldsymbol{y}) \, d\Omega \;\; ; \;\; \theta_f = \frac{1}{dV_f} \int_\Omega r^f(\boldsymbol{y}) \theta(\boldsymbol{y}) \, d\Omega, \tag{3.4}$$

where $\theta(\boldsymbol{y})$ is the small-scale temperature field. Here, if the solid and fluid temperatures at the same material point are different from each other, the constituents are said to be in local thermal non-equilibrium (LTNE), where the heat exchange between two phases should be taken into account [188, 189, 195–197]. On the other hand, for the case where two temperatures are identical to each other at the same material point, two constituents are said to be in local thermal equilibrium (LTE), implying a zero heat exchange between the phases. Note that the previous works that adopt a single temperature field (i.e., one-temperature model) often rely on the assumption that the solid and fluid temperatures reach a local equilibrium instantly (i.e., $\theta_s = \theta_f = \theta_m$). In this case, the homogenized large-scale temperature θ_m may no longer depend on the volume fraction of the constituents nor their

microstructural attributes, i.e.,

$$\theta_m = \frac{1}{dV} \int_{\Omega} \theta(\boldsymbol{y})\, d\Omega. \tag{3.5}$$

For the kinematic assumptions, we follow the classical theory of porous media [81–84, 198] and directly adopt the macroscopic descriptions. Specifically, we assume that the solid constituent forms a deformable skeletal structure (i.e., solid skeleton or solid matrix) at the RVE scale so that the evolution of our target porous material can be described in terms of the deformation of its solid skeleton. Since this study considers distinctive temperature fields for each phase constituents, the volume-averaged thermal expansion of the constituents is not used to compute thermal expansion of the porous medium [199–201]. Instead, we assume that the solid skeleton is linear thermoelastic, while the thermal expansion of solid skeleton solely depends on the solid temperature θ_s. Considering a body of two-phase continuum mixture $\mathcal{B}$ with material points identified by the large-scale position vectors $\boldsymbol{x} \in \mathcal{B}$, we denote the displacement of the solid skeleton by $\boldsymbol{u}(\boldsymbol{x}, t)$ at time t, so that the strain measure $\boldsymbol{\varepsilon}$ can be defined as follows:

$$\boldsymbol{\varepsilon} = \boldsymbol{\varepsilon}^e + \boldsymbol{\varepsilon}^{\theta_s} = \frac{1}{2} \left(\nabla \boldsymbol{u} + \nabla \boldsymbol{u}^{\mathrm{T}} \right), \tag{3.6}$$

where $\boldsymbol{\varepsilon}^e$ is the elastic component of the strain tensor and $\boldsymbol{\varepsilon}^{\theta_s} = \alpha_s(\theta_s - \theta_{s,\mathrm{ref}})\boldsymbol{I}$ is its thermal component, where $\theta_{s,\mathrm{ref}}$ is the reference temperature and α_s is the linear thermal expansion coefficient of the solid constituent. Notice that, as pointed out in Khalili, Uchaipichat, and Javadi [202], the linear thermal expansion coefficient of the solid skeleton is solely controlled by and is equivalent to that of solid phase constituent. In other words, by revisiting the homogenization strategy in Eq. (3.4), it implies that the macroscopic temperature of the solid phase θ_s can be considered to be equivalent to that of solid skeleton.

3.2.2 Phase field approximation of crack topology

This study adopts the diffuse representation of fracture by using the phase field approach [75–77]. By letting Γ be the sharp crack surface within a body of mixture $\mathcal{B}$, the total fracture surface area A_Γ can be approximated as A_{Γ_d}, which is the volume integral over body $\mathcal{B}$ of the surface density $\Gamma_d(d, \nabla d)$. In other words,

$$A_\Gamma \approx A_{\Gamma_d} = \int_{\mathcal{B}} \Gamma_d \left(d, \nabla d\right) \, dV, \tag{3.7}$$

where $d \in [0, 1]$ is the phase field that serves as a damage parameter in which $d = 0$ indicates the intact region while $d = 1$ denotes the completely damaged region. Here, the approximation A_{Γ_d} must be able to recover A_Γ by reducing the regularization length scale parameter l_c to zero (i.e., Γ-convergence), while the generalized form of the corresponding crack density functional [203] reads,

$$\Gamma_d \left(d, \nabla d\right) = \frac{1}{c_0} \left[\frac{1}{l_c} w(d) + l_c \left(\nabla d \cdot \nabla d\right)\right] \;\; ; \;\; c_0 = 4 \int_0^1 \sqrt{w(s)} \, ds, \tag{3.8}$$

where c_0 is the normalization constant, and $w(d)$ is the monotonically increasing local dissipation function that controls the shape of the regularized profile of the phase field [204–206]. Note that a linear local dissipation along with a quadratic stiffness degradation yields a threshold energy model (existence of a linear elastic phase before the onset of damage), which is contrary to the quadratic model for which damage starts at zero loading. However, the threshold energy model can be converted to a critical stress which is dependent of the length scale parameter l_c. Both approaches have been used to model brittle fracture as two alternative regularizations of the variational theory of brittle fracture of [207]. Meanwhile, previous work, such as Suh and Sun [132], Lorentz [208], Geelen et al. [209], and Suh, Sun, and O'Connor [210], have used non-quadratic degradation function which may yield a critical stress independent of l_c.

In this study, we adopt the quadratic local dissipation model, so that the crack resistance force $\mathcal{R}^c$ can be expressed as [128]:

$$\mathcal{R}^c = \frac{\partial W^c}{\partial d} - \nabla \cdot \left(\frac{\partial W^c}{\partial \nabla d} \right) \; ; \; W^c = \mathcal{G}_c \Gamma_d \left(d, \nabla d \right) = \frac{\mathcal{G}_c}{l_c} \left[\frac{d^2}{2} + \frac{l_c^2}{2} (\nabla d \cdot \nabla d) \right], \quad (3.9)$$

where $\mathcal{G}_c = \mathcal{G}_c(\theta_s)$ is the critical energy release rate that quantifies the resistance to cracking, which will be explicitly defined in Section 3.4.2.

3.2.3 Free energy and effective stress principle

We adopt the effective stress principle that decomposes the total macroscopic stress $\boldsymbol{\sigma}$ into the effective stress $\boldsymbol{\sigma}'$ and the contribution due to the pore fluid pressure p_f. As the effective stress is solely caused by the macroscopic deformation of the solid skeleton, it constitute a energy-conjugate relationship with the strain measure [211, 212]. As such, the free energy (ψ) of the porous media may take the following form (cf. Miehe and Mauthe [138]):

$$\psi = \psi'(\boldsymbol{\varepsilon}, \theta_s, d) + \psi^*(\boldsymbol{\varepsilon}, \vartheta^*, d) + \psi^{\theta_s}(\theta_s) + \psi^{\theta_f}(\theta_f). \quad (3.10)$$

Note that the energy required for crack growth [i.e., W^c in Eq. (3.9)] is dissipatve by nature and hence not included in this stored energy function ψ [88, 128, 168]. Our definition of free energy will be used for constructing the energy balance equations based on the first law of thermodynamics in Section 3.3.1, while this section defines all the terms in detail first, and then presents the effective stress principle.

The effective part of the strain energy density $\psi'(\boldsymbol{\varepsilon}, \theta_s, d)$ can be viewed as a stored energy density due to the intergranular stress acting on the solid skeleton that leads to its deformation. In particular, we assume that the effective part of the strain energy density $\psi'(\boldsymbol{\varepsilon}, \theta_s, d)$ is composed of the fictitious undamaged thermoelastic strain energy $\psi'_0(\boldsymbol{\varepsilon}, \theta_s)$

and the degradation function $g(d) \in [0, 1]$ [131, 170, 213], i.e.,

$$\psi'(\boldsymbol{\varepsilon}, \theta_s, d) = g(d)\psi'_0(\boldsymbol{\varepsilon}, \theta_s) \;\; ; \;\; \psi'_0(\boldsymbol{\varepsilon}, \theta_s) = \frac{1}{2}\boldsymbol{\varepsilon} : \mathbb{C}^e : \boldsymbol{\varepsilon} - 3\alpha_s K(\theta_s - \theta_{s,\text{ref}})\,\text{tr}\,(\varepsilon), \quad (3.11)$$

where $\mathbb{C}^e$ is the elastic moduli and K is the bulk modulus of the solid skeleton. This approach allows us to interpret the cracking in a saturated porous material as the fracture of the solid matrix.

Following Miehe and Mauthe [138], and by assuming that the effect of thermal expansion (or contraction) of the pore fluid is negligible (i.e., its linear thermal expansion coefficient $\alpha_f = 0$), the contribution of pore fluid to the free energy $\psi^*(\boldsymbol{\varepsilon}, \vartheta^*, d)$ can be defined as follows:

$$\psi^*(\boldsymbol{\varepsilon}, \vartheta^*, d) = \frac{1}{2}M^*(d)\left[B^*(d)\,\text{tr}\,(\boldsymbol{\varepsilon}) - \vartheta^*\right]^2 \;\; ; \;\; \vartheta^* = B^*(d)\,\text{tr}\,(\varepsilon) + \frac{p_f}{M^*(d)}, \quad (3.12)$$

where the expression for ϑ^* is similar to Eq. (2.12) in [214], while $B^*(d)$ and $M^*(d)$ are the modified Biot's coefficient and the modified Biot's modulus, respectively:

$$B^*(d) = 1 - \frac{K^*(d)}{K_s} \;\; ; \;\; \frac{1}{M^*(d)} = \frac{B^*(d) - \phi^f}{K_s} + \frac{\phi^f}{K_f}. \quad (3.13)$$

Here, $K^*(d) = g(d)K$, while K_s and K_f denote the bulk moduli of the solid and fluid phases, respectively. As shown in Eq. (3.13), this study assumes that the damage of the solid skeleton degrades the elastic bulk modulus $K^*(d)$, so that $B^*(d)$ and $M^*(d)$ may evolve according to the deformation. In other words, if the solid skeleton remains undamaged, the modified coefficient recovers the classical definition of Biot's coefficient (i.e., $B^* = 1 - K/K_s$) that is often less than 1 for rock [177, 215, 216], while we have $B^*(1) = 1$ for the case where the solid skeleton is completely damaged, which has been accepted in previous studies on hydraulic fracture [138, 139, 217]. Following Heider and Sun [143], we assume that crack opening leads to a complete fragmentation of the solid skeleton, such

that we adopt the following relation for the porosity (i.e., the volume fraction of fluid phase constituent ϕ^f):

$$\phi^f = 1 - g(d)(1 - \phi^f_{\text{ref}})(1 - \nabla\cdot\boldsymbol{u}), \tag{3.14}$$

where ϕ^f_{ref} is the reference porosity. We also define $\varphi = \vartheta^* - B^*(d)\,\text{tr}\,(\boldsymbol{\varepsilon})$ for convenience, which is related to the variation of the fluid content and is the energy conjugate to the pore fluid pressure p_f. In this case, Eq. (3.12) can be re-written in a simple quadratic form:

$$\psi^*(\boldsymbol{\varepsilon}, \vartheta^*, d) = \psi^*(\varphi, d) = \frac{1}{2}M^*(d)\varphi^2. \tag{3.15}$$

The pure thermal contribution on the stored energy density $\psi^{\theta_i}(\theta_i)$ may have the simple form as [131, 170, 213, 218],

$$\psi^{\theta_i}(\theta_i) = \rho^i c_i \left[(\theta_i - \theta_{i,\text{ref}}) - \theta_i \ln\left(\frac{\theta_i}{\theta_{i,\text{ref}}}\right)\right], \tag{3.16}$$

where $i = \{s, f\}$, while c_i indicates the specific heat capacity and $\theta_{i,\text{ref}}$ is the reference temperature for the i-phase constituent. Note that, as shown in Eq. (3.16), we simplify the coupled thermo-mechanical-fracture problem by assuming that the thermal part of the stored energy densities $\psi^{\theta_s}(\theta_s)$ and $\psi^{\theta_f}(\theta_f)$ are not affected by the fracture (cf. [128, 138, 170]).

Having defined all the terms for the free energy, we now present the effective stress principle based on the hyperelastic relations. From Eqs. (3.10), (3.11), and (3.12), the total stress $\boldsymbol{\sigma}$ can be found by taking the partial derivative of the total energy density ψ with respect to the strain $\boldsymbol{\varepsilon}$:

$$\boldsymbol{\sigma} = \frac{\partial\psi}{\partial\boldsymbol{\varepsilon}} = \underbrace{\frac{\partial}{\partial\boldsymbol{\varepsilon}}\psi'(\boldsymbol{\varepsilon}, \theta_s, d)}_{=\boldsymbol{\sigma}'} + \underbrace{\frac{\partial}{\partial\boldsymbol{\varepsilon}}\psi^*(\boldsymbol{\varepsilon}, \vartheta^*, d)}_{=-B^*(d)p_f\boldsymbol{I}}. \tag{3.17}$$

A similar decomposition can be found in a number of studies on theories of porous media

[81–84, 198], where the first term of the right hand side in Eq. (3.17) becomes the effective stress $\boldsymbol{\sigma}'$, while the second term indicates the contribution of the pore pressure which is assumed to produce a hydrostatic stress state [138]. From Eqs. (3.11) and (3.17), the effective stress tensor can also be expressed as,

$$\boldsymbol{\sigma}' = \boldsymbol{\sigma} + B^*(d) p_f \boldsymbol{I} = g(d)\boldsymbol{\sigma}'_0, \tag{3.18}$$

where $\boldsymbol{\sigma}'_0 = \partial \psi'_0 / \partial \boldsymbol{\varepsilon}$ is the fictitious undamaged effective stress.

3.3 Conservation laws for thermally non-equilibrated porous media

In this section, we derive the balance principles that govern the brittle fracture in saturated porous media with constituents of different temperatures. While previous work such as [127, 131, 170, 180] has introduced a framework to address the thermal effect of brittle or quasi-brittle fracture in porous media, our new contribution here is to introduce the heat exchange between the two thermally connected constituents, such that the multi-scale nature of the heat transfer can be considered. Since our homogenization strategy enables us to consider two macroscopic temperatures for each constituent, we derive two distinct energy balance equations by assuming that the thermodynamic state of each phase is measured by their own temperature, internal energy, and entropy. Our derivation in Section 3.3.1 shows that the two-temperature approach can be reduced into a classical heat equation with a single temperature field if we consider the special case where two constituents are thermally equilibrated. Then, in addition to two energy equations, we present a thermodynamically consistent phase field model and the balances of linear momentum and mass, that complete the set of governing equations which not only describes the thermo-hydro-mechanical behavior of porous media in local thermal non-equilibrium, but also the evolution of the fracture.

3.3.1 Balance of energy

In contrast to the models that employ a single temperature field, i.e., one-temperature model, [175, 178, 179], our approach requires two energy balance equations for each phase constituent in order to account for the transient period, i.e., local thermal non-equilibrium [95, 188, 189]. Hence, following Gelet, Loret, and Khalili [95], we assume that thermodynamic states of the solid skeleton and pore fluid can respectively be measured by their own temperature θ_i, internal energy E_i and entropy H_i per unit mass. Based on the assumption, the internal energy per unit volume e can additively be decomposed as follows,

$$e = e^s + e^f \;\; ; \;\; e^i = \rho^i E_i, \tag{3.19}$$

where $i = \{s, f\}$ so that e^i is the partial quantity. Similarly, entropy per unit volume of the mixture η can also be decomposed into,

$$\eta = \eta^s + \eta^f \;\; ; \;\; \eta^i = \rho^i H_i, \tag{3.20}$$

where we assume that each partitioned entropies satisfy:

$$\eta^i = -\frac{\partial \psi^i}{\partial \theta_i}. \tag{3.21}$$

Here, by revisiting Section 3.2.3, we define ψ^i as,

$$\psi = \psi^s + \psi^f \;\; ; \;\; \begin{cases} \psi^s = \psi'(\boldsymbol{\varepsilon}, \theta_s, d) + \psi^{\theta_s}(\theta_s), \\ \psi^f = \psi^*(\varphi, d) + \psi^{\theta_f}(\theta_f), \end{cases} \tag{3.22}$$

such that ψ^s and ψ^f are the partial free energy of the solid and fluid phase constituents, respectively. As shown in Eq. (3.22), this study assumes that the effects of the skeletal structure of the solid phase constituent (e.g., effective stress and degradation) on the free

energy is solely stored in ψ^s, while ψ^f only includes the contribution of its intrinsic pressure and temperature. Furthermore, we postulate that the partial quantities of internal energy e^i and entropy η^i can be subjected to a Legendre transformation, i.e.,

$$\psi^i = e^i - \theta_i \eta^i, \tag{3.23}$$

so that the following classical relation [219–221] can be recovered if two constituents are in thermal equilibrium (i.e., $\theta_s = \theta_f = \theta_m$):

$$\psi = \sum_{i=\{s,f\}} \psi^i = \sum_{i=\{s,f\}} (e^i - \theta_i \eta^i) = e - \theta_m \eta. \tag{3.24}$$

On the other hand, the energy exchange between the constituents can be described by introducing the rates of energy transfer χ^i, in which energy conservation requires the following constraint to be satisfied:

$$\chi^s + \chi^f = 0. \tag{3.25}$$

Based on the first law of thermodynamics, the balance of energy for the solid constituent that accounts for the flux of thermal energy due to heat conduction ($\boldsymbol{q}^s$), the rate of energy exchange (χ^s), and the heat source ($\hat{r}^s$) can be written as,

$$\dot{e}^s = \boldsymbol{\sigma}' : \dot{\boldsymbol{\varepsilon}} - \nabla \cdot \boldsymbol{q}^s + \chi^s + \hat{r}^s, \tag{3.26}$$

where $\dot{(\bullet)} = d(\bullet)/dt$ is the total material time derivative following the solid phase. Although will be discussed later in Section 3.3.2, we briefly show that the second law of thermodynamics (i.e., Clausius–Duhem inequality) yields the following expression for the dissipation functional $\mathcal{D}^s$:

$$\mathcal{D}^s = \left(\boldsymbol{\sigma}' - \frac{\partial \psi^s}{\partial \boldsymbol{\varepsilon}} \right) : \dot{\boldsymbol{\varepsilon}} - \left(\eta^s + \frac{\partial \psi^s}{\partial \theta_s} \right) \dot{\theta}_s \underbrace{- \frac{\partial \psi^s}{\partial d} \dot{d}}_{=\mathcal{D}^s_{\text{int}}} \underbrace{- \frac{1}{\theta_s} \boldsymbol{q}^s \cdot \nabla \theta_s}_{=\mathcal{D}^s_{\text{con}}} \geq 0, \tag{3.27}$$

where the entropy input is assumed to be related to the heat flux across the boundary and the heat source [127, 170]. From the relations defined previously [Eqs. (3.17) and (3.21)], dissipation functional in Eq. (3.27) can be reduced into,

$$\mathcal{D}^s = \mathcal{D}^s_{\text{int}} + \mathcal{D}^s_{\text{con}} \geq 0. \tag{3.28}$$

Finally, from Eqs. (3.23) and (3.26), the solid phase energy balance equation in Eq. (3.26) becomes:

$$\dot{\psi}^s - \dot{e}^s + \dot{\overline{\theta_s \eta^s}} = \theta_s \dot{\eta}^s - \mathcal{D}^s_{\text{int}} + \nabla \cdot \boldsymbol{q}^s - \chi^s - \hat{r}^s = 0. \tag{3.29}$$

By substituting the explicit expression for η^s [i.e., from Eqs. (3.20) and (3.22)], Eq. (3.29) can be re-written as follows, where similar form can be found in [69, 144, 170].

$$\rho^s c_s \dot{\theta}_s = [\mathcal{D}^s_{\text{int}} - H_{\theta_s}] - \nabla \cdot \boldsymbol{q}^s + \chi^s + \hat{r}^s. \tag{3.30}$$

In this study, to simplify the equation, we assume that structural heating/cooling is negligible (i.e., $H_{\theta_s} = 0$) compared to the internal dissipation $\mathcal{D}_{\text{int}}$.

We now repeat the same procedure for the fluid phase. Again, from the first law, the internal energy for the pore fluid that accounts for the heat flux due to the conduction ($\boldsymbol{q}^f$), the rate of energy exchange (χ^f), the heat convection ($\mathcal{A}^f$), and the heat source ($\hat{r}^f$) can be written as,

$$\dot{e}^f = -p_f \dot{\varphi} - \mathcal{A}^f - \nabla \cdot \boldsymbol{q}^f + \chi^f + \hat{r}^f, \tag{3.31}$$

where we take $\mathcal{A}^f = \rho_f c_f (\boldsymbol{w} \cdot \nabla \theta_f)$ with $\boldsymbol{w}$ denoting Darcy's velocity, by assuming that the advection process is governed by the movement of the pore fluid relative to that of the solid skeleton [95, 101]. Recall that from Eqs. (3.12), (3.15) and (3.21) we have: $p_f = -M^* \varphi$ and $\eta^f = -\partial \psi^f / \partial \theta_f$. Thus, from Eqs. (3.23) and (3.31), the fluid energy balance equation reads,

$$\dot{\psi}^f - \dot{e}^f + \dot{\overline{\theta_f \eta^f}} = \theta_f \dot{\eta}^f + \mathcal{A}^f + \nabla \cdot \boldsymbol{q}^f - \chi^f - \hat{r}^f, \tag{3.32}$$

where we assume that the contribution of the phase field on ψ^f is negligible. Then, by substituting the explicit expression for η^f, the fluid phase energy balance equation can be re-written as,

$$\rho^f c_f \dot{\theta}_f = -\rho_f c_f (\boldsymbol{w} \cdot \nabla \theta_f) - \nabla \cdot \boldsymbol{q}^f + \chi^f + \hat{r}^f, \tag{3.33}$$

where Eq. (3.33) is similar to the form that seen in [222–224].

Remark 2. Eqs. (3.30) and (3.33) describes the heat transfer process in porous media under LTNE condition, however, one may obtain a different form of governing equations if adopting either different form of the free energy functional or different decomposition scheme on the internal energy. Based on our approach, for the situation where the material is undamaged ($d = 0$) and is under LTE condition (i.e., $\theta_s = \theta_f = \theta_m$), adding Eqs. (3.30) and (3.33) yields the classical one-temperature model [84, 175, 177, 178]:

$$\rho c_m \dot{\theta}_m = -\rho_f c_f (\boldsymbol{w} \cdot \nabla \theta_m) - \nabla \cdot \boldsymbol{q} + \hat{r}, \tag{3.34}$$

where $\rho c_m = \rho^s c_s + \rho^f c_f$, $\boldsymbol{q} = \boldsymbol{q}^s + \boldsymbol{q}^f$, and $\hat{r} = \hat{r}^s + \hat{r}^f$. Here, Eq. (3.34) not only demonstrates the connection between one- and two-temperature approaches but also implies that the classical model assumes a special case where all the phase constituents instantly reach a local thermal equilibrium.

3.3.2 Dissipation inequality and crack evolution

By revisiting the expression for the dissipation functional $\mathcal{D}^s$ in Eq. (3.28), the following thermodynamic restriction must be satisfied:

$$\mathcal{D}^s_{\text{int}} = \mathcal{F}^c \dot{d} \geq 0, \tag{3.35}$$

since the dissipation due to heat conduction $\mathcal{D}^s_{\text{con}}$ is guaranteed positive by the Fourier's law, while:

$$\mathcal{F}^c = -\frac{\partial \psi^s}{\partial d} = -g'(d)\psi_0' \tag{3.36}$$

indicates the crack driving force [127, 128]. Notice that a sufficient condition for the inequality in Eq. (3.35) is that all the components $\mathcal{F}^c$ and $\dot{d}$ are individually non-negative. By adopting the quadratic degradation function, i.e., $g(d) = (1-d)^2$, that satisfies the following conditions [210, 225]:

$$g(0) = 1 \;\; ; \;\; g(1) = 0 \;\; ; \;\; g'(d) \leq 0 \text{ for } d \in [0,1], \tag{3.37}$$

the non-negative crack driving force $\mathcal{F}^c$ is automatically guaranteed since $\psi_0' \geq 0$. In this case, the thermodynamic restriction in Eq. (3.35) becomes:

$$\dot{d} \geq 0. \tag{3.38}$$

While the stored energy functional in the microforce approach often contains the fracture energy [170, 226, 227], recall Section 3.2.3 that our energy functional ψ does not include the energy used to create a fracture. Again, it allows us to consider crack growth as a fully dissipative process, resulting in the solid phase energy balance equation [Eq. (3.30)] that contains the internal dissipation $\mathcal{D}^s_{\text{int}}$. Based on this setting, we adopt a concept similar to the variational framework for fracture that characterizes the crack propagation process by energy dissipation [75, 87, 207]. By assuming that the viscous resistance is neglected, thermodynamic consistency requires the balance between the crack driving force $\mathcal{F}^c$ in Eq. (3.36) and the crack resistance $\mathcal{R}^c$ in Eq. (3.9), i.e.,

$$\mathcal{R}^c - \mathcal{F}^c = g'(d)\psi_0' + \frac{\mathcal{G}_c}{l_c}(d - l_c^2 \nabla^2 d) = 0, \tag{3.39}$$

where $\nabla^2(\bullet) = \nabla \cdot \nabla\,(\bullet)$ indicates the Laplacian operator. Here, we adopt the volumetric-

deviatoric split proposed by Amor, Marigo, and Maurini [130], which is the stored energy that may contribute as the driving force for crack growth, i.e.,

$$\psi_0'^{+} = \frac{1}{2}K\langle\varepsilon^{\text{vol}}\rangle_+^2 + \mu(\boldsymbol{\varepsilon}^{\text{dev}} : \boldsymbol{\varepsilon}^{\text{dev}}) - 3\alpha_s K(\theta_s - \theta_{s,\text{ref}})\langle\varepsilon^{\text{vol}}\rangle_+, \tag{3.40}$$

$$\psi_0'^{-} = \frac{1}{2}K\langle\varepsilon^{\text{vol}}\rangle_-^2 - 3\alpha_s K(\theta_s - \theta_{s,\text{ref}})\langle\varepsilon^{\text{vol}}\rangle_-, \tag{3.41}$$

where $\varepsilon^{\text{vol}} = \text{tr}\,(\boldsymbol{\varepsilon})$, $\boldsymbol{\varepsilon}^{\text{dev}} = \boldsymbol{\varepsilon} - (\varepsilon^{\text{vol}}/3)\boldsymbol{I}$, and $\langle\bullet\rangle_\pm = (\bullet \pm |\bullet|)/2$ indicates the Macaulay bracket operator. To prevent healing of the crack, we adopt a normalized local history field $\mathcal{H} \geq 0$ of the maximum positive reference energy, i.e.,

$$\mathcal{H} = \max_{\tau\in[0,t]}\left(\frac{\psi_0'^{+}}{\mathcal{G}_c/l_c}\right), \tag{3.42}$$

which satisfies the following Karush–Kuhn–Tucker condition [77, 168]:

$$W^+ - \mathcal{H} \leq 0 \;;\; \dot{\mathcal{H}} \geq 0 \;;\; \dot{\mathcal{H}}(W^+ - \mathcal{H}) = 0, \tag{3.43}$$

where $W^+ = \psi_0'^{+}/(\mathcal{G}_c/l_c)$ denote the portion of nondimensional ψ_0' that contributes to cracking.

By replacing the stored energy term in Eq.(3.39) by $(\mathcal{G}_c/l_c)\mathcal{H}$, the governing equation for the phase field d can be re-written as follows:

$$g'(d)\mathcal{H} + (d - l_c^2\nabla^2 d) = 0. \tag{3.44}$$

Note that Eq. (3.44) is based on balance of the material force (cf. [77]) and is not a Euler-Lagrangian equation obtained from the minimization of an energy functional.

3.3.3 Balance of linear momentum

By neglecting the inertial force, the balance of linear momentum for the solid-fluid mixture can be written as,

$$\nabla\cdot\boldsymbol{\sigma}+\rho\boldsymbol{g}=\mathbf{0}, \tag{3.45}$$

where $\boldsymbol{\sigma}=\boldsymbol{\sigma}^s+\boldsymbol{\sigma}^f$ is the total Cauchy stress that can be obtained from the sum of partial stresses $\boldsymbol{\sigma}^i$ for i-phase constituents [228, 229]. Hence, from Eq. (3.18), the mean pressure p can be expressed as:

$$p=-\frac{1}{3}\,\mathrm{tr}\,(\boldsymbol{\sigma})=\phi^s p_s+\phi^f p_f=-K^*\,\nabla\cdot\boldsymbol{u}+3\alpha_s K^*(\theta_s-\theta_{s,\mathrm{ref}})+B^* p_f, \tag{3.46}$$

where p_s and p_f are the intrinsic pressures defined in dV_s and dV_f, respectively, while the detailed constitutive model for the solid skeleton will be presented in Section 3.4.2.

3.3.4 Balance of mass

Assuming that there is no phase transition between two constituents, the balance of mass for the solid skeleton and the pore fluid reads,

$$\dot{\rho}^s+\rho^s\,\nabla\cdot\boldsymbol{v}=0, \tag{3.47}$$

$$\dot{\rho}^f+\rho^f\,\nabla\cdot\boldsymbol{v}+\nabla\cdot\left[\rho^f(\boldsymbol{v}_f-\boldsymbol{v})\right]=\rho_f\hat{s}, \tag{3.48}$$

where $\rho_f\hat{s}$ is the rate of prescribed fluid mass source/sink per unit volume, while $\boldsymbol{v}$ and $\boldsymbol{v}_f$ indicate the solid and fluid velocities, respectively. Since the change of dV_s depends on both the intrinsic pressure p_s and the temperature θ_s, the total time derivative of partial density ρ^s can be expanded as,

$$\dot{\rho}^s=\dot{\overline{\phi^s\rho_s}}=\dot{\phi}^s\rho_s+\phi^s\left(\frac{d\rho_s}{dp_s}\dot{p}_s+\frac{d\rho_s}{d\theta_s}\dot{\theta}_s\right)=\dot{\phi}^s\rho_s+\phi^s\rho_s\left(\frac{1}{K_s}\dot{p}_s-3\alpha_s\dot{\theta}_s\right), \tag{3.49}$$

so that the solid phase mass balance equation in Eq. (3.47) can be re-expressed as,

$$-\dot{\phi}^s = \frac{\phi^s}{K_s}\dot{p}_s - 3\alpha_s\phi^s\dot{\theta}_s + \phi^s\,\nabla\cdot\boldsymbol{v}. \tag{3.50}$$

Also, from Eq. (3.46), the total time derivative of mean pressure p yields:

$$\dot{p} = \dot{\overline{\phi^s p_s + \phi^f p_f}} = -K^*\,\nabla\cdot\boldsymbol{v} + 3\alpha_s K^*\dot{\theta}_s + B^*\dot{p}_f. \tag{3.51}$$

Following Sun, Ostien, and Salinger [230], we assume that the change of porosity at an infinitesimal time is small (i.e., $\dot{\phi}^i p_i$ is relatively small compared to $\phi^i\dot{p}_i$), so that Eq. (3.51) reduces into,

$$\phi^s\dot{p}_s = -K^*\,\nabla\cdot\boldsymbol{v} + 3\alpha_s K^*\dot{\theta}_s + (B^* - \phi^f)\dot{p}_f. \tag{3.52}$$

By substituting Eq. (3.52) into Eq. (3.50), the solid phase mass balance equation now reads,

$$-\dot{\phi}^s = \frac{B^* - \phi^f}{K_s}\dot{p}_f - 3\alpha_s\left(\phi^s - \frac{K^*}{K_s}\right)\dot{\theta}_s + \left(\phi^s - \frac{K^*}{K_s}\right)\nabla\cdot\boldsymbol{v}. \tag{3.53}$$

Similar to Eq. (3.50), the fluid phase mass balance equation in Eq. (3.48) can also be expanded as,

$$\dot{\phi}^f + \frac{\phi^f}{K_f}\dot{p}_f - 3\alpha_f\phi^f\dot{\theta}_f + \phi^f\,\nabla\cdot\boldsymbol{v} + \nabla\cdot\boldsymbol{w} = \hat{s}, \tag{3.54}$$

where K_f is the bulk modulus of the fluid, $\boldsymbol{w} = \phi^f(\boldsymbol{v}_f - \boldsymbol{v})$ indicates Darcy's velocity, and α_f is the linear thermal expansion coefficient of the pore fluid which has been assumed to be zero in Section 3.2.3. Recall that Eq. (3.2) yields the condition $\phi^s + \phi^f = 1$, which leads to: $\dot{\phi}^f = -\dot{\phi}^s$. Thus, we substitute Eq. (3.53) into the first term in Eq. (3.54) that gives the following expression for the fluid phase mass balance equation:

$$\frac{1}{M^*}\dot{p}_f - 3\alpha_s(B^* - \phi^f)\dot{\theta}_s - 3\alpha_f\phi^f\dot{\theta}_f + B^*\,\nabla\cdot\boldsymbol{v} + \nabla\cdot\boldsymbol{w} = \hat{s}. \tag{3.55}$$

Remark 3. If we assume that the solid and fluid temperatures are locally equilibrated (i.e.,

$\theta_s = \theta_f = \theta_m$) and $\hat{s} = 0$, Eq. (3.55) can be reduced into a similar form that is shown in [84, 178, 201]:

$$\frac{1}{M^*}\dot{p}_f - 3\alpha_m\dot{\theta}_m + B^*\,\nabla\cdot\boldsymbol{v} + \nabla\cdot\boldsymbol{w} = 0, \tag{3.56}$$

where $\alpha_m = (B^* - \phi^f)\alpha_s + \phi^f\alpha_f$ is the coefficient of linear thermal expansion for thermally equilibrated medium. Furthermore, if we consider a special case where thermal expansion is negligible and each constituent is incompressible (i.e., $K_i \to \infty$), Eq. (3.56) further reduces to the form identical to that seen in [101, 230, 231]:

$$\nabla\cdot\boldsymbol{v} + \nabla\cdot\boldsymbol{w} = 0, \tag{3.57}$$

since $B^* = 1$ and $1/M^* = 0$ in this case, regardless of the damage parameter d.

3.4 Constitutive responses

The goal of this section is to identify constitutive relations that capture thermo-hydro-mechanically coupled behavior of the material of interest. We begin this section by the constitutive relationships for partial heat fluxes for each phase, where we assume both the solid and fluid constituents obey Fourier's law. We also present the explicit expression for the heat exchange χ^i between the solid skeleton and pore fluid based on Newton's law of cooling. We then briefly summarize the linear thermoelasticity for the undamaged solid skeleton, while the hydraulic responses in both the bulk and crack regions are modeled by the Darcy's law, where we adopt permeability enhancement approach in order to account for the anisotropy due to the crack opening. In addition, this study adopts an empirical two-parameter model for the pore fluid viscosity, which is capable of predicting the temperature-dependent viscosity of typical liquids in geomaterials.

3.4.1 Thermal responses and heat exchange model

In this section, we adopt the homogenization strategy that we previously described in Section 3.2.1. Similar to the large-scale temperatures, by letting $\boldsymbol{f}(\boldsymbol{y})$ the small scale heat flux vector, the large-scale heat flux $\boldsymbol{q}$ can be expressed as,

$$\begin{aligned}\boldsymbol{q} &= \frac{1}{dV}\int_{\Omega}\boldsymbol{f}(\boldsymbol{y})\,d\Omega = \frac{1}{dV}\int_{\Omega}\underbrace{r^{s}(\boldsymbol{y})\boldsymbol{f}(\boldsymbol{y})}_{=\boldsymbol{f}^{s}(\boldsymbol{y})} + \underbrace{r^{f}(\boldsymbol{y})\boldsymbol{f}(\boldsymbol{y})}_{=\boldsymbol{f}^{f}(\boldsymbol{y})}\,d\Omega \\ &= \underbrace{\frac{dV_s}{dV}\overbrace{\left[\frac{1}{dV_s}\int_{\Omega}\boldsymbol{f}^{s}(\boldsymbol{y})\,d\Omega\right]}^{=\boldsymbol{q}_s}}_{=\boldsymbol{q}^{s}} + \underbrace{\frac{dV_f}{dV}\overbrace{\left[\frac{1}{dV_f}\int_{\Omega}\boldsymbol{f}^{f}(\boldsymbol{y})\,d\Omega\right]}^{=\boldsymbol{q}_f}}_{=\boldsymbol{q}^{f}},\end{aligned} \tag{3.58}$$

so that $\boldsymbol{q} = \boldsymbol{q}^{s} + \boldsymbol{q}^{f}$. For the constitutive model that describes the heat conduction, we assume that both the solid and fluid constituents obey the Fourier's law, such that their partial heat flux $\boldsymbol{q}^{i}$ ($i \in \{s, f\}$) can be written as,

$$\boldsymbol{q}^{i} = \phi^{i}\boldsymbol{q}_{i} = -\phi^{i}\kappa_{i}\,\nabla\,\theta_{i}, \tag{3.59}$$

where κ_i indicates the intrinsic thermal conductivity of the i-phase constituent [232–234]. Notice that the volume-averaged approach is only valid for the case where solid and fluid constituents are connected in parallel while computing the correct partial heat fluxes in Eq. (3.59) requires the geometric and topologic information of the pore structure obtained from 3D X-ray CT images [101–103, 230, 235, 236]. Since the detailed geometrical attributes of the target porous media are not readily available, this extension will be considered in the future.

Let us now consider a small scale problem $\nabla\cdot\,\boldsymbol{f}(\boldsymbol{y}) = 0$, while homogeneous energy balance requires $\nabla\cdot\,\boldsymbol{q}^{s} = 0$ and $\nabla\cdot\,\boldsymbol{q}^{f} = 0$ from Eqs. (3.30) and (3.33), respectively. Since $\boldsymbol{f}(\boldsymbol{y})$ can be additively decomposed into two parts, i.e., $\boldsymbol{f}^{s}(\boldsymbol{y})$ and $\boldsymbol{f}^{f}(\boldsymbol{y})$, the volume aver-

age of $\nabla\cdot\boldsymbol{f}(\boldsymbol{y})$ can also be decomposed as,

$$\frac{1}{dV}\int_{\Omega}\nabla\cdot\boldsymbol{f}(\boldsymbol{y})\,d\Omega=\frac{1}{dV}\int_{\Omega}\nabla\cdot\boldsymbol{f}^{s}(\boldsymbol{y})\,d\Omega+\frac{1}{dV}\int_{\Omega}\nabla\cdot\boldsymbol{f}^{f}(\boldsymbol{y})\,d\Omega=0. \tag{3.60}$$

Then, the averaging theorem [237] allows us to express the volume average of $\nabla\cdot\boldsymbol{f}^{i}(\boldsymbol{y})$ ($i\in\{s,f\}$) as,

$$\frac{1}{dV}\int_{\Omega}\nabla\cdot\boldsymbol{f}^{i}(\boldsymbol{y})\,d\Omega=\underbrace{\nabla\cdot\left[\frac{1}{dV}\int_{\Omega}\boldsymbol{f}^{i}(\boldsymbol{y})\,d\Omega\right]}_{=\nabla\cdot\boldsymbol{q}^{i}}+\underbrace{\frac{1}{dV}\int_{\Gamma_{\Omega}}\boldsymbol{f}^{i}(\boldsymbol{y})\cdot\boldsymbol{n}_{i}\,d\Gamma}_{=-\chi^{i}}, \tag{3.61}$$

where $\boldsymbol{n}_i$ is the outward unit normal vector from Ω_i, which satisfies $\boldsymbol{n}_s=-\boldsymbol{n}_f$, while Γ_Ω indicates the interface between the solid and fluid within a porous element Ω. Here, the second term on the right hand side of Eq. (3.61) is related to the rate of energy exchanges such that substituting both equations into the small scale problem in Eq. (3.61) yields the constraint $\chi^s+\chi^f=0$ in Eq. (3.25). It underscores that the energy transfer between the constituents occurs at their interface Γ_Ω, implying that the macroscopic level description of heat exchange should be related to the specific surface area of the material. Hence, this study adopts the model proposed by [195, 237], which is based on Newton's law of cooling:

$$\begin{aligned}\chi^{s}&=-\frac{1}{dV}\int_{\Gamma_{\Omega}}\boldsymbol{f}^{s}(\boldsymbol{y})\cdot\boldsymbol{n}_{s}\,d\Gamma=a_{m}h_{m}(\theta_{f}-\theta_{s});\\ \chi^{f}&=-\frac{1}{dV}\int_{\Gamma_{\Omega}}\boldsymbol{f}^{f}(\boldsymbol{y})\cdot\boldsymbol{n}_{f}\,d\Gamma=a_{m}h_{m}(\theta_{s}-\theta_{f}),\end{aligned} \tag{3.62}$$

where a_m is the specific surface area of the porous matrix, and h_m is the interfacial heat transfer coefficient. Since we assumed that crack opening leads to complete fragmentation of solid skeleton, this study adopts the following relation for the specific surface area which assumes $a_m=a_{m,\text{max}}$ inside the fracture to replicate the case where fragmented solid particles are in suspension:

$$a_{m}=g(d)a_{m,\text{ref}}+[1-g(d)]a_{m,\text{max}}, \tag{3.63}$$

where $a_{m,\text{ref}}$ is the reference specific surface area of the material of interest, while we use $a_{m,\text{max}} = 3.0 \times 10^4$ m^{-1} which is a typical value for coarse sands [238]. Although the interfacial heat transfer coefficient may not only depend on the pore space geometry but also the flow velocity, as we focus on low Reynolds number flow in both the bulk and crack regions, this study regards h_m as an independent material parameter for simplicity, following [95, 223].

3.4.2 Hydromechanical responses in bulk and crack regions

At this point, we explicitly define the constitutive law that relates the fictitious undamaged effective stress $\boldsymbol{\sigma}'_0$ and the strain measure $\boldsymbol{\varepsilon}$, and also the temperature-dependent critical energy release rate $\mathcal{G}_c$. For porous medium with thermoelastic solid skeleton, the constitutive moduli can be defined as $\mathbb{C}^e = \lambda(\boldsymbol{I} \otimes \boldsymbol{I}) + \mu(\mathbb{I} + \bar{\mathbb{I}})$, where λ and μ are lamé constants, while undamaged effective stress in Eq. (3.18) becomes:

$$\boldsymbol{\sigma}'_0 = \lambda \,\text{tr}\,(\boldsymbol{\varepsilon})\boldsymbol{I} + 2\mu\boldsymbol{\varepsilon} - 3\alpha_s K(\theta_s - \theta_{s,\text{ref}})\boldsymbol{I}. \tag{3.64}$$

As previous studies [167, 239, 240] have shown the relationship between fracture toughness and the temperature for rock, this study adopts the following constitutive model that can describe the θ_s-dependent $\mathcal{G}_c$, since we interpret cracking as the fracture of the solid skeleton [127]:

$$\mathcal{G}_c = \mathcal{G}_{c,\text{ref}} \left[1 - a_c \left(\frac{\theta_s - \theta_{s,\text{ref}}}{\theta_{s,\text{ref}}} \right) \right], \tag{3.65}$$

where $\mathcal{G}_{c,\text{ref}}$ is the critical energy release rate at the reference temperature $\theta_{s,\text{ref}}$, and $a_c > 0$ is the model parameter that accounts for temperature-dependent decrease of crack resistance.

In this study, the fluid flow within both undamaged porous matrix and fracture is assumed to be similar to the laminar flow of a Newtonian fluid that possesses a low Reynolds number. This approach has been widely accepted in modeling hydraulic fracture in porous media [139, 140, 142, 241, 242] such that the laminar fracture flow is approximated as the

flow between two parallel plates which leads to an increase in permeability along the flow direction (i.e., cubic law). Hence, we assume that the fluid flow inside both the host matrix and the fracture obeys the generalized Darcy's law, i.e.,

$$\boldsymbol{w} = -\frac{\boldsymbol{k}}{\mu_f}(\nabla p_f - \rho_f \boldsymbol{g}), \tag{3.66}$$

where $\boldsymbol{k}$ is the permeability tensor and $\mu_f = \mu_f(\theta_f)$ is the dynamic viscosity of the pore fluid. Here, the permeability tensor can be idealized as the summation of the isotropic matrix permeability and the part that accounts for the anisotropic enhancement due to the crack opening [88, 139, 140, 217]:

$$\boldsymbol{k} = \boldsymbol{k}^{\text{mat}} + \boldsymbol{k}^{c} = k_{\text{mat}}\boldsymbol{I} + d^2 k_c(\boldsymbol{I} - \boldsymbol{n}_c \otimes \boldsymbol{n}_c), \tag{3.67}$$

where k_{mat} is the permeability of the undamaged porous matrix, $\boldsymbol{n}_c = \nabla d / \| \nabla d \|$ is the unit normal of crack surface, and k_c is the fracture permeability that depends on the fracture aperture w_c:

$$k_c = \frac{w_c^2}{12} \;\; ; \;\; w_c = H(d)\left[l_f(1 + \boldsymbol{n}_c \cdot \boldsymbol{\varepsilon} \cdot \boldsymbol{n}_c)\right] \;\; ; \;\; H(d) = \begin{cases} 0 & \text{if } d \leq 0.5, \\ 1 & \text{if } d > 0.5, \end{cases} \tag{3.68}$$

with l_f denoting the characteristic length that is often assumed to be equivalent to the size of typical finite element (i.e., $l_f = h_e$) [138, 139, 142], while $H(d)$ is the Heaviside function that explicitly defines the fractured zone based on the assumption that fracture flow is initiated if the material is half-damaged [143]. By revisiting Eq. (3.14), notice that semi-empirical porosity-permeability relation may not be applicable in this study since $\phi^f = 1$ if the host matrix is completely damaged. In this case, precise prediction of matrix permeability may require other geometrical features such as formation factor, tortuosity, or shape of pores [103, 243–246]. This extension is out of the scope of this study, and hence, we

consider k_{mat} as a constant.

As the viscosity of many fluids are temperature-dependent, numerical results drawn from the fluid flow with constant viscosity are often not applicable in the non-isothermal state [247–249]. Specifically, the temperature dependence of pore fluid viscosity affects the diffusion coefficient in Eq. (3.66) which may lead to different flow patterns compared to the idealized case where viscosity is assumed to be a constant. In this study, we adopt the most popular empirical formula that consists of two parameters (A_μ and B_μ) as follows [250, 251]:

$$\mu_f = A_\mu \exp\left(B_\mu \theta_f^{-1}\right). \tag{3.69}$$

Even though there is no one formula that works for all fluids, the two-parameter exponential model is capable of predicting the temperature-dependent viscosity of water and crude oil as shown in Fig. 3.2, which are the two most common types of pore fluids in geomaterials. Note that the circular symbols in Figs. 3.2(a) and 3.2(b) denote experimentally measured data for water [252] and A-95 crude oil [253], respectively, while solid curves indicate the curve-fitted results from Eq. (3.69).

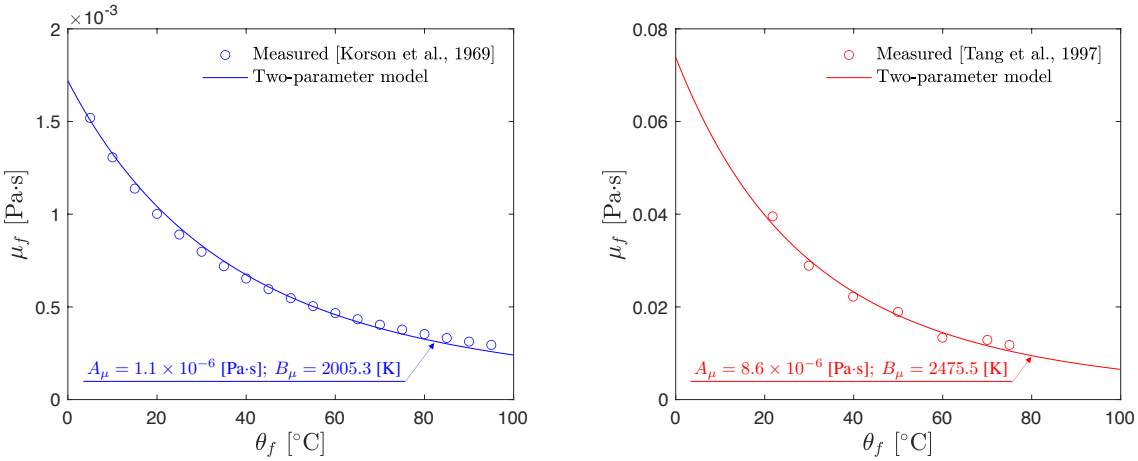

Figure 3.2: Temperature-dependent viscosity of (a) pure water, and (b) A-95 crude oil.

3.5 Finite element discretization

In this section, we present the weak form of the governing field equations, and then develop a semi-discrete formulation for the numerical solution of the thermo-hydro-mechanical and phase field fracture model we described in Sections 3.3 and 3.4. We start by summarizing the governing equations and the relevant initial boundary value problem, and then follow the standard weighted residual procedure to recover the weak form. For robust spatial discretization of the coupled problem, we use the Taylor-Hood finite element space for the displacement and pore pressure fields, and standard linear interpolation for the solid and fluid temperatures, while adopting streamline upwind Petrov-Galerkin (SUPG) stabilization for the fluid phase energy balance equation. Meanwhile, the phase field is also interpolated by linear function to ensure the efficiency of the staggered solver which sequentially updates the phase field and non-isothermal poromechanics problem.

3.5.1 Weak form

By revisiting Sections 3.3 and 3.4, the governing field equations with primary unknowns $\{\boldsymbol{u}, p_f, \theta_s, \theta_f, d\}$ are summarized as follows:

$$
\begin{cases}
\nabla\cdot\boldsymbol{\sigma} + \rho\boldsymbol{g} = \mathbf{0}, \\
\dfrac{1}{M^*}\dot{p}_f - 3\alpha_s(B^* - \phi^f)\dot{\theta}_s + B^*\,\nabla\cdot\boldsymbol{v} + \nabla\cdot\boldsymbol{w} = \hat{s}, \\
\rho^s c_s\dot{\theta}_s - \mathcal{D}^s_{\text{int}} + \nabla\cdot\boldsymbol{q}^s + a_m h_m(\theta_s - \theta_f) = \hat{r}^s, \\
\rho^f c_f\dot{\theta}_f + \rho_f c_f(\boldsymbol{w}\cdot\nabla\,\theta_f) + \nabla\cdot\boldsymbol{q}^f + a_m h_m(\theta_f - \theta_s) = \hat{r}^f, \\
g'(d)\mathcal{H} + (d - l_c^2\nabla^2 d) = 0,
\end{cases}
\tag{3.70}
$$

and the prescribed boundary conditions can be specified as,

$$\begin{cases} \boldsymbol{u} = \hat{\boldsymbol{u}} & \text{on } \partial\mathcal{B}_u \\ p_f = \hat{p}_f & \text{on } \partial\mathcal{B}_p \\ \theta_s = \hat{\theta}_s & \text{on } \partial\mathcal{B}_{\theta_s} \\ \theta_f = \hat{\theta}_f & \text{on } \partial\mathcal{B}_{\theta_f} \end{cases} ; \quad \begin{cases} \boldsymbol{\sigma} \cdot \boldsymbol{n} = \hat{\boldsymbol{t}} & \text{on } \partial\mathcal{B}_t \\ -\boldsymbol{w} \cdot \boldsymbol{n} = \hat{w} & \text{on } \partial\mathcal{B}_w \\ -\boldsymbol{q}^s \cdot \boldsymbol{n} = \hat{q}_s & \text{on } \partial\mathcal{B}_{q^s} \\ -\boldsymbol{q}^f \cdot \boldsymbol{n} = \hat{q}_f & \text{on } \partial\mathcal{B}_{q^f} \end{cases} . \tag{3.71}$$

Here, $\boldsymbol{n}$ is the outward-oriented unit normal on the boundary surface $\partial\mathcal{B}$ that consists of Dirichlet boundaries (displacement boundary $\partial\mathcal{B}_u$, pore pressure boundary $\partial\mathcal{B}_p$, solid temperature boundary $\partial\mathcal{B}_{\theta_s}$, and fluid temperature boundary $\partial\mathcal{B}_{\theta_f}$) and Neumann boundaries (traction boundary $\partial\mathcal{B}_t$, fluid flux boundary $\partial\mathcal{B}_w$, solid heat flux boundary $\partial\mathcal{B}_{q^s}$, and fluid heat flux boundary $\partial\mathcal{B}_{q^f}$) satisfying:

$$\partial\mathcal{B} = \overline{\partial\mathcal{B}_u \cup \partial\mathcal{B}_t} = \overline{\partial\mathcal{B}_p \cup \partial\mathcal{B}_w} = \overline{\partial\mathcal{B}_{\theta_s} \cup \partial\mathcal{B}_{q^s}} = \overline{\partial\mathcal{B}_{\theta_f} \cup \partial\mathcal{B}_{q^f}}, \tag{3.72}$$

$$\emptyset = \partial\mathcal{B}_u \cap \partial\mathcal{B}_t = \partial\mathcal{B}_p \cap \partial\mathcal{B}_w = \partial\mathcal{B}_{\theta_s} \cap \partial\mathcal{B}_{q^s} = \partial\mathcal{B}_{\theta_f} \cap \partial\mathcal{B}_{q^f}, \tag{3.73}$$

while the following boundary condition on $\partial\mathcal{B}$ is prescribed for the phase field d:

$$\nabla d \cdot \boldsymbol{n} = 0. \tag{3.74}$$

For model closure, the initial conditions are imposed as,

$$\boldsymbol{u} = \boldsymbol{u}_0 \ ; \ p_f = p_{f0} \ ; \ \theta_s = \theta_{s0} \ ; \ \theta_f = \theta_{f0} \ ; \ d = d_0, \tag{3.75}$$

at time $t = 0$. Then, we define the trial spaces V_u, V_p, V_{θ_s}, V_{θ_f} and V_d for the solution variables as follows:

$$
\begin{aligned}
V_u &= \left\{ \boldsymbol{u} : \mathcal{B} \to \mathbb{R}^{\mathrm{n_{dim}}} \mid \boldsymbol{u} \in [H^1(\mathcal{B})]^{\mathrm{n_{dim}}},\ \boldsymbol{u}|_{\partial \mathcal{B}_u} = \hat{\boldsymbol{u}} \right\}, \\
V_p &= \left\{ p_f : \mathcal{B} \to \mathbb{R} \mid p_f \in H^1(\mathcal{B}),\ p_f|_{\partial \mathcal{B}_p} = \hat{p}_f \right\}, \\
V_{\theta_s} &= \left\{ \theta_s : \mathcal{B} \to \mathbb{R} \mid \theta_s \in H^1(\mathcal{B}),\ \theta_s|_{\partial \mathcal{B}_{\theta_s}} = \hat{\theta}_s \right\}, \\
V_{\theta_f} &= \left\{ \theta_f : \mathcal{B} \to \mathbb{R} \mid \theta_f \in H^1(\mathcal{B}),\ \theta_f|_{\partial \mathcal{B}_{\theta_f}} = \hat{\theta}_f \right\}, \\
V_d &= \left\{ d : \mathcal{B} \to \mathbb{R} \mid d \in H^1(\mathcal{B}) \right\},
\end{aligned}
\tag{3.76}
$$

where $\mathrm{n_{dim}}$ is the spatial dimension while H^1 indicates the Sobolev space of order 1. Similarly, the corresponding admissible spaces for Eq. (3.76) are defined as,

$$
\begin{aligned}
V_\eta &= \left\{ \boldsymbol{\eta} : \mathcal{B} \to \mathbb{R}^{\mathrm{n_{dim}}} \mid \boldsymbol{\eta} \in [H^1(\mathcal{B})]^{\mathrm{n_{dim}}},\ \boldsymbol{\eta}|_{\partial \mathcal{B}_u} = \mathbf{0} \right\}, \\
V_\xi &= \left\{ \xi : \mathcal{B} \to \mathbb{R} \mid \xi \in H^1(\mathcal{B}),\ \xi|_{\partial \mathcal{B}_p} = 0 \right\}, \\
V_{\zeta_s} &= \left\{ \zeta_s : \mathcal{B} \to \mathbb{R} \mid \zeta_s \in H^1(\mathcal{B}),\ \zeta_s|_{\partial \mathcal{B}_{\theta_s}} = 0 \right\}, \\
V_{\zeta_f} &= \left\{ \zeta_f : \mathcal{B} \to \mathbb{R} \mid \zeta_f \in H^1(\mathcal{B}),\ \zeta_f|_{\partial \mathcal{B}_{\theta_f}} = 0 \right\}, \\
V_\omega &= \left\{ \omega : \mathcal{B} \to \mathbb{R} \mid \omega \in H^1(\mathcal{B}) \right\}.
\end{aligned}
\tag{3.77}
$$

Applying the standard weighted residual procedure, the weak statements for Eq. (3.70) is to: find $\{\boldsymbol{u}, p_f, \theta_s, \theta_f, d\} \in V_u \times V_p \times V_{\theta_s} \times V_{\theta_f} \times V_d$ such that for all $\{\boldsymbol{\eta}, \xi, \zeta_s, \zeta_f, \omega\} \in V_\eta \times V_\xi \times V_{\zeta_s} \times V_{\zeta_f} \times V_\omega$,

$$
G_u = G_p = G_{\theta_s} = G_{\theta_f} = G_d = 0, \tag{3.78}
$$

where:

$$
G_u = \int_{\mathcal{B}} \nabla \boldsymbol{\eta} : \boldsymbol{\sigma}\, dV - \int_{\mathcal{B}} \boldsymbol{\eta} \cdot \rho \boldsymbol{g}\, dV - \int_{\partial \mathcal{B}_t} \boldsymbol{\eta} \cdot \hat{\boldsymbol{t}}\, d\Gamma = 0, \tag{3.79}
$$

$$G_p = \int_{\mathcal{B}} \xi \frac{1}{M^*} \dot{p}_f \, dV - \int_{\mathcal{B}} \xi \left[3\alpha_s (B^* - \phi^f) \right] \dot{\theta}_s \, dV$$
$$+ \int_{\mathcal{B}} \xi (B^* \nabla \cdot \boldsymbol{v}) \, dV - \int_{\mathcal{B}} \nabla \xi \cdot \boldsymbol{w} \, dV - \int_{\mathcal{B}} \xi \hat{s} \, dV - \int_{\partial \mathcal{B}_w} \xi \hat{w} \, d\Gamma = 0, \tag{3.80}$$

$$G_{\theta_s} = \int_{\mathcal{B}} \zeta_s \rho^s c_s \dot{\theta}_s \, dV - \int_{\mathcal{B}} \zeta_s \mathcal{D}^s_{\text{int}} \, dV - \int_{\mathcal{B}} \nabla \zeta_s \cdot \boldsymbol{q}^s \, dV$$
$$- \int_{\mathcal{B}} \zeta_s \hat{r}^s \, dV + \int_{\mathcal{B}} \zeta_s \left[a_m h_m (\theta_s - \theta_f) \right] \, dV - \int_{\partial \mathcal{B}_{q^s}} \zeta_s \hat{q}^s \, d\Gamma = 0, \tag{3.81}$$

$$G_{\theta_f} = \int_{\mathcal{B}} \zeta_f^{\text{SUPG}} \rho^f c_f \dot{\theta}_f \, dV + \int_{\mathcal{B}} \zeta_f^{\text{SUPG}} \rho_f c_f (\boldsymbol{w} \cdot \nabla \theta_f) \, dV - \int_{\mathcal{B}} \nabla \zeta_f^{\text{SUPG}} \cdot \boldsymbol{q}^f \, dV$$
$$- \int_{\mathcal{B}} \zeta_f^{\text{SUPG}} \hat{r}^f \, dV + \int_{\mathcal{B}} \zeta_f \left[a_m h_m (\theta_f - \theta_s) \right] \, dV - \int_{\partial \mathcal{B}_{q^f}} \zeta_f \hat{q}^f \, d\Gamma = 0, \tag{3.82}$$

$$G_d = \int_{\mathcal{B}} \omega g'(d) \mathcal{H} \, dV + \int_{\mathcal{B}} \omega d \, dV + \int_{\mathcal{B}} \nabla \omega \cdot (l_c^2 \nabla d) \, dV = 0. \tag{3.83}$$

Here, ζ_f^{SUPG} indicates the modified weighting function:

$$\zeta_f^{\text{SUPG}} = \zeta_f + \tau_{\text{SUPG}} (\boldsymbol{w} \cdot \nabla \zeta_f), \tag{3.84}$$

while τ_{SUPG} is the stabilization coefficient which is explicitly defined in Section 3.6.

3.5.2 Galerkin form

By letting $\mathbf{N}_{\text{u}}$, $\mathbf{N}_{\text{p}}$, $\mathbf{N}_{\text{s}}$, $\mathbf{N}_{\text{f}}$, and $\mathbf{N}_{\text{d}}$ be the shape function matrices for the displacement, pore pressure, solid temperature, fluid temperature, and phase field respectively; and $\boldsymbol{\eta}$, $\boldsymbol{\xi}$, $\boldsymbol{\zeta}_{\text{s}}$, $\boldsymbol{\zeta}_{\text{f}}$, and $\boldsymbol{\omega}$ be the nodal values of the corresponding test functions, the following approximations are adopted:

$$\begin{cases} \boldsymbol{u} \approx \boldsymbol{u}^h = \mathbf{N}_{\text{u}} \mathbf{u} \\ p_f \approx p_f^h = \mathbf{N}_{\text{p}} \mathbf{p} \\ \theta_s \approx \theta_s^h = \mathbf{N}_{\text{s}} \mathbf{T}_{\text{s}} \\ \theta_f \approx \theta_f^h = \mathbf{N}_{\text{f}} \mathbf{T}_{\text{f}} \\ d \approx d^h = \mathbf{N}_{\text{d}} \mathbf{d} \end{cases} ; \quad \begin{cases} \boldsymbol{\eta} \approx \boldsymbol{\eta}^h = \mathbf{N}_{\text{u}} \boldsymbol{\eta} \\ \xi \approx \xi^h = \mathbf{N}_{\text{p}} \boldsymbol{\xi} \\ \zeta_s \approx \zeta_s^h = \mathbf{N}_{\text{s}} \boldsymbol{\zeta}_{\text{s}} \\ \zeta_f \approx \zeta_f^h = \mathbf{N}_{\text{f}} \boldsymbol{\zeta}_{\text{f}} \\ \omega \approx \omega^h = \mathbf{N}_{\text{d}} \boldsymbol{\omega} \end{cases} , \tag{3.85}$$

and we define the following transformation matrices:

$$\mathbf{B}_{\mathrm{i}} = \nabla \mathbf{N}_{\mathrm{i}} \ ; \ \mathbf{b}_{\mathrm{i}} = \nabla \cdot \mathbf{N}_{\mathrm{i}} \ ; \ \mathrm{i} = \{\mathrm{u}, \mathrm{p}, \mathrm{s}, \mathrm{f}, \mathrm{d}\}. \tag{3.86}$$

Similarly, for the modified weighting function ζ_f^{SUPG}, we also define the following matrices:

$$\zeta_f^{\mathrm{SUPG}} \approx \mathbf{N}_{\mathrm{f}}^{\mathrm{SUPG}} \boldsymbol{\zeta}_{\mathrm{f}} \ ; \ \mathbf{B}_{\mathrm{f}}^{\mathrm{SUPG}} = \nabla \mathbf{N}_{\mathrm{f}}^{\mathrm{SUPG}} \ ; \ \mathbf{b}_{\mathrm{f}}^{\mathrm{SUPG}} = \nabla \cdot \mathbf{N}_{\mathrm{f}}^{\mathrm{SUPG}}. \tag{3.87}$$

Then, by following the standard procedure, we obtain the semi-discrete forms that we summarized in Eqs. (3.90)-(3.94), while the detailed expressions for all the vectors and matrices are as follows:

$$\begin{cases} \mathbf{K} = \displaystyle\int_{\mathcal{B}} \mathbf{B}_{\mathrm{u}}^{\mathrm{T}} \tilde{\boldsymbol{C}} \mathbf{B}_{\mathrm{u}} \, dV \\ \mathbf{G} = \displaystyle\int_{\mathcal{B}} \mathbf{b}_{\mathrm{u}}^{\mathrm{T}} B^* \mathbf{N}_{\mathrm{p}} \, dV \\ \mathbf{P} = \displaystyle\int_{\mathcal{B}} \mathbf{b}_{\mathrm{u}}^{\mathrm{T}} (3\alpha_s K^*) \mathbf{N}_{\mathrm{s}} \, dV \\ \mathbf{C} = \displaystyle\int_{\mathcal{B}} \mathbf{N}_{\mathrm{p}}^{\mathrm{T}} \frac{1}{M^*} \mathbf{N}_{\mathrm{p}} \, dV \\ \mathbf{H} = \displaystyle\int_{\mathcal{B}} \mathbf{N}_{\mathrm{p}}^{\mathrm{T}} \left[3\alpha_s (B^* - \phi^f) \right] \mathbf{N}_{\mathrm{s}} \, dV \\ \boldsymbol{\phi} = \displaystyle\int_{\mathcal{B}} \mathbf{B}_{\mathrm{p}}^{\mathrm{T}} \frac{\boldsymbol{k}}{\mu_f} \mathbf{B}_{\mathrm{p}} \, dV \\ \mathbf{S}_{\mathrm{s}} = \displaystyle\int_{\mathcal{B}} \mathbf{N}_{\mathrm{s}}^{\mathrm{T}} \rho^s c_s \mathbf{N}_{\mathrm{s}} \, dV \\ \mathbf{Q}_{\mathrm{s}} = \displaystyle\int_{\mathcal{B}} \mathbf{B}_{\mathrm{s}}^{\mathrm{T}} \phi^s \kappa_s \mathbf{B}_{\mathrm{s}} \, dV \\ \mathbf{E}_{\mathrm{s}} = \displaystyle\int_{\mathcal{B}} \mathbf{N}_{\mathrm{s}}^{\mathrm{T}} a_m h_m \mathbf{N}_{\mathrm{s}} \, dV \\ \mathbf{D} = \displaystyle\int_{\mathcal{B}} \mathbf{N}_{\mathrm{s}}^{\mathrm{T}} a_m h_m \mathbf{N}_{\mathrm{f}} \, dV \end{cases}, \tag{3.88}$$

$$
\begin{cases}
\mathbf{S}_{\mathrm{f}} = \displaystyle\int_{\mathcal{B}} (\mathbf{N}_{\mathrm{f}}^{\mathrm{SUPG}})^{\mathrm{T}} \rho^f c_f \mathbf{N}_{\mathrm{f}} \, dV \\
\mathbf{A} = \displaystyle\int_{\mathcal{B}} (\mathbf{N}_{\mathrm{f}}^{\mathrm{SUPG}})^{\mathrm{T}} \rho_f c_f \boldsymbol{w} \mathbf{B}_{\mathrm{f}} \, dV \\
\mathbf{Q}_{\mathrm{f}} = \displaystyle\int_{\mathcal{B}} (\mathbf{B}_{\mathrm{f}}^{\mathrm{SUPG}})^{\mathrm{T}} \phi^f \kappa_f \mathbf{B}_{\mathrm{f}} \, dV \\
\mathbf{E}_{\mathrm{f}} = \displaystyle\int_{\mathcal{B}} \mathbf{N}_{\mathrm{f}}^{\mathrm{T}} a_m h_m \mathbf{N}_{\mathrm{f}} \, dV \\
\boldsymbol{\lambda} = \displaystyle\int_{\mathcal{B}} \mathbf{N}_{\mathrm{d}}^{\mathrm{T}} (2\mathcal{H} + 1) \mathbf{N}_{\mathrm{d}} \, dV + \int_{\mathcal{B}} \mathbf{B}_{\mathrm{d}}^{\mathrm{T}} l_c^2 \mathbf{B}_{\mathrm{d}} \, dV \\
\mathbf{f}_{\mathrm{u}} = \displaystyle\int_{\partial \mathcal{B}_t} \mathbf{N}_{\mathrm{u}}^{\mathrm{T}} \hat{\boldsymbol{t}} \, d\Gamma + \int_{\mathcal{B}} \mathbf{N}_{\mathrm{u}}^{\mathrm{T}} \rho \boldsymbol{g} \, dV - \int_{\mathcal{B}} \mathbf{b}_{\mathrm{u}}^{\mathrm{T}} (3\alpha_s K^* \theta_{s,\mathrm{ref}}) \, dV \\
\mathbf{f}_{\mathrm{p}} = \displaystyle\int_{\partial \mathcal{B}_w} \mathbf{N}_{\mathrm{p}}^{\mathrm{T}} \hat{w} \, d\Gamma + \int_{\mathcal{B}} \mathbf{N}_{\mathrm{p}}^{\mathrm{T}} \hat{s} \, dV + \int_{\mathcal{B}} \mathbf{B}_{\mathrm{p}}^{\mathrm{T}} \frac{\boldsymbol{k}}{\mu_f} (\rho_f \boldsymbol{g}) \, dV \\
\mathbf{f}_{\mathrm{s}} = \displaystyle\int_{\partial \mathcal{B}_{q^s}} \mathbf{N}_{\mathrm{s}}^{\mathrm{T}} \hat{q}^s \, d\Gamma + \int_{\mathcal{B}} \mathbf{N}_{\mathrm{s}}^{\mathrm{T}} \hat{r}^s \, dV + \int_{\mathcal{B}} \mathbf{N}_{\mathrm{s}}^{\mathrm{T}} \mathcal{D}_{\mathrm{int}}^s \, dV \\
\mathbf{f}_{\mathrm{f}} = \displaystyle\int_{\partial \mathcal{B}_{q^f}} \mathbf{N}_{\mathrm{f}}^{\mathrm{T}} \hat{q}^f \, d\Gamma + \int_{\mathcal{B}} (\mathbf{N}_{\mathrm{f}}^{\mathrm{SUPG}})^{\mathrm{T}} \hat{r}^f \, dV \\
\mathbf{f}_{\mathrm{d}} = \displaystyle\int_{\mathcal{B}} \mathbf{N}_{\mathrm{d}}^{\mathrm{T}} (2\mathcal{H}) \, dV
\end{cases}, \tag{3.89}
$$

where $\tilde{\boldsymbol{C}}$ indicates the tangential stiffness [i.e., matrix form of $g(d)\mathbb{C}^e$].

3.6 Asynchronous time integration scheme

This section focuses on the solution strategy for the coupled problem. We introduce a special time integration scheme that adopts different time step sizes for the solid and fluid temperatures by using the concept of isothermal operator split and subcycling method [144, 254, 255]. Compared to two other solution strategies (i.e., monolithic and isothermal split solvers with a single time step), numerical analysis in Section 3.7.1 hints that our approach yields consistent results while being computationally more efficient. We also conduct a stability analysis for the multi-time-step integration through investigating the generalized eigenvalue problem, while we suggest the optimal time step size and cycling period for the implicit time integration scheme by adopting more restrictive conditions: the discrete

maximum and the monotonicity principles [256–259].

3.6.1 Operator splitting and multi-time-step integration

By letting $\mathbf{u}$, $\mathbf{p}$, $\mathbf{T}_\mathrm{s}$, $\mathbf{T}_\mathrm{f}$, and $\mathbf{d}$ be the nodal vectors for the displacement, pore pressure, solid temperature, fluid temperature, and phase field, respectively, the semi-discrete form of the governing field equations [Eqs. (3.79)-(3.83)] can be expressed as follows:

$$\mathbf{K}\mathbf{u} - \mathbf{G}\mathbf{p} - \mathbf{P}\mathbf{T}_\mathrm{s} = \mathbf{f}_\mathrm{u}, \tag{3.90}$$

$$\mathbf{G}^\mathrm{T}\dot{\mathbf{u}} + \mathbf{C}\dot{\mathbf{p}} - \mathbf{H}\dot{\mathbf{T}}_\mathrm{s} + \boldsymbol{\phi}\mathbf{p} = \mathbf{f}_\mathrm{p}, \tag{3.91}$$

$$\mathbf{S}_\mathrm{s}\dot{\mathbf{T}}_\mathrm{s} + (\mathbf{Q}_\mathrm{s} + \mathbf{E}_\mathrm{s})\mathbf{T}_\mathrm{s} - \mathbf{D}\mathbf{T}_\mathrm{f} = \mathbf{f}_\mathrm{s}, \tag{3.92}$$

$$\mathbf{S}_\mathrm{f}\dot{\mathbf{T}}_\mathrm{f} - \mathbf{D}^\mathrm{T}\mathbf{T}_\mathrm{s} + (\mathbf{A} + \mathbf{Q}_\mathrm{f} + \mathbf{E}_\mathrm{f})\mathbf{T}_\mathrm{f} = \mathbf{f}_\mathrm{f}, \tag{3.93}$$

$$\boldsymbol{\lambda}\mathbf{d} = \mathbf{f}_\mathrm{d}, \tag{3.94}$$

while the complete procedure including detailed expressions for all the vectors and matrices are summarized in Eqs. (3.88) and (3.89). In this study, we adopt the staggered scheme that updates the phase field $\mathbf{d}$ and all other variables $\{\mathbf{u}, \mathbf{p}, \mathbf{T}_\mathrm{s}, \mathbf{T}_\mathrm{f}\}$ separately, which may potentially be more robust compared to the solution scheme that simultaneously solves the complete system of equations [i.e., Eqs. (3.90)-(3.94)] with a single solver [76, 132, 210, 260, 261]. Thus, by regarding the staggered scheme for the phase field $\mathbf{d}$ as a default setting, we will use the term *monolithic* to indicate the case where we use a single solver to solve Eqs. (3.90)-(3.93), while the term *operator split* will indicate the case where the field variables $\mathbf{u}$, $\mathbf{p}$, $\mathbf{T}_\mathrm{s}$, and $\mathbf{T}_\mathrm{f}$ are updated separately even if they are advanced in a staggered manner.

To solve the semi-discrete form of the governing equations numerically, it is required to choose a time-stepping integrator that leads to a different structure of the algebraic problem [144, 145, 179, 262, 263]. Although one may choose different strategies to solve the same system, this study focuses on three different time integration methods as shown in

Fig. 3.3. The first method, i.e., case (a), is often referred to as monolithic or simultaneous solution scheme and can be obtained by adopting a single time integrator which updates $\{\mathbf{u}, \mathbf{p}, \mathbf{T}_s, \mathbf{T}_f\}$ simultaneously, while the second case (b) adopts a time integration scheme that requires decoupling of the semi-discrete field equations into two parts: isothermal poromechanics problem that solves $\{\mathbf{u}, \mathbf{p}\}$ and heat transfer problem that advances $\{\mathbf{T}_s, \mathbf{T}_f\}$. This strategy is often referred to as an isothermal operator split [144, 145, 264]. Our new contribution here is to develop a third strategy (c) that uses different time steps for solid and fluid constituents that are thermally non-equilibrated. Similar to the subcycling method [254, 255, 265, 266], this approach eliminates the need to update the entire set of variables $\{\mathbf{T}_s, \mathbf{T}_f\}$ with a single time step, while it allows us to adopt different time step sizes for $\mathbf{T}_s$ and $\mathbf{T}_f$ that may be computationally more efficient compared to the cases (a) and (b).

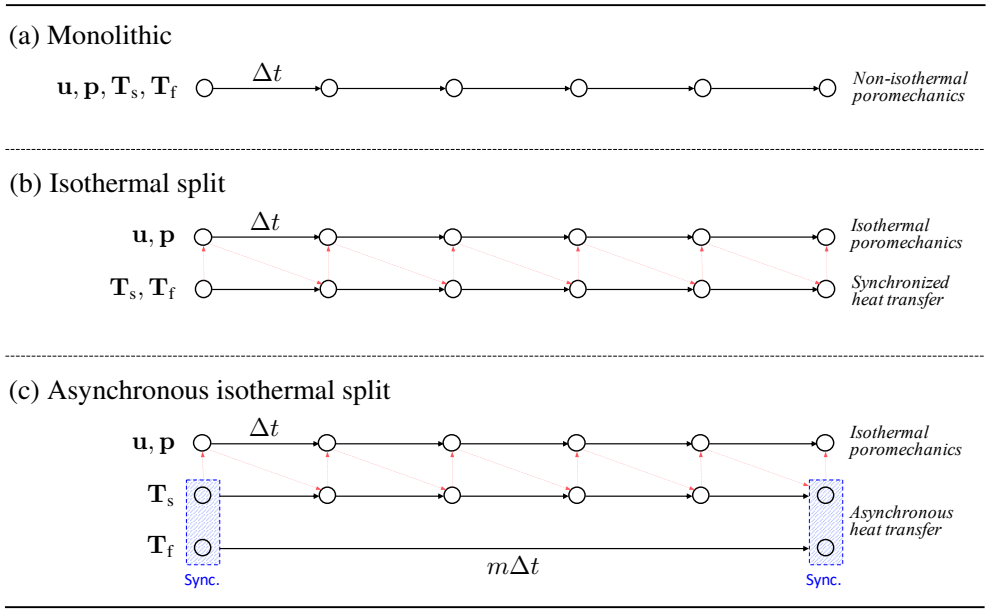

Figure 3.3: Time integration schemes: (a) monolithic, (b) isothermal split, and (c) asynchronous isothermal split.

The first method (a) shown in Fig. 3.3 is the simplest approach that monolithically

solves the following block-partitioned system:

$$\underbrace{\begin{bmatrix} \mathbf{0} & \mathbf{0} & \mathbf{0} & \mathbf{0} \\ \mathbf{G}^{\mathrm{T}} & \mathbf{C} & -\mathbf{H} & \mathbf{0} \\ \mathbf{0} & \mathbf{0} & \mathbf{S}_{\mathrm{s}} & \mathbf{0} \\ \mathbf{0} & \mathbf{0} & \mathbf{0} & \mathbf{S}_{\mathrm{f}} \end{bmatrix}}_{=\bar{\mathbf{M}}_{\mathrm{mono}}} \underbrace{\begin{bmatrix} \dot{\mathbf{u}} \\ \dot{\mathbf{p}} \\ \dot{\mathbf{T}}_{\mathrm{s}} \\ \dot{\mathbf{T}}_{\mathrm{f}} \end{bmatrix}}_{=\dot{\mathbf{x}}_{\mathrm{mono}}} + \underbrace{\begin{bmatrix} \mathbf{K} & -\mathbf{G} & -\mathbf{P} & \mathbf{0} \\ \mathbf{0} & \boldsymbol{\phi} & \mathbf{0} & \mathbf{0} \\ \mathbf{0} & \mathbf{0} & \mathbf{Q}_{\mathrm{s}} + \mathbf{E}_{\mathrm{s}} & -\mathbf{D} \\ \mathbf{0} & \mathbf{0} & -\mathbf{D}^{\mathrm{T}} & \mathbf{A} + \mathbf{Q}_{\mathrm{f}} + \mathbf{E}_{\mathrm{f}} \end{bmatrix}}_{=\bar{\mathbf{K}}_{\mathrm{mono}}} \underbrace{\begin{bmatrix} \mathbf{u} \\ \mathbf{p} \\ \mathbf{T}_{\mathrm{s}} \\ \mathbf{T}_{\mathrm{f}} \end{bmatrix}}_{=\mathbf{x}_{\mathrm{mono}}} = \underbrace{\begin{bmatrix} \mathbf{f}_{\mathrm{u}} \\ \mathbf{f}_{\mathrm{p}} \\ \mathbf{f}_{\mathrm{s}} \\ \mathbf{f}_{\mathrm{f}} \end{bmatrix}}_{=\bar{\mathbf{f}}_{\mathrm{mono}}}, \quad (3.95)$$

with the following stabilization parameter [267–269]:

$$\tau_{\mathrm{SUPG}} = \left[\left(\frac{2}{\Delta t} \right)^2 + \left(\frac{2\|\boldsymbol{w}\|}{\rho_f c_f h_e} \right)^2 + 9 \left(\frac{4\phi^f \kappa_f}{\rho_f c_f h_e^2} \right)^2 \right]^{-1/2}. \quad (3.96)$$

From Eq. (3.95), the generalized trapezoidal rule [e.g., $\mathbf{x}_{\mathrm{mono}}^{\mathrm{n}+1} = \mathbf{x}_{\mathrm{mono}}^{\mathrm{n}} + (1-\beta)\Delta t \dot{\mathbf{x}}_{\mathrm{mono}}^{\mathrm{n}} + \beta \Delta t \dot{\mathbf{x}}_{\mathrm{mono}}^{\mathrm{n}+1}$] yields the following system that needs to be solved:

$$\begin{aligned} &\text{(a) } (\bar{\mathbf{M}}_{\mathrm{mono}} + \beta \Delta t \bar{\mathbf{K}}_{\mathrm{mono}}) \mathbf{x}_{\mathrm{mono}}^{\mathrm{n}+1} \\ &\quad = \left[\bar{\mathbf{M}}_{\mathrm{mono}} + (1-\beta)\Delta t \bar{\mathbf{K}}_{\mathrm{mono}} \right] \mathbf{x}_{\mathrm{mono}}^{\mathrm{n}} + \Delta t \left[(1-\beta) \bar{\mathbf{f}}_{\mathrm{mono}}^{\mathrm{n}} + \beta \bar{\mathbf{f}}_{\mathrm{mono}}^{\mathrm{n}+1} \right], \end{aligned} \quad (3.97)$$

where $\mathbf{x}_{\mathrm{mono}}^{\mathrm{n}} = \mathbf{x}_{\mathrm{mono}}(t^{\mathrm{n}}) = \mathbf{x}_{\mathrm{mono}}(\mathrm{n}\Delta t)$, and the parameter β determines the integration algorithm, e.g., $\beta = 0$ yields a forward Euler and $\beta = 1$ recovers a backward Euler method. Note that the integration is implicit without any restriction on Δt if $\beta \geq 1/2$.

On the other hand, the isothermal operator split used for the cases (b) and (c) requires the following block-partitioned systems that are decoupled:

$$\underbrace{\begin{bmatrix} \mathbf{0} & \mathbf{0} \\ \mathbf{G}^{\mathrm{T}} & \mathbf{C} \end{bmatrix}}_{=\bar{\mathbf{M}}_{\mathrm{up}}} \underbrace{\begin{bmatrix} \dot{\mathbf{u}} \\ \dot{\mathbf{p}} \end{bmatrix}}_{=\dot{\mathbf{x}}_{\mathrm{up}}} + \underbrace{\begin{bmatrix} \mathbf{K} & -\mathbf{G} \\ \mathbf{0} & \boldsymbol{\phi} \end{bmatrix}}_{=\bar{\mathbf{K}}_{\mathrm{up}}} \underbrace{\begin{bmatrix} \mathbf{u} \\ \mathbf{p} \end{bmatrix}}_{=\mathbf{x}_{\mathrm{up}}} = \underbrace{\begin{bmatrix} \mathbf{f}_{\mathrm{u}} + \mathbf{P}\hat{\mathbf{T}}_{\mathrm{s}} \\ \mathbf{f}_{\mathrm{p}} + \mathbf{H}\hat{\dot{\mathbf{T}}}_{\mathrm{s}} \end{bmatrix}}_{=\bar{\mathbf{f}}_{\mathrm{up}}}, \quad (3.98)$$

$$\underbrace{\begin{bmatrix}\mathbf{S}_\mathrm{s} & \mathbf{0}\\ \mathbf{0} & \mathbf{S}_\mathrm{f}\end{bmatrix}}_{=\bar{\mathbf{M}}_\mathrm{sf}}\underbrace{\begin{bmatrix}\dot{\mathbf{T}}_\mathrm{s}\\ \dot{\mathbf{T}}_\mathrm{f}\end{bmatrix}}_{=\dot{\mathbf{x}}_\mathrm{sf}}+\underbrace{\begin{bmatrix}\mathbf{Q}_\mathrm{s}+\mathbf{E}_\mathrm{s} & -\mathbf{D}\\ -\mathbf{D}^\mathrm{T} & \mathbf{A}+\mathbf{Q}_\mathrm{f}+\mathbf{E}_\mathrm{f}\end{bmatrix}}_{=\bar{\mathbf{K}}_\mathrm{sf}}\underbrace{\begin{bmatrix}\mathbf{T}_\mathrm{s}\\ \mathbf{T}_\mathrm{f}\end{bmatrix}}_{=\mathbf{x}_\mathrm{sf}}=\underbrace{\begin{bmatrix}\mathbf{f}_\mathrm{s}\\ \mathbf{f}_\mathrm{f}\end{bmatrix}}_{=\bar{\mathbf{f}}_\mathrm{sf}}, \tag{3.99}$$

Here, the superimposed hat in Eq. (3.98) indicates that corresponding nodal vectors are readily determined since isothermal splitting solution scheme implies that $\mathbf{T}_\mathrm{s}$ and $\mathbf{T}_\mathrm{f}$ are no longer unknown variables for the poromechanics problem under isothermal condition [144, 270–272].

For case (b) illustrated in Fig. 3.3, the isothermal poromechanics problem and the heat transfer problem share the same Δt. Specifically, as indicated with red dashed lines with arrows in Fig. 3.3, omitting the Gauss-Seidel iteration, $\hat{\mathbf{T}}_\mathrm{s}$ and $\hat{\dot{\mathbf{T}}}_\mathrm{s}$ in Eq. (3.98) are updated from Eq. (3.99) (i.e., $\hat{\mathbf{T}}_\mathrm{s}=\mathbf{T}_\mathrm{s}^{\mathrm{n}+1}$ and $\hat{\dot{\mathbf{T}}}_\mathrm{s}=\dot{\mathbf{T}}_\mathrm{s}^{\mathrm{n}+1}$). In this case, the stabilization parameter τ_SUPG remains unchanged compared to case (a), while the generalized trapezoidal rule yields the following system:

$$\text{(b)}\begin{cases}(\bar{\mathbf{M}}_\mathrm{up}+\beta_\mathrm{up}\Delta t\bar{\mathbf{K}}_\mathrm{up})\mathbf{x}_\mathrm{up}^{\mathrm{n}+1}\\ \quad=[\bar{\mathbf{M}}_\mathrm{up}+(1-\beta_\mathrm{up})\Delta t\bar{\mathbf{K}}_\mathrm{up}]\,\mathbf{x}_\mathrm{up}^{\mathrm{n}}+\Delta t\left[(1-\beta_\mathrm{up})\bar{\mathbf{f}}_\mathrm{up}^{\mathrm{n}}+\beta_\mathrm{up}\bar{\mathbf{f}}_\mathrm{up}^{\mathrm{n}+1}\right], & (3.100)\\ (\bar{\mathbf{M}}_\mathrm{sf}+\beta_\mathrm{sf}\Delta t\bar{\mathbf{K}}_\mathrm{sf})\mathbf{x}_\mathrm{sf}^{\mathrm{n}+1}\\ \quad=[\bar{\mathbf{M}}_\mathrm{sf}+(1-\beta_\mathrm{sf})\Delta t\bar{\mathbf{K}}_\mathrm{sf}]\,\mathbf{x}_\mathrm{sf}^{\mathrm{n}}+\Delta t\left[(1-\beta_\mathrm{sf})\bar{\mathbf{f}}_\mathrm{sf}^{\mathrm{n}}+\beta_\mathrm{sf}\bar{\mathbf{f}}_\mathrm{sf}^{\mathrm{n}+1}\right], & (3.101)\end{cases}$$

where the parameters β_up and β_sf indicate that the isothermal operator splitting in case (b) requires two distinct time integrators.

For case (c) where we adopt the mixed time integration for the heat transfer problem (i.e., asynchronous heat transfer), we assume that the nodal groups $\mathbf{T}_\mathrm{s}$ and $\mathbf{T}_\mathrm{f}$ in a column vector $\mathbf{x}_\mathrm{sf}$ are integrated with different time steps Δt and $m\Delta t$, respectively (Fig. 3.3), where $m\geq 1$ is an integer. Here, time step $m\Delta t$ is called cycle [254, 273] that corresponds to the synchronized step in this study where both $\mathbf{T}_\mathrm{s}$ and $\mathbf{T}_\mathrm{f}$ are updated simultaneously. The

integration cycle for $\mathbf{x}_{\text{sf}}$ can be defined by re-writing the generalized trapezoidal rule as,

$$\mathbf{x}_{\text{sf}}^{\text{n}+1} = \mathbf{x}_{\text{sf}}^{\text{n}} + \Delta t \mathbf{W}_1 \dot{\mathbf{x}}_{\text{sf}}^{\text{n}} + \Delta t \mathbf{W}_2 \dot{\mathbf{x}}_{\text{sf}}^{\text{n}+1}, \tag{3.102}$$

with,

$$\begin{aligned}
\mathbf{W}_1 &= \begin{cases} \begin{bmatrix} (1-\beta_{\text{sf}})\mathbf{I} & \mathbf{0} \\ \mathbf{0} & \mathbf{0} \end{bmatrix} & \text{if } 1 \leq \text{n} \leq m-1, \\ \begin{bmatrix} (1-\beta_{\text{sf}})\mathbf{I} & \mathbf{0} \\ \mathbf{0} & m(1-\beta_{\text{sf}})\mathbf{I} \end{bmatrix} & \text{if n} = m, \end{cases} \\
\mathbf{W}_2 &= \begin{cases} \begin{bmatrix} \beta_{\text{sf}}\mathbf{I} & \mathbf{0} \\ \mathbf{0} & \mathbf{0} \end{bmatrix} & \text{if } 1 \leq \text{n} \leq m-1, \\ \begin{bmatrix} \beta_{\text{sf}}\mathbf{I} & \mathbf{0} \\ \mathbf{0} & m\beta_{\text{sf}}\mathbf{I} \end{bmatrix} & \text{if n} = m, \end{cases}
\end{aligned} \tag{3.103}$$

where $\mathbf{I}$ is the unit matrix that is different from the identity tensor $\boldsymbol{I}$. Substituting Eq. (3.102) into Eq. (3.99) yields the following set of equations that needs to be solved, while we assume that the solution for the isothermal poromechanics problem is advanced by Δt, such that the system in Eq. (3.104) remains the same compared to Eq. (3.100), i.e.,

$$\text{(c)} \begin{cases} (\bar{\mathbf{M}}_{\text{up}} + \beta_{\text{up}} \Delta t \bar{\mathbf{K}}_{\text{up}}) \mathbf{x}_{\text{up}}^{\text{n}+1} \\ = \left[\bar{\mathbf{M}}_{\text{up}} + (1-\beta_{\text{up}}) \Delta t \bar{\mathbf{K}}_{\text{up}}\right] \mathbf{x}_{\text{up}}^{\text{n}} + \Delta t \left[(1-\beta_{\text{up}}) \bar{\mathbf{f}}_{\text{up}}^{\text{n}} + \beta_{\text{up}} \bar{\mathbf{f}}_{\text{up}}^{\text{n}+1}\right], & (3.104) \\ (\bar{\mathbf{M}}_{\text{sf}} + \Delta t \mathbf{W}_2 \bar{\mathbf{K}}_{\text{sf}}) \mathbf{x}_{\text{sf}}^{\text{n}+1} \\ = (\bar{\mathbf{M}}_{\text{sf}} - \Delta t \mathbf{W}_1 \bar{\mathbf{K}}_{\text{sf}}) \mathbf{x}_{\text{sf}}^{\text{n}} + \Delta t (\mathbf{W}_1 \bar{\mathbf{f}}_{\text{sf}}^{\text{n}} + \mathbf{W}_2 \bar{\mathbf{f}}_{\text{sf}}^{\text{n}+1}), & (3.105) \end{cases}$$

while the stabilization parameter is redefined accordingly for this case:

$$\tau_{\text{SUPG}} = \left[\left(\frac{2}{m \Delta t} \right)^2 + \left(\frac{2 \|\boldsymbol{w}\|}{\rho_f c_f h_e} \right)^2 + 9 \left(\frac{4 \phi^f \kappa_f}{\rho_f c_f h_e^2} \right)^2 \right]^{-1/2}. \tag{3.106}$$

Note that Eqs. (3.104) and (3.105) summarizes the solution scheme in a single cycle for case (c), while the entire code structure for the mixed time integration is illustrated in Fig. 3.4, where the gray blocks denote the initialization steps, the red blocks represent time-marching procedure, and blue blocks indicate the Gauss-Seidel iteration. Here, if we set the maximum number of iterations to be 1, the Gauss-Seidel iteration reduces to a series of staggered solution schemes.

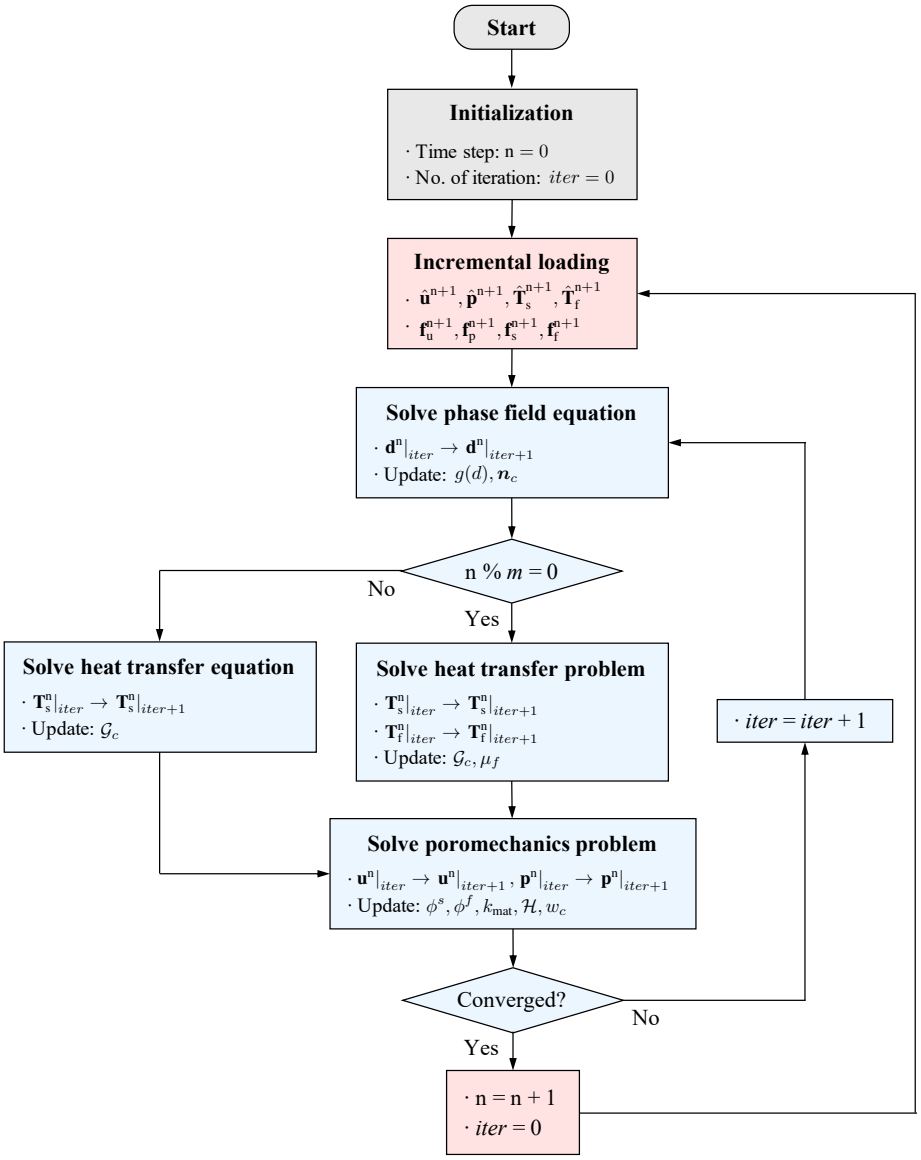

Figure 3.4: Flowchart of the asynchronous operator splitting scheme for phase field fracture in fluid-saturated porous media under local thermal non-equilibrium.

3.6.2 Stability of mixed time integration

As previous studies [264, 274, 275] have investigated the stability and convergence for the hydro-mechanically coupled problem, we focus on the stability analysis on the mixed time integration in Eq. (3.105) since it reduces to a standard isothermal split setting for case (b) shown in Fig. 3.3 if $m = 1$. In specific, this section focuses on the case where the stabilization parameter τ_{SUPG} is small, so that the matrices $\mathbf{S}_{\text{f}}$, $\mathbf{A}$, and $\mathbf{Q}_{\text{f}}$ are considered symmetric.

Considering the homogeneous case, Eq. (3.105) reduces into,

$$\underbrace{(\bar{\mathbf{M}}_{\text{sf}} + \Delta t \mathbf{W}_2 \bar{\mathbf{K}}_{\text{sf}})}_{=\bar{\mathbf{A}}_2} \mathbf{x}_{\text{sf}}^{\text{n}+1} = \underbrace{(\bar{\mathbf{M}}_{\text{sf}} - \Delta t \mathbf{W}_1 \bar{\mathbf{K}}_{\text{sf}})}_{=\bar{\mathbf{A}}_1} \mathbf{x}_{\text{sf}}^{\text{n}}, \tag{3.107}$$

which leads to the following generalized eigenvalue problem that is essential to investigate the stability characteristics:

$$\bar{\mathbf{A}}_1 \mathbf{y}_{\text{sf}} = \lambda_{\text{sf}} \bar{\mathbf{A}}_2 \mathbf{y}_{\text{sf}} \ ; \ \mathbf{y}_{\text{sf}} = \begin{bmatrix} \mathbf{y}_{\text{s}} \\ \mathbf{y}_{\text{f}} \end{bmatrix}, \tag{3.108}$$

where the vector $\mathbf{y}_{\text{sf}}$ is composed of total $N_n^{\text{sf}} = N_n^{\text{s}} + N_n^{\text{f}}$ components so that its ith element corresponds to $\mathbf{y}_{\text{s}}$ that is related to the solid temperature, if $1 \leq i \leq N_n^{\text{s}}$; while corresponds to $\mathbf{y}_{\text{f}}$ (i.e., the fluid temperature) if $N_n^{\text{s}} + 1 \leq i \leq N_n^{\text{sf}}$.

For the non-synchronized step where $1 \leq \text{n} \leq m - 1$, we get the following by substituting Eq. (3.103) into Eq. (3.108):

$$\begin{aligned} \begin{bmatrix} \mathbf{Q}_{\text{s}} + \mathbf{E}_{\text{s}} & -\mathbf{D} \\ \mathbf{0} & \mathbf{0} \end{bmatrix} \mathbf{y}_{\text{sf}} &= \underbrace{\frac{1 - \lambda_{\text{sf}}}{(1 - \beta_{\text{sf}})\Delta t + \lambda_{\text{sf}} \beta_{\text{sf}} \Delta t}}_{=\gamma_{\text{sf}}} \bar{\mathbf{M}}_{\text{sf}} \mathbf{y}_{\text{sf}} \\ &\longrightarrow \begin{cases} (\mathbf{Q}_{\text{s}} + \mathbf{E}_{\text{s}}) \mathbf{y}_{\text{s}} - \mathbf{D} \mathbf{y}_{\text{f}} = \gamma_{\text{sf}} \mathbf{S}_{\text{s}} \mathbf{y}_{\text{s}}, \\ \mathbf{0} = \gamma_{\text{sf}} \mathbf{S}_{\text{f}} \mathbf{y}_{\text{f}}. \end{cases} \end{aligned} \tag{3.109}$$

Following Smolinski, Belytschko, and Neal [254], due to the positive definiteness of $\mathbf{S}_{\mathrm{s}}$, the second row in Eq. (3.109) implies either $\gamma_{\mathrm{sf}} = 0$ or $\mathbf{y}_{\mathrm{f}} = \mathbf{0}$. In specific, if $1 \leq i \leq N_n^{\mathrm{s}}$, we have $\gamma_{\mathrm{sf}} = 0$; while $\mathbf{y}_{\mathrm{f}} = \mathbf{0}$ for $N_n^{\mathrm{s}} + 1 \leq i \leq N_n^{\mathrm{sf}}$. Considering the first case where $\gamma_{\mathrm{sf}} = 0$, the first row in Eq. (3.109) yields $\mathbf{y}_{\mathrm{s}} = [(\mathbf{Q}_{\mathrm{s}} + \mathbf{E}_{\mathrm{s}})^{-1}\mathbf{D}]\,\mathbf{y}_{\mathrm{f}}$, such that the vector $\mathbf{y}_{\mathrm{sf}}$ spans $\mathbb{R}^{N_n^{\mathrm{f}}}$ since $\mathbf{Q}_{\mathrm{s}} + \mathbf{E}_{\mathrm{s}}$ is a symmetric and non-singular matrix, i.e.,

$$\tilde{\mathbf{y}}_{\mathrm{sf}} = \begin{bmatrix} [(\mathbf{Q}_{\mathrm{s}} + \mathbf{E}_{\mathrm{s}})^{-1}\mathbf{D}]\,\tilde{\mathbf{y}}_{\mathrm{f}} \\ \tilde{\mathbf{y}}_{\mathrm{f}} \end{bmatrix} \quad \text{if } 1 \leq i \leq N_n^{\mathrm{s}}, \tag{3.110}$$

where the superposed tilde indicates the prospective eigenvectors that correspond to $\gamma_{\mathrm{sf}} = 0$. On the other hand, for the second case where $\mathbf{y}_{\mathrm{f}} = \mathbf{0}$, vector $\mathbf{y}_{\mathrm{sf}}$ spans $\mathbb{R}^{N_n^{\mathrm{s}}}$ and is given by,

$$\check{\mathbf{y}}_{\mathrm{sf}} = \begin{bmatrix} \check{\mathbf{y}}_{\mathrm{s}} \\ \mathbf{0} \end{bmatrix} \quad \text{if } N_n^{\mathrm{s}} + 1 \leq i \leq N_n^{\mathrm{sf}}. \tag{3.111}$$

Here, the superposed check symbol in Eq. (3.111) denotes the prospective eigenvectors that correspond to the case where $\mathbf{y}_{\mathrm{f}} = \mathbf{0}$. Notice that Eqs. (3.110) and (3.111) hints that the set of vectors ($\tilde{\mathbf{y}}_{\mathrm{sf}}$ and $\check{\mathbf{y}}_{\mathrm{sf}}$) span $\mathbb{R}^{N_n^{\mathrm{sf}}}$. It implies that we have two sets of eigenvectors that correspond to the case where the eigenvalues are either $\gamma_{\mathrm{sf}} = 0$ or $\gamma_{\mathrm{sf}} \neq 0$, respectively, since they are orthogonal with respect to $\bar{\mathbf{K}}_{\mathrm{sf}}$. Specifically, the vectors $\check{\mathbf{y}}_{\mathrm{sf}}$ are B-orthogonal to each other [276–278]:

$$\begin{aligned} \check{\mathbf{y}}_{\mathrm{sf},i}^{\mathrm{T}} \bar{\mathbf{K}}_{\mathrm{sf}} \check{\mathbf{y}}_{\mathrm{sf},j} &= \begin{bmatrix} \check{\mathbf{y}}_{\mathrm{s},i}^{\mathrm{T}} & \mathbf{0}^{\mathrm{T}} \end{bmatrix} \begin{bmatrix} \mathbf{Q}_{\mathrm{s}} + \mathbf{E}_{\mathrm{s}} & -\mathbf{D} \\ -\mathbf{D}^{\mathrm{T}} & \mathbf{A} + \mathbf{Q}_{\mathrm{f}} + \mathbf{E}_{\mathrm{f}} \end{bmatrix} \begin{bmatrix} \check{\mathbf{y}}_{\mathrm{s},j} \\ \mathbf{0} \end{bmatrix} \\ &= \begin{bmatrix} \check{\mathbf{y}}_{\mathrm{s},i}^{\mathrm{T}} & \mathbf{0}^{\mathrm{T}} \end{bmatrix} \begin{bmatrix} (\mathbf{Q}_{\mathrm{s}} + \mathbf{E}_{\mathrm{s}})\check{\mathbf{y}}_{\mathrm{s},j} \\ -\mathbf{D}^{\mathrm{T}}\check{\mathbf{y}}_{\mathrm{s},j} \end{bmatrix} \\ &= \check{\mathbf{y}}_{\mathrm{s},i}^{\mathrm{T}} (\mathbf{Q}_{\mathrm{s}} + \mathbf{E}_{\mathrm{s}})\check{\mathbf{y}}_{\mathrm{s},j} = \gamma_{\mathrm{sf},i}\delta_{ij} \quad \text{if } \{i,j\} \in [1, N_n^{\mathrm{s}}], \end{aligned} \tag{3.112}$$

since the first row in Eq. (3.109) gives $(\mathbf{Q}_{\mathrm{s}} + \mathbf{E}_{\mathrm{s}})\check{\mathbf{y}}_{\mathrm{s}} = \gamma_{\mathrm{sf}}\mathbf{S}_{\mathrm{s}}\check{\mathbf{y}}_{\mathrm{s}}$, such that $\check{\mathbf{y}}_{\mathrm{s}}$ can be orthog-

onalized with respect to $\mathbf{Q}_\mathrm{s} + \mathbf{E}_\mathrm{s}$ and $\mathbf{S}_\mathrm{s}$, whereas the vectors $\tilde{\mathbf{y}}_\mathrm{sf}$ are orthogonal to $\check{\mathbf{y}}_\mathrm{sf}$ with respect to $\bar{\mathbf{K}}_\mathrm{sf}$:

$$\begin{aligned}\check{\mathbf{y}}_{\mathrm{sf},i}^\mathrm{T}\bar{\mathbf{K}}_\mathrm{sf}\tilde{\mathbf{y}}_{\mathrm{sf},j} &= \begin{bmatrix}\check{\mathbf{y}}_{\mathrm{s},i}^\mathrm{T} & \mathbf{0}^\mathrm{T}\end{bmatrix}\begin{bmatrix}\mathbf{Q}_\mathrm{s}+\mathbf{E}_\mathrm{s} & -\mathbf{D} \\ -\mathbf{D}^\mathrm{T} & \mathbf{A}+\mathbf{Q}_\mathrm{f}+\mathbf{E}_\mathrm{f}\end{bmatrix}\begin{bmatrix}[(\mathbf{Q}_\mathrm{s}+\mathbf{E}_\mathrm{s})^{-1}\mathbf{D}]\,\tilde{\mathbf{y}}_{\mathrm{f},j} \\ \tilde{\mathbf{y}}_{\mathrm{f},j}\end{bmatrix} \\ &= \begin{bmatrix}\check{\mathbf{y}}_{\mathrm{s},i}^\mathrm{T} & \mathbf{0}^\mathrm{T}\end{bmatrix}\begin{bmatrix}\mathbf{0} \\ [-\mathbf{D}^\mathrm{T}(\mathbf{Q}_\mathrm{s}+\mathbf{E}_\mathrm{s})\mathbf{D}+(\mathbf{A}+\mathbf{Q}_\mathrm{f}+\mathbf{E}_\mathrm{f})]\,\tilde{\mathbf{y}}_{\mathrm{f},j}\end{bmatrix} = 0 \\ &\text{if } \{i,j\} \in [N_n^\mathrm{s}+1, N_n^\mathrm{sf}].\end{aligned} \tag{3.113}$$

Therefore, the non-synchronized solution at time step n can be expanded in terms of eigenvectors as,

$$\mathbf{x}_\mathrm{sf}^\mathrm{n} = \check{c}_i\check{\mathbf{y}}_{\mathrm{sf},i} + \tilde{c}_j\tilde{\mathbf{y}}_{\mathrm{sf},j}, \tag{3.114}$$

where $\check{c}_i$ and $\tilde{c}_j$ are constants, while the repeated indices imply the summation following the Einstein's notation [221, 279]. Then, substituting Eq. (3.114) into Eq. (3.107) yields the following expression for the updated solution:

$$\mathbf{x}_\mathrm{sf}^{\mathrm{n}+1} = \check{c}_i\lambda_{\mathrm{sf},i}\check{\mathbf{y}}_{\mathrm{sf},i} + \tilde{c}_j\tilde{\mathbf{y}}_{\mathrm{sf},j}, \tag{3.115}$$

where $\lambda_\mathrm{sf} = 1$ for $\tilde{\mathbf{y}}_\mathrm{sf}$ since $\gamma_\mathrm{sf} = 0$. By defining the norm E_sf as,

$$E_\mathrm{sf} = \frac{1}{2}\mathbf{x}_\mathrm{sf}^\mathrm{T}\bar{\mathbf{K}}_\mathrm{sf}\mathbf{x}_\mathrm{sf}, \tag{3.116}$$

the B-orthogonality shown in Eqs. (3.112) and (3.113) gives the following expression for time step n:

$$E_\mathrm{sf}^\mathrm{n} = (\check{c}_i\check{\mathbf{y}}_{\mathrm{sf},i} + \tilde{c}_j\tilde{\mathbf{y}}_{\mathrm{sf},j})^\mathrm{T}\bar{\mathbf{K}}_\mathrm{sf}(\check{c}_k\check{\mathbf{y}}_{\mathrm{sf},k} + \tilde{c}_l\tilde{\mathbf{y}}_{\mathrm{sf},l}) = \check{c}_i^2\gamma_{\mathrm{sf},i} + \tilde{c}_j\tilde{c}_l\tilde{\mathbf{y}}_{\mathrm{sf},j}^\mathrm{T}\bar{\mathbf{K}}_\mathrm{sf}\tilde{\mathbf{y}}_{\mathrm{sf},l}, \tag{3.117}$$

while $E_{\mathrm{sf}}^{\mathrm{n}+1}$ at time step $\mathrm{n}+1$ reads,

$$E_{\mathrm{sf}}^{\mathrm{n}+1} = (\check{c}_i \lambda_{\mathrm{sf},i} \check{\mathbf{y}}_{\mathrm{sf},i} + \tilde{c}_j \tilde{\mathbf{y}}_{\mathrm{sf},j})^{\mathrm{T}} \bar{\mathbf{K}}_{\mathrm{sf}} (\check{c}_k \lambda_{\mathrm{sf},k} \check{\mathbf{y}}_{\mathrm{sf},k} + \tilde{c}_l \tilde{\mathbf{y}}_{\mathrm{sf},l}) = \check{c}_i^2 \lambda_{\mathrm{sf},i}^2 \gamma_{\mathrm{sf},i} + \tilde{c}_j \tilde{c}_l \tilde{\mathbf{y}}_{\mathrm{sf},j}^{\mathrm{T}} \bar{\mathbf{K}}_{\mathrm{sf}} \tilde{\mathbf{y}}_{\mathrm{sf},l}. \tag{3.118}$$

Comparing Eqs. (3.117) and (3.118), notice that the stability $E_{\mathrm{sf}}^{\mathrm{n}+1} \leq E_{\mathrm{sf}}^{\mathrm{n}}$ is ensured if the following condition is satisfied:

$$|\lambda_{\mathrm{sf}}| = \left| \frac{1 - \gamma_{\mathrm{sf}}(1 - \beta_{\mathrm{sf}})\Delta t}{1 + \gamma_{\mathrm{sf}} \beta_{\mathrm{sf}} \Delta t} \right| \leq 1. \tag{3.119}$$

If $\gamma_{\mathrm{sf}} \geq 0$, Eq. (3.119) reduces into,

$$\Delta t \leq \frac{2}{\gamma_{\mathrm{sf}}(1 - 2\beta_{\mathrm{sf}})}. \tag{3.120}$$

For the synchronized step where $\mathrm{n} = m$, Eqs. (3.107) and (3.108) yield the following expression with some rearrangements:

$$\bar{\mathbf{K}}_{\mathrm{sf}} \mathbf{y}_{\mathrm{sf}} = \underbrace{\frac{1 - \lambda'_{\mathrm{sf}}}{m\left[(1 - \beta_{\mathrm{sf}})\Delta t + \lambda'_{\mathrm{sf}} \beta_{\mathrm{sf}} \Delta t\right]}}_{=\gamma'_{\mathrm{sf}}} \underbrace{\begin{bmatrix} m\mathbf{S}_{\mathrm{s}} & \mathbf{0} \\ \mathbf{0} & \mathbf{S}_{\mathrm{f}} \end{bmatrix}}_{=\bar{\mathbf{M}}'_{\mathrm{sf}}} \mathbf{y}_{\mathrm{sf}}, \tag{3.121}$$

where λ'_{sf}, γ'_{sf} and $\bar{\mathbf{M}}'_{\mathrm{sf}}$ designate the quantities associated with the synchronized step. Here, since $\bar{\mathbf{K}}_{\mathrm{sf}}$ and $\bar{\mathbf{M}}'_{\mathrm{sf}}$ are symmetric and non-singular based on the assumption $\tau_{\mathrm{SUPG}} \to 0$, the values γ'_{sf} are real and possess distinct eigenvectors $\mathbf{y}_{\mathrm{sf}}$ that are B-orthogonal [276–278]. Thus, following the similar procedure that is used for the non-synchronized step [i.e., Eqs. (3.116)-(3.119)], the stability condition reads,

$$|\lambda'_{\mathrm{sf}}| = \left| \frac{1 - m\gamma'_{\mathrm{sf}}(1 - \beta_{\mathrm{sf}})\Delta t}{1 + m\gamma'_{\mathrm{sf}} \beta_{\mathrm{sf}} \Delta t} \right| \leq 1. \tag{3.122}$$

Similarly, if $\gamma'_{\text{sf}} \geq 0$, Eq. (3.122) reduces into,

$$\Delta t \leq \frac{2}{m\gamma'_{\text{sf}}(1-2\beta_{\text{sf}})}. \tag{3.123}$$

This stability analysis highlights that our mixed time integration is unconditionally stable if we adopt implicit schemes. For example, if we employ the backward Euler method (i.e., $\beta_{\text{sf}} = 1$), the stability conditions are automatically satisfied since both $|\lambda_{\text{sf}}|$ and $|\lambda'_{\text{sf}}|$ are less than 1, i.e.,

$$|\lambda_{\text{sf}}| = \left|\frac{1}{1+\gamma_{\text{sf}}\Delta t}\right| < 1 \ ; \ |\lambda'_{\text{sf}}| = \left|\frac{1}{1+m\gamma'_{\text{sf}}\Delta t}\right| < 1. \tag{3.124}$$

3.6.3 Time step size and cycling period for implicit algorithm

As pointed out in Liu et al. [280], even though we adopt quadratic interpolation for the displacement and linear interpolations for all other fields, the solution may still result in oscillatory results if Δt is small. In this section, by employing the implicit backward Euler method (i.e., $\beta_{\text{up}} = \beta_{\text{sf}} = 1$), we suggest the optimal sizes for Δt and the cycling period m for the mixed time integration scheme that may completely avoid the spurious oscillations by adopting more restrictive conditions. The first condition is the discrete maximum principle (DMP) that requires the positivity (or negativity) of an incremental solution if the right hand side in Eqs. (3.128)-(3.130) is positive (or negative), while the second condition requires the monotonicity of the solution, which is called the monotonicity principle (MP) [256–258]. For a system of equation, e.g., $\bar{\mathbf{A}}\mathbf{x} = \mathbf{b}$, Li and Wei [259] pointed out that both DMP and MP are satisfied if the coefficient matrix $\bar{\mathbf{A}}$ is an M-matrix [281, 282] that satisfies:

$$\bar{\mathbf{A}}_{ii} > 0 \text{ (no sum)} \ ; \ \bar{\mathbf{A}}_{ij} \leq 0 \ (i \neq j). \tag{3.125}$$

In other words, in order to ensure non-oscillatory results, the diagonal components of the coefficient matrices should be positive while the off-diagonal terms should be non-positive.

Since the asynchronous isothermal split scheme [i.e., case (c) in Fig. 3.3] solves the decoupled systems separately, we apply the criteria in Eq. (3.125) to each coefficient matrices to suggest the optimal time step size and the cycling period. By revisiting Eqs. (3.90)-(3.93) and Eq. (3.104), the backward Euler method yields the following expression for the isothermal poromechanics problem:

$$\mathbf{K}\mathbf{u}^{n+1} = \mathbf{G}\mathbf{p}^{n+1} + \mathbf{f}_u^{n+1} + \mathbf{P}\hat{\mathbf{T}}_s, \tag{3.126}$$

$$\mathbf{G}^T\mathbf{u}^{n+1} + (\mathbf{C} + \Delta t\boldsymbol{\phi})\mathbf{p}^{n+1} = \mathbf{G}^T\mathbf{u}^n + \mathbf{C}\mathbf{p}^n + \Delta t(\mathbf{f}_p^{n+1} + \mathbf{H}\hat{\dot{\mathbf{T}}}_s). \tag{3.127}$$

Substituting Eq. (3.126) into Eq. (3.127) yields,

$$\begin{aligned} &\underbrace{(\mathbf{G}^T\mathbf{K}^{-1}\mathbf{G} + \mathbf{C} + \Delta t\boldsymbol{\phi})}_{=\bar{\mathbf{A}}_{up}}\mathbf{p}^{n+1} \\ &= \mathbf{G}^T\mathbf{u}^n + \mathbf{C}\mathbf{p}^n - \mathbf{G}^T\mathbf{K}^{-1}(\mathbf{f}_u^{n+1} + \mathbf{P}\hat{\mathbf{T}}_s) + \Delta t(\mathbf{f}_p^{n+1} + \mathbf{H}\hat{\dot{\mathbf{T}}}_s). \end{aligned} \tag{3.128}$$

Similarly, the heat transfer problem can be re-expressed as follows:

$$\underbrace{[\mathbf{S}_s + \Delta t(\mathbf{Q}_s + \mathbf{E}_s)]}_{=\bar{\mathbf{A}}_s}\mathbf{T}_s^{n+1} = \mathbf{S}_s\mathbf{T}_s^n + \Delta t(\mathbf{D}\mathbf{T}_f^{n+1} + \mathbf{f}_s^{n+1}), \tag{3.129}$$

$$\underbrace{[\mathbf{S}_f + m\Delta t(\mathbf{A} + \mathbf{Q}_f + \mathbf{E}_f)]}_{=\bar{\mathbf{A}}_f}\mathbf{T}_f^{n+1} = \mathbf{S}_f\mathbf{T}_f^n + m\Delta t(\mathbf{D}^T\mathbf{T}_s^{n+1} + \mathbf{f}_f^{n+1}). \tag{3.130}$$

Here, although we solve for $\{\mathbf{T}_s, \mathbf{T}_f\}$ simultaneously at the synchronized step (Fig. 3.4), we consider the decoupled situation to investigate their coefficient matrices separately. In this case, Eqs. (3.128)-(3.130) are discrete linear equations to be solved, where the coefficient matrices are: $\bar{\mathbf{A}}_{up}$, $\bar{\mathbf{A}}_s$, and $\bar{\mathbf{A}}_f$. Notice that the diagonal components of the coefficient matrix are positive so that the first criterion in Eq. (3.125) is automatically satisfied.

In order to illustrate the idea behind our suggestions, we explore the most simple one-dimensional case, while we neglect the heat convection term for simplicity. Since we adopt the Taylor-Hood finite element for the displacement and pore pressure, and linear

element for the solid and fluid temperatures, exact Gauss quadrature yields the following off-diagonal terms of element coefficient matrices $\bar{\mathbf{A}}^e_{\text{up},ij}$, $\bar{\mathbf{A}}^e_{\text{s},ij}$, and $\bar{\mathbf{A}}^e_{\text{f},ij}$ $(i \neq j)$, if $\tau_{\text{SUPG}} \to 0$:

$$\bar{\mathbf{A}}^e_{\text{up},ij} = \frac{h_e}{6M^*} - \frac{h_e B^{*2}}{6C^*} - \Delta t \left(\frac{k}{h_e \mu_f} \right), \tag{3.131}$$

$$\bar{\mathbf{A}}^e_{\text{s},ij} = \frac{h_e \rho^s c_s}{6} + \Delta t \left(\frac{h_e a_m h_m}{6} - \frac{\phi^s \kappa_s}{h_e} \right), \tag{3.132}$$

$$\bar{\mathbf{A}}^e_{\text{f},ij} = \frac{h_e \rho^f c_f}{6} + m\Delta t \left(\frac{h_e a_m h_m}{6} - \frac{\phi^f \kappa_f}{h_e} \right), \tag{3.133}$$

where C^* and k indicate the scalar stiffness and permeability coefficients, respectively. Then, applying the second criterion in Eq. (3.125) to Eqs. (3.131)-(3.133), we get:

$$\Delta t \geq \underbrace{\frac{h_e^2 \mu_f}{k} \left(\frac{1}{6M^*} - \frac{B^{*2}}{6C^*} \right)}_{=\Delta t_{\text{up,min}}}, \tag{3.134}$$

$$\Delta t \geq \underbrace{\frac{h_e^2 \rho^s c_s}{6\phi^s \kappa_s - h_e^2 a_m h_m}}_{=\Delta t_{\text{s,min}}}, \tag{3.135}$$

$$m\Delta t \geq \underbrace{\frac{h_e^2 \rho^f c_f}{6\phi^f \kappa_f - h_e^2 a_m h_m}}_{=\Delta t_{\text{f,min}}}, \tag{3.136}$$

respectively. This 1D example underscores that the minimum time step size Δt for the mixed time integration should satisfy Eqs. (3.134)-(3.136) at the same time. Also notice that, unless employing a different interpolation strategy, the criteria remain the same in two- or three-dimensional cases, while $\Delta t_{\text{up,min}}$, $\Delta t_{\text{s,min}}$, and $\Delta t_{\text{f,min}}$ may have different expressions depending on the spatial dimension.

Overall, for the asynchronous isothermal splitting scheme shown in Fig. 3.4, we propose the following general criteria for the cycling period m as:

$$m \approx \frac{\rho_f c_f \kappa_s}{\rho_s c_s \kappa_f}, \tag{3.137}$$

so that $m\Delta t_{\text{s,min}} \approx \Delta t_{\text{f,min}}$, while the time step size can be chosen as,

$$\Delta t \geq \max\left(\Delta t_{\text{up,min}}, \Delta t_{\text{s,min}}\right). \tag{3.138}$$

To be conservative, we set Δt one to two orders of magnitudes larger than $\max\left(\Delta t_{\text{up,min}}, \Delta t_{\text{s,min}}\right)$ for all the numerical examples in Section 3.7.

Remark 4. The phase field approach to fracture requires a mesh that is locally refined along the potential crack path, where element sizes may substantially vary over the domain. For a thermo-hydro-mechanical-fracture problem that involves high pressure or temperature gradients near the crack, $\Delta t_{\text{up,min}}$ and $\Delta t_{\text{s,min}}$ in Eqs. (3.134) and (3.135) can be determined by using the minimum element size, i.e., $\min\left(h_e\right)$, in order to capture the detailed coupled processes near damaged regions.

3.7 Numerical examples

This section presents three sets of numerical examples to showcase the capacities of the proposed model, focusing on transient problems that involve heat exchange between the solid and fluid constituents. We limit our attention to one- or two-dimensional simulations at cm-scale and neglect the gravitational effects (i.e., $\boldsymbol{g} = \mathbf{0}$), while adopting implicit backward Euler time integration scheme with a Newton-Raphson solver. As a preliminary study, the first example compares three different time integration schemes illustrated in Fig. 3.3 by simulating one-dimensional heat transfer process in a water-saturated porous column to demonstrate the computational efficiency of the asynchronous isothermal split solution scheme. In the second numerical example, we compare the one-temperature model that considers local thermal equilibrium (LTE) state with the two-temperature model where the solid and fluid constituents are in local thermal non-equilibrium (LTNE). Specifically, we focus on the effect of the different growth rates of thermal boundary layers on the fracture pattern by simulating a mechanically driven crack propagation on an oil-saturated double-

edge-notched specimen. Finally, the third example highlights the modeling capacity of capturing the coupled thermo-hydro-mechanical-fracture processes by simulating the interaction of two cracks that are hydraulically stimulated by injecting hot fluid into pre-existing flaws. The implementation of the model including the finite element discretization and the solution scheme relies on the finite element package `FEniCS` [146–148] with `PETSc` scientific computational toolkit [149], while all the numerical simulations rely on meshes that are sufficiently refined around the potential crack trajectory in order to capture the damage field around crack surfaces properly.

3.7.1 Comparative study: one-dimensional heat transfer

This example simulates the one-dimensional heat transfer process in a porous column by prescribing a raised temperature at the top surface. Assuming that the solid and fluid constituents are in LTNE state and remain undamaged, this numerical example serves as a preliminary study that compares the performance between three different time integration schemes shown in Fig. 3.3.

In this example, we choose the material properties of the problem domain similar to a typical water-saturated sandstone, which is summarized in Table 3.1. As illustrated in Fig. 3.5, our 0.1 m long porous column with initial temperatures of $\theta_{s0} = \theta_{f0} = 20°\text{C}$ is subjected to thermal loading of $\hat{\theta}_s = \hat{\theta}_f = 50°\text{C}$ at the top, while we impose fixed temperature boundary conditions $\hat{\theta}_s = \hat{\theta}_f = 20°\text{C}$ at the bottom. During the simulation, the bottom part of the porous column is held fixed and is subjected to a zero pore pressure boundary condition, whereas no fluid flux is allowed at the top. Within this setup, we conduct a number of numerical experiments by using three different time integration schemes (i.e., monolithic, isothermal split, and asynchronous isothermal split). By spatially discretizing the domain into uniform elements with $h_e = 0.4$ mm, we have: $\Delta t_{\text{up,min}} \approx 0.09$ sec and $\Delta t_{\text{s,min}} \approx 0.02$ sec from Eqs. (3.134)-(3.135). Hence, from Eq. (3.138), we choose $\Delta t = 5$ sec for all three solution schemes, while we set the cycling period as $m = 10$ for the asynchronous

Table 3.1: Material parameters for one-dimensional heat conduction problem.

Parameter	Description [Unit]	Value
ρ_s	Intrinsic solid mass density [kg/m^3]	2700.0
ρ_f	Intrinsic fluid mass density [kg/m^3]	1000.0
K_s	Bulk modulus of solid [Pa]	40.0×10^9
K_f	Bulk modulus of pore fluid [Pa]	2.1×10^9
c_s	Specific heat of solid [J/kg/K]	1.0×10^3
c_f	Specific heat of pore fluid [J/kg/K]	4.2×10^3
κ_s	Thermal conductivity of solid [W/m/K]	4.2
κ_f	Thermal conductivity of pore fluid [W/m/K]	0.6
α_s	Linear thermal expansion coefficient of solid [1/K]	10.0×10^{-6}
A_μ	Viscosity parameter [Pa·s]	1.1×10^{-6}
B_μ	Viscosity parameter [K]	2005.3
$T_{s,\text{ref}}$	Reference solid temperature [K]	293.15
E	Elastic modulus of solid skeleton [Pa]	18.0×10^9
ν	Poisson's ratio of solid skeleton [-]	0.2
k_{mat}	Matrix permeability [m^2]	1.0×10^{-17}
ϕ^f_{ref}	Reference porosity [-]	0.2
$a_{m,\text{ref}}$	Reference specific surface area [1/m]	20.0
h_m	Heat transfer coefficient [W/m^2·K]	4.7

isothermal splitting scheme since $\rho_f c_f \kappa_s / \rho_s c_s \kappa_f = 10.88$.

Fig. 3.6 shows the variations of displacement, pore pressure, solid temperature, and fluid temperature along the height of the column. Here, circular and triangular symbols indicate the results obtained from the monolithic and isothermal splitting solvers, respectively, whereas square symbols denote the simulation results from the asynchronous isothermal split solver. As illustrated in Figs. 3.6(c) and 3.6(d), the solid constituent tends to conduct heat better than the fluid phase, while the fluid heat transfer process is accelerated as time proceeds due to the heat exchange between two constituents. Also, due to the thermal loads, the porous matrix experiences thermal expansion that leads to the build-up of pore pressure which dissipates over time, as shown in Figs. 3.6(a) and 3.6(b). Although the good agreement between the solutions obtained by different time integration schemes confirms the validity of the proposed solution strategy, there exists a noticeable time lagging error for θ_f

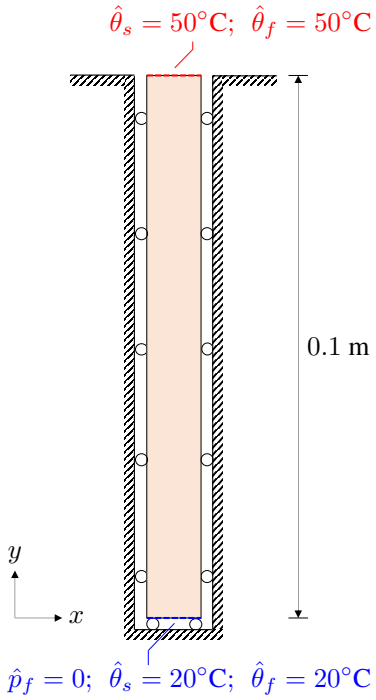

Figure 3.5: Schematic of geometry and boundary conditions for the one-dimensional heat transfer problem.

at $t = 100$ sec [Fig. 3.6(d)]. As illustrated in Fig. 3.7, this time lagging error may lead to inaccurate results at an earlier stage if we use large m even though it becomes marginal as time goes on. However, it should be noted that choosing a cycling period smaller than our suggestion in Eq. (3.137) may either prevent proper utilization of computational efficiency of the asynchronous time integration scheme, or result in spurious oscillations since it may violate the discrete maximum principle (DMP) or monotonicity principle (MP) even if the time step size is greater than max $(\Delta t_{\text{up,min}}, \Delta t_{\text{s,min}})$.

Based on this experimental setup, we further quantitatively analyze the computational efficiency of the asynchronous isothermal splitting scheme. In order to do so, we repeat the same set of numerical experiments with different spatial and temporal discretizations, and record their CPU times. Specifically, by adopting a cycling period of $m = 10$, we investigate the effect of element size h_e by using different meshes with the same $\Delta t = 10$ sec, whereas the effect of time stepping size is examined by conducting the simulations with different Δt while element size is set to be $h_e = 0.04$ mm. Here, the numerical simulations

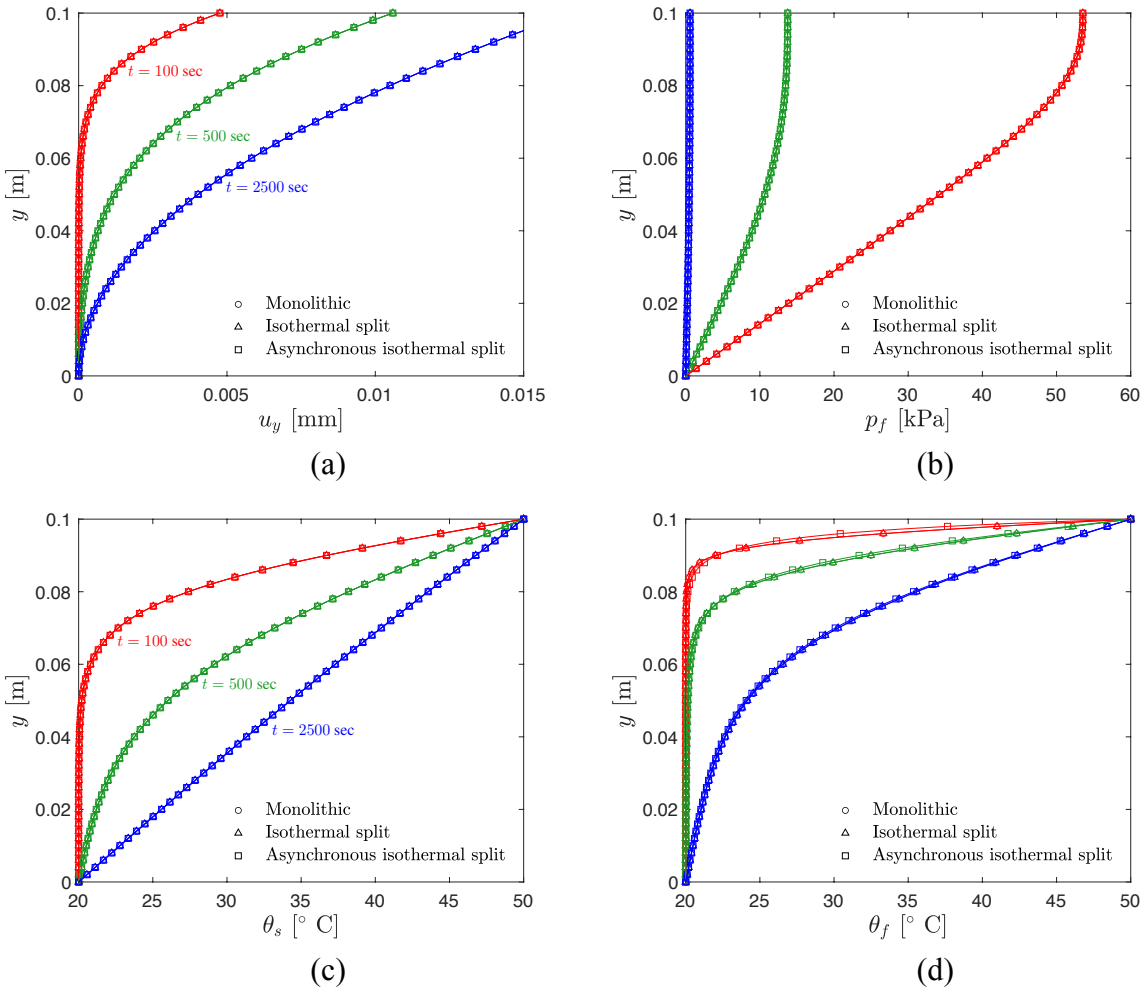

Figure 3.6: Transient responses of porous column. (a) displacement; (b) pore pressure; (c) solid temperature; and (d) fluid temperature.

are conducted on a single core of Intel i9-9880H processor with 16 GB memory at 2667 MHz (DDR4), while we use the same convergence tolerances for all the Newton-Raphson iterations.

Fig. 3.8 illustrates the measured computational costs for the monolithic (circular symbols), isothermal split (triangular symbols), and asynchronous isothermal split (square symbols) solution schemes. As illustrated in Figs. 3.8(a) and 3.8(b), the observed CPU times are inversely proportional to both the element size h_e and the time step size Δt, indicating that both the spatial and temporal refinements increase computational costs. In both two cases, we observe that the monolithic scheme is the most computationally expensive ap-

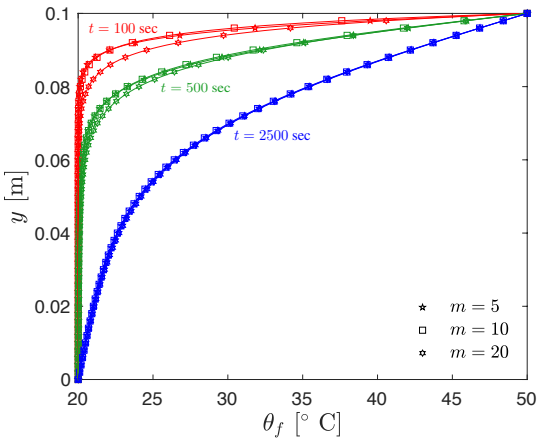

Figure 3.7: Evolution of θ_f obtained from the asynchronous isothermal split solution scheme with different cycling periods.

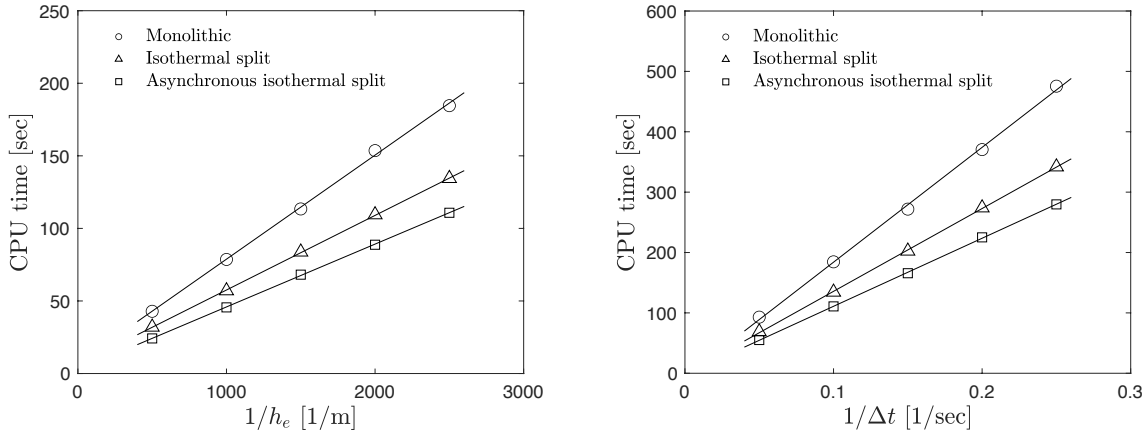

Figure 3.8: Performance comparison between different time integration schemes. (a) CPU time vs. $1/h_e$, and (b) CPU time vs. $1/\Delta t$.

proach, while the isothermal split and asynchronous isothermal split schemes require ~ 72 % and ~ 60 % less CPU times, respectively, compared to the monolithic solver. This time saving can be attributed to the reduced number of calculation afforded by the asynchronous time steps. On the other hand, it can also be related to the larger system of equation and the higher condition number of the tangential matrix of the monolithic solver. The results highlight that our proposed asynchronous isothermal splitting scheme yields similar results compared to the other two approaches, while being computationally more efficient.

3.7.2 Interaction of two mechanically driven cracks

This numerical example investigates the effect of thermally non-equilibrated constituents (i.e., LTNE) on the fracture pattern due to different growth rates of thermal boundary layers compared to the one-temperature model that assumes LTE state. For the case where two constituents are in LTE state, we replace Eqs. (3.30) and (3.33) with Eq. (3.34) by adopting an isothermal splitting scheme with a single time step, while two-temperature approach adopts the proposed asynchronous isothermal operator split.

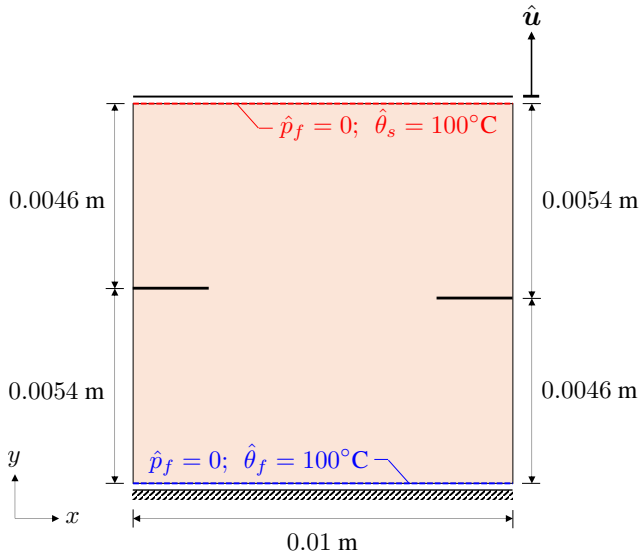

Figure 3.9: Schematic of geometry and boundary conditions for the tension test.

As illustrated in Fig. 3.9, the problem domain is 0.01 m wide and 0.01 m long square plate with two 0.002 m long asymmetric horizontal edge notches, while we choose the material properties similar to a oil-saturated rock which is summarized in Table 3.2. While the initial temperatures are set to be 20°C (i.e., $\theta_{m0} = 20°\text{C}$ for the one-temperature model and $\theta_{s0} = \theta_{f0} = 20°\text{C}$ for the two-temperature model), we impose zero pore pressure and fixed temperature boundary conditions at the top (i.e., $\hat{\theta}_m = 100°\text{C}$ for the one-temperature model and $\hat{\theta}_s = 100°\text{C}$ for the two-temperature model) and the bottom (i.e., $\hat{\theta}_m = 100°\text{C}$ for the one-temperature model and $\hat{\theta}_f = 100°\text{C}$ for the two-temperature model). Within this setup, we conduct numerical experiments, where the crack growth from the pre-existing

Table 3.2: Material parameters for the tension test.

Parameter	Description [Unit]	Value
ρ_s	Intrinsic solid mass density [kg/m^3]	2600.0
ρ_f	Intrinsic fluid mass density [kg/m^3]	880.0
K_s	Bulk modulus of solid [Pa]	38.0×10^9
K_f	Bulk modulus of pore fluid [Pa]	1.3×10^9
c_s	Specific heat of solid [J/kg/K]	1.0×10^3
c_f	Specific heat of pore fluid [J/kg/K]	2.0×10^3
κ_s	Thermal conductivity of solid [W/m/K]	4.2
κ_f	Thermal conductivity of pore fluid [W/m/K]	0.15
α_s	Linear thermal expansion coefficient of solid [1/K]	12.0×10^{-6}
A_μ	Viscosity parameter [Pa·s]	8.6×10^{-6}
B_μ	Viscosity parameter [K]	2475.5
$T_{s,\text{ref}}$	Reference solid temperature [K]	293.15
E	Elastic modulus of solid skeleton [Pa]	18.0×10^9
ν	Poisson's ratio of solid skeleton [-]	0.25
k_{mat}	Matrix permeability [m^2]	2.5×10^{-16}
ϕ^f_{ref}	Reference porosity [-]	0.3
$a_{m,\text{ref}}$	Reference specific surface area [1/m]	20.0
h_m	Heat transfer coefficient [W/m^2·K]	4.7
$\mathcal{G}_{c,\text{ref}}$	Reference critical energy release rate [N/m]	20.0
a_c	Model parameter [-]	1.0
l_c	Regularization length scale parameter [m]	0.45×10^{-4}

notches is mechanically driven, by prescribing vertical displacement at the top at a rate of 0.75×10^{-5} m/s whereas the bottom part is held fixed during the simulation. The problem domain is spatially discretized with a mesh which is refined along the potential crack path with $\min(h_e) = 1.5 \times 10^{-5}$ m, while we use $\max(h_e) = 2.0 \times 10^{-4}$ m near the external boundaries. Hence, we choose $\Delta t = 0.005$ sec $> \max(\Delta t_{\text{up,min}}, \Delta t_{\text{s,min}})$ for both two cases (i.e., LTE and LTNE), while the cycling period for the two-temperature model is set to be $m = 20$ since $\rho_f c_f \kappa_s / \rho_s c_s \kappa_f = 18.95$.

Fig. 3.10 illustrates the crack trajectories at $t = 1.8$ sec for both cases where the constituents are in LTE and LTNE states. As shown in Fig. 3.11(a), two models exhibit a different growth rates of thermal boundary layers, since the two-temperature model is capa-

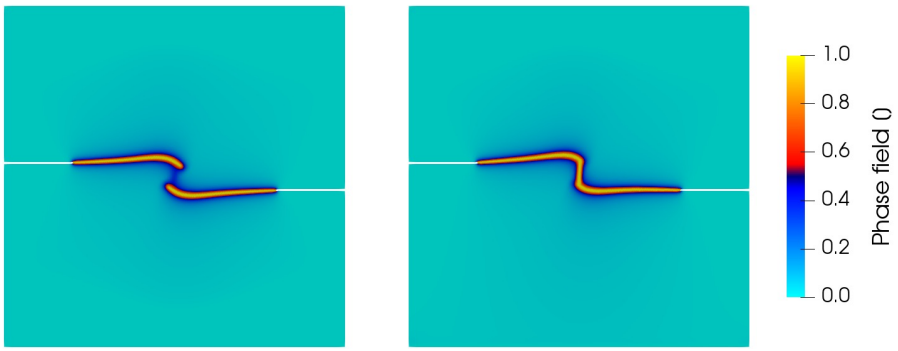

Figure 3.10: Snapshots of the phase fields obtained from the tension tests by using the one-temperature (LTE) and two-temperature (LTNE) models at $t = 1.8$ sec.

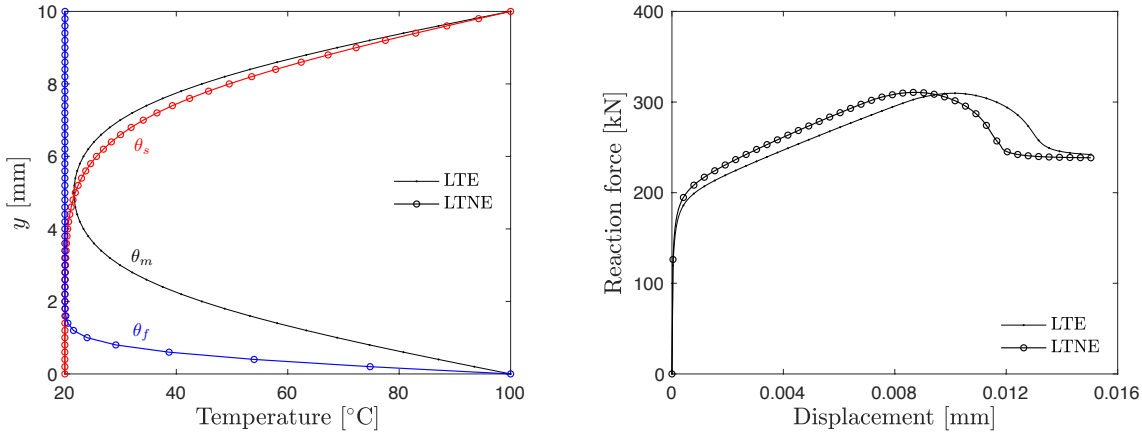

(a) (b)

Figure 3.11: (a) Distribution of the temperatures along the center axis of the specimen at $t = 1.5$ sec, and (b) force-displacement curves from the tension tests.

ble of imposing separate temperature boundary conditions for each constituent. In specific, the limitation of the LTE assumption yields the symmetric thermal boundary layer growth of equilibrated temperature θ_m that leads to symmetric crack growth, while the asymmetric distributions of two temperatures in LTNE state tend to break the symmetry of crack propagation from the notches and eventually coalescence toward each other, resulting in different global responses shown in Fig. 3.11(b). In addition, as illustrated in Fig. 3.12, due to the discrepancy between the peaks shown in Fig. 3.11(b), the LTE model tends to exhibit higher negative pore pressure compared to the LTNE model at $t = 1.8$ sec, even though the LTE assumption may underestimate the temperature-dependent viscosity μ_f.

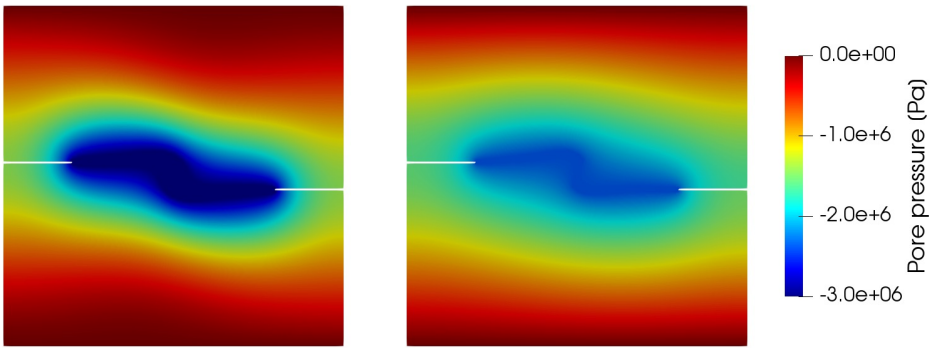

Figure 3.12: Snapshots of the pore pressure fields obtained from the tension tests obtained from the one-temperature (LTE) and two-temperature (LTNE) models at $t = 1.8$ sec.

3.7.3 Interaction of two hydraulically induced cracks

This section simulates the interaction of two hydraulically induced cracks by injecting hot fluid into pre-existing notches. As illustrated in Fig. 3.13(a), the 0.2 m $\times$ 0.1 m sized rectangular domain possesses two 0.02 m long edge notches that are perpendicular to each other with a distance of 0.01 m. The crack growth from the notches is triggered by injecting hot water ($\hat{\theta}_f = 100°$C) with a rate of $A_c\hat{s}$ into a cold water-saturated medium with initial temperatures of $\theta_{s0} = \theta_{f0} = 0°$C. Here, the total area of the pre-existing notches is set to be $A_c = 16$ mm^2 while the applied fluid source varies with time, i.e., $\hat{s} = \hat{s}(t)$, as shown in Fig. 3.13(b). This scenario is designed to capture both the hydraulic fracturing process and the post-cracking behavior of the material. We first apply the fluid source at a constant rate of $\hat{s} = 0.1$ sec^{-1} during the fracturing stage ($t \leq 1$ sec), and then smoothly reduce the injection rate by applying $\hat{s} = 0.05 + 0.025/(t - 0.5)$ sec^{-1} at the injecting stage ($t > 1$ sec). During the simulation, all the external boundaries are held fixed and are subjected to zero pore pressure and zero temperature boundary conditions, i.e., $\hat{p}_f = 0$ and $\hat{\theta}_s = \hat{\theta}_f = 0°$C, while the chosen material parameters are summarized in Table 3.3.

Similar to Section 3.7.2, we compare the one- and two-temperature models within this experimental setup. Since this example relies on a mesh that possesses $\min(h_e) = 0.36$ mm, we choose $\Delta t = 0.01$ sec $> \max(\Delta t_{\text{up,min}}, \Delta t_{\text{s,min}})$ for both two models, i.e., LTE and

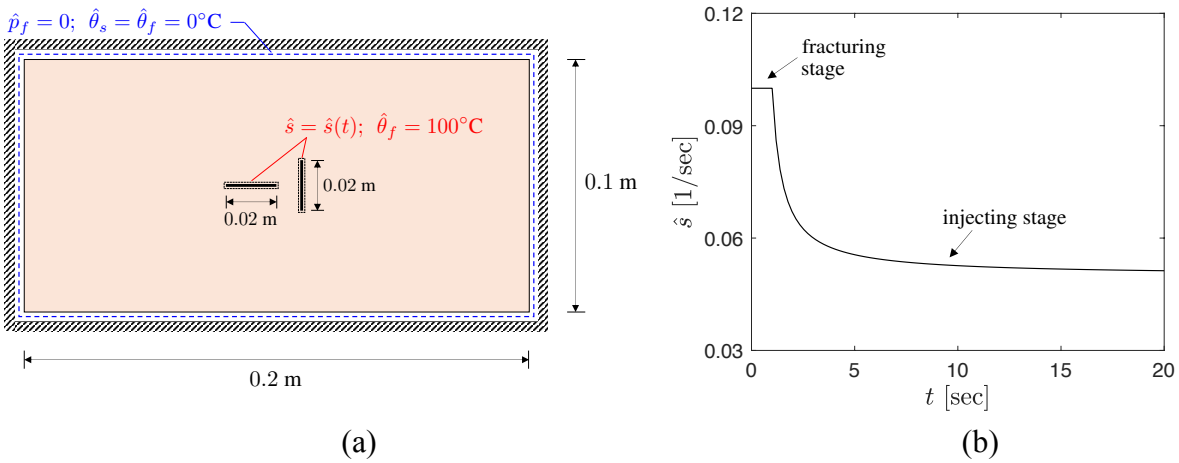

Figure 3.13: (a) Schematic of geometry and boundary conditions for the injection problem, and (b) applied fluid source along the pre-existing cracks.

LTNE, and we set the cycling period $m = 10$ for the two-temperature model as the chosen material parameters yield: $\rho_f c_f \kappa_s / \rho_s c_s \kappa_f = 10.88$.

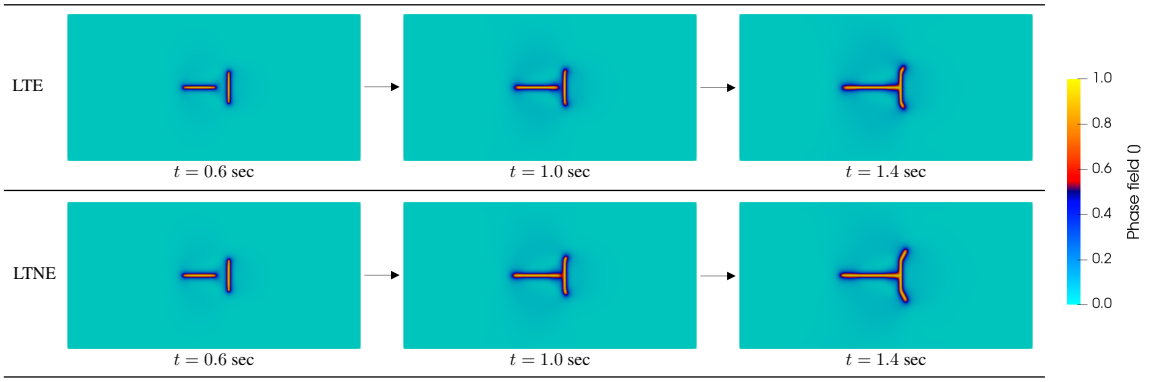

Figure 3.14: Evolution of the phase field due to fluid injection obtained from the one-temperature (LTE) and two-temperature (LTNE) models.

Fig. 3.14 shows the crack patterns at different time steps, obtained from both the LTE and LTNE models, while corresponding pore pressure fields are shown in Fig. 3.15. The crack growth simulated by both the one- and two-temperature models reach their final configurations at $t \approx 1.4$ sec as we reduce the injection rate after $t = 1$ sec. As illustrated in Fig. 3.16, for the case where two constituents are in LTNE state, the boundary layer of the solid temperature grows at a much slower rate compared to the fluid temperature since the heat transfer process is convection-dominant. On the other hand, the LTE model tends to

Table 3.3: Material parameters for the injection problem.

Parameter	Description [Unit]	Value
ρ_s	Intrinsic solid mass density [kg/m^3]	2700.0
ρ_f	Intrinsic fluid mass density [kg/m^3]	1000.0
K_s	Bulk modulus of solid [Pa]	40.0×10^9
K_f	Bulk modulus of pore fluid [Pa]	2.1×10^9
c_s	Specific heat of solid [J/kg/K]	1.0×10^3
c_f	Specific heat of pore fluid [J/kg/K]	4.2×10^3
κ_s	Thermal conductivity of solid [W/m/K]	4.2
κ_f	Thermal conductivity of pore fluid [W/m/K]	0.6
α_s	Linear thermal expansion coefficient of solid [1/K]	10.0×10^{-6}
A_μ	Viscosity parameter [Pa·s]	1.1×10^{-6}
B_μ	Viscosity parameter [K]	2005.3
$T_{s,\text{ref}}$	Reference solid temperature [K]	273.15
E	Elastic modulus of solid skeleton [Pa]	25.0×10^9
ν	Poisson's ratio of solid skeleton [-]	0.3
k_{mat}	Matrix permeability [m^2]	1.25×10^{-16}
ϕ^f_{ref}	Reference porosity [-]	0.2
$a_{m,\text{ref}}$	Reference specific surface area [1/m]	20.0
h_m	Heat transfer coefficient [W/m^2·K]	4.7
$\mathcal{G}_{c,\text{ref}}$	Reference critical energy release rate [N/m]	20.0
a_c	Model parameter [-]	1.0
l_c	Regularization length scale parameter [m]	1.25×10^{-3}

convect heat similar to the LTNE model, while it overestimates the diffusivity due to the difference in the diffusion coefficients, resulting in different patterns of temperature evolution. More importantly, Eq. (3.11) hints that the two-temperature model accumulates the effective strain energy ψ' around the cracks at a higher rate compared to the one-temperature model. The cracks therefore start to propagate at earlier time steps in LTNE state (Fig. 3.14), resulting in a faster rate of pore pressure dissipation (Fig. 3.15).

3.8 Conclusion

In this study, we present a phase field framework that captures the coupled thermo-hydro-mechanical processes of brittle porous media and propose an asynchronous time integrator

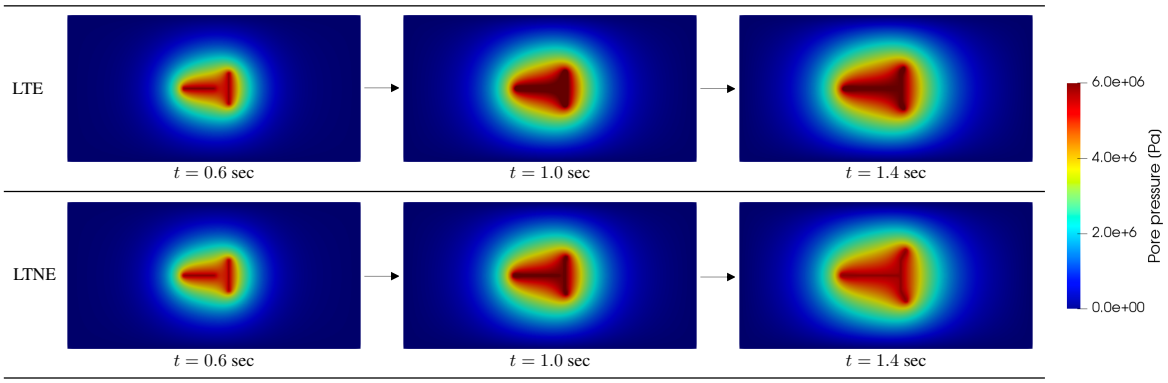

Figure 3.15: Pore pressure evolution due to the field injection obtained from the one-temperature (LTE) and two-temperature (LTNE) models.

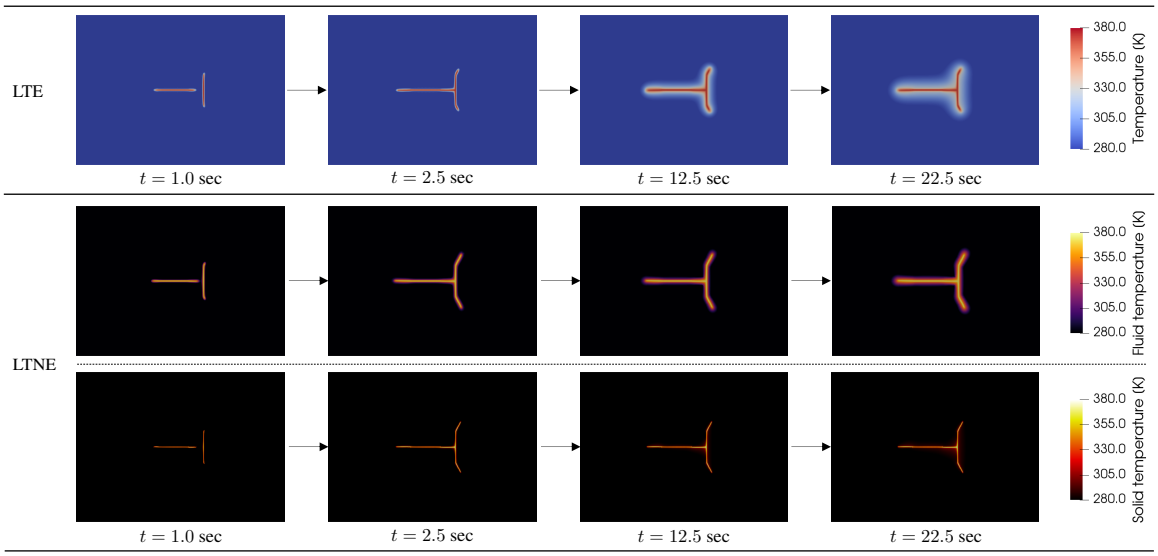

Figure 3.16: Evolution of temperature fields due to the fluid injection obtained from the one-temperature (LTE) and two-temperature (LTNE) models.

to handle the diffusion process that spans different time scales. To the best of the authors' knowledge, this is the first mathematical framework that captures the brittle fracture in multi-phase fluid-infiltrating porous media where the constituents are in a local thermal non-equilibrium state. By introducing a new effective medium theory that independently homogenizes the constituent temperatures, we provide a theoretical basis for distinctive energy balance equations for each deformable constituent, while capturing the heat exchange between the two thermally connected constituents. The two-temperature poromechanics model presented in this work is a generalization of the one-temperature model in the sense

that the results of the classical one-temperature model can be recovered by assuming that all the constituents instantly reach a local thermal equilibrium. By explicitly modeling the heat transfer of the two constituents, we bypass the need to homogenize the intrinsic specific heat capacities and thermal conductivities of each constituent. This treatment simplifies the calibration process, which is by no mean trivial for porous media where the motions of the fluid and solid constituents do not coincide and the conductivity of the effective medium are not necessarily isotropic. In addition, we propose a new time integration scheme that updates the field variables in an asynchronous manner, for which we also suggest an estimated optimal time step size and cycling period by adopting the discrete maximum and monotonicity principles. The asynchronous time integrator greatly reduces the computational cost, while being capable of reproducing physically consistent results with the synchronous counterpart.

Note that a more precise and accuracy calculation of heat transfer will have a even more profound effect on poromechanics problems with phase transitions of either/both the solid and fluid constituents, such as the freeze-thaw action, crystallization induced damage and injection of supercritical CO_2. The proposed work may lay the groundwork for a more precise predictions for those important problems without the necessity of additional calibrations of the thermal diffusivity of the effective medium. Another important future work of this study is to simulate three dimensional cases. A major challenge for 3D simulations of the phase field fracture in the non-equilibrium porous media is the computational effort. Accurately representing the crack growth via phase field will require a sufficiently high mesh resolution and small time step, which can be computationally demanding. At this point we are considering a more efficient parallelism that involves GPGPU as well as adaptive finite element that involves proper way to project the driving force. Works in these areas are currently in progress.

This page intentionally left blank.

Chapter 4: An immersed phase field fracture model for microporomechanics with coupled Darcy–Stokes flow

This chapter is published as: H.S. Suh, W.C. Sun, An immersed phase field fracture model for microporomechanics with Darcy–Stokes flow, Physics of Fluids, Volume 33, 2021, doi.org/10.1063/5.0035602.

4.1 Introduction

Geomaterials such as carbonate rocks, sandstone or limestone often contain geometrical features such as cracks, joints, vugs or cavities. When the defects are partially or fully saturated with pore fluid, the geometry of the features may affect effective stiffness, permeability, water retention characteristics and drained or undrained shear strength of the material [140, 244–246, 283–285]. Furthermore, brittle fracture in materials that possess geometrical features may lead to pore fluid in cavities migrate into the flow channels and cause flow conduits that lead to often undesirable outcomes. Modeling geometrical features in porous media are thus highly important and at the same time challenging subject for the hydromechanically coupled analysis in geomechanics problems like hydrocarbon resources recovery or development of enhanced geothermal energy reservoirs [286–292].

One possible modeling choice is to consider a fictitious effective medium at a scale where representative elementary volume exists. In this case, the geometrical features of the material are not explicitly modeled but the influences of the these geometrical fea-

tures are incorporated in the constitutive relations by treating defects as a different pore system that interacts with the matrix pores [293–296]. The upshot of the multi-porosity and multi-permeability models is mainly the simple numerical treatment since there is no need for complex meshing techniques or embedded strong discontinuities, and the computational efficiency compared to pore-scale models that require extremely large domain in order to reproduce hydromechanical behavior at large scales [103, 297–302]. However, the drawback of this approach is that the homogenized effective medium may not sufficiently represent the microstructural details. This makes the identification of material parameters more complicated since the effective permeability of multiple interacting systems are not isotropic and the constitutive law for the fluid mass exchanges inherently depends on the microstructure.

Another common alternative to model the interaction between the cavities and the crack growth is to conduct simulations via a fracture network model [303–306]. However, the obvious drawback is that the fracture in those models must either be straight line (in the two-dimensional case) or a plane (in the three-dimensional case) and hence the geometrical effect on the porous media can not be captured precisely.

In this research, we introduce a phase field framework that allows us to enable a unified treatment to simulate the evolving geometry of cracks and the cavities. By introducing the phase field as an unified representation of the void space that is not suitable to be treated as as an effective medium, we introduce a framework that enables us to analyze how crack propagation in vuggy porous media may affect the flow mechanism differently than the porous media with pores well distributed in the host matrix. Our result indicates that interaction between the propagating cracks of the cavities is important for capturing the hydromechanical responses of the porous media and that existing effective medium approach which characterizes the pore space with a single hydraulic model such as cubic law and Kozeny-Carmen model may not be sufficient to capture the cavity-crack-host-matrix interactions.

4.2 The model problem

We consider a fully saturated Biot-Stokes system (Fig. 4.1) that consists of two regions (intact porous matrix $\mathcal{B}_D$, and cracks or cavities $\mathcal{B}_S$) separated by the sharp interface Γ^*, where we assume that the solid phase in $\mathcal{B}_D$ forms a deformable porous matrix while solid particles in $\mathcal{B}_S$ are in suspension. In this case, both the solid and fluid phases coexist in both regions. By considering our material of interest as a multi-phase continuum, we utilize the effective stress principle for the intact porous matrix where the fluid flow is modeled with the Darcy's law, while the motion of solid-fluid mixture is modeled by the Stokes equation [307]. Two distinct regions are then coupled by properly imposing three transmissibility conditions at the interface. The model problem with the sharp interface will be later on extended into a diffuse Biot-Stokes model by introducing the phase field in Section 4.3.

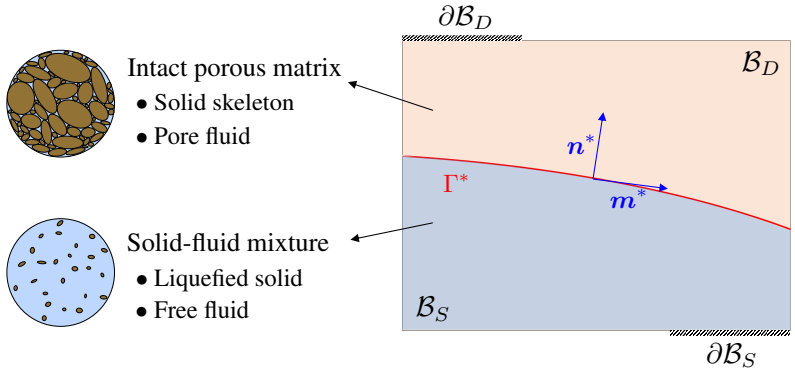

Figure 4.1: Schematic representation of Biot-Stokes system that possesses sharp interface Γ^*.

4.2.1 Continuum representation

Although Biot-Stokes system only contains two immiscible solid and fluid phases, for mathematical convenience, we idealize the material of interest as a three-phase continuum where each constituent [i.e., solid (s), pore fluid (f_D), and free fluid (f_S)] occupies a fraction of volume at the same material point. By letting $dV = dV_s + dV_f$ denote the representative

elementary volume of the material, we define the volume fractions for the constituents as,

$$\phi^{\alpha} := \frac{dV_{\alpha}}{dV} \;\; ; \;\; \alpha = \{s, f\}\,, \tag{4.1}$$

where the index s refer to the solid phase and f indicates the fluid phase. Since the sharp interface separates our system of interest into two regions, the volume fraction of the pore and free fluids can be expressed as:

$$\phi^{f} = \underbrace{(1 - H_{\Gamma^*})\frac{dV_{f_D}}{dV}}_{:=\phi^{f_D}} + \underbrace{H_{\Gamma^*}\frac{dV_{f_S}}{dV}}_{:=\phi^{f_S}}, \tag{4.2}$$

where H_{Γ^*} is the Heaviside function that satisfies,

$$H_{\Gamma^*} = \begin{cases} 0 & \text{in } \mathcal{B}_D, \\ 1 & \text{in } \mathcal{B}_S. \end{cases} \tag{4.3}$$

In addition, by letting ρ_s and ρ_f denote the intrinsic mass densities of solid and fluid, respectively, the partial mass densities for each constituent (ρ^{α}, where $\alpha = s, f_D, f_S$) are given by,

$$\rho^{s} := \phi^{s}\rho_s \;\; ; \;\; \rho^{f_D} := \phi^{f_D}\rho_f \;\; ; \;\; \rho^{f_S} := \phi^{f_S}\rho_f \;\; ; \;\; \rho := \rho^{s} + \rho^{f_D} + \rho^{f_S}, \tag{4.4}$$

where ρ is the mass density of the entire system. In this study, we assume that both the solid and fluid phases are incompressible, so that intrinsic mass densities ρ_s and ρ_f are considered as constants.

4.2.2 Governing equations

This section briefly reviews the balance principles, constitutive laws in the bulk volume of a porous medium, the region where solid-fluid mixture flows freely, and the sharp interface between two regions.

Conservation laws for an intact porous matrix

For the region where the solid forms an intact porous matrix, we adopt the effective stress principle [211, 308] so that the external loading imposed on the matrix is assumed to be carried by both the solid skeleton and the pore fluid. In this case, the region $\mathcal{B}_D$ is governed by the following system of equations [230, 231, 309]:

$$\nabla\cdot(\boldsymbol{\sigma}' - Bp_{f_D}\boldsymbol{I}) + \rho\boldsymbol{g} = \boldsymbol{0} \text{ in } \mathcal{B}_D, \tag{4.5}$$

$$\frac{1}{M}\dot{p}_{f_D} + \nabla\cdot\boldsymbol{v}_s + \nabla\cdot\boldsymbol{w}_{f_D} = 0 \text{ in } \mathcal{B}_D, \tag{4.6}$$

where $\boldsymbol{\sigma}'$ is the effective stress, $B = 1 - K/K_s$ is the Biot's coefficient, M is the Biot's modulus, p_{f_D} is the pore pressure, $\boldsymbol{g}$ is the gravitational acceleration, $\boldsymbol{v}_\alpha$ is the intrinsic velocity of constituent α, and $\boldsymbol{w}_{f_D} = \phi^{f_D}(\boldsymbol{v}_{f_D} - \boldsymbol{v}_s)$ is the Eulerian relative flow vector of the pore fluid (i.e., Darcy's velocity). Here, we assume that $B \approx 1$ and $1/M \approx 0$ to simplify the formulation. Note that the Biot's coefficient of many sandstone and shale specimens are often less than one, whereas it is more reasonable to assume Biot's coefficient equal to 1 for granite (e.g.. Westerly granite) [177, 216, 310]. In either cases, the damage of the solid skeleton may reduce the elastic bulk modulus of the solid skeleton. Therefore both the Biot's coefficient and modulus may evolve according to the solid deformation. This nonlinear effect is not considered in this study but will be considered in the future. We also assume that the behavior of intact matrix in $\mathcal{B}_D$ is linear and isotropic elastic and hence only two independent elastic modulii are needed to capture the elastic response. The constitutive relation for the solid skeleton can therefore be written as follows:

$$\boldsymbol{\sigma}'_0 = \lambda\,\mathrm{tr}\,(\boldsymbol{\varepsilon})\boldsymbol{I} + 2\mu\boldsymbol{\varepsilon} \text{ in } \mathcal{B}_D, \tag{4.7}$$

where $\boldsymbol{\sigma}'_0$ indicates the effective stress of the undamaged matrix. The actual and undamaged effective stress are related by a degradation function, which will later be discussed in

Section 4.3.2. Furthermore, $\boldsymbol{\varepsilon} = (\nabla \boldsymbol{u}_s + \nabla \boldsymbol{u}_s^{\mathrm{T}})/2$ is the infinitesimal solid strain tensor that depends on the solid displacement $\boldsymbol{u}_s$, and parameters λ and μ are the Lamé constants. For the constitutive equation that describes laminar pore fluid flow in $\mathcal{B}_D$, we use the generalized Darcy's law that linearly relates the relative velocity $\boldsymbol{w}_{f_D}$ and pore pressure gradient ∇p_{f_D}, i.e.,

$$\boldsymbol{w}_{f_D} = -\frac{k}{\mu_f}(\nabla p_{f_D} - \rho_f \boldsymbol{g}) \text{ in } \mathcal{B}_D, \tag{4.8}$$

where μ_f is the dynamic viscosity of the pure fluid phase, and k is the effective permeability of the porous matrix. Additionally, in order to incorporate the effect of deformation of the matrix on the porous medium flow [311, 312], this study adopts the Kozeny-Carman equation to empirically capture the porosity-permeability relation [140, 313, 314]. Note that the Kozeny-Carmen equation is often considered a rough approximation of the porosity-permeability relation. A more precise predictions of permeability may requires new geometrical attributes such as tortuosity [243, 244], formation factor [246, 315], and percolation threshold [316]. This extension is out of the scope of this study but will be considered in future work.

Recall Section 4.2.1 that $\phi^s + \phi^{f_D} = 1$ in $\mathcal{B}_D$. Then, by letting $\phi := \phi^{f_D}$ the porosity of the matrix, the Kozeny-Carman equation reads,

$$k = k_0 \left[\frac{(1-\phi_0)^2}{\phi_0^3}\right] \left[\frac{\phi^3}{(1-\phi)^2}\right] \text{ in } \mathcal{B}_D, \tag{4.9}$$

where k_0 and ϕ_0 denote the reference permeability and porosity, respectively.

Conservation laws for solid-fluid mixture

This study attempts to model suspension flow in $\mathcal{B}_S$, where mass and linear momentum balances for both solid and fluid phases should be satisfied. We therefore write the governing

balance equations for $\mathcal{B}_S$ as,

$$\nabla\cdot\boldsymbol{\sigma}^{f_S}+\rho^{f_S}\boldsymbol{g}=\mathbf{0}\ \text{ in }\mathcal{B}_S, \tag{4.10}$$

$$\nabla\cdot\boldsymbol{\sigma}^{s}+\rho^{s}\boldsymbol{g}=\mathbf{0}\ \text{ in }\mathcal{B}_S, \tag{4.11}$$

$$\nabla\cdot\boldsymbol{v}_s+\nabla\cdot\boldsymbol{w}_{f_S}=0\ \text{ in }\mathcal{B}_S, \tag{4.12}$$

where $\boldsymbol{\sigma}^{\alpha}$ is the Cauchy stress tensor of α constituent, and the relative flow vector of the free fluid can be defined as $\boldsymbol{w}_{f_S}=\phi^{f_S}(\boldsymbol{v}_{f_S}-\boldsymbol{v}_s)$. By assuming that the free fluid resides in $\mathcal{B}_S$ with low Reynolds number (i.e., $Re\ll 1$), we adopt a simplified version of the Navier-Stokes model, i.e., the Stokes equation. The Stokes model for the steady-state motion of an incompressible fluid yields the following relationship for the free fluid stress tensor $\boldsymbol{\sigma}^{f_S}$ as,

$$\boldsymbol{\sigma}^{f_S}=-p_{f_S}\boldsymbol{I}+\mu_{\text{eff}}(\nabla\,\boldsymbol{v}_{f_S}+\nabla\,\boldsymbol{v}_{f_S}^{\mathrm{T}})\ \text{ in }\mathcal{B}_S, \tag{4.13}$$

where p_{f_S} is the free fluid pressure and μ_{eff} is the effective viscosity of the solid-fluid mixture [317, 318], i.e.,

$$\mu_{\text{eff}}=\mu_f\exp\left(\frac{2.5c}{1-c/c_{\text{max}}}\right)\ \text{ in }\mathcal{B}_S, \tag{4.14}$$

where $c:=1-\phi^{f_S}$ indicates the solid particle concentration, and c_{max} denotes its upper bound. Again, notice that we introduce only one solid constituent for the entire system since it is convenient for us to later on impose interface conditions and further adopt the phase field fracture model that simulates evolving interface. This approach may not be suitable for modeling complete suspension flow where $\boldsymbol{v}_s=\boldsymbol{v}_{f_S}$. However, we assume that solid particles in $\mathcal{B}_S$ follows the same constitutive relations as the free fluid in order to replicate the suspension flow as close as possible, i.e.,

$$\boldsymbol{\sigma}^{s}=-p_{f_S}\boldsymbol{I}+\mu_{\text{eff}}(\nabla\,\boldsymbol{v}_{s}+\nabla\,\boldsymbol{v}_{s}^{\mathrm{T}})\ \text{ in }\mathcal{B}_S. \tag{4.15}$$

Conservation laws for the sharp interface between intact matrix and solid-fluid mixture

In order to properly model the interaction between the porous matrix ($\mathcal{B}_D$) and the vugs or cavities ($\mathcal{B}_S$), complete mass conservation and force equilibrium for the entire system should be satisfied. Since we have two different constituents for the same type of fluid (f_D and f_S) while considering only one solid constituent (s), coupling two subsystems thus requires the enforcement of fluid transmissibility conditions at the sharp interface Γ^* that models the coupled Stokes-Darcy flow [319–323].

The first interface condition is the fluid continuity that ensures the mass conservation. Since we assume that the fluid phase is incompressible, the interfacial fluid fuxes for each subsystem ($\mathcal{M}^*_{f_D}$ and $\mathcal{M}^*_{f_S}$) can be expressed as follows:

$$\mathcal{M}^*_{f_D} = \int_{\Gamma^*} \underbrace{\boldsymbol{w}_{f_D} \cdot \boldsymbol{n}^*_D}_{:=m^*_{f_D}} \, d\Gamma \;\; ; \;\; \mathcal{M}^*_{f_S} = \int_{\Gamma^*} \underbrace{\boldsymbol{w}_{f_S} \cdot \boldsymbol{n}^*_S}_{:=m^*_{f_S}} \, d\Gamma, \tag{4.16}$$

where $\boldsymbol{n}^*_D$ and $\boldsymbol{n}^*_S$ denote the outward-oriented normal vectors from $\mathcal{B}_D$ and $\mathcal{B}_S$, respectively. From Eq. (4.16), mass continuity ($\mathcal{M}^*_{f_D} + \mathcal{M}^*_{f_S} = m^*_{f_D} + m^*_{f_S} = 0$) yields the following transmissibility condition:

$$\boldsymbol{w}_{f_D} \cdot \boldsymbol{n}^*_D + \boldsymbol{w}_{f_S} \cdot \boldsymbol{n}^*_S = (\boldsymbol{w}_{f_S} - \boldsymbol{w}_{f_D}) \cdot \boldsymbol{n}^* = 0 \;\text{ on } \Gamma^*, \tag{4.17}$$

where we take $\boldsymbol{n}^* = \boldsymbol{n}^*_S = -\boldsymbol{n}^*_D$ for notational convenience (Fig. 4.1). Here, Eq. (4.16) implies that the normal component of the fluid velocities ($\boldsymbol{w}_{f_S}$ and $\boldsymbol{w}_{f_D}$) should be identical in order to guarantee that the exchange of fluid mass between $\mathcal{B}_S$ and $\mathcal{B}_D$ is conservative.

The second condition is the force equilibrium at the interface Γ^*. From each subsystem,

total forces acting on the interface ($\boldsymbol{\mathcal{F}}^*_{f_D}$ and $\boldsymbol{\mathcal{F}}_{f_S}$) may be written as,

$$\boldsymbol{\mathcal{F}}^*_{f_D} = \int_{\Gamma^*} \underbrace{p_{f_D}\boldsymbol{n}^*}_{:=\boldsymbol{t}^*_{f_D}} \, d\Gamma \;\; ; \;\; \boldsymbol{\mathcal{F}}^*_{f_S} = \int_{\Gamma^*} \underbrace{\boldsymbol{\sigma}^{f_S}\cdot\boldsymbol{n}^*}_{:=\boldsymbol{t}^*_{f_S}} \, d\Gamma, \tag{4.18}$$

where $\boldsymbol{t}^*_{f_D}$ and $\boldsymbol{t}^*_{f_S}$ indicate the tractions at the interface. The force equilibrium requires $\boldsymbol{\mathcal{F}}^*_{f_D} + \boldsymbol{\mathcal{F}}^*_{f_S} = \boldsymbol{t}^*_{f_D} + \boldsymbol{t}^*_{f_S} = \boldsymbol{0}$, implying that the normal and shear components should be balanced at the same time. By decomposing the traction vectors as,

$$\boldsymbol{t}^*_i = (\boldsymbol{t}^*_i \cdot \boldsymbol{n}^*)\boldsymbol{n}^* + \sum_{j=1}^{2} (\boldsymbol{t}^*_i \cdot \boldsymbol{m}^*_j)\boldsymbol{m}^*_j \;\; ; \;\; i = \{f_D, f_S\}\,, \tag{4.19}$$

where $\boldsymbol{m}^*_1$ and $\boldsymbol{m}^*_2$ are the interfacial tangent vectors, we get two more transmissibility conditions that describe normal and shear force equilibrium, respectively:

$$\boldsymbol{t}^*_{f_S}\cdot\boldsymbol{n}^* + p_{f_D} = 0 \;\text{ on } \Gamma^*, \tag{4.20}$$

$$\boldsymbol{t}^*_{f_S}\cdot\boldsymbol{m}^*_j + \mu_f \frac{\alpha_{SD}}{\sqrt{k}}(\boldsymbol{w}_{f_S} - \boldsymbol{w}_{f_D})\cdot\boldsymbol{m}^*_j = 0 \;\text{ on } \Gamma^*. \tag{4.21}$$

Eq. (4.21) is the Beavers-Joseph-Saffman condition [320, 324–326]. This idealized condition relates the slip velocity and the shear stress through the dimensionless slippage coefficient α_{SD}, which depends on the microstructural attributes of the interfaces, such as surface roughness, irregular patterns, as well as the flow velocity [324, 327, 328]. The validity and limitations of the Beavers-Joseph-Saffman condition are documented in a number of literature such as Auriault [329], Mikelic and Jäger [330], and Monchiet, Ly, and Grande [331] and will not repeated here. Possible extensions of the interface conditions to turbulent and multiphase flows are an active research area that is clearly out of the scope of this study but will be considered in the future.

4.3 The phase field Biot-Stokes model with evolving fractures

This section introduces the mathematical model that uses smooth implicit function, i.e., the phase field, to approximate evolving sharp interfaces due to damage. We first review the general procedure that employs an implicit function to approximate sharp interfaces (Section 4.3.1) shown in Fig. 4.2. Since the phase field is a smooth representation of the Heaviside function, we derive the corresponding mathematical model that approximates interfacial transmissibility conditions suitable for the diffuse representation of the interface. To capture crack growth according to the Griffith's theory, we adopt the classical variational fracture model to allow crack growth represented by the evolution of the phase field defined over the spatial domain (Section 4.3.2). These techniques are then applied into the derivation shown in Section 4.3.3 in which a mathematical model to capture the hydromechanical coupling of pore fluid flows in both the host matrix and evolving interfaces in brittle porous media. The resultant model does not require locally defined enrichment function or remeshing and can be implemented in a standard finite element or finite element/volume solver.

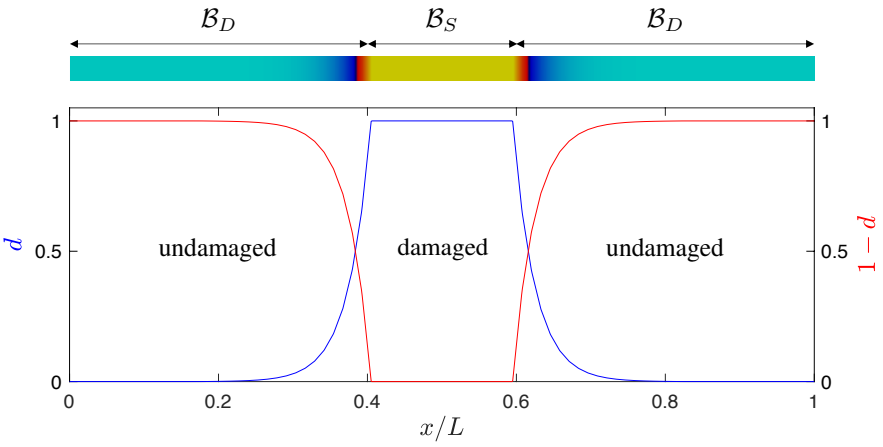

Figure 4.2: Diffuse representation of the interface where exemplary 1D domain consists of $\mathcal{B}_S$ in $x/L \in [0.4, 0.6]$ sandwiched between undamaged porous matrix $\mathcal{B}_D$.

4.3.1 Diffuse interface approximation

This study employs a diffuse approximation for the sharp interface Γ^* by introducing a phase field variable $d \in [0, 1]$ which varies smoothly from 0 in $\mathcal{B}_D$ to 1 in $\mathcal{B}_S$. Specifically, we approximate the interfacial area A_{Γ^*} as $A_{\Gamma^*_d}$, which can be expressed in terms of volume integration of surface density functional $\Gamma^*_d(d, \nabla d)$ over $\mathcal{B} = \overline{\mathcal{B}_D \cup \mathcal{B}_S}$ [76, 77, 132, 210]:

$$A_{\Gamma^*} \approx A_{\Gamma^*_d} = \int_{\mathcal{B}} \Gamma^*_d(d, \nabla d)\, dV. \tag{4.22}$$

Here, the size of diffusive zone [i.e., transition zone where $d \in (0, 1)$] is controlled by the regularization length scale parameter l^* such that $A_{\Gamma^*_d}$ Γ-converge to A_{Γ^*} [203], i.e.,

$$A_{\Gamma^*} = \lim_{l^* \to 0} A_{\Gamma^*_d}. \tag{4.23}$$

Based on this approach, phase field d and its gradient ∇d can be regarded as smooth approximations of the Heaviside function H_{Γ^*} and the Dirac delta function δ_{Γ^*}, respectively [292, 332]. Therefore, the volume integrals of an arbitrary function $\tilde{G}$ over $\mathcal{B}_D$ and $\mathcal{B}_S$ can respectively be approximated as,

$$\int_{\mathcal{B}_D} \tilde{G}\, dV = \int_{\mathcal{B}} \tilde{G}(1 - H_{\Gamma^*})\, dV = \lim_{l^* \to 0} \int_{\mathcal{B}} \tilde{G}(1 - d)\, dV \approx \int_{\mathcal{B}} \tilde{G}(1 - d)\, dV, \tag{4.24}$$

$$\int_{\mathcal{B}_S} \tilde{G}\, dV = \int_{\mathcal{B}} \tilde{G} H_{\Gamma^*}\, dV = \lim_{l^* \to 0} \int_{\mathcal{B}} \tilde{G} d\, dV \approx \int_{\mathcal{B}} \tilde{G} d\, dV. \tag{4.25}$$

Similarly, the surface integral of the function $\tilde{G}$ along the sharp interface Γ^* can be approximated as,

$$\int_{\Gamma^*} \tilde{G}\, d\Gamma = \int_{\Gamma^*} \tilde{G} \delta_{\Gamma^*}\, dV = \lim_{l^* \to 0} \int_{\mathcal{B}} \tilde{G} \| \nabla d \|\, dV \approx \int_{\mathcal{B}} \tilde{G} \| \nabla d \|\, dV, \tag{4.26}$$

and we also approximate the normal vector $\boldsymbol{n}^*$ as,

$$\boldsymbol{n}^* \approx -\frac{\nabla d}{\| \nabla d\|}. \tag{4.27}$$

4.3.2 Crack growth approximated by evolving phase field

For completeness, this section reviews the phase field model for brittle fracture. We consider the following surface density functional, which is widely used in modeling brittle or quasi-brittle fracture [75–77, 90, 210] that possesses quadratic local dissipation function:

$$\Gamma_d^*(d, \nabla d) = \frac{d^2}{2l^*} + \frac{l^*}{2}(\nabla d \cdot \nabla d). \tag{4.28}$$

At this point, we highlight that the evolution of the phase field (i.e., propagation of cavities or cracks) is a mechanical process driven by the effective stress $\boldsymbol{\sigma}'$. In other words, we assume that the solid skeleton is completely damaged in the liquefied zone $\mathcal{B}_S$, whereas in $\mathcal{B}_D$, the solid skeleton remains undamaged. We thus omit the terms that are unrelated to the deformation and fracture in this section. Having critical energy $\mathcal{G}_c$ that is required to create new free surfaces, potential energy density ψ reads,

$$\psi = \underbrace{g(d)\psi_e^+(\boldsymbol{\varepsilon}) + \psi_e^-(\boldsymbol{\varepsilon})}_{\psi_{\text{bulk}}(\boldsymbol{\varepsilon},d)} + \mathcal{G}_c\Gamma_d^*(d, \nabla d), \tag{4.29}$$

where $\psi_{\text{bulk}}(\boldsymbol{\varepsilon}, d)$ is the degrading elastic bulk energy and $g(d) = (1-d)^2$ is the degradation function that induces energy dissipation. Following Amor, Marigo, and Maurini [130], we adopt additive decomposition scheme that splits the elastic energy ψ_e into compressive (ψ_e^-), and tensile and deviatoric (ψ_e^+) modes, where we only degrade ψ_e^+ in order to avoid crack propagation under compression [143, 170, 333], i.e.,

$$\psi_e^+ = \frac{1}{2}K \left\langle \boldsymbol{\varepsilon}^{\text{vol}} \right\rangle_+^2 + \mu(\boldsymbol{\varepsilon}^{\text{dev}} : \boldsymbol{\varepsilon}^{\text{dev}}), \tag{4.30}$$

$$\psi_e^- = \frac{1}{2} K \left\langle \boldsymbol{\varepsilon}^{\text{vol}} \right\rangle_-^2 , \tag{4.31}$$

where $K = \lambda + 2\mu/3$ is the bulk modulus of the porous matrix, and $\langle \bullet \rangle_\pm = (\bullet \pm | \bullet |)/2$ is the Macaulay bracket operator. In this case, the effective stress tensor $\boldsymbol{\sigma}'$ can also be decomposed as follows:

$$\boldsymbol{\sigma}' = g(d)\boldsymbol{\sigma}_0'^+ + \boldsymbol{\sigma}_0'^- , \tag{4.32}$$

where $\boldsymbol{\sigma}_0'^\pm = \partial \psi_e^\pm / \partial \boldsymbol{\varepsilon}$ is the fictitious undamaged effective stress, in which we previously assumed $\boldsymbol{\sigma}_0'$ to be linear elastic [Eq. (4.7)].

Based on the fundamental lemma of calculus of variations, the damage evolution equation can be obtained by seeking the stationary point where the functional derivative of Eq. (4.29) with respect to d vanishes, i.e.,

$$\frac{\partial \psi}{\partial d} - \nabla \cdot \frac{\partial \psi}{\partial \nabla d} = 0, \tag{4.33}$$

where:

$$\frac{\partial \psi}{\partial d} = g'(d)\psi_e^+ + \frac{\mathcal{G}_c}{l^*} d \ ; \ \nabla \cdot \frac{\partial \psi}{\partial \nabla d} = \mathcal{G}_c l^* \nabla^2 d. \tag{4.34}$$

Here, the superposed prime denotes derivative with respect to d and $\nabla^2(\bullet) = \nabla \cdot \nabla (\bullet)$ is the Laplacian operator. Furthermore, by following the treatment used in Miehe, Hofacker, and Welschinger [76], we introduce a history function $\mathcal{H}$ which is the pseudo-temporal maximum of the positive energy density (ψ_e^+) in order to ensure crack irreversibility constraint:

$$\mathcal{H} = \max_{\tau \in [0,t]} \psi_e^+ . \tag{4.35}$$

By replacing ψ_e^+ in Eq. (4.34) with $\mathcal{H}$, Eq. (4.33) finally yields the following phase field equation that governs the evolution of the interface:

$$g'(d)\mathcal{H} + \frac{\mathcal{G}_c}{l^*}(d - l^{*2}\nabla^2 d) = 0 \ \text{ in } \mathcal{B}. \tag{4.36}$$

Note that we can obtain the diffuse representation of the interface by solving Eq. (4.36), as shown in Fig. 4.2.

In this study, we leverage the phase field not only as an indicator function for the location of cracks but also for other defects such as cavities or geometrically complicated voids that does not fit for computational homogenization. This approach may efficiently couple the Stokes flow inside the vugs ($\mathcal{B}_S$) that interact with pore fluid in the intact porous matrix ($\mathcal{B}_D$) while both regions are evolving due to the crack growth. A major advantage of this work is that free flow inside the fracture is explicitly replicated and hence there is no need to introduce permeability enhancement models (e.g., cubic law) [334–336]. This explicit treatment enables the simulations to remain physical even in the situations (e.g., high Reynolds number, rough surface, aperture variation) where the validity of the cubic law is questioned [88, 138, 140, 163, 242, 291, 334, 337].

Verification and experimental validation of the phase field fracture model for brittle solid has been well documented in the literature. For brevity, similar studies are not provided in this paper. Interested readers may refer to, for instance, such as Nguyen et al. [338] and Pham, Ravi-Chandar, and Landis [339].

4.3.3 Variational formulation of the phase field Biot-Stokes model

We present a immersed phase field Biot-Stokes model designed to simulate the coupled hydro-mechanical behaviors of flow of vuggy porous media with evolving fractures in the brittle regime. This section omits the gravitational effects for brevity (i.e., $\boldsymbol{g} = \boldsymbol{0}$).

The model problem with the sharp interface (Section 4.2) in which the system possesses two distinct boundaries $\partial\mathcal{B}_D$ and $\partial\mathcal{B}_S$ that can both be decomposed into Dirichlet ($\partial\mathcal{B}^u_D$, $\partial\mathcal{B}^p_D$, $\partial\mathcal{B}^w_S$ and $\partial\mathcal{B}^p_S$) and Neumann ($\partial\mathcal{B}^t_D$, $\partial\mathcal{B}^q_D$, $\partial\mathcal{B}^t_S$ and $\partial\mathcal{B}^q_S$) boundaries satisfying,

$$\partial\mathcal{B}_D = \overline{\partial\mathcal{B}^u_D \cup \partial\mathcal{B}^t_D} = \overline{\partial\mathcal{B}^p_D \cup \partial\mathcal{B}^q_D} \;\; ; \;\; \emptyset = \partial\mathcal{B}^u_D \cap \partial\mathcal{B}^t_D = \partial\mathcal{B}^p_D \cap \partial\mathcal{B}^q_D, \tag{4.37}$$

$$\partial\mathcal{B}_S = \overline{\partial\mathcal{B}^w_S \cup \partial\mathcal{B}^t_S} = \overline{\partial\mathcal{B}^p_S \cup \partial\mathcal{B}^q_S} \;\; ; \;\; \emptyset = \partial\mathcal{B}^w_S \cap \partial\mathcal{B}^t_S = \partial\mathcal{B}^p_S \cap \partial\mathcal{B}^q_S, \tag{4.38}$$

where the union of $\mathcal{B}_S$ and $\mathcal{B}_D$ is $\mathcal{B}$ and the boundary domain follows the same treatment. Here we capture the transition of the constitutive responses of the solid constituent in the intact and liquefied states through a partition of unity argument in the local constitutive responses. As such, we adopt only one solid constituent and the balance of linear momentum equations in the sub-domains $\mathcal{B}_D$ and $\mathcal{B}_S$ [Eqs (4.5) and (4.11)] are combined into one set of equations over the domains $\mathcal{B}$. The governing equations for the model problem are summarized as follows:

$$
\begin{cases}
(1-d)\left[\nabla\cdot(\boldsymbol{\sigma}' - p_{f_D}\boldsymbol{I})\right] + d\,(\nabla\cdot\boldsymbol{\sigma}^s) = \mathbf{0} \ \text{ in } \mathcal{B}, & (4.39)\\
\nabla\cdot\boldsymbol{v}_s + \nabla\cdot\boldsymbol{w}_{f_D} = 0 \ \text{ in } \mathcal{B}_D, & (4.40)\\
\nabla\cdot\boldsymbol{\sigma}^{f_S} + \rho^{f_S}\boldsymbol{g} = \mathbf{0} \ \text{ in } \mathcal{B}_S, & (4.41)\\
\nabla\cdot\boldsymbol{v}_s + \nabla\cdot\boldsymbol{w}_{f_S} = 0 \ \text{ in } \mathcal{B}_S, & (4.42)\\
g'(d)\mathcal{H} + \dfrac{\mathcal{G}_c}{l^*}(d - l^{*2}\nabla^2 d) = 0 \ \text{ in } \mathcal{B}, & (4.43)\\
(\boldsymbol{w}_{f_S} - \boldsymbol{w}_{f_D})\cdot\boldsymbol{n}^* = 0 \ \text{ on } \Gamma^*, & (4.44)\\
\boldsymbol{t}^*_{f_S}\cdot\boldsymbol{n}^* + p_{f_D} = 0 \ \text{ on } \Gamma^*, & (4.45)\\
\boldsymbol{t}^*_{f_S}\cdot\boldsymbol{m}^*_j + \mu_f\dfrac{\alpha_{SD}}{\sqrt{k}}(\boldsymbol{w}_{f_S} - \boldsymbol{w}_{f_D})\cdot\boldsymbol{m}^*_j = 0 \ \text{ on } \Gamma^*, & (4.46)
\end{cases}
$$

where the natural and essential boundary conditions are not included for brevity. Following the standard weighted residual procedure, we multiply Eqs. (4.39)-(4.43) with proper weight functions ($\boldsymbol{\eta}_s$, ξ_{f_D}, $\boldsymbol{\eta}_{f_S}$, ξ_{f_S} and ζ), and integrating over their corresponding domain. The resultant weighted-residual statement reads [321, 332],

$$
\int_{\mathcal{B}} \nabla\boldsymbol{\eta}_s : (\boldsymbol{\sigma}' - p_{f_D}\boldsymbol{I})(1-d)\,dV + \int_{\mathcal{B}} \nabla\boldsymbol{\eta}_s : \boldsymbol{\sigma}^s d\,dV - \int_{\partial\mathcal{B}^t_D} \boldsymbol{\eta}_s\cdot\hat{\boldsymbol{t}}_D\,d\Gamma = 0, \quad (4.47)
$$

$$
\begin{aligned}
&\int_{\mathcal{B}_D} \xi_{f_D}(\nabla\cdot\dot{\boldsymbol{u}}_s)\,dV - \int_{\mathcal{B}_D} \nabla\xi_{f_D}\cdot\boldsymbol{w}_{f_D}\,dV\\
&- \int_{\partial\mathcal{B}^q_D} \xi_{f_D}\hat{q}_D\,d\Gamma + \int_{\Gamma^*} \xi_{f_D}\underbrace{\boldsymbol{w}_{f_D}\cdot(-\boldsymbol{n}^*)}_{=m^*_{f_D}}\,d\Gamma = 0, \qquad (4.48)
\end{aligned}
$$

$$\int_{\mathcal{B}_S} \nabla \boldsymbol{\eta}_{f_S} : \boldsymbol{\sigma}^{f_S}\, dV - \int_{\partial \mathcal{B}_S^t} \boldsymbol{\eta}_{f_S} \cdot \hat{\boldsymbol{t}}_S\, d\Gamma - \int_{\Gamma^*} \boldsymbol{\eta}_{f_S} \cdot \underbrace{\boldsymbol{\sigma}^{f_S} \cdot \boldsymbol{n}^*}_{=\boldsymbol{t}^*_{f_S}}\, d\Gamma = 0, \tag{4.49}$$

$$\int_{\mathcal{B}_S} \xi_{f_S} (\nabla \cdot \dot{\boldsymbol{u}}_s)\, dV + \int_{\mathcal{B}_S} \xi_{f_S} (\nabla \cdot \boldsymbol{w}_{f_S})\, dV = 0, \tag{4.50}$$

$$\int_{\mathcal{B}} \zeta \left[g'(d)\mathcal{H} + \frac{\mathcal{G}_c}{l^*} d \right] dV + \int_{\mathcal{B}} \nabla \zeta \cdot \mathcal{G}_c l^* \nabla d\, dV = 0, \tag{4.51}$$

where $\hat{\boldsymbol{t}}_D$ and $\hat{q}_D$ is the prescribed traction and flux at the porous matrix, respectively; and $\hat{\boldsymbol{t}}_S$ is the fluid traction. Then, we directly impose the interfacial transmissibility conditions [Eqs. (4.44)-(4.46)] into the field equations Eqs. (4.48) and (4.50). Due to the fluid mass continuity (i.e., $m^*_{f_D} + m^*_{f_S} = 0$), the fourth term on the left hand side of Eq. (4.48) becomes:

$$\int_{\Gamma^*} \xi_{f_D} \boldsymbol{w}_{f_D} \cdot (-\boldsymbol{n}^*)\, d\Gamma = -\int_{\Gamma^*} \xi_{f_D} \boldsymbol{w}_{f_S} \cdot \boldsymbol{n}^*\, d\Gamma, \tag{4.52}$$

while normal and shear force equilibrium (i.e., $\boldsymbol{t}^*_{f_D} + \boldsymbol{t}^*_{f_S} = \boldsymbol{0}$) can be imposed at the third term on the left hand side of Eq. (4.49), i.e.,

$$\begin{aligned} &- \int_{\Gamma^*} \boldsymbol{\eta}_{f_S} \cdot \boldsymbol{\sigma}^{f_S} \cdot \boldsymbol{n}^*\, d\Gamma \\ &= \int_{\Gamma^*} \boldsymbol{\eta}_{f_S} \cdot (p_{f_D} \boldsymbol{n}^*)\, d\Gamma + \sum_{j=1}^{2} \int_{\Gamma^*} \boldsymbol{\eta}_{f_S} \cdot \left[\mu_f \frac{\alpha_{SD}}{\sqrt{k}} (\boldsymbol{w}_{f_S} - \boldsymbol{w}_{f_D}) \cdot \boldsymbol{m}^*_j \right] \boldsymbol{m}^*_j\, d\Gamma. \end{aligned} \tag{4.53}$$

Finally, we apply Eqs. (4.24)-(4.27) in order to convert subdomain integrals ($\mathcal{B}_D$ and $\mathcal{B}_S$) into integral over the entire domain ($\mathcal{B}$), and to also transform the interface equations [Eqs. (4.52)-(4.53)] into a set of immersed boundary conditions. As a result, we get the weak statements for a phase field Biot-Stokes model, which is to: find $\{\boldsymbol{u}_s, p_{f_D}, \boldsymbol{w}_{f_S}, p_{f_S}, d\}$ such that for all $\{\boldsymbol{\eta}_s, \xi_{f_D}, \boldsymbol{\eta}_{f_S}, \xi_{f_S}, \zeta\}$,

$$G^u = G^p_D = G^w_S = G^p_S = G^d = 0, \tag{4.54}$$

where:

$$G_u = \int_{\mathcal{B}} \nabla\, \boldsymbol{\eta}_s : (\boldsymbol{\sigma}' - p_{f_D}\boldsymbol{I})(1-d)\, dV + \int_{\mathcal{B}} \nabla\, \boldsymbol{\eta}_s : \boldsymbol{\sigma}^s d\, dV - \int_{\partial\mathcal{B}^t_D} \boldsymbol{\eta}_s \cdot \hat{\boldsymbol{t}}_D\, d\Gamma, \quad (4.55)$$

$$\begin{aligned} G^p_D = &\int_{\mathcal{B}} \xi_{f_D}(\nabla\cdot \dot{\boldsymbol{u}}_s)(1-d)\, dV - \int_{\mathcal{B}} \nabla\, \xi_{f_D} \cdot \boldsymbol{w}_{f_D}(1-d)\, dV \\ &+ \int_{\mathcal{B}} \xi_{f_D}(\boldsymbol{w}_{f_S} \cdot \nabla\, d)\, dV - \int_{\partial\mathcal{B}^q_D} \xi_{f_D}\hat{q}_D\, d\Gamma, \end{aligned} \quad (4.56)$$

$$\begin{aligned} G^w_S = &\int_{\mathcal{B}} \nabla\, \boldsymbol{\eta}_{f_S} : \boldsymbol{\sigma}^{f_S} d\, dV - \int_{\mathcal{B}} \boldsymbol{\eta}_{f_S} \cdot (p_{f_D} \nabla\, d)\, dV \\ &+ \sum_{j=1}^{2} \int_{\mathcal{B}} \boldsymbol{\eta}_{f_S} \cdot \left[\mu_f \frac{\alpha_{SD}}{\sqrt{k}} (\boldsymbol{w}_{f_S} - \boldsymbol{w}_{f_D}) \cdot \boldsymbol{m}^*_j\right] \boldsymbol{m}^*_j \| \nabla\, d\|\, dV \\ &- \int_{\partial\mathcal{B}^t_S} \boldsymbol{\eta}_{f_S} \cdot \hat{\boldsymbol{t}}_S\, d\Gamma, \end{aligned} \quad (4.57)$$

$$G^p_S = \int_{\mathcal{B}} \xi_{f_S}(\nabla\cdot \dot{\boldsymbol{u}}_s) d\, dV + \int_{\mathcal{B}} \xi_{f_S}(\nabla\cdot \boldsymbol{w}_{f_S}) d\, dV, \quad (4.58)$$

$$G^d = \int_{\mathcal{B}} \zeta \left[g'(d)\mathcal{H} + \frac{\mathcal{G}_c}{l^*} d\right] dV + \int_{\mathcal{B}} \nabla\, \zeta \cdot \mathcal{G}_c l^* \nabla\, d\, dV. \quad (4.59)$$

Here, as pointed out in Stoter et al. [332], the Γ-convergence ensures that the immersed boundary conditions imposed in Eqs. (4.56)-(4.57) are consistent with the interface conditions [Eqs. (4.44)-(4.46)] if $l^* \to 0$, which in turn confirms the mass conservation and force equilibrium for the entire system $\mathcal{B}$.

4.4 Numerical examples

This section highlights the capacities of the immersed phase field model to capture the hydromechanical interactions among the pore fluid in the cavities, cracks and the homogenized pore space and the host matrix in two numerical experiments. Our focus is on modeling the problems that involve the mechanically-driven pore fluid migration due to deformation and crack growth inside the solid skeleton. The first example simulates the consolidation process of the porous material that contains a semi-circular cavity at the bottom that serves as a pore fluid outlet, while the second problem showcases the fracture-induced

Stokes-Darcy flow in vuggy porous medium.

In order to solve Eqs. (4.55)-(4.59) numerically, we adopt standard finite element method where the solution procedure is based on the operator-split [76, 210, 260] that successively updates the field variables. In other words, the phase field d is updated first by solving $G^d = 0$, while all other field variables are held fixed, and the solver then advances the remaining variables by solving $\{G^u, G^p_D, G^w_S, G^p_S\}^{\mathrm{T}} = \mathbf{0}$. The implementation of our proposed model including finite element discretization and the solution scheme relies on the finite element package `FEniCS` [147, 148, 340]. It is noted that there exists multiple different strategies to solve the same system of equations. Since the exploration of different solution schemes are out of the scope of this study, we omit the details for the implementation for brevity.

4.4.1 Consolidation of porous matrix with a semi-circular cavity

We first simulate a consolidation problem, which has always been one of the key problems in geotechnical engineering. While classical consolidation problem considers time-dependent water expulsion from the homogeneous porous material, as illustrated in Fig. 4.3, this numerical example explores the case where the system includes a cavity at the bottom that serves as a pore fluid outlet. This specific setting is designed to simulate mechanically driven Stokes-Darcy flow without significant changes in microstructural attributes.

The problem domain is a water-saturated 1 m $\times$ 2 m sized rectangular porous matrix ($\mathcal{B}_D$) that contains a semi-circular cavity ($\mathcal{B}_S$) whose diameter is 0.2 m. We prescribe a 1 kPa compressive mechanical traction at the top, while zero pressure boundary is imposed at the bottom of the cavity so that the time-dependent dissipation of pore pressure can be observed. The material parameters for this example are chosen as follows. Intrinsic mass densities for the solid and fluid: $\rho_s = 2700$ kg/m^3 and $\rho_f = 1000$ kg/m^3; Young's modulus and Poisson's ratio of the solid skeleton: $E = 100$ MPa and $\nu = 0.25$; initial permeability and initial porosity of the matrix: $k_0 = 1.0 \times 10^{-8}$ m^2 and $\phi_0 = 0.4$; dynamic viscosity

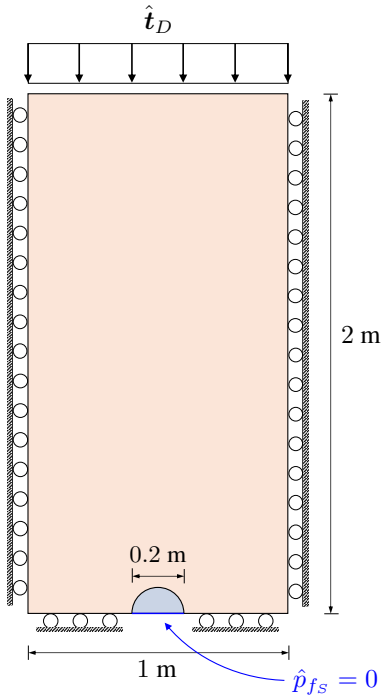

Figure 4.3: Schematic of geometry and boundary conditions for the consolidation problem.

of the fluid phase: $\mu_f = 1.0 \times 10^{-3}$ Pa·sec; slippage coefficient $\alpha_{SD} = 0$; and regularization length for the interface $l^* = 0.002$ m. Furthermore, we assume that solid constituent remains intact in $\mathcal{B}_D$ throughout the simulation while free fluid inside the cavity has zero particle concentration (i.e., $c = 0$).

Fig. 4.4 shows the spatial distributions for the prime variables at $t = 1.0 \times 10^{-3}$ sec. Here, we compute fluid pressure and relative fluid velocity for the entire system as: $p_f = (1-d)p_{f_D} + dp_{f_S}$ and $\boldsymbol{w}_f = (1-d)\boldsymbol{w}_{f_D} + d\boldsymbol{w}_{f_S}$, respectively, since we have separate degrees of freedoms for pore and free fluids residing in each regions $\mathcal{B}_D$ and $\mathcal{B}_S$. The results imply that applied mechanical load $\hat{\boldsymbol{t}}_D$ at $t = 0$ builds up the pore pressure which in turn affects the pore fluid to migrate towards the cavity. Furthermore, free fluid inside the cavity tends to exhibit higher velocity and lower pressure compared to those of pore fluid, because of different constitutive relations (i.e., Stokes equation and Darcy's law) in each region. As illustrated in Fig. 4.5, we also investigate the time-dependent response of the system that clearly describes the consolidation process and at the same time highlights

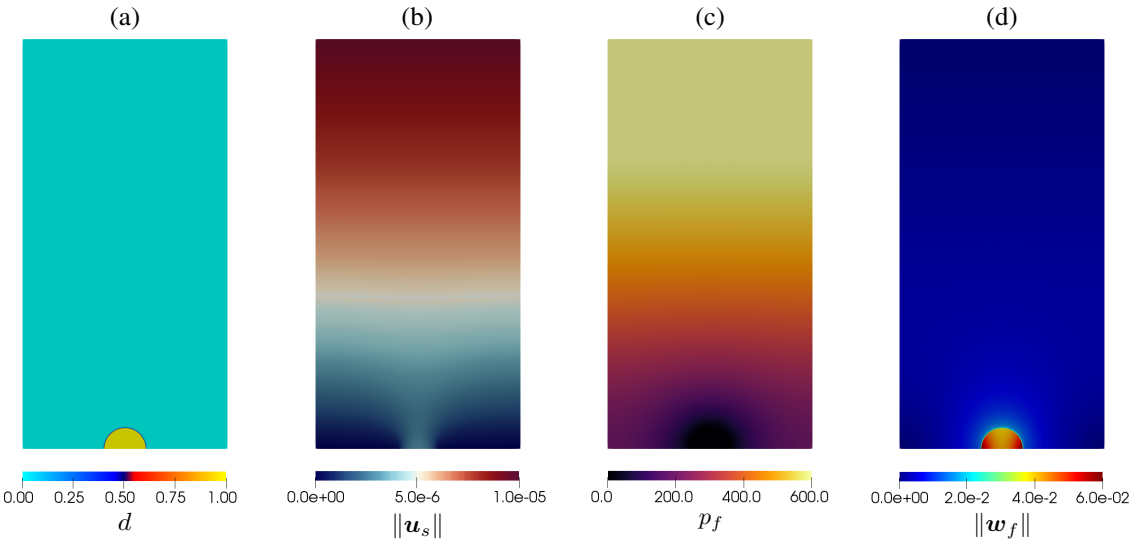

Figure 4.4: Spatial distributions of the (a) phase field d; (b) solid displacement $\|\boldsymbol{u}_s\|$ [m]; (c) fluid pressure $p_f = (1-d)p_{f_D} + dp_{f_S}$ [Pa]; and (d) relative fluid velocity $\|\boldsymbol{w}_f\| = \|(1-d)\boldsymbol{w}_{f_D} + d\boldsymbol{w}_{f_S}\|$ [m/s], at $t = 1.0 \times 10^{-3}$ sec.

the continuous pressure and velocity fields along y-axis (i.e., from the center point of the cavity to the top-central point of the external boundary). At $t = 0$, the entire load is taken by the incompressible pore water which triggers the fluid flow inside the medium. This fluid flow is accompanied by a dissipation of pore pressure over time and an increase in the compression of the entire system, which is consistent with previous studies on homogeneous materials [275, 309, 341, 342]. In addition, the continuous pressure and velocity profiles imply that our model is capable of imposing mass continuity and force equilibrium at the interface as a set of immersed boundary conditions, which confirms the validity of the model.

4.4.2 Comparison studies on fracture-induced flow in vuggy porous media

In the second set of experiment, we conduct numerical simulations within two different types of domains that possess horizontal edge crack (Fig. 4.6): one explicitly captures the geometry of the large cavities in the porous media; another one captures the influence of

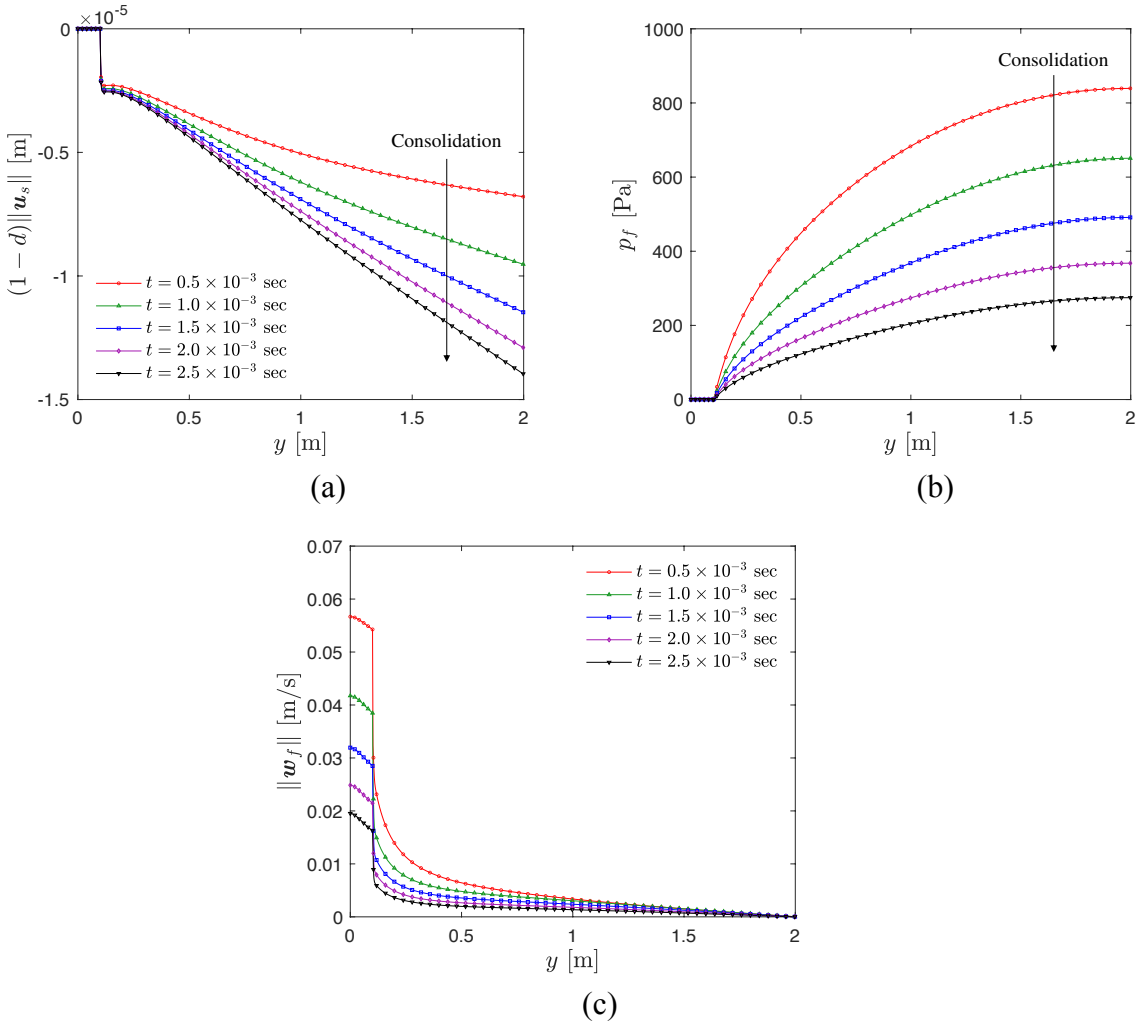

Figure 4.5: Response of the saturated Biot-Stokes system under 1 kPa consolidation pressure. (a) Solid displacement; (b) Fluid pressure; and (c) Fluid velocity.

the cavities by increasing the porosity of the homogenized effective medium. While the former approach adopt a more explicit representation of the pore geometry and hence may provide more detailed information on the interactions between the vugs and the propagating cracks, the latter approach could be numerically more efficient. Our objective is to demonstrate, quantitatively, the difference of the two approaches such that a fuller picture on the trade-off between computational efficiency, accuracy and precision of the predictions ca be established.

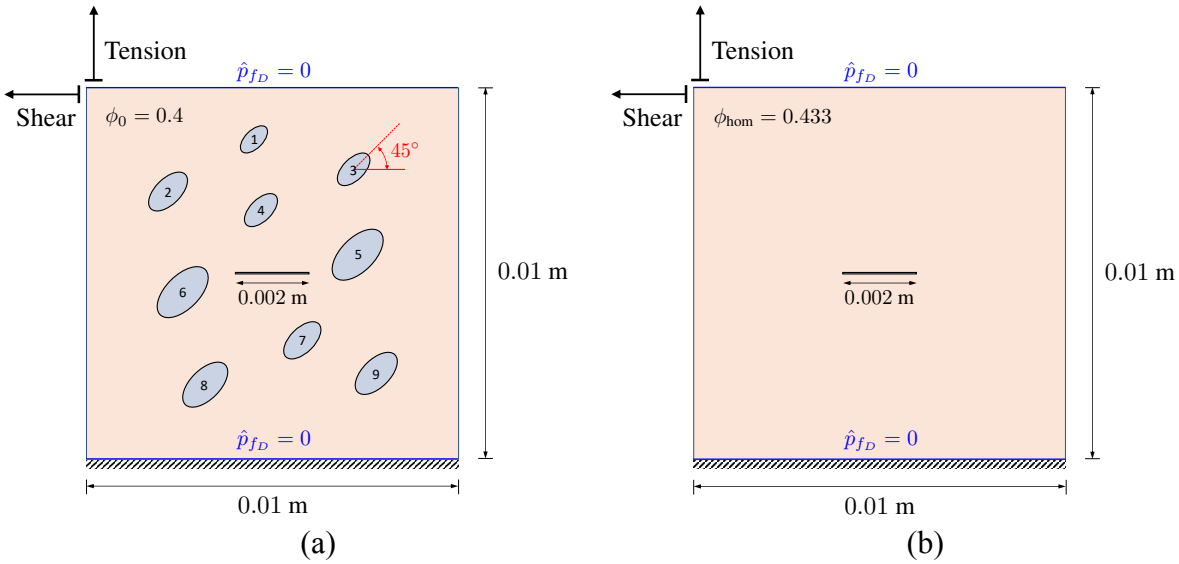

Figure 4.6: Schematic of geometry and boundary conditions for the fracture problem. (a) The domain with explicitly modeled cavities; and (b) its homogenized counterpart.

Modeling vuggy porous media

As illustrated in Fig. 4.6(a), we first consider a domain that consists of porous matrix with explicitly modeled cavities. Our first representation consists of total nine cavities with different major and minor radii (Table 4.1) that share the same aspect ratio of 2:1 and are tilted by 45°, such that the volume fraction of the cavities θ_{cav} is 0.056. Here, we assume that the solid skeleton inside the cavities are completely damaged (i.e., $d = 1$), while the porous matrix initially remains completely undamaged (i.e., $d = 0$). The material properties for this case is chosen as follows: $\rho_s = 2700$ kg/m^3, $\rho_f = 1000$ kg/m^3, $E = 20$ GPa, $\nu = 0.2$, $k_0 = 1.0 \times 10^{-12}$ m^2, $\mu_f = 1.0 \times 10^{-3}$ Pa·sec, $\alpha_{SD} = 0.1$, $\mathcal{G}_c = 20$ J/m^2, and $l^* = 0.125 \times 10^{-3}$ m. In addition, the initial particle concentration is chosen as $c_0 = 0.6$ and its upper bound as $c_{\text{max}} = 0.7$, in order to mimic the mudflow inside the cracks or cavities [343, 344].

In contrast, our second domain in Fig. 4.6(b) is a homogenized representation of Fig. 4.6(a), where all the cavities are considered as a part of matrix pores. In this case, the porosity of the homogenized medium is determined as: $\phi_{\text{hom}} = (1 - \theta_{\text{cav}})\phi_0 + \theta_{\text{cav}} = 0.433$.

Table 4.1: The major and minor radii [mm] of the explicitly modeled elliptical cavities in Fig. 4.6(a).

Index	1	2	3	4	5	6	7	8	9
Major radius r_a	0.400	0.600	0.500	0.500	0.820	0.800	0.580	0.700	0.650
Minor radius r_b	0.200	0.300	0.250	0.250	0.410	0.400	0.290	0.350	0.325

It is noted the correct homogenized effective properties often depend on the geometry of the vugs or inclusions, which can be determined from computed tomographic images or directly obtained from the experiment [102, 243, 244, 345]. Since the micro-structural attributes are not always available, this study adopts an alternative approach where the effective material properties are determined by using the equivalent inclusion method [346–348]. Following Ramakrishnan and Arunachalam [348] and by assuming that the matrix shares the same material properties of those chosen for Fig. 4.6(a), the effective bulk modulus (K_{hom}) and shear modulus (μ_{hom}) for the homogenized representation [Fig. 4.6(b)] are determined as follows:

$$K_{\text{hom}} = \frac{K(1-\theta_{\text{cav}})^2}{1+\frac{1+\nu}{2(1-2\nu)}\theta_{\text{cav}}} \;\; ; \;\; \mu_{\text{hom}} = \frac{\mu(1-\theta_{\text{cav}})^2}{1+\frac{11-19\nu}{4(1+\nu)}\theta_{\text{cav}}}, \tag{4.60}$$

so that the effective Young's modulus $E_{\text{hom}} = 16.50$ GPa and Poisson's ratio $\nu_{\text{hom}} = 0.206$. Assuming that the inclusion permeability is much higher than the matrix permeability, we approximate the effective permeability (k_{hom}) by following Markov et al. [349] which is obtained based on the Maxwell's formula, i.e.,

$$k_{\text{hom}} = \frac{k_0(1+2\theta_{\text{cav}})}{1-\theta_{\text{cav}}} = 1.18 \times 10^{-12}\ [\text{m}^2]. \tag{4.61}$$

In addition, since all the cavities in Fig. 4.6(a) are completely isolated, we adopt the following effective critical energy $\mathcal{G}_{c,\text{hom}}$ proposed by Jelitto and Schneider [350] for the homogenized representation, which depends on the volume fraction of the cavities, i.e.,

$$\mathcal{G}_{c,\text{hom}} = \mathcal{G}_c(1-\theta_{\text{cav}}^{2/3}) = 17.07\ [\text{J/m}^2]. \tag{4.62}$$

Mechanically driven fracture-induced flow

As illustrated in Fig. 4.6, we conduct two different types of simulations within each domain: the tension tests with prescribed vertical displacement rate of 0.01×10^{-3} m/s, and the shear tests with horizontal displacement rate of 0.01×10^{-3} m/s. In both tension and shear tests, the displacements are prescribed at the upper boundary, whereas the bottom part of the domain is held fixed. We also impose hydraulically insulated boundary conditions for the left and right boundaries while we permit water intake from the upper and lower boundaries by imposing $\hat{p}_{f_D} = 0$.

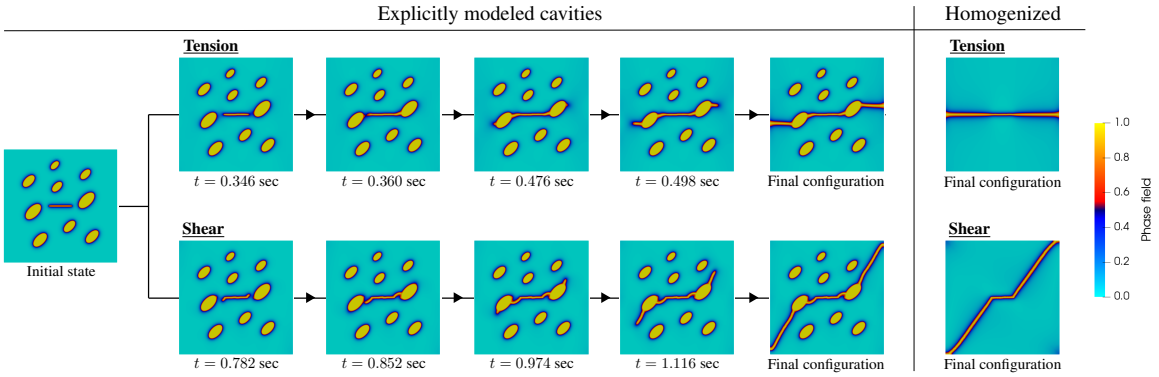

Figure 4.7: Evolution of the phase field of the specimens subjected to the numerical tension and shear tests.

Fig. 4.7 illustrates the evolution of the phase field for both tension and shear tests in a computational domain where the cavities are explicitly modeled, compared with the crack trajectories obtained from the homogenized domain. The domain without cavities exhibits the crack patterns that are similar to the results of previous studies on homogeneous solids [76, 77, 90, 210], while the domain with explicitly modeled cavities exhibit distinct crack patterns. More importantly, Fig. 4.8 and Fig. 4.9 reveals that neglecting the interaction between the cavity and crack in the homogenized model may lead to over-simplified global responses that lacks the distinctive characteristics of the cavity-crack coalescence.

During the numerical experiments, the porous matrix initially undergoes linear elastic deformation until the crack nucleation takes place. At this point, since tensile loading directly influences the volume change of the material, both specimens under tensile load

exhibit higher fluid influx at the top, compared to those measured from the shear tests. After the first peaks shown in Fig. 4.8(a) and Fig. 4.8(b), cracks start to initiate from the tips of the pre-existing flaw since they experience higher stress concentration compared to the matrix-cavity interface.

In both tensile and shear experiments performed on the vuggy specimen, the crack nucleation increases the surface influx rate at the permeable boundaries as pore fluid starts to leak from the intact matrix to the damaged regions regardless of the spatial homogenization. The two numerical specimens, nevertheless, begin to behave differently when the cracks propagate towards the adjacent vugs and coalesce with each other in both tension and shear tests in the vuggy specimen (Fig. 4.7) [292, 351]. These changes in surface influx cannot be replicated in the homogenized porous specimen as the homogenization takes away the possibility of simulating the coalescence between the cavity and the crack.

After the coalescence of the cavity and the crack in the vuggy specimen, the reaction force in both cases increases again with lower influx rates until it reaches the second peak (i.e., where crack nucleation takes place at the matrix-cavity interface), and the crack eventually reaches both end of the specimens. This result implies that the existence of vugs or cavities has a profound impact on the material behavior that cannot be easily replicated in the homogenized effective medium. Consequently, either a more effective macroscopic theory or a suitable multiscale technique is needed to incorporate the cavity-crack interaction into the predictions.

Fig. 4.10 illustrates the pressure (p_f) and x-directional velocity ($\boldsymbol{w}_{f_S}$) fields from a domain with explicitly modeled cavities under tensile and shear loadings, at $t = 0.476$ sec and $t = 1.012$ sec, respectively, where cracks start to propagate from the cavities. Here, the superimposed arrows in Fig. 4.10 indicate the direction of the velocity vector $\boldsymbol{w}_f = (1-d)\boldsymbol{w}_{f_D} + d\boldsymbol{w}_{f_S}$. In both cases, the leakage of pore fluid takes place towards the interconnected cracks and cavities at the middle, while free fluid in $\mathcal{B}_S$ tends to migrate towards the center, the region where large crack opening displacement occurs. However,

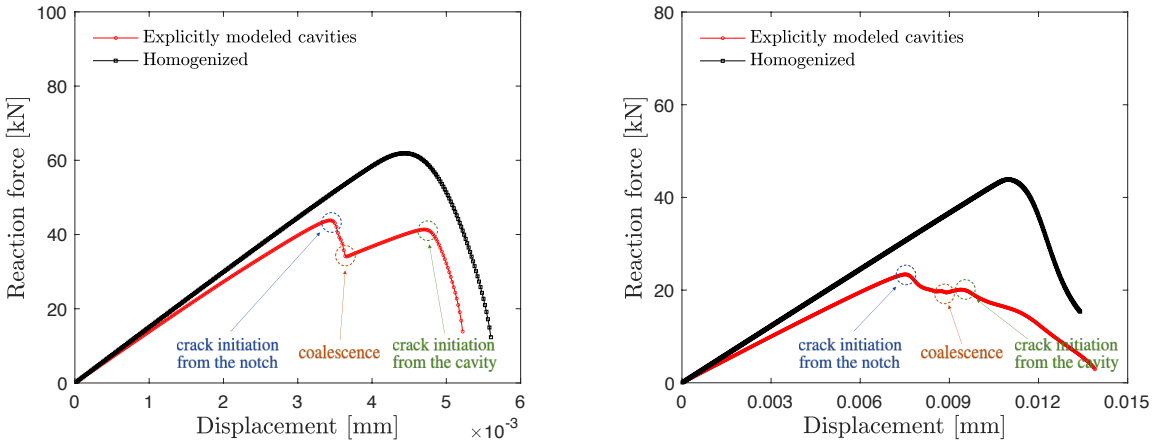

Figure 4.8: Force-displacement curves obtained from (a) tension and (b) shear tests.

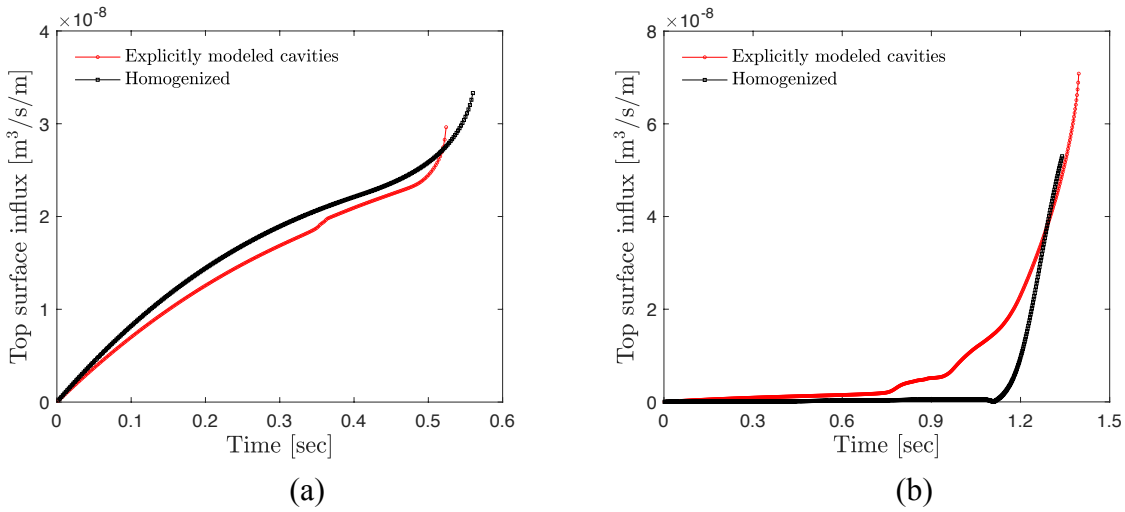

Figure 4.9: Fluid influx at the top surface over time measured from (a) tension and (b) shear tests.

it is worthy to note that the fluid flow occurs from the region that has negative pressure to the damaged zone where $p_{fs} \approx 0$. Unlike previous studies that use the cubic law to predict the hydraulic responses of the flow conduit [139, 140, 242, 291], the pore pressure distribution inside the void space is governed by the Stokes equation directly. This set of numerical experiments again highlight that our proposed model is capable of simulating fracture-cavity interaction with evolving interface, which may not be easily captured either by using hydraulic phase field fracture models or by adopting classical Biot-Stokes model

with sharp interface.

To assess the computational efficiency of the proposed model, we record the CPU time for both simulations. A laptop with a Intel Core i9-9880H Processor CPU with 16 GB memory at 2667MHz (DDR4) is used to run both simulation on a single core. Both simulations are solved by the same Scalable Nonlinear Equation Solver (SNES) available in FEniCS. In the case where vuggy pores are explicitly modeled, the time taken to assemble the system of equation is 1.13 second and the averaged time taken to advance one time step with (on average) 5 Newton-Raphson iteration is 35.69 seconds. Meanwhile, in the homogenized case, it takes 1.17 second to assemble the system of equation and 33.34 seconds to advance one time step with also (on average) 5 Newton-Raphson iteration. In general, simulations with the explicitly captured vuggy pores require about 7% more CPU time to run the same simulation.

Future work may consider flow with higher Reynold's number suitable for the Navier-Stokes equation in the fluid domain. Such an extension is nevertheless out of the scope of the current study.

4.5 Conclusion

This article presents a new immersed phase field model that captures the hydro-mechanical coupling mechanisms in vuggy porous media where brittle cracks filled with water may coalescence with pores that trigger both redistribution of flow and macroscopic softening that cannot be captured without the Stokes-Darcy flow. By generalizing the phase field as an indicator of defects, we introduce a simple and unified treatment to handle the evolving geometries due to crack growths and the resultant changes of constitutive responses without the need of re-meshing or introduction of enrichment functions. By directly simulating the flow inside the cracks, we bypass the need of introducing phenomenological permeability enhancement model to replicate the flow conduit. This explicit approach can be

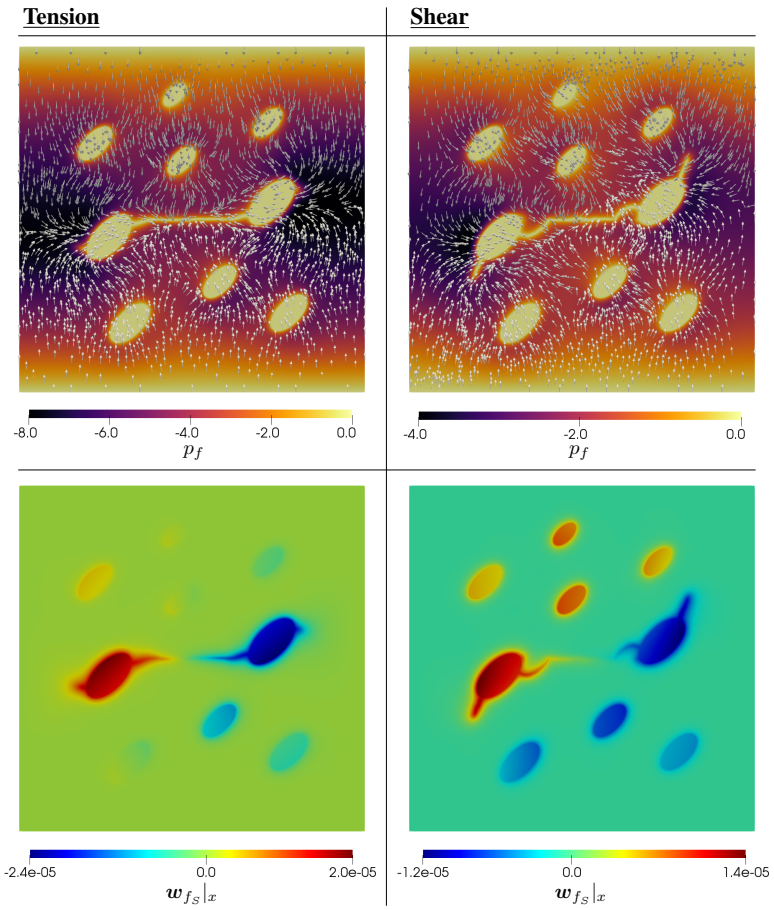

Figure 4.10: Snapshots of the pressure $p_f = (1-d)p_{f_D} + dp_{f_S}$ [Pa] and velocity $\boldsymbol{w}_{f_S}$ [m/s] fields obtained from the tension ($t = 0.476$ sec) and shear ($t = 1.012$ sec) tests.

advantageous over the embedded discontinuity approach when there is a substantial crack opening and a flow near the locations with void-crack interaction where a homogenized pore pressure jump would not be sufficient to capture the pattern of the pore pressure field in the defects. Future work may include the extension of the proposed model to three-dimensional cases as well as extending the Stokes-Darcy flow model for the generalized Navier-Stokes-Darcy flow for injection and other problems with higher Reynolds numbers.

Chapter 5: Phase field model for cohesive fracture in higher-order continua

This chapter is published as: H.S. Suh, W.C. Sun, D. O'Connor, A phase field model for cohesive fracture in micropolar continua, Computer Methods in Applied Mechanics and Engineering, Volume 369, 2020, doi.org/10.1016/j.cma.2020.113181.

5.1 Introduction

The size effect and the corresponding length scale parameter associated with the phase field fracture model for brittle or quasi-brittle materials have been a subject of intensive research in recent years [75, 88, 90, 140, 207, 351–356]. Due to the fact that the phase field approach employ regularized (smoothed) implicit function to represent sharp interface, the physical interpretation of the length scale parameter (and in some cases, the lack thereof) has become a hotly debated topic among the computational fracture mechanics community. The lack of consensus on the definition of length scale has also been sometimes perceived as a weakness, especially when compared with the embedded discontinuity approaches such as XFEM or assumed strain models [296, 337, 357–359].

The early attempt to justify the introduction of the length scale parameter for phase field fracture models can be tracked back to the first variational fracture model in Francfort and Marigo [207] where the variational fracture model is expected to exhibit $\Gamma-$convergence and therefore may converge to the sharp interface model as the mesh size and the length

scale parameter approaches zero. While this line of work (e.g., Bourdin, Francfort, and Marigo [75] and May, Vignollet, and De Borst [360]) provides a theoretical justification, in practice, the length scale parameter must still be sufficiently large compared to the mesh size in order to solve the phase field governing equation. This could be problematic if the simulations are designed for boundary value problems at the large scales (e.g., hydraulic fracture, faulting of geological formation) where the small mesh size, even concentrated at a local regions, become impractical.

One strategy to overcome this issue is to decouple or eliminate the effect of the length scale parameters on the constitutive responses such that a relatively large length scale parameter can be used for numerical purposes without compromising the accuracy of the constitutive responses. To derive a phase field fracture model that exhibits macroscopic responses independent or at least not sensitive to the length scale parameters, Wu and Nguyen [354] and Geelen et al. [209] both introduce new crack surface density functionals and the corresponding degradation function derived from cohesive zone models such that the underlying traction-separation law is independent of the length scale parameter. Their simulations have shown that the resultant fracture patterns and the macroscopic constitutive responses are both insensitive to the length scale parameters in the sub-critical regime.

Another strategy to circumvent the length scale issue is to determine the underlying relationship among the length scale parameters and other material parameters (e.g., Young's modulus, tensile strength) that can be obtained from a specific set of experimental tests [168, 338, 339]. However, these previous works also show that the analytical expression of the length scale parameter may vary in according to the chosen inverse problems and hence the length scale parameter is likely only valid for backward calibration for a specific problem but cannot be used for general-purposed forward predictions. Furthermore, identifying the correct length scale parameter for a given inverse problem does not imply that such a length scale parameter is sufficiently large to ensure the solvability of the discretized governing equation(s).

Nevertheless, *one key aspect that is often overlooked in the phase field fracture modeling is that materials with internal structures that enables size effects on damage and fracture may likely exhibit size effect in the elastic regimes*. Examples of these materials include concrete, composite, particulate materials as well as some metamaterials [361–365]. Since these materials exhibit large internal length scales compared to the length scale of damage or fracture, suitable size effect must be carefully incorporated in *both* the elastic and path-dependent regimes to capture the size-dependence properly. This paper is the first attempt to formulate a new cohesive micropolar phase field fracture theory that leads to a physically justified/identifiable size-dependent effect for both the path-independent elastic responses and the path-dependent damage and fracture in a higher-order continuum undergoing infinitesimal deformation. By extending the length-scale-parameter insensitive formulation that approximates cohesive-type of response to the micropolar materials, we introduce a third strategy where one may employ sufficiently large phase field length scale parameters to address the numerical needs without comprising the correct size effect that should exhibit in the numerical simulations. In order words, the resultant model is the best of both worlds, one that benefits from the physical justification of having a consistent size effect in both the elastic and damage regimes and yet retains the convenience of the approach in Wu and Nguyen [354], Geelen et al. [209], and Wu, Mandal, and Nguyen [366].

The rest of the chapter is organized as follows. We first briefly summarize the theory of micropolar elasticity, and introduce the strain energy split approach that enables one to explore the effects of the partitioned energy densities. We then extend the regularized length-scale-insensitive phase field formulation to the micropolar material models such that the length scale parameter for the phase field is insensitive to the macroscopic responses. This treatment then enables us to replicate the size effect characterized by the higher-order material parameters (e.g., bending and torsion stiffnesses) that can be experimentally sought. Furthermore, by enforcing the macroscopic responses not sensitive to the phase field length scale parameter, it enables us to conduct simulations in a spatial domain without the size

constraint imposed by the ratio between the phase field length scale and mesh. For completeness, the details of the finite element discretization and operator-split solution scheme are discussed. Numerical examples are given to verify the implementation, provide evidences on how micropolarity affects the macroscopic behaviors for quasi-brittle materials, and showcase the applicability of the proposed models.

5.2 Theory of micropolar elasticity

In this section, we briefly summarize the kinematic and constitutive relations of an isotropic micropolar elastic materials undergoing infinitesimal deformation. In this case, the kinematics of micropolar materials is characterized by both the displacement field and the micro-rotations. The resultant strain tensor is no longer symmetric due to the higher-order kinematics. We thus decompose the strain tensor into symmetric and skew-symmetric parts, which consequently enables us to split the stored energy density into three different parts. This energy split approach opens the door for us to explore the effects of distinct degradation of partitioned energy conjugated pairs, which will be discussed later in this study.

5.2.1 Kinematics

Let us consider a micropolar elastic body $\mathcal{B} \subset \mathbb{R}^3$ with material points $\mathcal{P}$ identified by the position vectors $\boldsymbol{x} \in \mathcal{B}$ that undergoes infinitesimal deformation. As illustrated in Fig. 5.1, unlike the classical non-polar (Boltzmann) approach, each material point experiences micro-rotation $\boldsymbol{\theta}(\boldsymbol{x}, t)$, in addition to the translational displacement $\boldsymbol{u}(\boldsymbol{x}, t)$ at time t. The micro-rotation represents the local rotation of the material point $\boldsymbol{x}$, which is independent of the displacement field. Consequently, the rotational part of the polar decomposition of the displacement gradient (i.e., macro-rotation) is also independent of the micro-rotation. The

micropolar strain $\bar{\boldsymbol{\varepsilon}}$ and micro-curvature $\bar{\boldsymbol{\kappa}}$ can be defined as follows [367–372]:

$$\bar{\boldsymbol{\varepsilon}} = \nabla \boldsymbol{u}^{\mathrm{T}} - \overset{3}{\boldsymbol{E}} \cdot \boldsymbol{\theta}, \tag{5.1}$$

$$\bar{\boldsymbol{\kappa}} = \nabla \boldsymbol{\theta}, \tag{5.2}$$

where $\overset{3}{\boldsymbol{E}} = \overset{3}{E}_{ijk}$ is the Levi-Civita permutation tensor. The definition of micropolar strain in Eq. (5.1) implies that the normal strains (i.e., diagonal entries of the micropolar strain tensor) that contributes to the stretching are equivalent to those in the classical approach, whereas the shear strains (i.e., off-diagonal entries of the micropolar strain tensor) are dependent on the micro-rotation. Since the micropolar strain tensor is non-symmetric, we therefore decompose the micropolar strain tensor into symmetric ($\bar{\boldsymbol{\varepsilon}}^{\mathrm{sym}}$) and skew-symmetric parts ($\bar{\boldsymbol{\varepsilon}}^{\mathrm{skew}}$), i.e.,

$$\bar{\boldsymbol{\varepsilon}} = \underbrace{\frac{1}{2}(\nabla \boldsymbol{u} + \nabla \boldsymbol{u}^{\mathrm{T}})}_{:=\bar{\boldsymbol{\varepsilon}}^{\mathrm{sym}}} + \underbrace{\frac{1}{2}(\nabla \boldsymbol{u}^{\mathrm{T}} - \nabla \boldsymbol{u}) - \overset{3}{\boldsymbol{E}} \cdot \boldsymbol{\theta}}_{:=\bar{\boldsymbol{\varepsilon}}^{\mathrm{skew}}}. \tag{5.3}$$

Notice that $\bar{\boldsymbol{\varepsilon}}^{\mathrm{sym}}$ is equivalent to the Boltzmann strain tensor in classical non-polar approach.

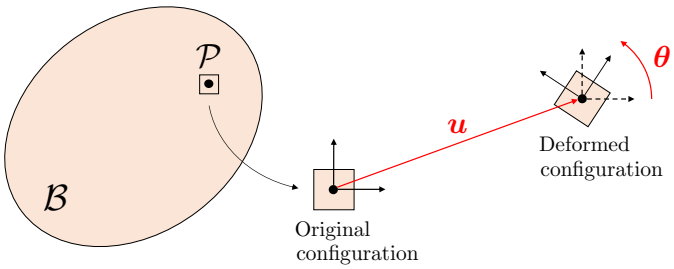

Figure 5.1: Kinematics of a micropolar continuum.

5.2.2 Constitutive model and strain energy split

To ensure stable elastic responses, the micropolar strain energy must fulfill strong ellipticity condition. To fulfill this requirement, we consider a micropolar strain energy density

$\psi_e(\bar{\boldsymbol{\varepsilon}}, \bar{\boldsymbol{\kappa}})$ that takes a quadratic form:

$$\psi_e(\bar{\boldsymbol{\varepsilon}}, \bar{\boldsymbol{\kappa}}) = \frac{1}{2}\bar{\boldsymbol{\varepsilon}} : \mathbb{C} : \bar{\boldsymbol{\varepsilon}} + \frac{1}{2}\bar{\boldsymbol{\kappa}} : \mathbb{D} : \bar{\boldsymbol{\kappa}}. \tag{5.4}$$

Here, $\mathbb{C}$ and $\mathbb{D}$ are constitutive moduli that possess the major symmetry (i.e., $\mathbb{C} = C_{ijkl} = C_{klij}$, and $\mathbb{D} = D_{ijkl} = D_{klij}$):

$$\mathbb{C} = \lambda\,(\boldsymbol{I} \otimes \boldsymbol{I}) + (\mu + \kappa)\,\mathbb{I} + \mu\bar{\mathbb{I}}\ ;\ \ \mathbb{D} = \alpha\,(\boldsymbol{I} \otimes \boldsymbol{I}) + \beta\bar{\mathbb{I}} + \gamma\mathbb{I}, \tag{5.5}$$

where λ, μ, κ, α, β, and γ are the material constants. The strong ellipticity of the strain energy density defined in Eq. (5.4) implies that the following inequalities must be hold [370, 373, 374]:

$$\begin{aligned} &3\lambda + 2\mu + \kappa \geq 0\,; \quad 2\mu + \kappa \geq 0\,; \quad \kappa \geq 0\,; \\ &3\alpha + \beta + \gamma \geq 0\,; \quad\ \ \gamma + \beta \geq 0\,; \quad\ \ \gamma - \beta \geq 0. \end{aligned} \tag{5.6}$$

These material constants, including the size-dependent ones are related to the following material parameters that have been individually identified via experiments [371, 375, 376]:

$$\begin{cases} E = \dfrac{(2\mu + \kappa)\,(3\lambda + 2\mu + \kappa)}{2\lambda + 2\mu + \kappa} & \text{Young's modulus,} \\ G = \dfrac{2\mu + \kappa}{2} & \text{shear modulus,} \\ \nu = \dfrac{\lambda}{2\lambda + 2\mu + \kappa} & \text{Poisson's ratio,} \\ l_t = \sqrt{\dfrac{\beta + \gamma}{2\mu + \kappa}} & \text{characteristic length in torsion,} \\ l_b = \sqrt{\dfrac{\gamma}{2\,(2\mu + \kappa)}} & \text{characteristic length in bending,} \\ \chi = \dfrac{\beta + \gamma}{\alpha + \beta + \gamma} & \text{polar ratio,} \\ N = \sqrt{\dfrac{\kappa}{2\,(\mu + \kappa)}} & \text{coupling number, } N \in [0, 1]. \end{cases} \tag{5.7}$$

The relations in Eq. (5.7) indicates that the size-dependence of the elasticity responses are related to the higher-order kinematics and kinetic. Although identification of the material parameters that characterize the size effect remains challenging as demonstrated in Bigoni and Drugan [377] and Neff, Jeong, and Fischle [378], these micropolar material parameters are obtainable through well-documented inverse problems or analytical solutions, at least for a subset of micropolar materials such as porous media [377]. This unambiguity is helpful for practical purposes.

In Eq. (5.7), the characteristic lengths l_t and l_b imply the nonlocal nature of micropolar material by quantifying the range of couple stress through their relationship to the micro-curvature. The coupling number N, on the other hand, quantifies the level of shear stress asymmetry that represents the degree of micropolarity of the material, e.g., $N = 0$ corresponds to the classical elasticity while $N = 1$ corresponds to the couple-stress theory [379–381]. In the remainder of this paper, unless specified, we set $N = 0.5$ for micropolar continuum simulations.

Since this study aims to develop a framework that explores the interaction between size-dependent micropolar elasticity and fracture mechanisms, we split the strain energy density into three different parts [based on the decomposition of the micropolar strain, cf. Eq. (5.3)]: (1) the Boltzmann part $\psi_e^B(\bar{\boldsymbol{\varepsilon}}^{\text{sym}})$; (2) the micro-continuum coupling part $\psi_e^C(\bar{\boldsymbol{\varepsilon}}^{\text{skew}})$; and (3) the pure micro-rotational part $\psi_e^R(\bar{\boldsymbol{\kappa}})$, i.e.,

$$\psi_e(\bar{\boldsymbol{\varepsilon}}, \bar{\boldsymbol{\kappa}}) = \psi_e^B(\bar{\boldsymbol{\varepsilon}}^{\text{sym}}) + \psi_e^C(\bar{\boldsymbol{\varepsilon}}^{\text{skew}}) + \psi_e^R(\bar{\boldsymbol{\kappa}}), \tag{5.8}$$

where the partitioned strain energy densities can be written as:

$$\psi_e^B(\bar{\boldsymbol{\varepsilon}}^{\text{sym}}) = \frac{1}{2}\left[\lambda(\bar{\boldsymbol{\varepsilon}}^{\text{sym}} : \boldsymbol{I})^2 + (2\mu + \kappa)\,\bar{\boldsymbol{\varepsilon}}^{\text{sym}} : \bar{\boldsymbol{\varepsilon}}^{\text{sym}}\right], \tag{5.9}$$

$$\psi_e^C(\bar{\boldsymbol{\varepsilon}}^{\text{skew}}) = \frac{1}{2}\kappa\bar{\boldsymbol{\varepsilon}}^{\text{skew}} : \bar{\boldsymbol{\varepsilon}}^{\text{skew}}, \tag{5.10}$$

$$\psi_e^R(\bar{\boldsymbol{\kappa}}) = \frac{1}{2}\left[\alpha(\bar{\boldsymbol{\kappa}} : \boldsymbol{I})^2 + \beta\bar{\boldsymbol{\kappa}} : \bar{\boldsymbol{\kappa}}^{\text{T}} + \gamma\bar{\boldsymbol{\kappa}} : \bar{\boldsymbol{\kappa}}\right]. \tag{5.11}$$

The force stress $\bar{\boldsymbol{\sigma}}$ can be found by taking partial derivative of the energy density with respect to the micropolar strain. By using Eq. (5.3), the force stress can also be partitioned into $\bar{\boldsymbol{\sigma}}^B$ and $\bar{\boldsymbol{\sigma}}^C$, which are the results of the pure non-polar deformation and the micro-continuum coupling effects, respectively:

$$\bar{\boldsymbol{\sigma}} = \frac{\partial \psi_e}{\partial \bar{\boldsymbol{\varepsilon}}} = \frac{\partial}{\partial \bar{\boldsymbol{\varepsilon}}}(\psi_e^B + \psi_e^C) = \underbrace{\lambda(\bar{\boldsymbol{\varepsilon}}^{\text{sym}} : \boldsymbol{I})\boldsymbol{I} + (2\mu + \kappa)\,\bar{\boldsymbol{\varepsilon}}^{\text{sym}}}_{:=\bar{\boldsymbol{\sigma}}^B} + \underbrace{\kappa \bar{\boldsymbol{\varepsilon}}^{\text{skew}}}_{:=\bar{\boldsymbol{\sigma}}^C}. \tag{5.12}$$

Similarly, the couple stress $\bar{\boldsymbol{m}}^R$ that is caused by the pure micro-rotation can be obtained as follows:

$$\bar{\boldsymbol{m}}^R = \frac{\partial \psi_e}{\partial \bar{\boldsymbol{\kappa}}} = \frac{\partial \psi_e^R}{\partial \bar{\boldsymbol{\kappa}}} = \alpha(\bar{\boldsymbol{\kappa}} : \boldsymbol{I})\boldsymbol{I} + \beta \bar{\boldsymbol{\kappa}}^{\text{T}} + \gamma \bar{\boldsymbol{\kappa}}. \tag{5.13}$$

Based on the split approach, notice that the partitioned energy densities in Eqs. (5.9)-(5.11) can be recovered by:

$$\psi_e^B = \frac{1}{2}\bar{\boldsymbol{\sigma}}^B : \bar{\boldsymbol{\varepsilon}}^{\text{sym}} \;\; ; \;\; \psi_e^C = \frac{1}{2}\bar{\boldsymbol{\sigma}}^C : \bar{\boldsymbol{\varepsilon}}^{\text{skew}} \;\; ; \;\; \psi_e^R = \frac{1}{2}\bar{\boldsymbol{m}}^R : \bar{\boldsymbol{\kappa}}, \tag{5.14}$$

where $(\bar{\boldsymbol{\sigma}} = \bar{\boldsymbol{\sigma}}^B + \bar{\boldsymbol{\sigma}}^C, \bar{\boldsymbol{\varepsilon}} = \bar{\boldsymbol{\varepsilon}}^{\text{sym}} + \bar{\boldsymbol{\varepsilon}}^{\text{skew}})$ and $(\bar{\boldsymbol{m}}^R, \bar{\boldsymbol{\kappa}})$ are the energy-conjugated pairs. This partition of energy then provides a mean to introduce different degradation mechanisms for different kinematic modes.

5.3 Phase field model for damaged micropolar continua

This section presents a variational phase field framework to model cohesive fracture in micropolar materials. Our starting point is the energy split introduced in Section 5.2. We introduce distinct degradation for the Boltzmann, coupling and micro-rotational energy-conjugated pairs and derive, for the first time, the action functional for the variational phase field fracture framework for micropolar continua. The governing equations are then sought by seeking the stationary point, i.e., the Euler-Lagrange equation. To ensure that the size

effect exhibited in the simulations are originated from the micropolar effect, we adopt the crack surface density functional originally proposed by Wu and Nguyen [354] and Geelen et al. [209] to eliminate the sensitivity of the regularization length scale for the phase field fracture in Boltzmann continua. Our 1D analysis in Section 5.3.5 and numerical results in Section 5.5.1 suggest that this same crack surface density functional may also eliminate the sensitivity of the regularization length scale parameter for the micropolar framework.

5.3.1 Phase field approximation of cohesive fracture

This study adopts a phase field approach to represent cracks via an implicit function [75–77, 382]. Let Γ be the discontinuous surface within a micropolar elastic body $\mathcal{B}$. We approximate the fracture surface area A_Γ as A_{Γ_d}, which is the volume integration of crack surface density $\Gamma_d\left(d, \nabla d\right)$ over $\mathcal{B}$,

$$A_\Gamma \approx A_{\Gamma_d} = \int_{\mathcal{B}} \Gamma_d\left(d, \nabla d\right)\, dV, \tag{5.15}$$

where d is the phase field which varies from 0 in undamaged regions to 1 in completely damaged regions. In this study, we consider the following crack surface density functional, which is originally used to introduce elliptic regularization of the Mumford-Shah functional for image segmentation [203], i.e.,

$$\Gamma_d\left(d, \nabla d\right) = \frac{1}{c_0}\left[\frac{1}{l_c} w(d) + l_c\left(\nabla d \cdot \nabla d\right)\right] \;\; ; \;\; c_0 = 4\int_0^1 \sqrt{w(s)}\, ds, \tag{5.16}$$

where l_c is the regularization length scale that governs the size of the diffusive crack zone, $c_0 > 0$ is a normalization constant, and $w(d)$ is one of the function that controls the shape of the regularized profile of the phase field [204–206]. $\Gamma-$convergence requires that the sharp cracks can be recovered by reducing the length scale parameter l_c to zero such that

[354, 382],

$$A_{\Gamma} = \lim_{l_c \to 0} A_{\Gamma_d}. \tag{5.17}$$

The local dissipation function $w(d)$ should be a monotonically increasing function of d, and we distinguish between the following two choices for this function:

$$w(d) = \begin{cases} d^2 \\ \\ d \end{cases}. \tag{5.18}$$

The quadratic local dissipation $w(d) = d^2$ is the most widely used approach in simulating brittle fracture, and has become the standard in the phase field approximation [75–77, 87, 90, 131, 168, 242, 353, 383, 384]. The major disadvantage of the quadratic local dissipation is that the damage evolution initiates as soon as the load is applied so that there is no pure elastic response. However, the linear model $w(d) = d$, combined with suitable degradation functions, describes the cohesive fracture that possesses a threshold energy that is independent of the regularization length l_c [205, 208, 209, 385]. Also, in this case, the material is characterized by an elastic phase until the stored energy density reaches the threshold value. Since this study aims to decouple the regularization length l_c for large-scale simulations, we adopt the linear dissipation function to take advantage of the aforementioned characteristics. The expression for the crack surface energy density in Eq. (5.16) then becomes:

$$\Gamma_d \left(d, \nabla d\right) = \frac{3}{8 l_c} d + \frac{3 l_c}{8} \left(\nabla d \cdot \nabla d\right). \tag{5.19}$$

5.3.2 Free energy functional

It should be noted that the crack propagation within a body $\mathcal{B}$ corresponds to the creation of new free surfaces Γ. This implies that the rate of change of the internal energy should be equal to the rate of change of the surface energy that contributes to the crack growth. By assuming that this concept can be applied to the micropolar elastic material as well, the

total potential energy Ψ can be defined as follows [209, 333]:

$$\Psi = \int_{\mathcal{B}} \psi_e(\bar{\boldsymbol{\varepsilon}}, \bar{\boldsymbol{\kappa}})\, dV + \int_{\Gamma} \mathcal{G}_c\, d\Gamma, \tag{5.20}$$

where $\mathcal{G}_c$ is critical energy release rate that quantifies the resistance to cracking. Then, revisiting Eqs. (5.8) and (5.15), we approximate the functional by

$$\Psi \approx \int_{\mathcal{B}} \psi\, dV, \tag{5.21}$$

with

$$\psi = \underbrace{g_B(d)\psi_e^{B+}(\bar{\boldsymbol{\varepsilon}}^{\text{sym}}) + g_C(d)\psi_e^{C}(\bar{\boldsymbol{\varepsilon}}^{\text{skew}}) + g_R(d)\psi_e^{R}(\bar{\boldsymbol{\kappa}}) + \psi_e^{B-}(\bar{\boldsymbol{\varepsilon}}^{\text{sym}})}_{:=\psi_{\text{bulk}}(\bar{\boldsymbol{\varepsilon}}^{\text{sym}}, \bar{\boldsymbol{\varepsilon}}^{\text{skew}}, \bar{\boldsymbol{\kappa}}, d)} + \mathcal{G}_c \Gamma_d\left(d, \nabla d\right), \tag{5.22}$$

where $\psi_{\text{bulk}}(\bar{\boldsymbol{\varepsilon}}^{\text{sym}}, \bar{\boldsymbol{\varepsilon}}^{\text{skew}}, \bar{\boldsymbol{\kappa}}, d)$ is the degrading elastic bulk energy, and $g_i(d)$ are the stiffness degradation functions for the corresponding fictitious undamaged energy density parts ψ_e^i $(i = B, C, R)$. Here, notice that we decompose $\psi_e^B(\bar{\boldsymbol{\varepsilon}}^{\text{sym}})$ into a positive and negative parts, and degrade only the positive part in order to avoid crack propagation under compression, i.e.,

$$\psi_e^B = \psi_e^{B+} + \psi_e^{B-}. \tag{5.23}$$

In this study, we adopt the spectral decomposition scheme of Miehe, Hofacker, and Welschinger [76], so that each part can be written as:

$$\psi_e^{B\pm} = \frac{1}{2}\left[\lambda \left\langle \bar{\boldsymbol{\varepsilon}}^{\text{sym}} : \boldsymbol{I} \right\rangle_{\pm}^2 + (2\mu + \kappa)\, \bar{\boldsymbol{\varepsilon}}_{\pm}^{\text{sym}} : \bar{\boldsymbol{\varepsilon}}_{\pm}^{\text{sym}}\right] \;;\; \bar{\boldsymbol{\varepsilon}}_{\pm}^{\text{sym}} = \sum_{a=1}^{3} \left\langle \bar{\varepsilon}_a^{\text{sym}} \right\rangle_{\pm} \left(\boldsymbol{n}_a \otimes \boldsymbol{n}_a\right), \tag{5.24}$$

where $\langle \bullet \rangle_{\pm} = (\bullet \pm |\bullet|)/2$ is the Macaulay bracket operator, $\bar{\varepsilon}_a^{\text{sym}}$ is the principal Boltzmann strains, and $\boldsymbol{n}_a$ are the corresponding principal directions.

In order to investigate the effects of each energy density part, one may assume that the

partitioned strain energy densities can either be degraded ($i \in \mathfrak{D}$) or remain completely undamaged ($i \in \mathfrak{U}$), i.e.,

$$g_i(d) = \begin{cases} g(d) & \text{if } i \in \mathfrak{D} \\ 1 & \text{if } i \in \mathfrak{U} \end{cases} \; ; \; \mathfrak{D} \cup \mathfrak{U} = \{B, C, R\} \; ; \; \mathfrak{D} \cap \mathfrak{U} = \emptyset. \tag{5.25}$$

Here, $g(d)$ is a monotonically decreasing function that satisfies the following conditions [225]:

$$g(0) = 1 \; ; \; g(1) = 0 \; ; \; g'(d) \leq 0 \text{ for } d \in [0, 1], \tag{5.26}$$

where the superposed prime denotes derivative with respect to d. Explicit form of this function is provided in Section 5.3.4. Notice that this general approach can be tailored to many different situations. For example, one may only degrade the pure Boltzmann part of the strain energy, i.e., $\mathfrak{D} = \{B\}, \mathfrak{U} = \{C, R\}$:

$$\psi_{\text{bulk}}(\bar{\boldsymbol{\varepsilon}}^{\text{sym}}, \bar{\boldsymbol{\varepsilon}}^{\text{skew}}, \bar{\boldsymbol{\kappa}}, d) = g(d)\psi_e^{B+}(\bar{\boldsymbol{\varepsilon}}^{\text{sym}}) + \psi_e^{C}(\bar{\boldsymbol{\varepsilon}}^{\text{skew}}) + \psi_e^{R}(\bar{\boldsymbol{\kappa}}) + \psi_e^{B-}(\bar{\boldsymbol{\varepsilon}}^{\text{sym}}), \tag{5.27}$$

or degrade the entire strain energy density, i.e., $\mathfrak{D} = \{B, C, R\}, \mathfrak{U} = \emptyset$:

$$\psi_{\text{bulk}}(\bar{\boldsymbol{\varepsilon}}^{\text{sym}}, \bar{\boldsymbol{\varepsilon}}^{\text{skew}}, \bar{\boldsymbol{\kappa}}, d) = g(d)\left[\psi_e^{B+}(\bar{\boldsymbol{\varepsilon}}^{\text{sym}}) + \psi_e^{C}(\bar{\boldsymbol{\varepsilon}}^{\text{skew}}) + \psi_e^{R}(\bar{\boldsymbol{\kappa}})\right] + \psi_e^{B-}(\bar{\boldsymbol{\varepsilon}}^{\text{sym}}). \tag{5.28}$$

5.3.3 Derivation of Euler-Lagrange equations via variational principle

Let $\mathbb{V}$ denote an appropriate function space. Then, based on the fundamental lemma of calculus of variations, the necessary condition for the energy functional $\Psi : \mathbb{V} \to \mathbb{R}$ in Eq. (5.21) to have a local extremum at a point $\boldsymbol{\chi}_0 \in \mathbb{V}$ is that,

$$\frac{\delta \psi}{\delta \boldsymbol{\chi}}(\boldsymbol{\chi}_0) = \mathbf{0}, \tag{5.29}$$

where ψ is the energy density that is previously defined in Eq. (5.22), $\boldsymbol{\chi} := \{\boldsymbol{u}, \boldsymbol{\theta}, d\}$ indicates the field variables, and $\delta(\bullet)/\delta\boldsymbol{\chi}$ denotes the functional derivative with respect to $\boldsymbol{\chi}$. Notice that Eq. (5.29) is the so-called Euler-Lagrange equations, which yield the governing partial differential equations to be solved.

The linear momentum balance equation can be recovered by seeking the stationary point where the functional derivative of ψ with respect to $\boldsymbol{u}$ vanishes. By assuming no body forces and by only considering the single derivative, we have,

$$\frac{\delta\psi}{\delta\boldsymbol{u}} = \frac{\partial\psi}{\partial\boldsymbol{u}} - \nabla\cdot\frac{\partial\psi}{\partial\nabla\boldsymbol{u}} = \boldsymbol{0}. \tag{5.30}$$

By revisiting Eq. (5.22), we get:

$$\frac{\partial\psi}{\partial\boldsymbol{u}} = \boldsymbol{0}, \tag{5.31}$$

and by Eq. (5.12),

$$\nabla\cdot\frac{\partial\psi}{\partial\nabla\boldsymbol{u}} = \nabla\cdot\left[g_B(d)\frac{\partial\psi_e^B}{\partial\nabla\boldsymbol{u}} + g_C(d)\frac{\partial\psi_e^C}{\partial\nabla\boldsymbol{u}}\right] = \nabla\cdot\left[g_B(d)\bar{\boldsymbol{\sigma}}^B + g_C(d)\bar{\boldsymbol{\sigma}}^C\right], \tag{5.32}$$

since the decomposition of the micropolar strain in Eq. (5.3) yields the following:

$$\frac{\partial\psi_e^B}{\partial\nabla\boldsymbol{u}} = \frac{\partial\psi_e^B}{\partial\bar{\boldsymbol{\varepsilon}}^{\text{sym}}} : \frac{\partial\bar{\boldsymbol{\varepsilon}}^{\text{sym}}}{\partial\nabla\boldsymbol{u}} = \frac{\partial\psi_e^B}{\partial\bar{\boldsymbol{\varepsilon}}^{\text{sym}}} : \frac{1}{2}\left(\mathbb{I} + \bar{\mathbb{I}}\right) = \frac{\partial\psi_e^B}{\partial\bar{\boldsymbol{\varepsilon}}^{\text{sym}}} = \bar{\boldsymbol{\sigma}}^B, \tag{5.33}$$

$$\frac{\partial\psi_e^C}{\partial\nabla\boldsymbol{u}} = \frac{\partial\psi_e^C}{\partial\bar{\boldsymbol{\varepsilon}}^{\text{skew}}} : \frac{\partial\bar{\boldsymbol{\varepsilon}}^{\text{skew}}}{\partial\nabla\boldsymbol{u}} = \frac{\partial\psi_e^C}{\partial\bar{\boldsymbol{\varepsilon}}^{\text{skew}}} : \frac{1}{2}\left(\bar{\mathbb{I}} - \mathbb{I}\right) = \frac{\partial\psi_e^C}{\partial\bar{\boldsymbol{\varepsilon}}^{\text{skew}}} = \bar{\boldsymbol{\sigma}}^C. \tag{5.34}$$

Similarly, assuming no body couples, the balance of angular momentum can be obtained by searching the local extremum where the functional derivative of ψ with respect to the micro-rotation $\boldsymbol{\theta}$ vanishes, i.e.,

$$\frac{\delta\psi}{\delta\boldsymbol{\theta}} = \frac{\partial\psi}{\partial\boldsymbol{\theta}} - \nabla\cdot\frac{\partial\psi}{\partial\nabla\boldsymbol{\theta}} = \boldsymbol{0}. \tag{5.35}$$

The partial derivative of ψ with respect to $\boldsymbol{\theta}$ is:

$$\frac{\partial \psi}{\partial \boldsymbol{\theta}} = g_C(d)\frac{\partial \psi_e^C}{\partial \boldsymbol{\theta}} = g_C(d)\frac{\partial \psi_e^C}{\partial \bar{\boldsymbol{\varepsilon}}^{\text{skew}}} : \frac{\partial \bar{\boldsymbol{\varepsilon}}^{\text{skew}}}{\partial \boldsymbol{\theta}} = -\overset{3}{\boldsymbol{E}} : \left[g_C(d)\bar{\boldsymbol{\sigma}}^C\right]. \tag{5.36}$$

By Eq. (5.13), the partial derivative of ψ with respect to $\nabla\boldsymbol{\theta}$ becomes:

$$\nabla\cdot\frac{\partial \psi}{\partial \nabla\boldsymbol{\theta}} = \nabla\cdot\left[g_R(d)\frac{\partial \psi_e^R}{\partial \bar{\boldsymbol{\kappa}}}\right] = \nabla\cdot\left[g_R(d)\bar{\boldsymbol{m}}^R\right]. \tag{5.37}$$

The damage evolution equation (i.e., functional derivative of ψ with respect to the phase field d) can also be recovered as follows:

$$\frac{\delta \psi}{\delta d} = \frac{\partial \psi}{\partial d} - \nabla\cdot\frac{\partial \psi}{\partial \nabla d} = 0, \tag{5.38}$$

where, by revisiting Eq. (5.19),

$$\frac{\partial \psi}{\partial d} = g'(d)\left[\sum_{i\in\mathfrak{D}}\psi_e^i\right] + \frac{3\mathcal{G}_c}{8l_c}, \tag{5.39}$$

and

$$\nabla\cdot\frac{\partial \psi}{\partial \nabla d} = \nabla\cdot\left(\frac{3\mathcal{G}_c l_c}{4}\nabla d\right). \tag{5.40}$$

Finally, collecting the terms from Eqs. (5.30)-(5.40), we obtain the following coupled system of partial differential equations to be solved:

$$\nabla\cdot\left[g_B(d)\bar{\boldsymbol{\sigma}}^B + g_C(d)\bar{\boldsymbol{\sigma}}^C\right] = \mathbf{0} \qquad \text{balance of linear momentum,} \tag{5.41}$$

$$\nabla\cdot\left[g_R(d)\bar{\boldsymbol{m}}^R\right] + \overset{3}{\boldsymbol{E}} : \left[g_C(d)\bar{\boldsymbol{\sigma}}^C\right] = \mathbf{0} \quad \text{balance of angular momentum,} \tag{5.42}$$

$$g'(d)\mathcal{F} + \frac{3}{8}\left(1 - 2l_c^2\nabla^2 d\right) = 0 \qquad \text{nondimensionalized damage evolution equation,} \tag{5.43}$$

where $\nabla^2(\bullet) = \nabla\cdot\nabla(\bullet)$ is the Laplacian operator, and $\mathcal{F}$ is the degrading nondimension-

alized strain energy density:

$$\mathcal{F} = \frac{\sum_{i \in \mathfrak{D}} \psi_e^i}{\mathcal{G}_c / l_c}. \tag{5.44}$$

5.3.4 Crack irreversibility and degradation function

As far as $\mathfrak{D} \neq \emptyset$, we prevent crack healing by following the treatment used in [90, 129, 168] which ensures the irreversibility constraint by enforcing the driving force to be non-negative. Although the stored energy density is split into three different parts, we simply introduce one distinct history function or driving force $\mathcal{H}$ which is the pseudo-temporal maximum of the degrading nondimensionalized energy density. Inserting our definition into Eq. (5.43) gives:

$$g'(d)\mathcal{H} + \frac{3}{8}\left(1 - 2l_c^2 \nabla^2 d\right) = 0. \tag{5.45}$$

Revisiting Section 5.3.1, the term cohesive denotes that the model should possess a threshold for the loading, where damage does not develop below this value. Therefore, we particularly restrict the crack growth to initiate above a threshold energy density ψ_{crit} by using the following history function, in order to approximate the cohesive response:

$$\mathcal{H} = \max_{\tau \in [0,t]} \left\{ \mathcal{F}_{\text{crit}} + \mathcal{F}_{\text{crit}} \left\langle \frac{\mathcal{F}}{\mathcal{F}_{\text{crit}}} - 1 \right\rangle_+ \right\} \;\; ; \;\; \mathcal{F}_{\text{crit}} = \frac{\psi_{\text{crit}}}{\mathcal{G}_c / l_c}, \tag{5.46}$$

where $\mathcal{F}_{\text{crit}}$ is the nondimensionalized threshold energy. Note that Eq. (5.45) is the field equation that is actually solved for the phase field in this study.

We complete our formulation by specifying the degradation function $g(d)$. This study adopts a quasi-quadratic degradation function [209, 385, 386], which is a rational function of the phase field d. The quasi-quadratic degradation function has an associated upper bound on the regularization length l_c, and is defined as:

$$g(d) = \frac{(1-d)^2}{(1-d)^2 + md\,(1+pd)} \;\; ; \;\; l_c \leq \frac{3\mathcal{G}_c}{8\,(p+2)\,\psi_{\text{crit}}}, \tag{5.47}$$

where $m \geq 1$ is constant, and $p \geq 1$ is a shape parameter that controls the peak stress and the fracture responses.

Recall that this study restricts the damage evolution to initiate above a threshold energy. In other words, below the threshold (i.e., $\mathcal{F}/\mathcal{F}_{\text{crit}} \leq 1$), the driving force and the phase field should satisfy $\mathcal{H} = \mathcal{F}_{\text{crit}}$ and $d = 0$, respectively. In this case, the damage evolution equation [Eq. (5.45)] becomes:

$$g'(0)\mathcal{F}_{\text{crit}} + \frac{3}{8} = 0. \tag{5.48}$$

Since the degradation function [Eq. (5.47)] yields $g'(0) = -m$, we require

$$m = \frac{3}{8\mathcal{F}_{\text{crit}}}, \tag{5.49}$$

in order to trivially satisfy Eq. (5.48). Again, the most common choice for the degradation function would be a simple quadratic function, i.e., $g(d) = (1-d)^2$. A phase field model that adopts the quadratic degradation function requires a particular critical energy ψ_{crit} that depends on l_c to satisfy Eq. (5.48). However, by using the quasi-quadratic degradation function in Eq. (5.47) with Eq. (5.49), it is noted that the threshold energy density ψ_{crit} is no longer dependent on l_c, since the degradation function itself is designed to automatically satisfy Eq. (5.48). It reveals that the elastic response (i.e., if stored energy is below the threshold) is regularization length independent. The regularization length insensitivity of the model, for the case where the stored energy exceeds the threshold, will be discussed in Section 5.3.5.

5.3.5 One-dimensional analysis on phase field regularization length sensitivity

In order to gain insights on the regularization length insensitive response, we consider a similiar 1D boundary value problem previously used in Wu and Nguyen [354] and Geelen et al. [209] for length scale analysis. Our major departure is that the material is now an analog to the micropolar material where an length scale dependent state variable (which replaces the micro-rotation due to the low-dimensional kinematics) is introduced to replicate the size effect of the elasticity response. Consider a one-dimensional bar $x \in [-L, L]$ subjected to a tensile loading on both ends. We assume that the length $2L$ is sufficiently long enough so that the any possible boundary effects can be neglected. We define the strain measures as $\bar{\varepsilon} = \mathrm{d}u/\mathrm{d}x$, and $\bar{\kappa} = l_e(\mathrm{d}\theta/\mathrm{d}x)$, where l_e is the length scale. Our goal here is to check whether the size-dependent responses in the damaged zone is sensitive to the regularization length scale for the phase field l_c. Note that this formulation does yield size-dependent responses in both elastic and damage zones, but the kinematics in 1D does not permit rotation. Hence, θ and $\bar{\kappa}$ no longer indicate micro-rotation and micro-curvature respectively. Thus, analogous to Eq. (5.8), we introduce a 1D size-dependent model of which the strain energy density takes a quadratic form as:

$$\psi_e = \frac{1}{2}C_B\left(\frac{\mathrm{d}u}{\mathrm{d}x}\right)^2 + \frac{1}{2}C_C\left(\frac{\mathrm{d}u}{\mathrm{d}x} - l_e\frac{\mathrm{d}\theta}{\mathrm{d}x}\right)^2 + \frac{1}{2}C_R l_e^2\left(\frac{\mathrm{d}\theta}{\mathrm{d}x}\right)^2, \tag{5.50}$$

where $C_B > 0$, $C_C > 0$ and $C_R > 0$ are the material parameters. Notice that (1) this stored energy functional does not admit non-trivial zero-energy mode provided that $C_B + C_C > 0$ and $C_R > 0$ and (2) if the length scale l_e vanishes, Eq. (5.50) reduces to an energy functional for the classical Boltzmann continuum. In this setting, the stress measures can be obtained as,

$$\bar{\sigma} = \frac{\partial \psi_e}{\partial \bar{\varepsilon}} = C_B\bar{\varepsilon} + C_C\left(\bar{\varepsilon} - \bar{\kappa}\right), \tag{5.51}$$

$$\bar{m} = \frac{\partial \psi_e}{\partial \bar{\kappa}} = C_R \bar{\kappa} - C_C \left(\bar{\varepsilon} - \bar{\kappa} \right), \tag{5.52}$$

where both $\bar{\sigma}$ and $\bar{m}$ are l_e-dependent. Assuming all energy density parts can be degraded, the Lagrangian for the damaged state where $\psi_e > \psi_{\text{crit}}$ then becomes:

$$\psi = g(d)\psi_e + \frac{3\mathcal{G}_c}{8 l_c} \left[d + l_c^2 \left(\frac{\mathrm{d}d}{\mathrm{d}x} \right)^2 \right], \tag{5.53}$$

where $g(d)$ is previously defined in Eq. (5.47). The first variation of Eq. (5.53) yields the following set of Euler-Lagrange equations:

$$\frac{\mathrm{d}}{\mathrm{d}x} \left[g(d)\bar{\sigma} \right] = 0, \tag{5.54}$$

$$\frac{\mathrm{d}}{\mathrm{d}x} \left[g(d)\bar{m} \right] = 0, \tag{5.55}$$

$$g'(d) \frac{\psi_e}{\mathcal{G}_c / l_c} + \frac{3}{8} \left(1 - 2 l_c^2 \frac{\mathrm{d}^2 d}{\mathrm{d}x^2} \right) = 0, \tag{5.56}$$

where Eqs. (5.54) and (5.55) are the balance equations, and Eq. (5.56) is the nondimensionalized damage evolution equation. Following Geelen et al. [209], we apply a specific amount of $\bar{\sigma}$ at both ends while the boundaries remain $\bar{m}$-free, such that Eq. (5.54) and Eq. (5.55) yields:

$$g(d)\bar{\sigma} = \bar{\sigma}_0 \;\; ; \;\; g(d)\bar{m} = 0, \tag{5.57}$$

where $\bar{\sigma}_0$ is the responding stress on the boundary ($x = \pm L$). By the constitutive relationships in Eqs. (5.51)- (5.52), we can now express the strain measures $\bar{\varepsilon}$ and $\bar{\kappa}$ as,

$$\bar{\varepsilon} = \frac{C_C - C_R}{C_B(C_C - C_R) - C_C C_R} \frac{\bar{\sigma}_0}{g(d)} \;\; ; \;\; \bar{\kappa} = \frac{C_C}{C_B(C_C - C_R) - C_C C_R} \frac{\bar{\sigma}_0}{g(d)}. \tag{5.58}$$

Thus, the energy density functional in Eq. (5.50) can be rewritten as:

$$\psi_e = \frac{\bar{\sigma}_0^2}{C^* g(d)^2} \;\; ; \;\; C^* = \frac{2 \left[C_B(C_C - C_R) - C_C C_R \right]^2}{C_B(C_C - C_R)^2 + C_C C_R (C_C + C_R)}. \tag{5.59}$$

Substituting Eq. (5.57) and Eq. (5.59) into Eq. (5.56), we get,

$$g'(d)\left[\frac{1}{\mathcal{G}_c/l_c}\frac{\bar{\sigma}_0^2}{C^* g(d)^2}\right] + \frac{3}{8}\left(1 - 2l_c^2\frac{\mathrm{d}^2 d}{\mathrm{d}x^2}\right) = 0. \tag{5.60}$$

By multiplying Eq. (5.60) with $\mathrm{d}d/\mathrm{d}x$, we can obtain the following differential equation:

$$\frac{\mathrm{d}}{\mathrm{d}x}\left\{\frac{3}{8}\left[d - l_c^2\left(\frac{\mathrm{d}d}{\mathrm{d}x}\right)^2\right] - \frac{1}{\mathcal{G}_c/l_c}\frac{\bar{\sigma}_0^2}{2C^* g(d)}\right\} = 0. \tag{5.61}$$

Following Wu and Nguyen [354] and Geelen et al. [209], we focus on the damaged zone $[-l_z, l_z]$ with $l_z \ll L$, where the outer edge of the zone is related to the parameter d^*, the maximum value of the damage across the bar (i.e., $d^* = 1$ if the bar is fully broken). Then, by symmetry, at $x = 0$ we have:

$$d(d^*, 0) = d^* \;\; ; \;\; \frac{\mathrm{d}d}{\mathrm{d}x}(d^*, 0) = 0, \tag{5.62}$$

while the boundary conditions at the outer edge $x = l_z$ are given by,

$$d(d^*, l_z) = 0 \;\; ; \;\; \frac{\mathrm{d}d}{\mathrm{d}x}(d^*, l_z) = 0. \tag{5.63}$$

By introducing the parameter d^*, notice that our goal is to find the expression for the responding stress $\bar{\sigma}_0$ as a function of the maximum damage d^*, or vice versa. Integration of Eq. (5.61), using boundary conditions in Eq. (5.63) admits the following:

$$\frac{3}{8}\left[d - l_c^2\left(\frac{\mathrm{d}d}{\mathrm{d}x}\right)^2\right] = \frac{1}{\mathcal{G}_c/l_c}\frac{\bar{\sigma}_0^2}{2C^*}\left(g(d)^{-1} - 1\right). \tag{5.64}$$

Applying the symmetry conditions [Eq. (5.62)], Eq. (5.64) becomes:

$$\frac{\bar{\sigma}_0^2}{2C^*} = \frac{3\mathcal{G}_c}{8l_c}\frac{d^*}{g(d^*)^{-1} - 1}. \tag{5.65}$$

Substituting the expression of the degradation function in Eq. (5.47) and the expression for the degradation parameter m in Eq. (5.49), we finally get:

$$\bar{\sigma}_0 = \sqrt{2C^*\psi_{\text{crit}}\frac{(1-d^*)^2}{1+pd^*}}. \tag{5.66}$$

Observe that the resultant stress $\bar{\sigma}_0$ can be expressed in terms of d^* but independent of the phase field regularization length l_c. Eq. (5.66) highlights that the proposed model is capable of replicating the global response insensitive to regularization length l_c for the phase field, while preserving the size effect introduced by the micropolar elasticity. This result is important, as this insensitivity to l_c enables us to simulate cohesive fracture in large spatial domain composed of micropolar materials. Extending this analysis for 2D and 3D cases is out of the scope of this study but will be considered in the future.

Remark 5. Previous works on phase field and gradient damage models for cohesive fracture in Cauchy continuum, such as Lorentz, Cuvilliez, and Kazymyrenko [385], Cazes et al. [387], and Wu [388], have established a connection between the cohesive zone models and the phase field and gradient damage models that represent cracks via implicit function. In principle, it is possible that similar connection can be established between the micropolar phase field model presented in this paper and the established micropolar cohesive zone models such as Larsson and Zhang [389], Zhang et al. [390], and Hirschberger, Sukumar, and Steinmann [391]. Such an endeavor is obviously out of the scope of this study due to the extensive length, but will be considered in future studies.

5.4 Finite element implementation

In this section, we describe the finite element discretization, followed by the solution strategy to solve the system of nonlinear equation incrementally. Starting from the strong form, we follow the standard procedure to recover the variational form while employing

the Taylor-Hood finite element space for the displacement and micro-rotation fields, and standard linear interpolation for the phase field. This finite element space is chosen to match the design of the operator-split algorithm. The displacement and micro-rotation are updated in a monolithic manner, where we use Taylor-Hood element such that the displacement field is interpolated by quadratic polynomials and the micro-rotation is interpolated by linear polynomials. Meanwhile, the phase field is also interpolated by linear function to ensure the efficiency of the staggered solver that updates the phase field while holding the displacement and micro-rotation fixed. The operator-split solution scheme (i.e., staggered scheme) that successively updates the field variables is described in Section 5.4.2.

5.4.1 Galerkin form

We derive the weak form and introduce the finite dimensional space to introduce the numerical scheme for the boundary value problems described in Eqs. (5.41)-(5.42) and Eq. (5.45). We consider a micropolar elastic domain $\mathcal{B}$ with boundary $\partial\mathcal{B}$ composed of Dirichlet boundaries (displacement $\partial\mathcal{B}_u$ and micro-rotation $\partial\mathcal{B}_\theta$) and Neumann boundaries (traction $\partial\mathcal{B}_{t_\sigma}$ and moment $\partial\mathcal{B}_{t_m}$) satisfying,

$$\partial\mathcal{B} = \overline{\partial\mathcal{B}_u \cup \partial\mathcal{B}_{t_\sigma}} = \overline{\partial\mathcal{B}_\theta \cup \partial\mathcal{B}_{t_m}} \;\; ; \;\; \emptyset = \partial\mathcal{B}_u \cap \partial\mathcal{B}_{t_\sigma} = \partial\mathcal{B}_\theta \cap \partial\mathcal{B}_{t_m}. \tag{5.67}$$

The prescribed boundary conditions can be specified as:

$$\begin{cases} \boldsymbol{u} = \hat{\boldsymbol{u}} & \text{on } \partial\mathcal{B}_u, \\ \boldsymbol{\theta} = \hat{\boldsymbol{\theta}} & \text{on } \partial\mathcal{B}_\theta, \\ \left[g_B(d)\bar{\boldsymbol{\sigma}}^B + g_C(d)\bar{\boldsymbol{\sigma}}^C\right]^{\mathrm{T}} \cdot \boldsymbol{n} = \hat{\boldsymbol{t}}_\sigma & \text{on } \partial\mathcal{B}_{t_\sigma}, \\ \left[g_R(d)\bar{\boldsymbol{m}}^R\right]^{\mathrm{T}} \cdot \boldsymbol{n} = \hat{\boldsymbol{t}}_m & \text{on } \partial\mathcal{B}_{t_m}, \\ \nabla d \cdot \boldsymbol{n} = 0 & \text{on } \partial\mathcal{B}, \end{cases} \tag{5.68}$$

where $\boldsymbol{n}$ is the outward-oriented unit normal on the boundary surface $\partial\mathcal{B}$; $\hat{\boldsymbol{u}}, \hat{\boldsymbol{\theta}}, \hat{\boldsymbol{t}}_\sigma, \hat{\boldsymbol{t}}_m$ are the prescribed displacement, micro-rotation, traction and moment, respectively; and the degradation functions $g_i(d)$ ($i = B, C, R$) are previously defined in Eq. (5.25). For the model closure, the initial conditions are imposed as,

$$\boldsymbol{u} = \boldsymbol{u}_0 \ ; \ \ \boldsymbol{\theta} = \boldsymbol{\theta}_0, \tag{5.69}$$

at $t = 0$.

We define the trial spaces V_u, V_θ, and V_d for the solution variables:

$$V_u = \left\{ \boldsymbol{u} : \mathcal{B} \to \mathbb{R}^3 \mid \boldsymbol{u} \in [H^1(\mathcal{B})]^3, \ \boldsymbol{u}|_{\partial\mathcal{B}_u} = \hat{\boldsymbol{u}} \right\}, \tag{5.70}$$

$$V_\theta = \left\{ \boldsymbol{\theta} : \mathcal{B} \to \mathbb{R}^3 \mid \boldsymbol{\theta} \in [H^1(\mathcal{B})]^3, \ \boldsymbol{\theta}|_{\partial\mathcal{B}_\theta} = \hat{\boldsymbol{\theta}} \right\}, \tag{5.71}$$

$$V_d = \left\{ d : \mathcal{B} \to \mathbb{R} \mid d \in H^1(\mathcal{B}) \right\}, \tag{5.72}$$

where H^1 denotes the Sobolev space of order 1. Notice that this study adopts Taylor-Hood finite element (i.e., quadratic interpolation for displacement and linear for micro-rotation) following Verhoosel and Borst [392], which showed that the cohesive fracture model exhibits stress oscillation when equal order polynomials are used for the solution field, while the discretization with high order interpolation function for the displacement and first order functions for the auxiliary field and the phase field seems to eliminate this oscillation. Similarly, the corresponding admissible spaces for Eqs. (5.70)-(5.72) with homogeneous boundary conditions are defined as,

$$V_\eta = \left\{ \boldsymbol{\eta} : \mathcal{B} \to \mathbb{R}^3 \mid \boldsymbol{\eta} \in [H^1(\mathcal{B})]^3, \ \boldsymbol{\eta}|_{\partial\mathcal{B}_u} = \boldsymbol{0} \right\}, \tag{5.73}$$

$$V_\xi = \left\{ \boldsymbol{\xi} : \mathcal{B} \to \mathbb{R}^3 \mid \boldsymbol{\xi} \in [H^1(\mathcal{B})]^3, \ \boldsymbol{\xi}|_{\partial\mathcal{B}_\theta} = \boldsymbol{0} \right\}, \tag{5.74}$$

$$V_\zeta = \left\{ \zeta : \mathcal{B} \to \mathbb{R} \mid \zeta \in H^1(\mathcal{B}) \right\}. \tag{5.75}$$

Applying the standard weighted residual procedure, the weak statements for Eqs. (5.41)-

(5.42) and Eq. (5.45) is to: find $\{\boldsymbol{u}, \boldsymbol{\theta}, d\} \in V_u \times V_\theta \times V_d$ such that for all $\{\boldsymbol{\eta}, \boldsymbol{\xi}, \zeta\} \in V_\eta \times V_\xi \times V_\zeta$,

$$G_u(\boldsymbol{u}, \boldsymbol{\theta}, d, \boldsymbol{\eta}) = G_\theta(\boldsymbol{u}, \boldsymbol{\theta}, d, \boldsymbol{\xi}) = G_d(\boldsymbol{u}, \boldsymbol{\theta}, d, \zeta) = 0. \tag{5.76}$$

Here, $G_u \to \mathbb{R}$ is the weak statement of the balance of linear momentum:

$$G_u = \int_{\mathcal{B}} \nabla \boldsymbol{\eta} : \left[g_B(d) \bar{\boldsymbol{\sigma}}^B + g_C(d) \bar{\boldsymbol{\sigma}}^C \right] \, dV - \int_{\partial \mathcal{B}_{t_\sigma}} \boldsymbol{\eta} \cdot \hat{\boldsymbol{t}}_\sigma \, dA = 0, \tag{5.77}$$

$G_\theta \to \mathbb{R}$ is the weak statement of the balance of angular momentum:

$$G_\theta = \int_{\mathcal{B}} \nabla \boldsymbol{\xi} : g_R(d) \bar{\boldsymbol{m}}^R \, dV - \int_{\mathcal{B}} \boldsymbol{\xi} \cdot \overset{3}{\boldsymbol{E}} : \left[g_C(d) \bar{\boldsymbol{\sigma}}^C \right] \, dV - \int_{\partial \mathcal{B}_{t_m}} \boldsymbol{\xi} \cdot \hat{\boldsymbol{t}}_m \, dA = 0, \tag{5.78}$$

and $G_d \to \mathbb{R}$ is the weak statement of the damage evolution equation:

$$G_d = \int_{\mathcal{B}} \zeta \cdot g'(d) \mathcal{H} \, dV + \frac{3}{8} \left[\int_{\mathcal{B}} \zeta + 2 l_c^2 \left(\nabla \zeta \cdot \nabla d \right) \, dV \right] = 0, \tag{5.79}$$

where $\mathcal{H}$ and $g(d)$ are previously defined in Eqs. (5.46) and (5.47), respectively.

5.4.2 Operator-split solution scheme

As previous studies on the phase field model showed that the operator splitting (i.e., staggered scheme) may potentially be more robust compared to the monolithic approach [76, 260, 261], this study adopts the solution procedure based on the operator-split scheme to successively update three field variables $\{\boldsymbol{u}, \boldsymbol{\theta}, d\}$. In this operator-split setting, the damage field is updated first while the displacement and micro-rotation fields are held fixed. A new damage field $d_{\text{n+1}}$ is obtained iteratively once the algorithm converges within a predefined tolerance. Then, the linear solver holds the damage field fixed and advances the displacement and the micro-rotation fields $\{\boldsymbol{u}_{\text{n+1}}, \boldsymbol{\theta}_{\text{n+1}}\}$. The schematic of the solution strategy can

be summarized as follows:

$$\begin{bmatrix} \boldsymbol{u}_{\mathrm{n}} \\ \boldsymbol{\theta}_{\mathrm{n}} \\ d_{\mathrm{n}} \end{bmatrix} \underbrace{\xrightarrow{\mathcal{R}(d)=0} \begin{bmatrix} \boldsymbol{u}_{\mathrm{n}} \\ \boldsymbol{\theta}_{\mathrm{n}} \\ d_{\mathrm{n+1}} \end{bmatrix}}_{\text{Iterative solver}} \overbrace{\xrightarrow{\mathcal{R}(\boldsymbol{u},\boldsymbol{\theta})=\boldsymbol{0}} \begin{bmatrix} \boldsymbol{u}_{\mathrm{n+1}} \\ \boldsymbol{\theta}_{\mathrm{n+1}} \\ d_{\mathrm{n+1}} \end{bmatrix}}^{\text{Linear solver}}, \tag{5.80}$$

where $\mathcal{R}(\boldsymbol{u},\boldsymbol{\theta})$ and $\mathcal{R}(d)$ are the residuals that are consistent with Eqs. (5.77)-(5.79):

$$\mathcal{R}(\boldsymbol{u},\boldsymbol{\theta}) : \begin{cases} \displaystyle\int_{\mathcal{B}} \nabla\boldsymbol{\eta} : \left[g_B(d_{\mathrm{n+1}})\bar{\boldsymbol{\sigma}}^B_{\mathrm{n+1}} + g_C(d_{\mathrm{n+1}})\bar{\boldsymbol{\sigma}}^C_{\mathrm{n+1}}\right]\, dV - \int_{\partial\mathcal{B}_{t_\sigma}} \boldsymbol{\eta}\cdot\hat{\boldsymbol{t}}_\sigma\big|_{\mathrm{n+1}}\, dA, \\ \displaystyle\int_{\mathcal{B}} \nabla\boldsymbol{\xi} : g_R(d_{\mathrm{n+1}})\bar{\boldsymbol{m}}^R_{\mathrm{n+1}}\, dV - \int_{\mathcal{B}} \boldsymbol{\xi}\cdot\overset{3}{\boldsymbol{E}} : \left[g_C(d_{\mathrm{n+1}})\bar{\boldsymbol{\sigma}}^C_{\mathrm{n+1}}\right]\, dV - \int_{\partial\mathcal{B}_{t_m}} \boldsymbol{\xi}\cdot\hat{\boldsymbol{t}}_m\big|_{\mathrm{n+1}}\, dA \end{cases} \tag{5.81}$$

$$\mathcal{R}(d) : \left\{ \int_{\mathcal{B}} \zeta\cdot g'(d_{\mathrm{n+1}})\mathcal{H}_{\mathrm{n}}\, dV + \frac{3}{8}\left[\int_{\mathcal{B}} \zeta + 2l_c^2\left(\nabla\zeta\cdot\nabla d_{\mathrm{n+1}}\right)\, dV\right]\right. . \tag{5.82}$$

It should be noticed that one may choose other strategies to solve the same system of equations, however, the exploration of different schemes are out of the scope of this study.

The implementation of the numerical models including the finite element discretization and the operator-split solution scheme rely on the finite element package `FEniCS` [146–148, 340] with `PETSc` scientific computation toolkit [149]. The scripts developed for this study are open-sourced (available at `https://github.com/hyoungsuksuh/micropolar_phasefield`), in order to aid third-party verification and validation [132].

5.5 Numerical examples

This section presents numerical examples to showcase the applicability of the proposed phase field model for damaged micropolar elastic material. For simplicity, we limit our attention to two-dimensional simulations in this section. Based on the 2D setting, the kine-

matic state of the micropolar elastic body can be described by two in-plane displacements $\boldsymbol{u} = [u_1, u_2]^{\mathrm{T}}$ and one out-of-plane micro-rotation angle θ_3. Since the material elasticity now only depends on bending characteristic length, we now require only four engineering material parameters (e.g., E, ν, N, and l_b).

The first example serves as a verification test that highlights the regularization length insensitive response of the phase field model with quasi-quadratic degradation function in Eq. (5.47). We then investigate the effect of scale-dependent elasticity on the crack patterns, by simulating asymmetric notched three-point bending tests with different coupling numbers N and single edge notched tests with different characteristic lengths l_b, respectively. Finally, we exhibit the applicability of the proposed energy split scheme by considering different degradation functions on the partitioned energy densities. All the numerical simulations rely on meshes that are sufficiently refined to properly capture the damage field around crack surfaces. Unless specified, we especially adopt the element size of $h^e \approx l_c/10$ around the potential crack propagation trajectory.

5.5.1 Verification exercise: the trapezoid problem

We first examine a problem proposed by Lorentz, Cuvilliez, and Kazymyrenko [385] that has a trapezoidal-shaped symmetrical domain with an initial notch. Since we prescribe the displacement $\bar{\boldsymbol{u}}$ in order to consider pure Mode I loading, as illustrated in Fig. 5.2, this specific geometry helps us to avoid crack kinking and to facilitate straight crack propagation. The aforementioned characteristics of the trapezoid problem makes it suitable for verifying the regularization length insensitive response of the cohesive phase field model with quasi-quadratic degradation. This example thus performs a parametric study for three different regularization lengths ($l_c = 7.5$, 15, and 30 mm, as depicted in Fig. 5.2), with two different shape parameters $p = 2.5$ and 10.

The material is assumed to be similar to the concrete studied in Lorentz, Cuvilliez, and Kazymyrenko [385]. The material parameters for this example are chosen as follows:

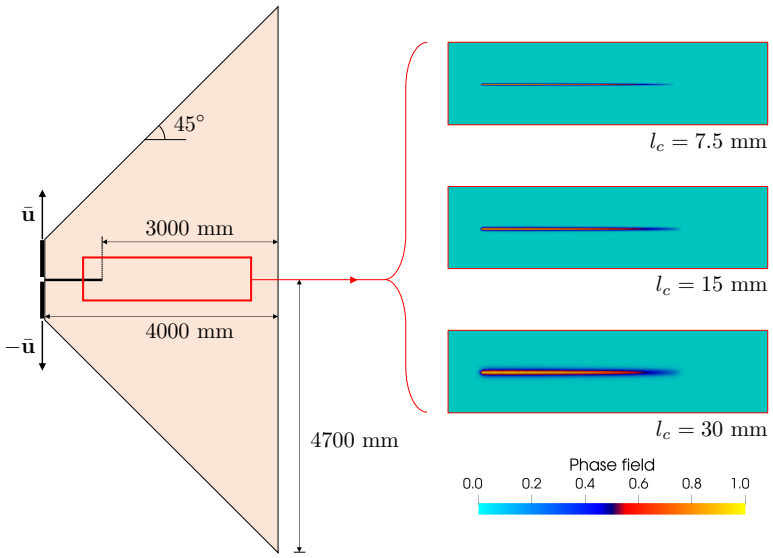

Figure 5.2: Schematic of geometry and boundary conditions for a trapezoidal domain and the observed crack patterns at $\bar{u} = 0.325$ mm with different regularization lengths.

Young's modulus $E = 30$ GPa, Poisson's ratio $\nu = 0.2$, critical energy release rate $\mathcal{G}_c = 0.1$ N/mm, and threshold energy density $\psi_{\text{crit}} = 0.1$ kJ/m^3. We also set coupling number $N = 0$ and bending characteristic length $l_b = 0$ mm in order to avoid all the micropolar effects, and at the same time damage only the pure Boltzmann part, i.e., $\mathfrak{D} = \{B\}$, $\mathfrak{U} = \{C, R\}$. We prescribe $\Delta\bar{u}_2 = 0.5 \times 10^{-3}$ mm on the left boundaries, while all other boundaries are maintained traction-free during the simulations.

Fig. 5.3 shows the force–displacement curves for the trapezoid problem, corroborated by other numerical observations [209, 385]. The results indicate that the shape parameter p is able to influence the peak force and the overall global force-displacement responses. In fact, the quasi-quadratic degradation function enables us to not only tailor the threshold for the elastic region by controlling ψ_{crit}, but also tune the peak stress by varying shape parameter p. As pointed out in Geelen et al. [209], higher value of p tend to significantly elongate the length of the fracture process zone, such that the stresses in the process zone can effectively be smeared over a large distance. As a result, we can observe that an increasing value of p yields the global force-displacement response where the effect of using

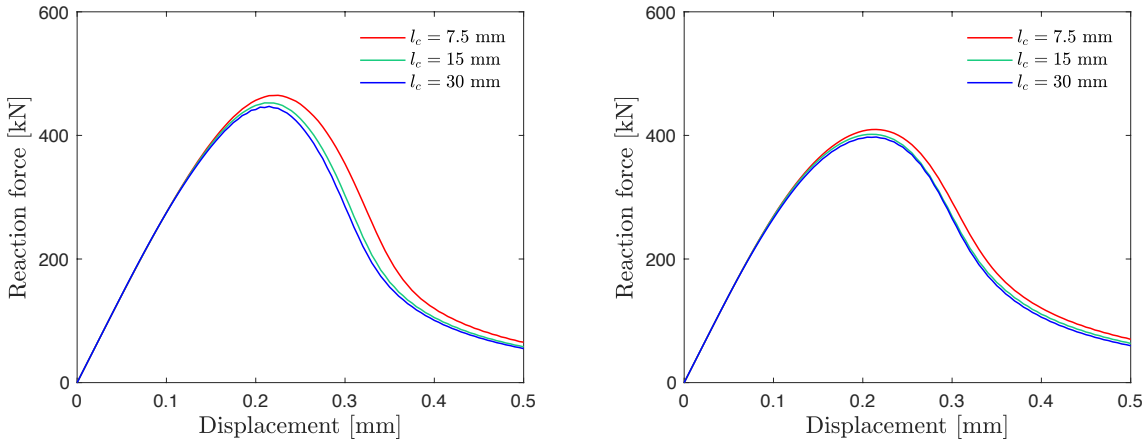

Figure 5.3: The force-displacement curves obtained from the trapezoid problem with different regularization lengths: non-polar case: (a) $p = 2.5$ and (b) $p = 10.0$.

different length scale parameters l_c becomes negligible, as previously reported in Geelen et al. [209], Wu and Nguyen [354], Wu, Mandal, and Nguyen [366], and Lorentz, Cuvilliez, and Kazymyrenko [385].

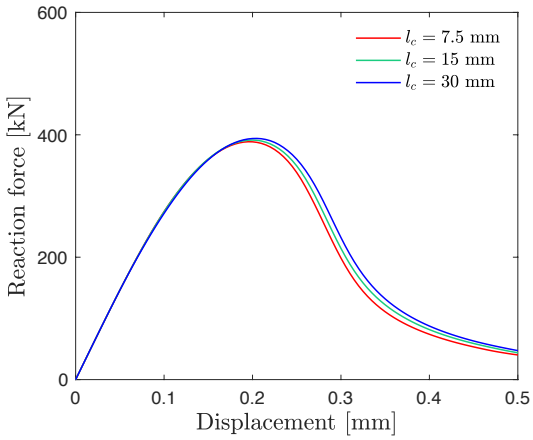

Figure 5.4: The force-displacement curve obtained from the trapezoid problem with different regularization lengths: micropolar case, $p = 10$, $l_b = 50$ mm, and $N = 0.5$.

We then repeat the same problem with the micropolar material, i.e., the case where $\mathfrak{D} = \{B, C, R\}$, $\mathfrak{U} = \emptyset$. Recall Section 5.3.5 that the regularization length insensitive response is expected for the micropolar material as well. For this problem, we set coupling number $N = 0.5$, and bending characteristic length $l_b = 50$ mm, while we choose the

shape parameter as $p = 10$ which produced regularization length insensitive results in Fig. 5.3(b). As illustrated in Fig. 5.4, the force-displacement curve confirms that our choice $p = 10$ yields the regularization length insensitive global response for micropolar material as well. From this numerical example, we again spotlight the fact that the high value of the shape parameter p yields the regularization length insensitive response in both non-polar and micropolar material.

5.5.2 Single edge notched tests

We now consider the classical boundary value problem, which serves as a platform to investigate the size effect of elasticity and energy dissipation on the crack nucleation and propagation. The problem domain is a square plate that has an initial horizontal edge crack placed at the middle from the left to the center (Fig. 5.5). Similar to the previous studies [76, 77], we choose material parameters as: $E = 210$ GPa, $\nu = 0.3$, $\mathcal{G}_c = 2.7$ N/mm, $l_c = 0.008$ mm, and $\psi_{\text{crit}} = 10$ MJ/m^3. Numerical experiments are conducted with different bending characteristic lengths: $l_b = 0.0$, 0.01, 0.05, and 0.25 mm while the coupling number is held fixed as $N = 0.5$. Also, for this problem we damage all the energy density parts, i.e., $\mathfrak{D} = \{B, C, R\}$, $\mathfrak{U} = \emptyset$. As illustrated in Fig. 5.5, two different types of simulations are conducted with the same specimen: the pure tensile test with prescribed vertical displacement $\Delta\bar{u}_2 = 2.0 \times 10^{-5}$ mm; and the pure shear test with prescribed horizontal displacement $\Delta\bar{u}_1 = 2.0 \times 10^{-5}$ mm. In both cases, the displacements are prescribed along the entire top boundary, while the bottom part of the domain is fixed.

Fig. 5.6 illustrates the crack trajectories at the completely damaged stages for both tension and shear tests with different the bending characteristic lengths. The results clearly show that pure tensile loading exhibits the same crack pattern regardless of l_b. This result is expected, as introducing the micro-polar effect should not break the symmetry of the boundary value problems in pure Mode I loading. Interestingly, the higher-order constitutive responses have a profound impact on the crack propagation direction in the Mode II

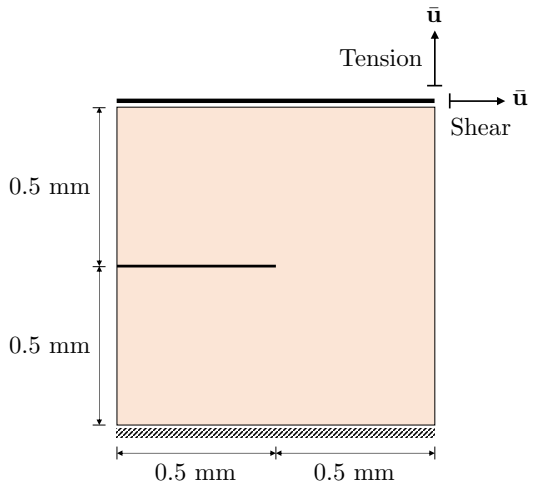

Figure 5.5: Schematic of geometry and boundary conditions for the single edge notched tests.

simulations. As shown in Fig. 5.6, the micropolar effect leads to a propagation direction bends counterclockwise. As the driving force for the phase field is affected by the micro-rotation induced by the coupling between shear and micro-rotation, this affect the energy dissipation mechanism and ultimately the energy minimizer of the action functional that provides the deformed configuration and crack patterns.

As pointed out in Yavari, Sarkani, and Moyer [375], the particles near crack tip resist micro-rotation and separation (i.e., interlocking), and the crack propagation mechanism in micropolar continuum therefore consists of the following steps. First, micro-rotational bonding between adjacent particles at the crack tip breaks and the particles starts to rotate with respect to each other. Second, the particles then move apart and the adjacent set of particles become the next crack-tip particles. Based on the mechanism, the crack path that minimizes the effort on breaking the micro-rotational bond (i.e., the path that maximizes the dissipation) is equivalent to the shortest path towards the boundary if the material is isotropic and homogeneous (e.g., a horizontal crack growth from the notch tip for the pure tensile loading case). The observed crack patterns shown in Fig. 5.6 is consistent with this interpretation. Furthermore, Fig. 5.6 also provides evidence to support that the non-polar model is a special case of the micropolar model in which $l_b \approx 0$. With a sufficiently

small bending characteristic length l_b, the difference in crack patterns for the non-polar and micropolar cases are negligible. The coupling and the micro-rotational parts (ψ_e^C and ψ_e^R) then become significant enough to play a bigger role for crack growth as the bending characteristic length l_b increases.

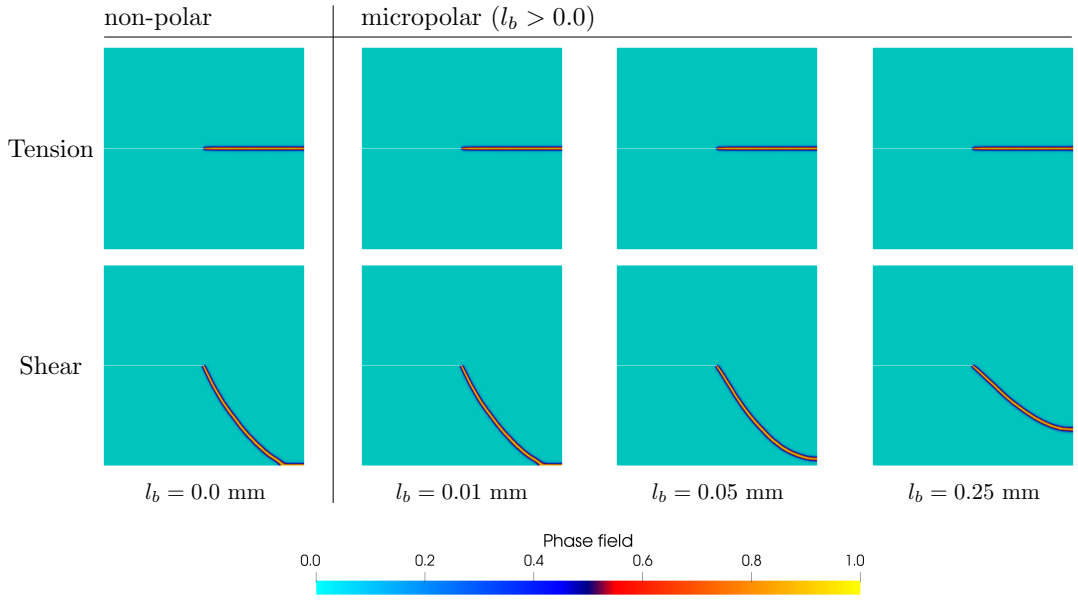

Figure 5.6: Fracture patterns for single edge notched tests under different micropolar characteristic length l_b.

As illustrated in Fig. 5.7, separated particles tend to rotate in opposite directions since they are no longer interlocked after crack formation. By revisiting Eq. (5.7) and Eq. (5.13), notice that the material constant γ that relates the fictitious undamaged couple stress $\bar{\boldsymbol{m}}^R$ to the micro-curvature $\bar{\boldsymbol{\kappa}}$ is proportional to the square of the characteristic lengths. The relationship implies that larger characteristic length leads to higher rigidity of the micropolar material, so that the separated particles tend to experience greater micro-rotation with smaller bending characteristic length.

Fig. 5.8 shows the load-deflection curves obtained from both tension and shear tests. The colored curves indicate the results with nonzero l_b, whereas the transparent gray curves denote the non-polar case. Since the force stress can be decomposed into two parts, e.g., $\bar{\boldsymbol{\sigma}} = \bar{\boldsymbol{\sigma}}^B + \bar{\boldsymbol{\sigma}}^C$, micropolar material that possesses a large characteristic length tend to exhibit

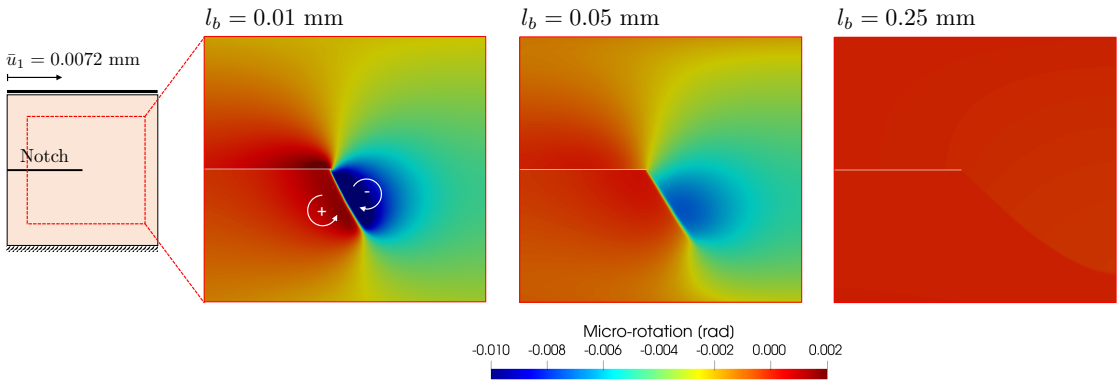

Figure 5.7: Resultant micro-rotation field for single edge notched shear tests where $\bar{u}_1 = 0.0072$ mm.

stiffer response compared to those with smaller characteristic lengths, due to the micro-continuum coupling effect. Unlike the tension test results in Fig. 5.8(a), the reaction forces reach their peak values under different strain level from the shearing tests [Fig. 5.8(b)]. This again highlights that the micropolar bending characteristic length affects the crack pattern, which in turn reflects different global response for the same boundary value problem.

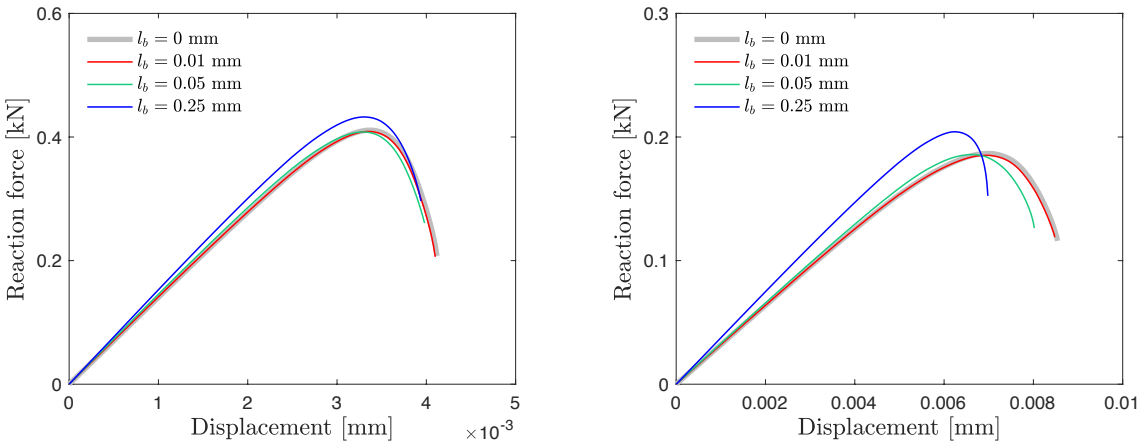

Figure 5.8: The force-displacement curves from the single edge notched (a) tension and (b) shear tests with regularization length $l_c = 0.008$ mm.

5.5.3 Asymmetric notched three-point bending tests

This section examines a problem originally designed by Ingraffea and Grigoriu [393], which involves a three-point bending of a specimen with three holes. The domain of the problem is illustrated in Fig. 5.9. Since previous studies [76, 351, 393, 394] have shown that different crack patterns can be observed depending on the notch depth and its position, we only focus on the case where the notch depth is set to be 25.4 mm.

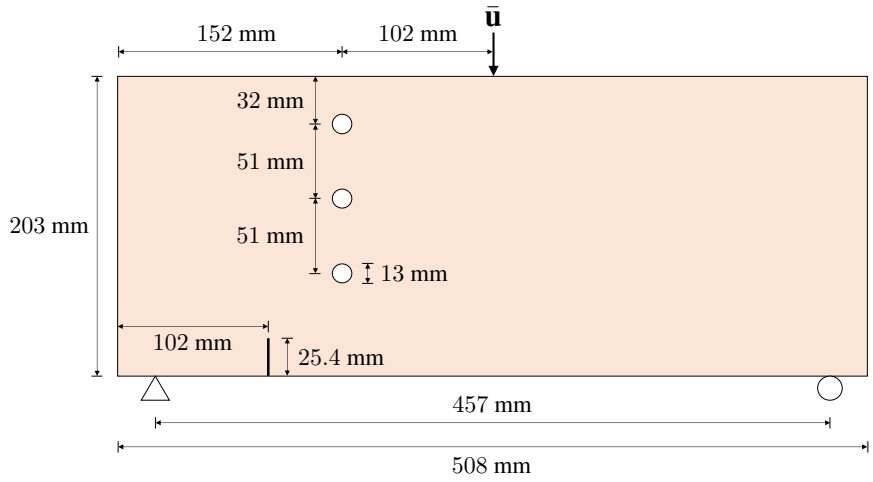

Figure 5.9: Schematic of geometry and boundary conditions for the three-point bending tests.

We consider a specimen composed of a micropolar material and choose Boltzmann material parameters close to the properties of Plexiglas specimen tested by Ingraffea and Grigoriu [393]: $E = 3.2$ GPa, $\nu = 0.3$, $\mathcal{G}_c = 0.31$ N/mm, $l_c = 1.0$ mm, and $\psi_{\text{crit}} = 7.5$ kJ/m^3. For this problem, we assume that all the energy density parts can be degraded, i.e., $\mathfrak{D} = \{B, C, R\}$, $\mathfrak{U} = \emptyset$.

Within the problem domain (Fig. 5.9), we first attempt to investigate the effect of coupling number on the crack trajectory by conducting multiple numerical tests with different values: $N = 0.1$, $N = 0.5$, and $N = 0.9$, while bending characteristic length is held fixed as $l_b = 10.0$ mm. The numerical simulation conducted under a displacement-controlled regime where we keep the load increment as $\Delta\bar{u}_2 = -2.0 \times 10^{-4}$ mm.

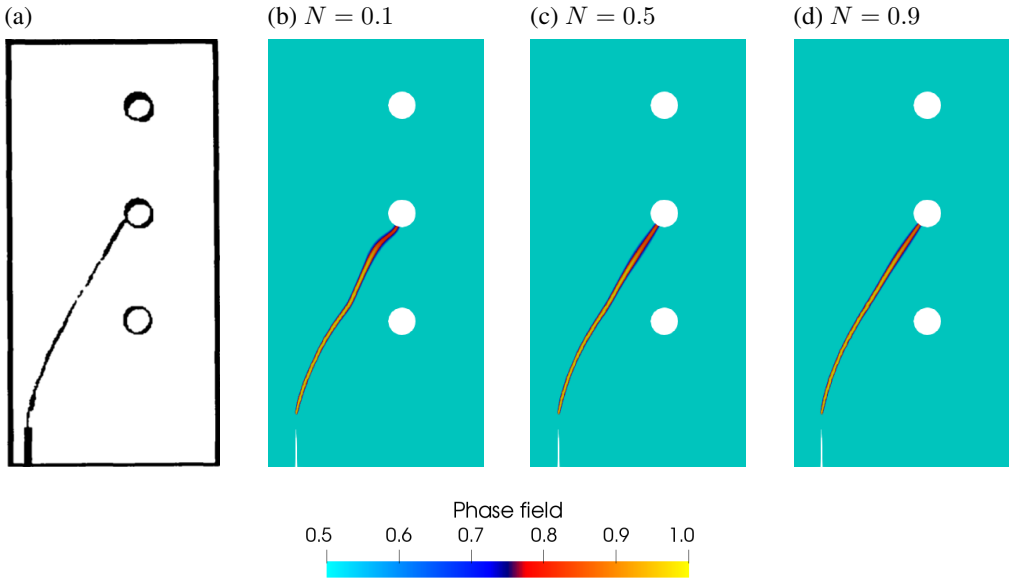

Figure 5.10: Crack topologies for asymmetric notched three-point bending test: (a) experimentally obtained pattern by Ingraffea and Grigoriu [393]; (b)-(d) numerically obtained parttern with different coupling number N.

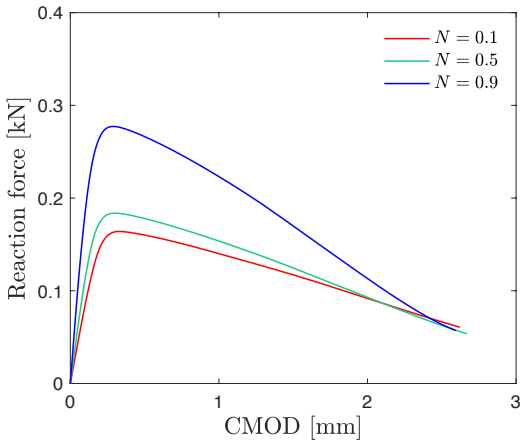

Figure 5.11: Load-CMOD curves from the three-point bending test.

Fig. 5.10 illustrates the crack trajectories obtained by numerical experiments with different coupling number N in comparison to the experimental result [393], while Fig. 5.11 shows the measured reaction forces as a function of crack-mouth-opening-displacement (CMOD). Similar to the experimental results in Fig. 5.10(a), numerical results [Fig. 5.10(b)-(d)] show that the cracks tend to deflect towards the holes, eventually coalescing with the

intermediate one. However, taking a closer look at Fig. 5.10(b)-(d), one can observe the slight differences on the concavity of the crack topologies especially when the crack passes close to the bottom hole. As we highlighted in Section 5.5.2, the crack tends to propagate through the path where the energy that takes to break the micro-rotational bond is minimized. At the same time, based on Saint-Venant's principle, the crack trajectory can also be affected by the bottom hole due to an increase of the singularity [351]. In this specific platform, it can thus be interpreted that the crack propagation may result from the competition between the two, based on the obtained results. Since the material that possesses higher degree of micropolarity requires more energy to break the micro-rotational bond, the bottom hole effect on the crack trajectory becomes negligible as coupling number N increases [Fig. 5.10(b)-(d)]. In addition, Fig. 5.11 implies that if more energy is required to break the micro-rotational bond, it results in higher material stiffness in the elastic regime, supporting our interpretation.

We then conduct a brief sensitivity analysis with respect to the time discretization (i.e., prescribed displacement increment $\Delta\bar{u}_2$) within the same problem domain, while we set the coupling number to be $N = 0.9$ during the analysis. Fig. 5.12 illustrates the simulated crack patterns for asymmetrically notched beam with three holes, with different prescribed displacement rates, varying from $\Delta\bar{u}_2 = -4.0 \times 10^{-4}$ mm to -16.0×10^{-4} mm. Since meaningful differences in the crack trajectories are not observed, the result confirms the practical applicability of the explicit operator-splitting solution scheme, if the load increment is small enough.

5.5.4 Double edge notched tests

This numerical example investigates the effect of partial degradation of the strain energy density on the crack patterns. As illustrated in Fig. 5.13, the problem domain is a 100 mm wide and 100 mm long square plate with two 25 mm long symmetric initial horizontal edge notches at the middle. We assign the following material properties for this problem:

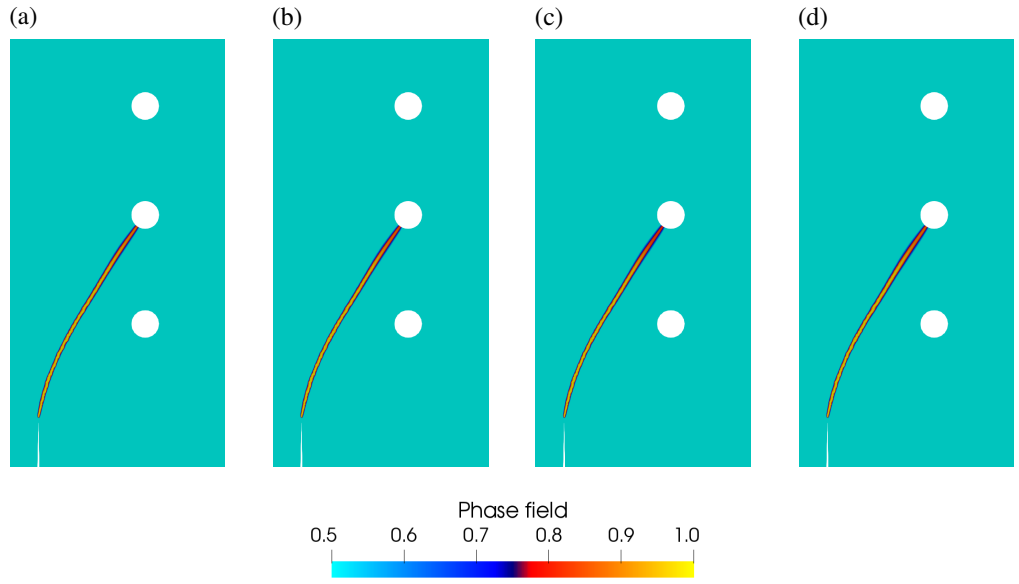

Figure 5.12: Observed crack patterns for asymmetric notched three-point bending tests: (a) $\Delta\bar{u}_2 = -2.0 \times 10^{-4}$ mm; (b) $\Delta\bar{u}_2 = -4.0 \times 10^{-4}$ mm; (c) $\Delta\bar{u}_2 = -8.0 \times 10^{-4}$ mm; (d) $\Delta\bar{u}_2 = -16.0 \times 10^{-4}$ mm.

$E = 30$ GPa, $\nu = 0.2$, $\mathcal{G}_c = 0.1$ N/mm, $l_c = 0.75$ mm, and $\psi_{\text{crit}} = 1.0$ kJ/m^3. Numerical experiments are simulated with bending characteristic length $l_b = 30.0$ mm and the coupling number is set to be $N = 0.5$. While the bottom part of the domain is held fixed, we prescribe the displacement along the entire top boundary at an angle of 45 degrees to the horizontal direction: $\Delta\bar{u}_1 = \Delta\bar{u}_2 = 5.0 \times 10^{-4}$ mm, such that the domain is subjected to combined tensile and shear loads.

Regarding partial degradation, recall Eq. (5.25) that energy density parts that corresponds to the set $\mathfrak{U}$ remains completely undamaged, such that $g_i(d) = 1$ for $i \in \mathfrak{U}$, where $\mathfrak{D} \cup \mathfrak{U} = \{B, C, R\}$ and $\mathfrak{D} \cap \mathfrak{U} = \emptyset$. Within this platform, we first explore the effects of each individual energy density part by considering three different settings: (a) $\mathfrak{D} = \{B\}$; (b) $\mathfrak{D} = \{C\}$; and (c) $\mathfrak{D} = \{R\}$. Fig. 5.14 shows the fracture patterns for double edge notched tests for three aforementioned cases where $\bar{u}_1 = \bar{u}_2 = 0.05$ mm. Under the same threshold energy density ψ_{crit}, partial Boltzmann degradation case shown in Fig. 5.14(a) undergoes crack propagation, whereas degrading ψ_e^C [Fig. 5.14(b)] or ψ_e^R [Fig. 5.14(c)] ex-

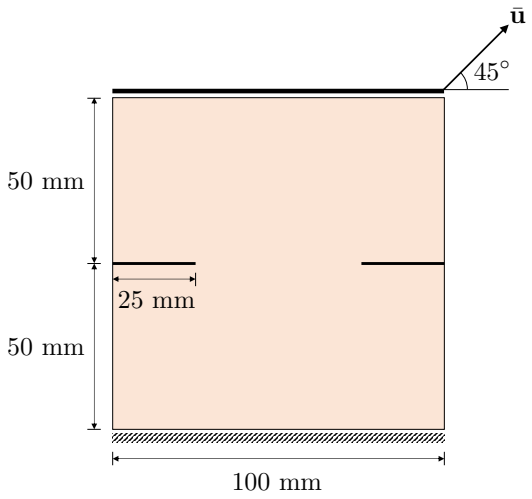

Figure 5.13: Schematic of geometry and boundary conditions for the double edge notched tests.

hibit small amount of damage accumulation at the crack tip, without complete rupturing. It reveals that in either force or displacement-driven setup, most of the elastic energy is stored in non-polar constituent; the amount of stored energy density parts: $\psi_e^B > \psi_e^C > \psi_e^R$. As illustrated in Fig. 5.15, only the fictitious undegraded Boltzmann energy density part locally exceeds the prescribed threshold $\psi_{\text{crit}} = 1.0$ kJ/m^3 through the cracks when $\mathfrak{D} = \{B\}$. Even though ψ_e^C and ψ_e^R do not exceed the threshold energy except the flaw tip region, the results also indirectly evidence that the coupling and pure micro-rotational energy density parts affect crack kinking, while the pure Boltzmann part mainly drives the crack to grow.

Since the pure Boltzmann part mainly drives the crack propagation, we now focus on the combined partial degradation with $B \in \mathfrak{D}$, also by considering three different settings within the same platform: (a) $\mathfrak{D} = \{B, R\}$; (b) $\mathfrak{D} = \{B, C\}$; and (c) $\mathfrak{D} = \{B, C, R\}$. Fig. 5.16 shows the crack patterns for double edge notched tests for three different combinations of partial degradation compared with the case where $\mathfrak{D} = \{B\}$, while Fig. 5.17 illustrates the obtained load-deflection curves. The results confirms that degradation of the energy density parts ψ_e^C and ψ_e^R affects the crack kinking and curving.

The combined degradation with $\mathfrak{D} = \{B, R\}$ tend to stimulate similar fracture patterns compared to the partial Boltzmann degradation case until $\bar{u}_1 = \bar{u}_2 = 0.04$ mm, and then

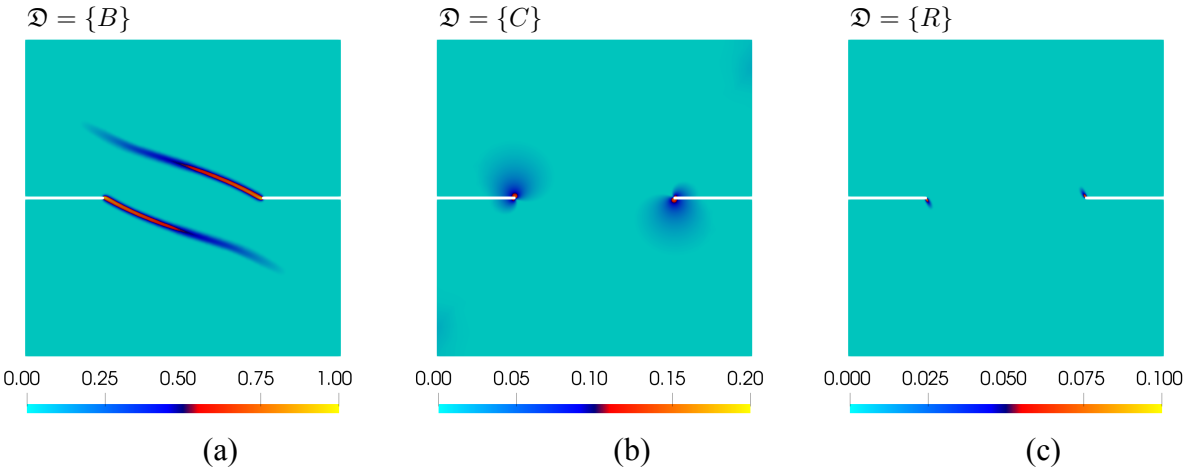

Figure 5.14: Crack patterns for double edge notched tests obtained by considering different degradation functions [i.e., $g_i(d) = g(d)$ if $i \in \mathfrak{D}$; $g_i(d) = 1$ otherwise] on each energy density part, where $\bar{u}_1 = \bar{u}_2 = 0.05$ mm.

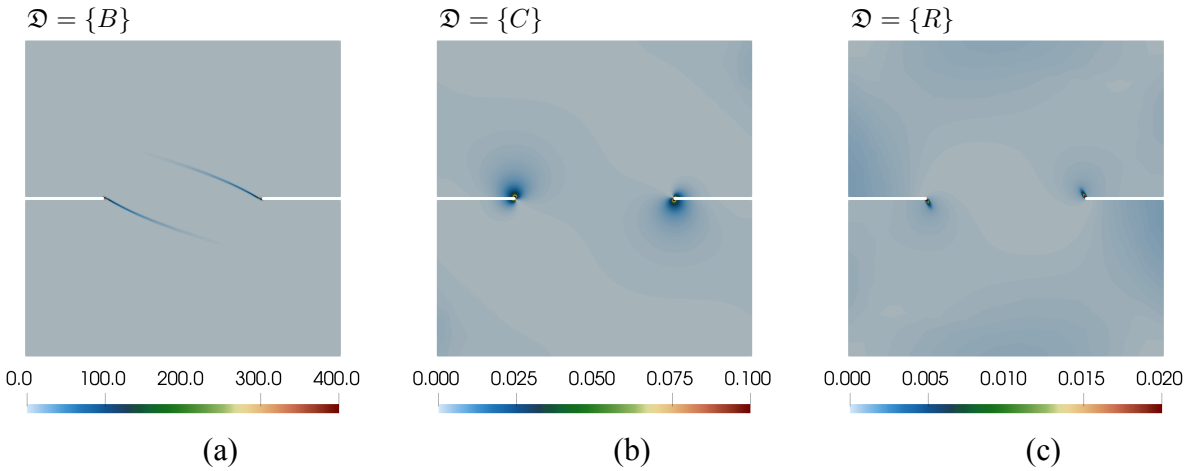

Figure 5.15: Fictitious undegraded energy density part ψ_e^i ($i \in \mathfrak{D}$), where $\bar{u}_1 = \bar{u}_2 = 0.05$ mm.

the cracks start to propagate towards the notches. Revisiting Fig. 5.15, this again indicates that the crack trajectories tend to follow the path that maximizes the energy dissipation (i.e., crack growth towards the adjacent flaw when the stored ψ_e^R at the tip becomes high enough). Similarly, the combined degradation with $\mathfrak{D} = \{B, C\}$ leads the cracks to grow towards the adjacent tip. In this case, however, the cracks tend to kink towards the adjacent notch from the beginning, and then two cracks coalescence toward each other after sufficient

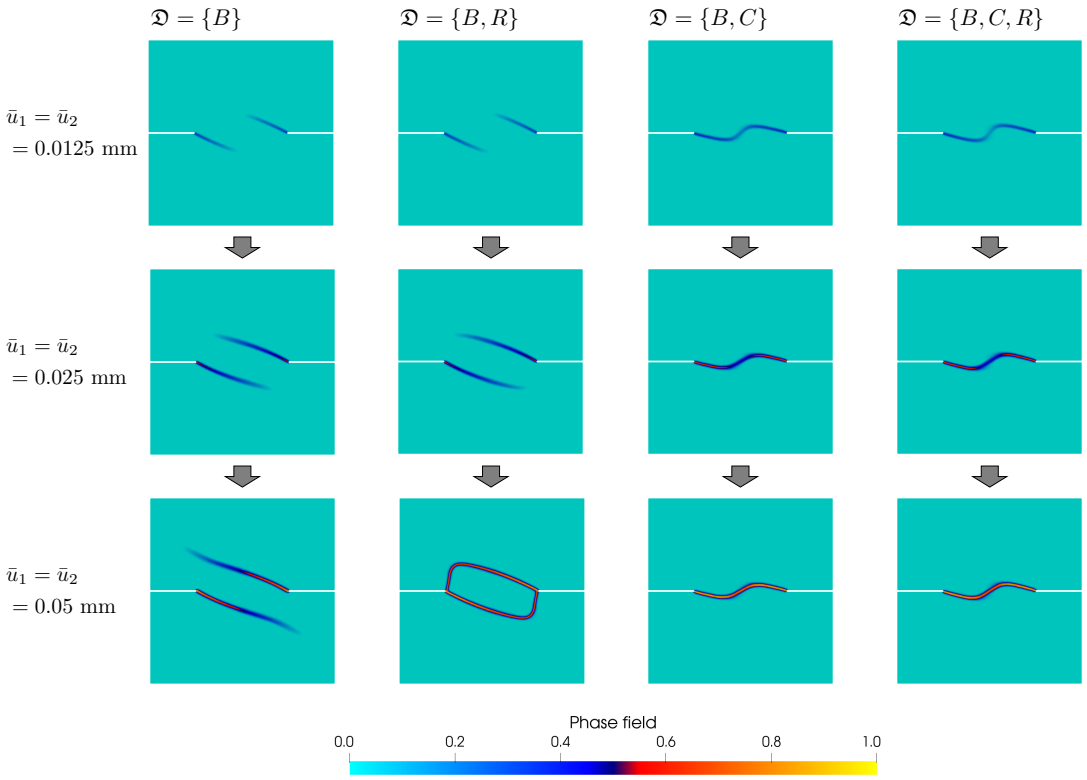

Figure 5.16: Crack patterns for double edge notched tests with different combination of degrading energy density parts at several load increments.

loading. Since the amount of stored coupling energy ψ_e^C is greater than the pure micro-rotational part ψ_e^R, we speculate that the coupling energy part influences the crack pattern more significantly compared to the micro-rotational energy part, so that we thus observe similar fracture pattern when $\mathfrak{D} = \{B, C, R\}$. In summary, this numerical experiment highlight that the pure Boltzmann energy density drives the crack growth, while the micro-continuum coupling energy density mainly influences the kinking direction.

5.6 Conclusion

This study presents a phase field fracture framework to model cohesive fracture in micropolar continua. To the best of the authors' knowledge, this is the first ever mathematics model that employs the phase field fracture framework to simulate crack growth in mate-

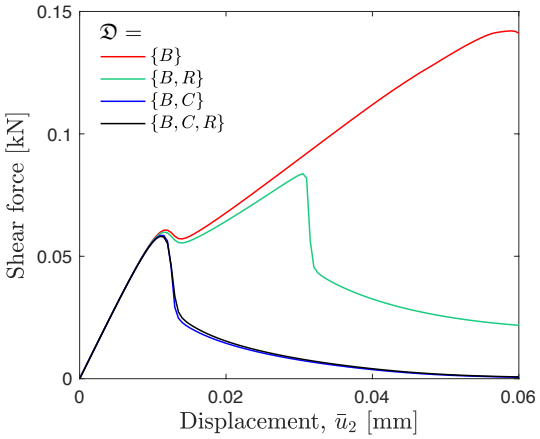

Figure 5.17: The force-displacement curves from the double edge notched tests with different combination of degrading energy density parts.

rials that exhibit size effect in both elastic and damaged regimes. To replicate a consistent size effect for both the elastic deformation and crack growth mechanisms, we introduce a method to incorporate distinctive degradation mechanisms via an energy-split approach for the non-polar, coupling and micropolar energies, while adopting the pair of degradation and regularization profiles that enables us to suppress the sensitivity of the length scale parameter that regularizes the phase field. One-dimensional analysis and numerical experiments demonstrate that the quasi-quadratic degradation function combined with linear local dissipation function successfully suppress the sensitivity of the length scale parameter for phase field while successfully incorporate the size effect with a length scale parameter that can be measured via standard inverse problems for micropolar materials. This result is significant, as the insensitivity of the length scale parameter will allow one to use coarser mesh to run simulations for a scale relevant to field applications (e.g. geological formations, structural components), while still able to replicating the size effect exhibited by materials of internal structures.

This page intentionally left blank.

Chapter 6: Closure

6.1 Scope and contribution

This dissertation explores and introduces a series of mathematical and computational frameworks that incorporate small scale information to predict coupled thermo-hydro-mechanical-fracture processes in phase-changing porous media at meso- and macro-scales. Specifically, this study adopts diffuse interface approaches that represent small scale features coupled with thermo-hydro-mechanics, and includes the development of corresponding finite element solvers. The author's main contribution in the field of computational microporomechanics presented in this dissertation are summarized as follows.

In Chapter 2, for the first time, we present a multi-phase-field framework to capture freeze-thaw action in a porous medium that may form ice lenses. Unlike previous studies that are restricted to one-dimensional space, the proposed model is capable of simulating freezing-induced fracture and phase transition in two- and three-dimensional spaces, by introducing two phase fields that represent the state of the pore fluid and the damaged/undamaged material state. We also extend the Bishop's effective stress principle for frozen porous media in order to distinguish crystallized ice inside the pore space and ice lenses, which induces deviatoric stress. As a result, this chapter opens the door for us to analyze how the homogeneous freezing process and the ice lens formation affect the coupled behavior of water-saturated porous medium in the transient regime.

Chapter 3 considers the case where the solid and fluid phase constituents are in thermal

non-equilibrium locally, which may have profound impact in microporomechanics problems with phase transitions. To the best of the author's knowledge, this is the first attempt to model brittle fracture in multi-phase fluid-infiltrating porous media that incorporates heat exchange mechanism between constituents. By introducing a new homogenization strategy that distinguishes the solid and fluid temperatures, this chapter provides a foundation for distinctive energy balance laws for each constituent. We show that this two-temperature approach is a generalization of the classical one-temperature model, since it can be recovered by assuming that all the phase constituents reach thermal equilibrium instantly. This approach bypasses the need to homogenize the intrinsic thermal properties of each component, which may simplify the calibration process since they are not necessarily isotropic. By proposing an asynchronous time integrator that updates solid and fluid temperatures with different time steps, numerical examples show that it greatly reduces the computational cost while reproducing physically consistent results compared to the synchronous counterpart.

Chapter 4 focuses on the case where fluid-saturated cracks may coalescence with existing voids that trigger redistribution of fluid flow, which cannot be captured without the coupled Stokes-Darcy flow. This approach leads to more accurate forward prediction of fluid motion, which may significantly affect the coupled behavior of phase-changing porous media. By considering the phase field variable as a damage parameter and at the same time an indicator of large voids, this chapter introduces a unified treatment that handles evolving microstructures without the needs of domain partitioning or introduction of enrichment functions. Smooth approximation of the interface between the free and porous medium flow regions enables us to incorporate transmissibility conditions as a set of immersed boundary conditions, where phenomenological permeability enhancement approach is no longer required. This approach enables us to explicitly model dual-porosity media, while being advantageous over the embedded discontinuity models in simulating crack-cavity interactions where homogenized pore pressure jump may not be sufficient to capture the flow patterns.

Finally, in Chatper 5, we introduce a simple phase field fracture framework that can

correctly capture the physical size effects in both micropolar elastic and damaged regimes. Specifically, elastic stored energy functional is decomposed into the pure Boltzmann, coupling, and pure micro-rotational parts while introducing distinctive degradation mechanisms with a specific regularization profile that is insensitive to the fictitious phase field length scale parameter. We also conduct one-dimensional analysis to demonstrate the regularization length scale independence, and our numerical examples show that this model can successfully incorporate the micropolar size effects. This work may have significant implications for phase-changing geological materials that possesses microstructural attributes as well as other field scale applications where the material characteristic lengths are much smaller than the regularization length scale.

6.2 Future perspective

While Chapter 2 attempts to construct a solid foundation in modeling phase-changing geomaterials, and Chapters 3, 4, and 5 introduce techniques that are crucial for incorporating small scale details in heat transfer, fluid mass transport, and microstructural size effects, rescpectively, this section now discusses the extension of the current family of proposed methods to address a larger class of energy and environmental techniques problems that involve phase transition. Based on the aforementioned advancements and progresses, future studies that can be further explored beyond this dissertation are summarized as follows.

For either partially or fully saturated soils, crack healing may occur during the thawing process since soil experiences compressive stress in this case. Melting of ice lenses in a highly plastic soil, such as clays, cracks may heal due to the interactions between water molecules, while in a less cohesive soil, relocation of eroded particles result in clogging of cracks and cavities. Furthermore, water adsorption on clay particles may have a profound impact on fluid motion inside the heterogeneous matrix, which can affect the freezing patterns and hence the microporomechanical responses. One possible approach is to allow

crack driving force to decrease by assuming that the healing process is activated if the material experiences volumetric compression, while incorporating adsorption process as a mass exchange process between the clay mineral and pore water. The work presented in Chapter 2 can be considered as a starting point for a new mathematical framework that incorporates these effects, which may have significant impacts in studying microporomechanical behavior of phase-changing geomaterials.

Since solid and fluid constituents may not be in thermal equilibrium state at small scales, two-temperature model presented in Chapter 3 will have more profound importance for the case where temperature difference does not only trigger thermal expansion but also lead to phase transition. For instance, CO_2 sequestration induced fracture simulations often injects supercritical carbon dioxide that stimulates rapid change in mechanical behavior of the fluid for different pressure-temperature combination, especially when near the critical point or at the phase transition regime. Incorporating thermal- or pressure-induced phase transition of the fluid constituent into the proposed two-temperature model will be considered in the future, since it may result in significant differences compared to the classical one-temperature approach.

Besides, freeze-thaw action in geological materials that contains large voids or size effects may exhibit different freezing patterns, compared to homogeneous medium. In this case, it is essential to incorporate its microporomechanical behavior by considering either coupled Stokes-Darcy flow (Chapter 4) or higher order continuum theory (Chapter 5) or both. Chapters 4 an 5 in this dissertation can serve as potential starting points for further development of computational frameworks to model meso- or macro-scale applications without sacrificing necessary details, which may be advantageous over particle/pore-scale or multi-scale simulators since they require significant amounts of computing resources.

As predictive computer simulations of phase-changing porous materials have become more critical for numerous energy and environmental geotechnics applications, my future research will continuously focus on theoretical and computational microporomechanics of

multi-phase media. Based on a series of mathematical and computational frameworks presented this dissertation, the following research topics can be further explored in the future: (1) micro-freezing patterns and hydrochemical processes in phase-changing clay materials, (2) development of frozen-soil-structure interaction model to investigate the effect of ice lenses on the pavements, (3) characterization of microthermoporomechanical behavior and/or multi-scale modeling of shallow and deep geothermal energy systems, and (4) investigation of hydro-chemo-mechanically coupled behavior of carbonate precipitated soils and numerical evaluation of environmental-friendly soil improvement techniques.

This page intentionally left blank.

Bibliography

[1] P Zhai et al. *IPCC 2021: Climate Change 2021: The Physical Science Basis. Contribution of Working Group I to the Sixth Assessment Report of the Intergovernmental Panel on Climate Change*. 2021.

[2] S. Corti, F. Molteni, and T. Palmer. "Signature of recent climate change in frequencies of natural atmospheric circulation regimes." *Nature* 398.6730 (1999), pp. 799–802.

[3] K. E. Trenberth. "Changes in precipitation with climate change." *Climate research* 47.1-2 (2011), pp. 123–138.

[4] T. G. Shepherd. "Atmospheric circulation as a source of uncertainty in climate change projections." *Nature Geoscience* 7.10 (2014), pp. 703–708.

[5] P. A. O'Gorman. "Precipitation extremes under climate change." *Current climate change reports* 1.2 (2015), pp. 49–59.

[6] F. M. O'Connor et al. "Possible role of wetlands, permafrost, and methane hydrates in the methane cycle under future climate change: A review." *Reviews of Geophysics* 48.4 (2010).

[7] S. I. Seneviratne et al. "Investigating soil moisture–climate interactions in a changing climate: A review." *Earth-Science Reviews* 99.3-4 (2010), pp. 125–161.

[8] C. D. Koven, W. J. Riley, and A. Stern. "Analysis of permafrost thermal dynamics and response to climate change in the CMIP5 Earth System Models." *Journal of Climate* 26.6 (2013), pp. 1877–1900.

[9] R. P. Allan et al. "IPCC, 2021: Summary for Policymakers" (2021).

[10] E. Martin et al. "Impact of a climate change on avalanche hazard." *Annals of Glaciology* 32 (2001), pp. 163–167.

[11] M. Keiler, J. Knight, and S. Harrison. "Climate change and geomorphological hazards in the eastern European Alps." *Philosophical Transactions of the Royal Society*

A: Mathematical, Physical and Engineering Sciences 368.1919 (2010), pp. 2461–2479.

[12] S. L. Gariano and F. Guzzetti. "Landslides in a changing climate." *Earth-Science Reviews* 162 (2016), pp. 227–252.

[13] A. I. Patton, S. L. Rathburn, and D. M. Capps. "Landslide response to climate change in permafrost regions." *Geomorphology* 340 (2019), pp. 116–128.

[14] P. J. Williams. "Permafrost and climate change: geotechnical implications." *Philosophical Transactions of the Royal Society of London. Series A: Physical and Engineering Sciences* 352.1699 (1995), pp. 347–358.

[15] J. Schweizer, J Bruce Jamieson, and M. Schneebeli. "Snow avalanche formation." *Reviews of Geophysics* 41.4 (2003).

[16] S. A. Zimov, E. A. Schuur, and F. S. Chapin III. "Permafrost and the global carbon budget." *Science* 312.5780 (2006), pp. 1612–1613.

[17] C. Tarnocai et al. "Soil organic carbon pools in the northern circumpolar permafrost region." *Global biogeochemical cycles* 23.2 (2009).

[18] E. A. Schuur et al. "Climate change and the permafrost carbon feedback." *Nature* 520.7546 (2015), pp. 171–179.

[19] Y. Zhang and R. L. Michalowski. "Thermal-hydro-mechanical analysis of frost heave and thaw settlement." *Journal of geotechnical and geoenvironmental engineering* 141.7 (2015), p. 04015027.

[20] F. Vahedifard, J. M. Williams, and A. AghaKouchak. "Geotechnical engineering in the face of climate change: Role of multi-physics processes in partially saturated soils." *IFCEE 2018*. 2018, pp. 353–364.

[21] M. Roser, H. Ritchie, and E. Ortiz-Ospina. "World population growth." *Our world in data* (2013).

[22] I. E. Agency. *World Energy Outlook 2021*. 2021.

[23] T. A. Boden, G. Marland, and R. J. Andres. "Global, regional, and national fossil-fuel CO2 emissions." *Carbon dioxide information analysis center, Oak ridge national laboratory, US department of energy, Oak Ridge, Tenn., USA doi* 10 (2009).

[24] J. C. Turnbull et al. "Toward quantification and source sector identification of fossil fuel CO2 emissions from an urban area: Results from the INFLUX experiment." *Journal of Geophysical Research: Atmospheres* 120.1 (2015), pp. 292–312.

[25] Z. Wang, B. Zhang, B. Wang, et al. “Renewable energy consumption, economic growth and human development index in Pakistan: evidence form simultaneous equation model.” *Journal of cleaner production* 184 (2018), pp. 1081–1090.

[26] N. Mahmood, Z. Wang, and S. T. Hassan. “Renewable energy, economic growth, human capital, and CO2 emission: an empirical analysis.” *Environmental Science and Pollution Research* 26.20 (2019), pp. 20619–20630.

[27] R. S. Haszeldine. “Carbon capture and storage: how green can black be?” *Science* 325.5948 (2009), pp. 1647–1652.

[28] M. E. Boot-Handford et al. “Carbon capture and storage update.” *Energy & Environmental Science* 7.1 (2014), pp. 130–189.

[29] A. N. Schofield and P. Wroth. *Critical state soil mechanics*. Vol. 310. McGraw-hill London, 1968.

[30] D. M. Wood. *Soil behaviour and critical state soil mechanics*. Cambridge university press, 1990.

[31] H. I. Ling et al. “Anisotropic elastoplastic bounding surface model for cohesive soils.” *Journal of engineering mechanics* 128.7 (2002), pp. 748–758.

[32] L. Dormieux, D. Kondo, and F.-J. Ulm. *Microporomechanics*. John Wiley & Sons, 2006.

[33] L. Dormieux and F.-J. Ulm. *Applied micromechanics of porous materials*. Vol. 480. Springer Science & Business Media, 2007.

[34] H. S. Suh and W. Sun. “Asynchronous phase field fracture model for porous media with thermally non-equilibrated constituents.” *Computer Methods in Applied Mechanics and Engineering* 387 (2021), p. 114182.

[35] A. C. Palmer and P. J. Williams. “Frost heave and pipeline upheaval buckling.” *Canadian Geotechnical Journal* 40.5 (2003), pp. 1033–1038.

[36] S. Zhang et al. “Analysis of frost heave mechanisms in a high-speed railway embankment.” *Canadian Geotechnical Journal* 53.3 (2016), pp. 520–529.

[37] A. Li et al. “Experimental measurement and numerical simulation of frost heave in saturated coarse-grained soil.” *Cold Regions Science and Technology* 137 (2017), pp. 68–74.

[38] C. B. Lake, M. A.-M. Yousif, and R. J. Jamshidi. “Examining freeze/thaw effects on performance and morphology of a lightly cemented soil.” *Cold Regions Science and Technology* 134 (2017), pp. 33–44.

[39] Y. Ji et al. “Frost heave in freezing soils: A quasi-static model for ice lens growth.” *Cold Regions Science and Technology* 158 (2019), pp. 10–17.

[40] A. F. DiMillio. *A quarter century of geotechnical research*. Tech. rep. Turner-Fairbank Highway Research Center, 1999.

[41] F. E. Nelson, O. A. Anisimov, and N. I. Shiklomanov. “Subsidence risk from thawing permafrost.” *Nature* 410.6831 (2001), pp. 889–890.

[42] F. E. Nelson, O. A. Anisimov, and N. I. Shiklomanov. “Climate change and hazard zonation in the circum-Arctic permafrost regions.” *Natural Hazards* 26.3 (2002), pp. 203–225.

[43] D. A. Streletskiy, N. I. Shiklomanov, and F. E. Nelson. “Permafrost, infrastructure, and climate change: a GIS-based landscape approach to geotechnical modeling.” *Arctic, Antarctic, and Alpine Research* 44.3 (2012), pp. 368–380.

[44] M. Leibman, A. Khomutov, and A. Kizyakov. “Cryogenic landslides in the West-Siberian plain of Russia: classification, mechanisms, and landforms.” *Landslides in cold regions in the context of climate change*. Springer, 2014, pp. 143–162.

[45] H. Mithan, T. Hales, and P. Cleall. “Topographic and Ground-Ice Controls on Shallow Landsliding in Thawing Arctic Permafrost.” *Geophysical Research Letters* 48.13 (2021), e2020GL092264.

[46] S. Taber. “Frost heaving.” *The Journal of Geology* 37.5 (1929), pp. 428–461.

[47] S. Taber. “The mechanics of frost heaving.” *The Journal of Geology* 38.4 (1930), pp. 303–317.

[48] S. S. Peppin and R. W. Style. “The physics of frost heave and ice-lens growth.” *Vadose Zone Journal* 12.1 (2013).

[49] L. Wilen and J. Dash. “Frost heave dynamics at a single crystal interface.” *Physical Review Letters* 74.25 (1995), p. 5076.

[50] J. Dash, H. Fu, and J. Wettlaufer. “The premelting of ice and its environmental consequences.” *Reports on Progress in Physics* 58.1 (1995), p. 115.

[51] J. Dash, A. Rempel, and J. Wettlaufer. “The physics of premelted ice and its geophysical consequences.” *Reviews of modern physics* 78.3 (2006), p. 695.

[52] R. Harlan. “Analysis of coupled heat-fluid transport in partially frozen soil.” *Water Resources Research* 9.5 (1973), pp. 1314–1323.

[53] R. Miller. “Freezing and heaving of saturated and unsaturated soils.” *Highway Research Record* 393.1 (1972), pp. 1–11.

[54] R. Miller. “Lens initiation in secondary heaving.” *Proceedings of the International Symposium on Frost Action in Soils*. Vol. 2. Luleå Alltryck AB Luleå, Sweden. 1977, pp. 68–74.

[55] K. O’Neill and R. D. Miller. “Exploration of a rigid ice model of frost heave.” *Water Resources Research* 21.3 (1985), pp. 281–296.

[56] A. Fowler. “Secondary frost heave in freezing soils.” *SIAM Journal on Applied Mathematics* 49.4 (1989), pp. 991–1008.

[57] A. C. Fowler and W. B. Krantz. “A generalized secondary frost heave model.” *Siam Journal on Applied Mathematics* 54.6 (1994), pp. 1650–1675.

[58] R. Gilpin. “A model for the prediction of ice lensing and frost heave in soils.” *Water Resources Research* 16.5 (1980), pp. 918–930.

[59] J. Zhou and D. Li. “Numerical analysis of coupled water, heat and stress in saturated freezing soil.” *Cold Regions Science and Technology* 72 (2012), pp. 43–49.

[60] J.-M. Konrad and N. R. Morgenstern. “A mechanistic theory of ice lens formation in fine-grained soils.” *Canadian Geotechnical Journal* 17.4 (1980), pp. 473–486.

[61] J. F. Nixon. “Field frost heave predictions using the segregation potential concept.” *Canadian Geotechnical Journal* 19.4 (1982), pp. 526–529.

[62] J.-M. Konrad and M Shen. “2-D frost action modeling using the segregation potential of soils.” *Cold regions science and technology* 24.3 (1996), pp. 263–278.

[63] E Tiedje and P Guo. “Frost heave modeling using a modified segregation potential approach.” *Cold Regions Engineering 2012: Sustainable Infrastructure Development in a Changing Cold Environment*. 2012, pp. 686–696.

[64] A. W. Rempel, J. Wettlaufer, and M. G. Worster. “Premelting dynamics in a continuum model of frost heave.” *Journal of fluid mechanics* 498 (2004), pp. 227–244.

[65] A. Rempel. “Formation of ice lenses and frost heave.” *Journal of Geophysical Research: Earth Surface* 112.F2 (2007).

[66] R. W. Style et al. “Ice-lens formation and geometrical supercooling in soils and other colloidal materials.” *Physical Review E* 84.4 (2011), p. 041402.

[67] S Nishimura et al. “THM-coupled finite element analysis of frozen soil: formulation and application.” *Géotechnique* 59.3 (2009), pp. 159–171.

[68] M. Zhou and G Meschke. “A three-phase thermo-hydro-mechanical finite element model for freezing soils.” *International journal for numerical and analytical methods in geomechanics* 37.18 (2013), pp. 3173–3193.

[69] S. Na and W. Sun. “Computational thermo-hydro-mechanics for multiphase freezing and thawing porous media in the finite deformation range.” *Computer Methods in Applied Mechanics and Engineering* 318 (2017), pp. 667–700.

[70] R. L. Michalowski and M. Zhu. “Frost heave modelling using porosity rate function.” *International journal for numerical and analytical methods in geomechanics* 30.8 (2006), pp. 703–722.

[71] S. Ghoreishian Amiri et al. “Constitutive model for rate-independent behavior of saturated frozen soils.” *Canadian Geotechnical Journal* 53.10 (2016), pp. 1646–1657.

[72] J. Wettlaufer and M. G. Worster. “Premelting dynamics.” *Annu. Rev. Fluid Mech.* 38 (2006), pp. 427–452.

[73] S. M. Allen and J. W. Cahn. “A microscopic theory for antiphase boundary motion and its application to antiphase domain coarsening.” *Acta metallurgica* 27.6 (1979), pp. 1085–1095.

[74] W. J. Boettinger et al. “Phase-field simulation of solidification.” *Annual review of materials research* 32.1 (2002), pp. 163–194.

[75] B. Bourdin, G. A. Francfort, and J.-J. Marigo. “The variational approach to fracture.” *Journal of elasticity* 91.1-3 (2008), pp. 5–148.

[76] C. Miehe, M. Hofacker, and F. Welschinger. “A phase field model for rate-independent crack propagation: Robust algorithmic implementation based on operator splits.” *Computer Methods in Applied Mechanics and Engineering* 199.45-48 (2010), pp. 2765–2778.

[77] M. J. Borden et al. “A phase-field description of dynamic brittle fracture.” *Computer Methods in Applied Mechanics and Engineering* 217 (2012), pp. 77–95.

[78] J. A. Warren and W. J. Boettinger. “Prediction of dendritic growth and microsegregation patterns in a binary alloy using the phase-field method.” *Acta Metallurgica et Materialia* 43.2 (1995), pp. 689–703.

[79] A. H. Sweidan, Y. Heider, and B. Markert. “A unified water/ice kinematics approach for phase-field thermo-hydro-mechanical modeling of frost action in porous media.” *Computer Methods in Applied Mechanics and Engineering* 372 (2020), p. 113358.

[80] J.-L. Chaboche. “Continuum damage mechanics: Part I—General concepts” (1988).

[81] R. M. Bowen. “Incompressible porous media models by use of the theory of mixtures.” *International Journal of Engineering Science* 18.9 (1980), pp. 1129–1148.

[82] O. C. Zienkiewicz et al. *Computational geomechanics*. Vol. 613. Citeseer, 1999.

[83] W. Ehlers. “Foundations of multiphasic and porous materials.” *Porous media*. Springer, 2002, pp. 3–86.

[84] O. Coussy. *Poromechanics*. John Wiley & Sons, 2004.

[85] K. O’Neill. *Numerical solutions for a rigid-ice model of secondary frost heave*. Vol. 82. 13. US Army Corps of Engineers, Cold Regions Research & Engineering Laboratory, 1982.

[86] H. S. Suh, W. Sun, and D. T. O’Connor. “A phase field model for cohesive fracture in micropolar continua.” *Computer Methods in Applied Mechanics and Engineering* 369 (2020), p. 113181.

[87] C. Miehe, F. Welschinger, and M. Hofacker. “Thermodynamically consistent phase-field models of fracture: Variational principles and multi-field FE implementations.” *International journal for numerical methods in engineering* 83.10 (2010), pp. 1273–1311.

[88] J. Choo and W. Sun. “Cracking and damage from crystallization in pores: Coupled chemo-hydro-mechanics and phase-field modeling.” *Computer Methods in Applied Mechanics and Engineering* 335 (2018), pp. 347–379.

[89] Y. Heider. “A review on phase-field modeling of hydraulic fracturing.” *Engineering Fracture Mechanics* 253 (2021), p. 107881.

[90] E. C. Bryant and W. Sun. “A mixed-mode phase field fracture model in anisotropic rocks with consistent kinematics.” *Computer Methods in Applied Mechanics and Engineering* 342 (2018), pp. 561–584.

[91] R. I. Borja, Q. Yin, and Y. Zhao. “Cam-Clay plasticity. Part IX: On the anisotropy, heterogeneity, and viscoplasticity of shale.” *Computer Methods in Applied Mechanics and Engineering* 360 (2020), p. 112695.

[92] J. Bluhm and T. Ricken. “Modeling of freezing and thawing processes in liquid filled thermo-elastic porous solids.” *Transport in Concrete: Nano-to Macrostructure, edited by M. Setzer (Aedificatio Publishers, Freiburg, 2007)* (2007), pp. 41–57.

[93] T. Ricken and J. Bluhm. “Modeling fluid saturated porous media under frost attack.” *GAMM-Mitteilungen* 33.1 (2010), pp. 40–56.

[94] M. T. Van Genuchten. “A closed-form equation for predicting the hydraulic conductivity of unsaturated soils.” *Soil science society of America journal* 44.5 (1980), pp. 892–898.

[95] R. Gelet, B. Loret, and N. Khalili. “A thermo-hydro-mechanical coupled model in local thermal non-equilibrium for fractured HDR reservoir with double porosity.” *Journal of Geophysical Research: Solid Earth* 117.B7 (2012).

[96] Z. Liu et al. “Measurement of freezing point depression of water in glass capillaries and the associated ice front shape.” *Physical Review E* 67.6 (2003), p. 061602.

[97] I. Loginova, G. Amberg, and J. Ågren. “Phase-field simulations of non-isothermal binary alloy solidification.” *Acta materialia* 49.4 (2001), pp. 573–581.

[98] V. Alexiades and A. D. Solomon. *Mathematical modeling of melting and freezing processes*. Routledge, 2018.

[99] J. D. Eshelby. “The determination of the elastic field of an ellipsoidal inclusion, and related problems.” *Proceedings of the royal society of London. Series A. Mathematical and physical sciences* 241.1226 (1957), pp. 376–396.

[100] H. Hiroshi and T. Minoru. “Equivalent inclusion method for steady state heat conduction in composites.” *International Journal of Engineering Science* 24.7 (1986), pp. 1159–1172.

[101] W. Sun. “A stabilized finite element formulation for monolithic thermo-hydro-mechanical simulations at finite strain.” *International Journal for Numerical Methods in Engineering* 103.11 (2015), pp. 798–839.

[102] C. Lee et al. “Particle shape effect on thermal conductivity and shear wave velocity in sands.” *Acta Geotechnica* 12.3 (2017), pp. 615–625.

[103] H. S. Suh and T. S. Yun. “Modification of capillary pressure by considering pore throat geometry with the effects of particle shape and packing features on water retention curves for uniformly graded sands.” *Computers and Geotechnics* 95 (2018), pp. 129–136.

[104] T. Takaki. “Phase-field modeling and simulations of dendrite growth.” *ISIJ international* 54.2 (2014), pp. 437–444.

[105] S. Aihara, T. Takaki, and N. Takada. “Multi-phase-field modeling using a conservative Allen–Cahn equation for multiphase flow.” *Computers & Fluids* 178 (2019), pp. 141–151.

[106] K. S. Henry. “A review of the thermodynamics of frost heave” (2000).

[107] A. A. Wheeler, W. J. Boettinger, and G. B. McFadden. “Phase-field model for isothermal phase transitions in binary alloys.” *Physical Review A* 45.10 (1992), p. 7424.

[108] G Caginalp and E. Socolovsky. “Efficient computation of a sharp interface by spreading via phase field methods.” *Applied Mathematics Letters* 2.2 (1989), pp. 117–120.

[109] G Caginalp and E. Socolovsky. “Computation of sharp phase boundaries by spreading: the planar and spherically symmetric cases.” *Journal of Computational Physics* 95.1 (1991), pp. 85–100.

[110] E Penner. “Aspects of ice lens growth in soils.” *Cold regions science and technology* 13.1 (1986), pp. 91–100.

[111] R. M. Espinosa, L. Franke, and G. Deckelmann. “Phase changes of salts in porous materials: Crystallization, hydration and deliquescence.” *Construction and Building Materials* 22.8 (2008), pp. 1758–1773.

[112] M. Koniorczyk and D. Gawin. “Modelling of salt crystallization in building materials with microstructure–Poromechanical approach.” *Construction and Building Materials* 36 (2012), pp. 860–873.

[113] H. Derluyn, P. Moonen, and J. Carmeliet. “Deformation and damage due to drying-induced salt crystallization in porous limestone.” *Journal of the Mechanics and Physics of Solids* 63 (2014), pp. 242–255.

[114] C. Guodong. “The mechanism of repeated-segregation for the formation of thick layered ground ice.” *Cold Regions Science and Technology* 8.1 (1983), pp. 57–66.

[115] C. Harris et al. “Permafrost and climate in Europe: Monitoring and modelling thermal, geomorphological and geotechnical responses.” *Earth-Science Reviews* 92.3-4 (2009), pp. 117–171.

[116] B. Evans, J. T. Fredrich, and T.-F. Wong. “The brittle-ductile transition in rocks: Recent experimental and theoretical progress.” *The Brittle-Ductile Transition in Rocks, Geophys. Monogr. Ser* 56 (1990), pp. 1–20.

[117] M. Y. Lee et al. “Frozen soil material testing and constitutive modeling.” *Sandia Report, SAND* 524 (2002), pp. 8–65.

[118] A Foriero and B Ladanyi. “FEM assessment of large-strain thaw consolidation.” *Journal of Geotechnical Engineering* 121.2 (1995), pp. 126–138.

[119] D. M. Anderson and A. R. Tice. “Predicting unfrozen water contents in frozen soils from surface area measurements.” *Highway research record* 393.2 (1972), pp. 12–18.

[120] R. W. R. Koopmans and R. Miller. “Soil freezing and soil water characteristic curves.” *Soil Science Society of America Journal* 30.6 (1966), pp. 680–685.

[121] P. B. Black and A. R. Tice. “Comparison of soil freezing curve and soil water curve data for Windsor sandy loam.” *Water Resources Research* 25.10 (1989), pp. 2205–2210.

[122] T. Ma et al. “Soil freezing and soil water retention characteristics: Connection and solute effects.” *Journal of performance of constructed facilities* 31.1 (2017), p. D4015001.

[123] R. Bai et al. “Theory and application of a novel soil freezing characteristic curve.” *Applied Thermal Engineering* 129 (2018), pp. 1106–1114.

[124] L Luckner, M. T. Van Genuchten, and D. Nielsen. “A consistent set of parametric models for the two-phase flow of immiscible fluids in the subsurface.” *Water Resources Research* 25.10 (1989), pp. 2187–2193.

[125] M. Seyfried and M. Murdock. “Use of air permeability to estimate infiltrability of frozen soil.” *Journal of Hydrology* 202.1-4 (1997), pp. 95–107.

[126] D. Demand, J. S. Selker, and M. Weiler. “Influences of macropores on infiltration into seasonally frozen soil.” *Vadose Zone Journal* 18.1 (2019), pp. 1–14.

[127] M Dittmann et al. “Variational modeling of thermomechanical fracture and anisotropic frictional mortar contact problems with adhesion.” *Computational Mechanics* 63.3 (2019), pp. 571–591.

[128] M Dittmann et al. “Phase-field modeling of porous-ductile fracture in non-linear thermo-elasto-plastic solids.” *Computer Methods in Applied Mechanics and Engineering* 361 (2020), p. 112730.

[129] C. Miehe, S. Mauthe, and S. Teichtmeister. “Minimization principles for the coupled problem of Darcy–Biot-type fluid transport in porous media linked to phase field modeling of fracture.” *Journal of the Mechanics and Physics of Solids* 82 (2015), pp. 186–217.

[130] H. Amor, J.-J. Marigo, and C. Maurini. “Regularized formulation of the variational brittle fracture with unilateral contact: Numerical experiments.” *Journal of the Mechanics and Physics of Solids* 57.8 (2009), pp. 1209–1229.

[131] C. Miehe, L.-M. Schaenzel, and H. Ulmer. “Phase field modeling of fracture in multi-physics problems. Part I. Balance of crack surface and failure criteria for brittle crack propagation in thermo-elastic solids.” *Computer Methods in Applied Mechanics and Engineering* 294 (2015), pp. 449–485.

[132] H. S. Suh and W. Sun. “An open-source FEniCS implementation of a phase field fracture model for micropolar continua.” *International Journal for Multiscale Computational Engineering* 17.6 (2019).

[133] E. C. Bryant and W. Sun. “Phase field modeling of frictional slip with slip weakening/strengthening under non-isothermal conditions.” *Computer Methods in Applied Mechanics and Engineering* 375 (2021), p. 113557.

[134] P. Viklander. “Permeability and volume changes in till due to cyclic freeze/thaw.” *Canadian Geotechnical Journal* 35.3 (1998), pp. 471–477.

[135] K. Eigenbrod. “Self-healing in fractured fine-grained soils.” *Canadian Geotechnical Journal* 40.2 (2003), pp. 435–449.

[136] M. Rayhani, E. Yanful, and A Fakher. “Physical modeling of desiccation cracking in plastic soils.” *Engineering Geology* 97.1-2 (2008), pp. 25–31.

[137] R. Ma and W. Sun. “Computational thermomechanics for crystalline rock. Part II: Chemo-damage-plasticity and healing in strongly anisotropic polycrystals.” *Computer Methods in Applied Mechanics and Engineering* 369 (2020), p. 113184.

[138] C. Miehe and S. Mauthe. “Phase field modeling of fracture in multi-physics problems. Part III. Crack driving forces in hydro-poro-elasticity and hydraulic fracturing of fluid-saturated porous media.” *Computer Methods in Applied Mechanics and Engineering* 304 (2016), pp. 619–655.

[139] S. Mauthe and C. Miehe. “Hydraulic fracture in poro-hydro-elastic media.” *Mechanics Research Communications* 80 (2017), pp. 69–83.

[140] K. Wang and W. Sun. “A unified variational eigen-erosion framework for interacting brittle fractures and compaction bands in fluid-infiltrating porous media.” *Computer Methods in Applied Mechanics and Engineering* 318 (2017), pp. 1–32.

[141] H. S. Suh and W. Sun. “An immersed phase field fracture model for microporomechanics with Darcy–Stokes flow.” *Physics of Fluids* 33.1 (2021), p. 016603.

[142] Z. A. Wilson and C. M. Landis. “Phase-field modeling of hydraulic fracture.” *Journal of the Mechanics and Physics of Solids* 96 (2016), pp. 264–290.

[143] Y. Heider and W. Sun. “A phase field framework for capillary-induced fracture in unsaturated porous media: Drying-induced vs. hydraulic cracking.” *Computer Methods in Applied Mechanics and Engineering* 359 (2020), p. 112647.

[144] J. Simo and C. Miehe. “Associative coupled thermoplasticity at finite strains: Formulation, numerical analysis and implementation.” *Computer Methods in Applied Mechanics and Engineering* 98.1 (1992), pp. 41–104.

[145] T. Nguyen and A. Selvadurai. “Coupled thermal-mechanical-hydrological behaviour of sparsely fractured rock: implications for nuclear fuel waste disposal.” *International journal of rock mechanics and mining sciences & geomechanics abstracts*. Vol. 32. 5. Elsevier. 1995, pp. 465–479.

[146] A. Logg and G. N. Wells. “DOLFIN: Automated finite element computing.” *ACM Transactions on Mathematical Software (TOMS)* 37.2 (2010), pp. 1–28.

[147] A. Logg, K.-A. Mardal, and G. Wells. *Automated solution of differential equations by the finite element method: The FEniCS book*. Vol. 84. Springer Science & Business Media, 2012.

[148] M. Alnæs et al. “The FEniCS project version 1.5.” *Archive of Numerical Software* 3.100 (2015).

[149] S. Abhyankar et al. “PETSc/TS: A modern scalable ODE/DAE solver library.” *arXiv preprint arXiv:1806.01437* (2018).

[150] A. Sweidan et al. “Experimental study and numerical modeling of the thermo-hydro-mechanical processes in soil freezing with different frost penetration directions.” *Acta Geotechnica* (2021), pp. 1–25.

[151] S. Feng et al. “Unidirectional freezing of phase change materials saturated in open-cell metal foams.” *Applied Thermal Engineering* 88 (2015), pp. 315–321.

[152] R. Lackner, A. Amon, and H. Lagger. “Artificial ground freezing of fully saturated soil: thermal problem.” *Journal of Engineering Mechanics* 131.2 (2005), pp. 211–220.

[153] K. Terzaghi, R. B. Peck, and G Mesri. “Soil mechanics.” *New York: John Wiley & Sons* (1996).

[154] G. Amato et al. “A glimpse into rapid freezing processes in clay with x-ray tomography.” *Acta Geotechnica* (2021), pp. 1–12.

[155] O. Uyanık. “Estimation of the porosity of clay soils using seismic P-and S-wave velocities.” *Journal of Applied Geophysics* 170 (2019), p. 103832.

[156] D. E. Dunn, L. J. LaFountain, and R. E. Jackson. “Porosity dependence and mechanism of brittle fracture in sandstones.” *Journal of Geophysical Research* 78.14 (1973), pp. 2403–2417.

[157] H. S. Al-Hadhrami and M. J. Blunt. “Thermally induced wettability alteration to improve oil recovery in fractured reservoirs.” *SPE Reservoir Evaluation & Engineering* 4.03 (2001), pp. 179–186.

[158] L. Rybach. “Geothermal energy: sustainability and the environment.” *Geothermics* 32.4-6 (2003), pp. 463–470.

[159] R. Pusch. “Geological storage of highly radioactive waste: current concepts and plans for radioactive waste disposal” (2009).

[160] R. Shukla et al. “A review of studies on CO2 sequestration and caprock integrity.” *Fuel* 89.10 (2010), pp. 2651–2664.

[161] A. R. Shaik et al. “Numerical simulation of fluid-rock coupling heat transfer in naturally fractured geothermal system.” *Applied thermal engineering* 31.10 (2011), pp. 1600–1606.

[162] Z. Dai et al. “CO2 accounting and risk analysis for CO2 sequestration at enhanced oil recovery sites.” *Environmental science & technology* 50.14 (2016), pp. 7546–7554.

[163] W. Sun, Z. Cai, and J. Choo. “Mixed Arlequin method for multiscale poromechanics problems.” *International Journal for Numerical Methods in Engineering* 111.7 (2017), pp. 624–659.

[164] S. Salimzadeh et al. “A three-dimensional coupled thermo-hydro-mechanical model for deformable fractured geothermal systems.” *Geothermics* 71 (2018), pp. 212–224.

[165] B. Bahmani and W. Sun. “A kd-tree-accelerated hybrid data-driven/model-based approach for poroelasticity problems with multi-fidelity multi-physics data.” *Computer Methods in Applied Mechanics and Engineering* 382 (2021), p. 113868.

[166] J. D. Byerlee. “Brittle-ductile transition in rocks.” *Journal of Geophysical Research* 73.14 (1968), pp. 4741–4750.

[167] M. S. Paterson and T.-f. Wong. *Experimental rock deformation-the brittle field*. Springer Science & Business Media, 2005.

[168] J. Choo and W. Sun. “Coupled phase-field and plasticity modeling of geological materials: From brittle fracture to ductile flow.” *Computer Methods in Applied Mechanics and Engineering* 330 (2018), pp. 1–32.

[169] F. D. Hansen and C. D. Leigh. *Salt disposal of heat-generating nuclear waste*. Sandia National Laboratories Albuquerque, NM, 2011.

[170] S. Na and W. Sun. “Computational thermomechanics of crystalline rock, Part I: A combined multi-phase-field/crystal plasticity approach for single crystal simulations.” *Computer Methods in Applied Mechanics and Engineering* 338 (2018), pp. 657–691.

[171] J. Rutqvist. “Status of the TOUGH-FLAC simulator and recent applications related to coupled fluid flow and crustal deformations.” *Computers & Geosciences* 37.6 (2011), pp. 739–750.

[172] O. Kolditz et al. “OpenGeoSys: an open-source initiative for numerical simulation of thermo-hydro-mechanical/chemical (THM/C) processes in porous media.” *Environmental Earth Sciences* 67.2 (2012), pp. 589–599.

[173] I Nozad, R. Carbonell, and S Whitaker. “Heat conduction in multiphase systems—I: theory and experiment for two-phase systems.” *Chemical Engineering Science* 40.5 (1985), pp. 843–855.

[174] I Nozad, R. Carbonell, and S Whitaker. “Heat conduction in multiphase systems—II: Experimental method and results for three-phase systems.” *Chemical engineering science* 40.5 (1985), pp. 857–863.

[175] D. McTigue. “Thermoelastic response of fluid-saturated porous rock.” *Journal of Geophysical Research: Solid Earth* 91.B9 (1986), pp. 9533–9542.

[176] M Kurashige. “A thermoelastic theory of fluid-filled porous materials.” *International Journal of Solids and Structures* 25.9 (1989), pp. 1039–1052.

[177] R. Zimmerman. “Coupling in poroelasticity and thermoelasticity.” *International Journal of Rock Mechanics and Mining Sciences* 37.1-2 (2000), pp. 79–87.

[178] A. Belotserkovets and J. H. Prevost. “Thermoporoelastic response of a fluid-saturated porous sphere: An analytical solution.” *International Journal of Engineering Science* 49.12 (2011), pp. 1415–1423.

[179] J. Kim. “Unconditionally stable sequential schemes for all-way coupled thermoporomechanics: Undrained-adiabatic and extended fixed-stress splits.” *Computer Methods in Applied Mechanics and Engineering* 341 (2018), pp. 93–112.

[180] N. Noii and T. Wick. “A phase-field description for pressurized and non-isothermal propagating fractures.” *Computer Methods in Applied Mechanics and Engineering* 351 (2019), pp. 860–890.

[181] H. Truong and G. E. Zinsmeister. “Experimental study of heat transfer in layered composites.” *International Journal of Heat and Mass Transfer* 21.7 (1978), pp. 905–909.

[182] L.-W. He, Z.-H. Jin, and Y Zhang. “Convective cooling/heating induced thermal stresses in a fluid saturated porous medium undergoing local thermal non-equilibrium.” *International Journal of Solids and Structures* 49.5 (2012), pp. 748–758.

[183] F. Jiang et al. “A three-dimensional transient model for EGS subsurface thermo-hydraulic process.” *Energy* 72 (2014), pp. 300–310.

[184] M Quintard, M Kaviany, and S Whitaker. “Two-medium treatment of heat transfer in porous media: numerical results for effective properties.” *Advances in Water resources* 20.2-3 (1997), pp. 77–94.

[185] C. Hsu. “A closure model for transient heat conduction in porous media” (1999).

[186] W. Minkowycz, A Haji-Sheikh, and K. Vafai. “On departure from local thermal equilibrium in porous media due to a rapidly changing heat source: the Sparrow number.” *International journal of heat and mass transfer* 42.18 (1999), pp. 3373–3385.

[187] A. Nakayama et al. “A two-energy equation model for conduction and convection in porous media.” *International journal of heat and mass transfer* 44.22 (2001), pp. 4375–4379.

[188] J. Fourie and J. Du Plessis. “A two-equation model for heat conduction in porous media (I: Theory).” *Transport in porous media* 53.2 (2003), pp. 145–161.

[189] J. Fourie and J. Du Plessis. "A two-equation model for heat conduction in porous media (ii: application)." *Transport in porous media* 53.2 (2003), pp. 163–174.

[190] L Virto et al. "Heating of saturated porous media in practice: several causes of local thermal non-equilibrium." *International journal of heat and mass transfer* 52.23-24 (2009), pp. 5412–5422.

[191] T. J. Hughes, M. Mallet, and M. Akira. "A new finite element formulation for computational fluid dynamics: II. Beyond SUPG." *Computer methods in applied mechanics and engineering* 54.3 (1986), pp. 341–355.

[192] T. J. Hughes, L. P. Franca, and G. M. Hulbert. "A new finite element formulation for computational fluid dynamics: VIII. The Galerkin/least-squares method for advective-diffusive equations." *Computer methods in applied mechanics and engineering* 73.2 (1989), pp. 173–189.

[193] Y. Bachmat and J. Bear. "Macroscopic modelling of transport phenomena in porous media. 1: The continuum approach." *Transport in porous media* 1.3 (1986), pp. 213–240.

[194] O. Coussy, L. Dormieux, and E. Detournay. "From mixture theory to Biot's approach for porous media." *International Journal of Solids and Structures* 35.34-35 (1998), pp. 4619–4635.

[195] W. G. Gray. "A derivation of the equations for multi-phase transport." *Chemical Engineering Science* 30.2 (1975), pp. 229–233.

[196] A Amiri, K Vafai, and T. Kuzay. "Effects of boundary conditions on non-Darcian heat transfer through porous media and experimental comparisons." *Numerical Heat Transfer, Part A: Applications* 27.6 (1995), pp. 651–664.

[197] B Alazmi and K Vafai. "Analysis of fluid flow and heat transfer interfacial conditions between a porous medium and a fluid layer." *International Journal of Heat and Mass Transfer* 44.9 (2001), pp. 1735–1749.

[198] R. De Boer. *Theory of porous media: highlights in historical development and current state*. Springer Science & Business Media, 2012.

[199] M. Preisig and J. H. Prévost. "Coupled multi-phase thermo-poromechanical effects. Case study: CO2 injection at In Salah, Algeria." *International Journal of Greenhouse Gas Control* 5.4 (2011), pp. 1055–1064.

[200] J. Rutqvist et al. "Thermohydromechanics of partially saturated geological media: governing equations and formulation of four finite element models." *Interna-*

tional Journal of Rock Mechanics and Mining Sciences 38.1 (2001). Decovalex II, pp. 105–127. ISSN: 1365-1609.

[201] S. Na and W. Sun. "Wave propagation and strain localization in a fully saturated softening porous medium under the non-isothermal conditions." *International Journal for Numerical and Analytical Methods in Geomechanics* 40.10 (2016), pp. 1485–1510.

[202] N Khalili, A Uchaipichat, and A. Javadi. "Skeletal thermal expansion coefficient and thermo-hydro-mechanical constitutive relations for saturated homogeneous porous media." *Mechanics of materials* 42.6 (2010), pp. 593–598.

[203] D. B. Mumford and J. Shah. "Optimal approximations by piecewise smooth functions and associated variational problems." *Communications on pure and applied mathematics* (1989).

[204] J. Clayton and J Knap. "Phase field modeling of twinning in indentation of transparent crystals." *Modelling and Simulation in Materials Science and Engineering* 19.8 (2011), p. 085005.

[205] A Mesgarnejad, B Bourdin, and M. Khonsari. "Validation simulations for the variational approach to fracture." *Computer Methods in Applied Mechanics and Engineering* 290 (2015), pp. 420–437.

[206] J. Bleyer and R. Alessi. "Phase-field modeling of anisotropic brittle fracture including several damage mechanisms." *Computer Methods in Applied Mechanics and Engineering* 336 (2018), pp. 213–236.

[207] G. A. Francfort and J.-J. Marigo. "Revisiting brittle fracture as an energy minimization problem." *Journal of the Mechanics and Physics of Solids* 46.8 (1998), pp. 1319–1342.

[208] E. Lorentz. "A nonlocal damage model for plain concrete consistent with cohesive fracture." *International Journal of Fracture* 207.2 (2017), pp. 123–159.

[209] R. J. Geelen et al. "A phase-field formulation for dynamic cohesive fracture." *Computer Methods in Applied Mechanics and Engineering* 348 (2019), pp. 680–711.

[210] H. S. Suh, W. Sun, and D. T. O'Connor. "A phase field model for cohesive fracture in micropolar continua." *Computer Methods in Applied Mechanics and Engineering* 369 (2020), p. 113181. ISSN: 0045-7825.

[211] R. I. Borja. "On the mechanical energy and effective stress in saturated and unsaturated porous continua." *International Journal of Solids and Structures* 43.6 (2006), pp. 1764–1786.

[212] R. I. Borja and A. Koliji. “On the effective stress in unsaturated porous continua with double porosity.” *Journal of the Mechanics and Physics of Solids* 57.8 (2009), pp. 1182–1193.

[213] Q. Yang, L. Stainier, and M. Ortiz. “A variational formulation of the coupled thermo-mechanical boundary-value problem for general dissipative solids.” *Journal of the Mechanics and Physics of Solids* 54.2 (2006), pp. 401–424.

[214] M. A. Biot. “General theory of three-dimensional consolidation.” *Journal of applied physics* 12.2 (1941), pp. 155–164.

[215] O Vincké et al. “Investigation of the poromechanical behavior of shales in the elastic domain.” *SPE/ISRM Rock Mechanics in Petroleum Engineering*. Society of Petroleum Engineers. 1998.

[216] J. C. Jaeger, N. G. Cook, and R. Zimmerman. *Fundamentals of rock mechanics*. John Wiley & Sons, 2009.

[217] S. J. Ha, J. Choo, and T. S. Yun. “Liquid CO 2 fracturing: Effect of fluid permeation on the breakdown pressure and cracking behavior.” *Rock Mechanics and Rock Engineering* 51.11 (2018), pp. 3407–3420.

[218] V. Lubarda. “On thermodynamic potentials in linear thermoelasticity.” *International Journal of Solids and Structures* 41.26 (2004), pp. 7377–7398.

[219] C. Truesdell and R. Toupin. “The classical field theories.” *Principles of classical mechanics and field theory/Prinzipien der Klassischen Mechanik und Feldtheorie*. Springer, 1960, pp. 226–858.

[220] R. Abraham, J. E. Marsden, and J. E. Marsden. *Foundations of mechanics*. Vol. 36. Benjamin/Cummings Publishing Company Reading, Massachusetts, 1978.

[221] G. A. Holzapfel. “Nonlinear solid mechanics: a continuum approach for engineering science.” *Meccanica* 37.4 (2002), pp. 489–490.

[222] F. T. Dórea and M. J. De Lemos. “Simulation of laminar impinging jet on a porous medium with a thermal non-equilibrium model.” *International Journal of Heat and Mass Transfer* 53.23-24 (2010), pp. 5089–5101.

[223] A Gandomkar and K. Gray. “Local thermal non-equilibrium in porous media with heat conduction.” *International Journal of Heat and Mass Transfer* 124 (2018), pp. 1212–1216.

[224] T. Heinze. “Possible effect of flow velocity on thawing rock-water-ice systems under local thermal non-equilibrium conditions.” *Cold Regions Science and Technology* 170 (2020), p. 102940.

[225] K. Pham and J.-J. Marigo. “From the onset of damage to rupture: construction of responses with damage localization for a general class of gradient damage models.” *Continuum Mechanics and Thermodynamics* 25.2 (2013), pp. 147–171.

[226] M. E. Gurtin. “Generalized Ginzburg-Landau and Cahn-Hilliard equations based on a microforce balance.” *Physica D: Nonlinear Phenomena* 92.3-4 (1996), pp. 178–192.

[227] Z. A. Wilson, M. J. Borden, and C. M. Landis. “A phase-field model for fracture in piezoelectric ceramics.” *International Journal of Fracture* 183.2 (2013), pp. 135–153.

[228] R. Atkin and R. Craine. “Continuum theories of mixtures: basic theory and historical development.” *The Quarterly Journal of Mechanics and Applied Mathematics* 29.2 (1976), pp. 209–244.

[229] J. H. Prévost. “Mechanics of continuous porous media.” *International Journal of Engineering Science* 18.6 (1980), pp. 787–800.

[230] W. Sun, J. T. Ostien, and A. G. Salinger. “A stabilized assumed deformation gradient finite element formulation for strongly coupled poromechanical simulations at finite strain.” *International Journal for Numerical and Analytical Methods in Geomechanics* 37.16 (2013), pp. 2755–2788.

[231] R. I. Borja and E. Alarcón. “A mathematical framework for finite strain elastoplastic consolidation Part 1: Balance laws, variational formulation, and linearization.” *Computer Methods in Applied Mechanics and Engineering* 122.1-2 (1995), pp. 145–171.

[232] J. H. Prevost. “Nonlinear transient phenomena in saturated porous media.” *Computer Methods in Applied Mechanics and Engineering* 30.1 (1982), pp. 3–18.

[233] M. N. Özışık. *Boundary value problems of heat conduction*. courier Corporation, 1989.

[234] A Amiri and K. Vafai. “Analysis of dispersion effects and non-thermal equilibrium, non-Darcian, variable porosity incompressible flow through porous media.” *International journal of heat and mass transfer* 37.6 (1994), pp. 939–954.

[235] H. S. Suh et al. “Quantification of bulk form and angularity of particle with correlation of shear strength and packing density in sands.” *Engineering geology* 220 (2017), pp. 256–265.

[236] Y. Heider, H. S. Suh, and W. Sun. “An offline multi-scale unsaturated poromechanics model enabled by self-designed/self-improved neural networks.” *International Journal for Numerical and Analytical Methods in Geomechanics* (2021).

[237] S. Whitaker. “Simultaneous heat, mass, and momentum transfer in porous media: a theory of drying.” *Advances in heat transfer*. Vol. 13. Elsevier, 1977, pp. 119–203.

[238] K. Pennell. “2.5 Specific Surface Area.” *Methods of Soil Analysis: Part 4 Physical Methods* 5 (2002), pp. 295–315.

[239] G. Feng, Y. Kang, and X.-c. Wang. “Fracture failure of granite after varied durations of thermal treatment: an experimental study.” *Royal Society open science* 6.7 (2019), p. 190144.

[240] G. Feng et al. “Effects of temperature on the relationship between mode-I fracture toughness and tensile strength of rock.” *Applied Sciences* 9.7 (2019), p. 1326.

[241] Y. Heider et al. “Modeling of hydraulic fracturing using a porous-media phase-field approach with reference to experimental data.” *Engineering Fracture Mechanics* 202 (2018), pp. 116–134.

[242] C. Chukwudozie, B. Bourdin, and K. Yoshioka. “A variational phase-field model for hydraulic fracturing in porous media.” *Computer Methods in Applied Mechanics and Engineering* 347 (2019), pp. 957–982.

[243] W. C. Sun, J. E. Andrade, and J. W. Rudnicki. “Multiscale method for characterization of porous microstructures and their impact on macroscopic effective permeability.” *International Journal for Numerical Methods in Engineering* 88.12 (2011), pp. 1260–1279.

[244] W. Sun et al. “Connecting microstructural attributes and permeability from 3D tomographic images of in situ shear-enhanced compaction bands using multiscale computations.” *Geophysical Research Letters* 38.10 (2011).

[245] H. S. Suh et al. “Capillary pressure at irregularly shaped pore throats: Implications for water retention characteristics.” *Advances in Water Resources* 110 (2017), pp. 51–58.

[246] W. Sun and T.-f. Wong. “Prediction of permeability and formation factor of sandstone with hybrid lattice Boltzmann/finite element simulation on microtomographic

images." *International Journal of Rock Mechanics and Mining Sciences* 106 (2018), pp. 269–277.

[247] J. R. Booker. "Thermal convection with strongly temperature-dependent viscosity." *Journal of Fluid Mechanics* 76.4 (1976), pp. 741–754.

[248] E. O. Egbogah and J. T. Ng. "An improved temperature-viscosity correlation for crude oil systems." *Journal of Petroleum Science and Engineering* 4.3 (1990), pp. 197–200.

[249] B. Bhadauria and P. Kiran. "Heat transport in an anisotropic porous medium saturated with variable viscosity liquid under temperature modulation." *Transport in porous media* 100.2 (2013), pp. 279–295.

[250] S. G. Brush. "Theories of Liquid Viscosity." *Chemical Reviews* 62.6 (1962), pp. 513–548.

[251] R. C. Reid, J. M. Prausnitz, and B. E. Poling. "The properties of gases and liquids" (1987).

[252] L. Korson, W. Drost-Hansen, and F. J. Millero. "Viscosity of water at various temperatures." *The Journal of Physical Chemistry* 73.1 (1969), pp. 34–39.

[253] G. Tang, N. Morrow, and T. Salinity. "Oil Composition, and Oil Recovery by Waterflooding." *SPE Reservoir Engineering* 12.04 (1997), pp. 269–276.

[254] P Smolinski, T Belytschko, and M Neal. "Multi-time-step integration using nodal partitioning." *International Journal for Numerical Methods in Engineering* 26.2 (1988), pp. 349–359.

[255] W. Daniel. "Analysis and implementation of a new constant acceleration subcycling algorithm." *International Journal for Numerical Methods in Engineering* 40.15 (1997), pp. 2841–2855.

[256] E. Rank, C. Katz, and H. Werner. "On the importance of the discrete maximum principle in transient analysis using finite element methods." *International Journal for Numerical Methods in Engineering* 19.12 (1983), pp. 1771–1782.

[257] H. Thomas and Z Zhou. "Minimum time-step size for diffusion problem in FEM analysis." *International Journal for Numerical Methods in Engineering* 40.20 (1997), pp. 3865–3880.

[258] W Cui et al. "Time-step constraints in transient coupled finite element analysis." *International Journal for Numerical Methods in Engineering* 106.12 (2016), pp. 953–971.

[259] W. Li and C. Wei. “Minimum time-step size in transient finite element analysis of coupled poromechanical problems.” *Computers and Geotechnics* 98 (2018), pp. 197–204.

[260] T. Heister, M. F. Wheeler, and T. Wick. “A primal-dual active set method and predictor-corrector mesh adaptivity for computing fracture propagation using a phase-field approach.” *Computer Methods in Applied Mechanics and Engineering* 290 (2015), pp. 466–495.

[261] S Teichtmeister et al. “Phase field modeling of fracture in anisotropic brittle solids.” *International Journal of Non-Linear Mechanics* 97 (2017), pp. 1–21.

[262] K. Park. “Partitioned transient analysis procedures for coupled-field problems: stability analysis” (1980).

[263] S. Lee, M. F. Wheeler, and T. Wick. “Pressure and fluid-driven fracture propagation in porous media using an adaptive finite element phase field model.” *Computer Methods in Applied Mechanics and Engineering* 305 (2016), pp. 111–132.

[264] E Turska and B. Schrefler. “On convergence conditions of partitioned solution procedures for consolidation problems.” *Computer Methods in Applied Mechanics and Engineering* 106.1-2 (1993), pp. 51–63.

[265] T Belytschko, W. K. Liu, and P Smolinksi. “Multi-stepping implicit-explicit procedures in transient analysis.” *Innovative methods in Nonlinear Analysis*. Pineridge Press, 1984, pp. 135–154.

[266] A. Gravouil and A. Combescure. “Multi-time-step explicit–implicit method for nonlinear structural dynamics.” *International Journal for Numerical Methods in Engineering* 50.1 (2001), pp. 199–225.

[267] T. E. Tezduyar and Y. Park. “Discontinuity-capturing finite element formulations for nonlinear convection-diffusion-reaction equations.” *Computer methods in applied mechanics and engineering* 59.3 (1986), pp. 307–325.

[268] T. E. Tezduyar. “Stabilized finite element formulations for incompressible flow computations.” *Advances in applied mechanics* 28 (1991), pp. 1–44.

[269] M. AbuAisha and B. Loret. “Stabilization of forced heat convection: applications to enhanced geothermal systems (EGS).” *Transport in Porous Media* 112.1 (2016), pp. 229–252.

[270] J Lemonds and A Needleman. “Finite element analyses of shear localization in rate and temperature dependent solids.” *Mechanics of Materials* 5.4 (1986), pp. 339–361.

[271] C. Miehe. “Entropic thermoelasticity at finite strains. Aspects of the formulation and numerical implementation.” *Computer Methods in Applied Mechanics and Engineering* 120.3-4 (1995), pp. 243–269.

[272] P. Erbts and A. DüSter. “Accelerated staggered coupling schemes for problems of thermoelasticity at finite strains.” *Computers & Mathematics with Applications* 64.8 (2012), pp. 2408–2430.

[273] P Smolinski, S Sleith, and T Belytschko. “Stability of an explicit multi-time step integration algorithm for linear structural dynamics equations.” *Computational Mechanics* 18.3 (1996), pp. 236–244.

[274] P. Vermeer and A Verruijt. “An accuracy condition for consolidation by finite elements.” *International Journal for numerical and analytical methods in geomechanics* 5.1 (1981), pp. 1–14.

[275] J. Kim, H. A. Tchelepi, R. Juanes, et al. “Stability, accuracy and efficiency of sequential methods for coupled flow and geomechanics.” *SPE reservoir simulation symposium*. Society of Petroleum Engineers. 2009.

[276] G. Strang et al. *Introduction to linear algebra*. Vol. 3. Wellesley-Cambridge Press Wellesley, MA, 1993.

[277] L. N. Trefethen and D. Bau III. *Numerical linear algebra*. Vol. 50. Siam, 1997.

[278] I. N. Bronshtein and K. A. Semendyayev. *Handbook of mathematics*. Springer Science & Business Media, 2013.

[279] W. M. Lai et al. *Introduction to continuum mechanics*. Butterworth-Heinemann, 2009.

[280] R Liu et al. “Modeling of convection-dominated thermoporomechanics problems using incomplete interior penalty Galerkin method.” *Computer methods in applied mechanics and engineering* 198.9-12 (2009), pp. 912–919.

[281] R. J. Plemmons. “M-matrix characterizations. I—nonsingular M-matrices.” *Linear Algebra and its Applications* 18.2 (1977), pp. 175–188.

[282] T. Fujimoto and R. Ranade. “Two characterizations of inverse-positive matrices: the Hawkins-Simon condition and the Le Chatelier-Braun principle.” *The Electronic Journal of Linear Algebra* 11 (2004).

[283] R. Juanes et al. “Impact of relative permeability hysteresis on geological CO2 storage.” *Water resources research* 42.12 (2006).

[284] D. H. Kang et al. “Effect of hydrate nucleation mechanisms and capillarity on permeability reduction in granular media.” *Geophysical Research Letters* 43.17 (2016), pp. 9018–9025.

[285] A. Selvadurai, C.-B. Couture, and S. Rezaei Niya. “Permeability of wormholes created by CO2-acidized water flow through stressed carbonate rocks.” *Physics of Fluids* 29.9 (2017), p. 096604.

[286] A Paterson and M Fermigier. “Wetting of heterogeneous surfaces: Influence of defect interactions.” *Physics of Fluids* 9.8 (1997), pp. 2210–2216.

[287] H. Class, R. Helmig, and P. Bastian. “Numerical simulation of non-isothermal multiphase multicomponent processes in porous media.: 1. An efficient solution technique.” *Advances in Water Resources* 25.5 (2002), pp. 533–550.

[288] J Rutqvist et al. “Estimating maximum sustainable injection pressure during geological sequestration of CO2 using coupled fluid flow and geomechanical fault-slip analysis.” *Energy Conversion and Management* 48.6 (2007), pp. 1798–1807.

[289] M. Grant. *Geothermal reservoir engineering*. Elsevier, 2013.

[290] J. L. Wagner et al. “Fluid-structure interactions in compressible cavity flows.” *Physics of Fluids* 27.6 (2015), p. 066102.

[291] Y Heider and B Markert. “A phase-field modeling approach of hydraulic fracture in saturated porous media.” *Mechanics Research Communications* 80 (2017), pp. 38–46.

[292] H. S. Suh and W. Sun. “An immersed phase field fracture model for fluid-infiltrating porous media with evolving Beavers-Joseph-Saffman condition.” *arXiv preprint arXiv:2008.11815* (2020).

[293] J. Choo and R. I. Borja. “Stabilized mixed finite elements for deformable porous media with double porosity.” *Computer Methods in Applied Mechanics and Engineering* 293 (2015), pp. 131–154.

[294] J. Choo, J. A. White, and R. I. Borja. “Hydromechanical modeling of unsaturated flow in double porosity media.” *International Journal of Geomechanics* 16.6 (2016), p. D4016002.

[295] C. Liu and Y. N. Abousleiman. “Shale Dual-Porosity Dual-Permeability Poromechanical and Chemical Properties Extracted from Experimental Pressure Transmission Tests.” *Journal of Engineering Mechanics* 143.9 (2017), p. 04017107.

[296] K. Wang and W. Sun. “A multiscale multi-permeability poroplasticity model linked by recursive homogenizations and deep learning.” *Computer Methods in Applied Mechanics and Engineering* 334 (2018), pp. 337–380.

[297] J. Ghaboussi and R. Barbosa. “Three-dimensional discrete element method for granular materials.” *International Journal for Numerical and Analytical Methods in Geomechanics* 14.7 (1990), pp. 451–472.

[298] M. A. Spaid and F. R. Phelan Jr. “Lattice Boltzmann methods for modeling microscale flow in fibrous porous media.” *Physics of fluids* 9.9 (1997), pp. 2468–2474.

[299] M. J. Blunt et al. “Detailed physics, predictive capabilities and macroscopic consequences for pore-network models of multiphase flow.” *Advances in Water Resources* 25.8-12 (2002), pp. 1069–1089.

[300] G. Tang, W. Tao, and Y. He. “Lattice Boltzmann method for gaseous microflows using kinetic theory boundary conditions.” *Physics of Fluids* 17.5 (2005), p. 058101.

[301] C. Arson and J.-M. Pereira. “Influence of damage on pore size distribution and permeability of rocks.” *International Journal for Numerical and Analytical Methods in Geomechanics* 37.8 (2013), pp. 810–831.

[302] J.-M. Pereira and C. Arson. “Retention and permeability properties of damaged porous rocks.” *Computers and Geotechnics* 48 (2013), pp. 272–282.

[303] E. Ozkan, R. S. Raghavan, O. G. Apaydin, et al. “Modeling of fluid transfer from shale matrix to fracture network.” *SPE Annual Technical Conference and Exhibition*. Society of Petroleum Engineers. 2010.

[304] C. T. Leung and R. W. Zimmerman. “Estimating the hydraulic conductivity of two-dimensional fracture networks using network geometric properties.” *Transport in porous media* 93.3 (2012), pp. 777–797.

[305] P. Fu, S. M. Johnson, and C. R. Carrigan. “An explicitly coupled hydro-geomechanical model for simulating hydraulic fracturing in arbitrary discrete fracture networks.” *International Journal for Numerical and Analytical Methods in Geomechanics* 37.14 (2013), pp. 2278–2300.

[306] J. D. Hyman et al. “dfnWorks: A discrete fracture network framework for modeling subsurface flow and transport.” *Computers & Geosciences* 84 (2015), pp. 10–19.

[307] Z. Li et al. “A least squares augmented immersed interface method for solving Navier–Stokes and Darcy coupling equations.” *Computers & Fluids* 167 (2018), pp. 384–399.

[308] P. Lade and R De Boer. “The concept of effective stress for soil, concrete and rock.” *Geotechnique* 47.1 (1997), pp. 61–78.

[309] J. A. White and R. I. Borja. “Stabilized low-order finite elements for coupled solid-deformation/fluid-diffusion and their application to fault zone transients.” *Computer Methods in Applied Mechanics and Engineering* 197.49-50 (2008), pp. 4353–4366.

[310] J. G. Berryman and H. F. Wang. “The elastic coefficients of double-porosity models for fluid transport in jointed rock.” *Journal of Geophysical Research: Solid Earth* 100.B12 (1995), pp. 24611–24627.

[311] S Mauran, L Rigaud, and O Coudevylle. “Application of the Carman–Kozeny correlation to a high-porosity and anisotropic consolidated medium: the compressed expanded natural graphite.” *Transport in porous media* 43.2 (2001), pp. 355–376.

[312] P. Schutjens et al. “Compaction-induced porosity/permeability reduction in sandstone reservoirs: data and model for elasticity-dominated deformation.” *SPE Reservoir Evaluation & Engineering* 7.03 (2004), pp. 202–216.

[313] R. P. Chapuis and M. Aubertin. “On the use of the Kozeny Carman equation to predict the hydraulic conductivity of soils.” *Canadian Geotechnical Journal* 40.3 (2003), pp. 616–628.

[314] A. Costa. “Permeability-porosity relationship: A reexamination of the Kozeny-Carman equation based on a fractal pore-space geometry assumption.” *Geophysical research letters* 33.2 (2006).

[315] P. F. Worthington. “The uses and abuses of the Archie equations, 1: The formation factor-porosity relationship.” *Journal of Applied Geophysics* 30.3 (1993), pp. 215–228.

[316] G. Mavko and A. Nur. “The effect of a percolation threshold in the Kozeny-Carman relation.” *Geophysics* 62.5 (1997), pp. 1480–1482.

[317] M. Mooney. “The viscosity of a concentrated suspension of spherical particles.” *Journal of colloid science* 6.2 (1951), pp. 162–170.

[318] N.-S. Cheng and A. W.-K. Law. “Exponential formula for computing effective viscosity.” *Powder Technology* 129.1-3 (2003), pp. 156–160.

[319] T. Arbogast and H. L. Lehr. “Homogenization of a Darcy–Stokes system modeling vuggy porous media.” *Computational Geosciences* 10.3 (2006), pp. 291–302.

[320] T. Arbogast and D. S. Brunson. “A computational method for approximating a Darcy–Stokes system governing a vuggy porous medium.” *Computational geosciences* 11.3 (2007), pp. 207–218.

[321] S. Badia, A. Quaini, and A. Quarteroni. “Coupling Biot and Navier–Stokes equations for modelling fluid–poroelastic media interaction.” *Journal of Computational Physics* 228.21 (2009), pp. 7986–8014.

[322] Z. Wu and P. Mirbod. “Experimental analysis of the flow near the boundary of random porous media.” *Physics of Fluids* 30.4 (2018), p. 047103.

[323] E. Bergkamp et al. “A staggered finite element procedure for the coupled Stokes-Biot system with fluid entry resistance.” *Computational Geosciences* (2020), pp. 1–26.

[324] G. S. Beavers and D. D. Joseph. “Boundary conditions at a naturally permeable wall.” *Journal of fluid mechanics* 30.1 (1967), pp. 197–207.

[325] P. G. Saffman. “On the boundary condition at the surface of a porous medium.” *Studies in applied mathematics* 50.2 (1971), pp. 93–101.

[326] W. J. Layton, F. Schieweck, and I. Yotov. “Coupling fluid flow with porous media flow.” *SIAM Journal on Numerical Analysis* 40.6 (2002), pp. 2195–2218.

[327] A Terzis et al. “Microscopic velocity field measurements inside a regular porous medium adjacent to a low Reynolds number channel flow.” *Physics of Fluids* 31.4 (2019), p. 042001.

[328] C. Guo et al. “Experimental study on the slip velocity of turbulent flow over and within porous media.” *Physics of Fluids* 32.1 (2020), p. 015111.

[329] J.-L. Auriault. “About the Beavers and Joseph boundary condition.” *Transport in porous media* 83.2 (2010), pp. 257–266.

[330] A. Mikelic and W. Jäger. “On the interface boundary condition of Beavers, Joseph, and Saffman.” *SIAM Journal on Applied Mathematics* 60.4 (2000), pp. 1111–1127.

[331] V. Monchiet, H.-B. Ly, and D. Grande. “Macroscopic permeability of doubly porous materials with cylindrical and spherical macropores.” *Meccanica* 54.10 (2019), pp. 1583–1596.

[332] S. K. Stoter et al. “A diffuse interface method for the Navier–Stokes/Darcy equations: Perfusion profile for a patient-specific human liver based on MRI scans.” *Computer Methods in Applied Mechanics and Engineering* 321 (2017), pp. 70–102.

[333] C. Bilgen and K. Weinberg. “On the crack-driving force of phase-field models in linearized and finite elasticity.” *Computer Methods in Applied Mechanics and Engineering* 353 (2019), pp. 348–372.

[334] P. A. Witherspoon et al. “Validity of cubic law for fluid flow in a deformable rock fracture.” *Water resources research* 16.6 (1980), pp. 1016–1024.

[335] J. S. Konzuk and B. H. Kueper. “Evaluation of cubic law based models describing single-phase flow through a rough-walled fracture.” *Water Resources Research* 40.2 (2004).

[336] W. Jin and C. Arson. “Fluid-driven transition from damage to fracture in anisotropic porous media: a multi-scale XFEM approach.” *Acta Geotechnica* 15.1 (2020), pp. 113–144.

[337] K. Wang and W. Sun. “An updated Lagrangian LBM–DEM–FEM coupling model for dual-permeability fissured porous media with embedded discontinuities.” *Computer Methods in Applied Mechanics and Engineering* 344 (2019), pp. 276–305.

[338] T. T. Nguyen et al. “On the choice of parameters in the phase field method for simulating crack initiation with experimental validation.” *International Journal of Fracture* 197.2 (2016), pp. 213–226.

[339] K. Pham, K Ravi-Chandar, and C. Landis. “Experimental validation of a phase-field model for fracture.” *International Journal of Fracture* 205.1 (2017), pp. 83–101.

[340] A. Logg, G. N. Wells, and J. Hake. “DOLFIN: A C++/Python finite element library.” *Automated solution of differential equations by the finite element method*. Springer, 2012, pp. 173–225.

[341] C. Li, R. I. Borja, and R. A. Regueiro. “Dynamics of porous media at finite strain.” *Computer methods in applied mechanics and engineering* 193.36-38 (2004), pp. 3837–3870.

[342] K. Wang and W. Sun. “A semi-implicit discrete-continuum coupling method for porous media based on the effective stress principle at finite strain.” *Computer Methods in Applied Mechanics and Engineering* 304 (2016), pp. 546–583.

[343] J. S. O’Brien and P. Y. Julien. “Laboratory analysis of mudflow properties.” *Journal of hydraulic engineering* 114.8 (1988), pp. 877–887.

[344] R. M. Iverson. “The physics of debris flows.” *Reviews of geophysics* 35.3 (1997), pp. 245–296.

[345] K. Y. Kim et al. “Effect of particle shape on the shear strength of fault gouge.” *Geosciences Journal* 20.3 (2016), pp. 351–359.

[346] Z. Hashin. *The elastic moduli of heterogeneous materials*. Tech. rep. HARVARD UNIV CAMBRIDGE MA, 1960.

[347] R. W. Zimmerman. “Elastic moduli of a solid containing spherical inclusions.” *Mechanics of Materials* 12.1 (1991), pp. 17–24.

[348] N Ramakrishnan and V. Arunachalam. “Effective elastic moduli of porous ceramic materials.” *Journal of the American Ceramic Society* 76.11 (1993), pp. 2745–2752.

[349] M Markov et al. “Permeability of the fluid-filled inclusions in porous media.” *Transport in porous media* 84.2 (2010), pp. 307–317.

[350] H. Jelitto and G. A. Schneider. “A geometric model for the fracture toughness of porous materials.” *Acta materialia* 151 (2018), pp. 443–453.

[351] A. Qinami et al. “Circumventing mesh bias by r-and h-adaptive techniques for variational eigenfracture.” *International Journal of Fracture* 220.2 (2019), pp. 129–142.

[352] R. de Borst and C. V. Verhoosel. “Gradient damage vs phase-field approaches for fracture: Similarities and differences.” *Computer Methods in Applied Mechanics and Engineering* 312 (2016), pp. 78–94.

[353] F. Aldakheel et al. “Phase-field modeling of brittle fracture using an efficient virtual element scheme.” *Computer Methods in Applied Mechanics and Engineering* 341 (2018), pp. 443–466.

[354] J.-Y. Wu and V. P. Nguyen. “A length scale insensitive phase-field damage model for brittle fracture.” *Journal of the Mechanics and Physics of Solids* 119 (2018), pp. 20–42.

[355] R. J. Geelen et al. “An optimization-based phase-field method for continuous-discontinuous crack propagation.” *International Journal for Numerical Methods in Engineering* 116.1 (2018), pp. 1–20.

[356] N. Noii et al. “An adaptive global–local approach for phase-field modeling of anisotropic brittle fracture.” *Computer Methods in Applied Mechanics and Engineering* 361 (2020), p. 112744.

[357] N. Moës, J. Dolbow, and T. Belytschko. “A finite element method for crack growth without remeshing.” *International journal for numerical methods in engineering* 46.1 (1999), pp. 131–150.

[358] F. Armero and C. Linder. “New finite elements with embedded strong discontinuities in the finite deformation range.” *Computer Methods in Applied Mechanics and Engineering* 197.33-40 (2008), pp. 3138–3170.

[359] K. Wang and W. Sun. “Meta-modeling game for deriving theory-consistent, microstructure-based traction–separation laws via deep reinforcement learning.” *Computer Methods in Applied Mechanics and Engineering* 346 (2019), pp. 216–241.

[360] S. May, J. Vignollet, and R. De Borst. “A numerical assessment of phase-field models for brittle and cohesive fracture: Γ-convergence and stress oscillations.” *European Journal of Mechanics-A/Solids* 52 (2015), pp. 72–84.

[361] A. Dietsche, P. Steinmann, and K. Willam. “Micropolar elastoplasticity and its role in localization.” *International Journal of Plasticity* 9.7 (1993), pp. 813–831.

[362] Z. P. Bazant and J. Planas. *Fracture and size effect in concrete and other quasibrittle materials*. Vol. 16. CRC press, 1997.

[363] P. Trovalusci et al. “Particulate random composites homogenized as micropolar materials.” *Meccanica* 49.11 (2014), pp. 2719–2727.

[364] K. Wang et al. “Identifying material parameters for a micro-polar plasticity model via X-ray micro-computed tomographic (CT) images: lessons learned from the curve-fitting exercises.” *International Journal for Multiscale Computational Engineering* 14.4 (2016).

[365] F. Aldakheel. “A microscale model for concrete failure in poro-elasto-plastic media.” *Theoretical and Applied Fracture Mechanics* 107 (2020), p. 102517.

[366] J.-Y. Wu, T. K. Mandal, and V. P. Nguyen. “A phase-field regularized cohesive zone model for hydrogen assisted cracking.” *Computer Methods in Applied Mechanics and Engineering* 358 (2020), p. 112614.

[367] A. C. Eringen. “Linear theory of micropolar elasticity.” *Journal of Mathematics and Mechanics* (1966), pp. 909–923.

[368] N. Sachio, R. Benedict, and R. Lakes. “Finite element method for orthotropic micropolar elasticity.” *International Journal of Engineering Science* 22.3 (1984), pp. 319–330.

[369] W Ehlers and W Volk. “On theoretical and numerical methods in the theory of porous media based on polar and non-polar elasto-plastic solid materials.” *International Journal of Solids and Structures* 35.34-35 (1998), pp. 4597–4617.

[370] A. C. Eringen. *Microcontinuum field theories: I. Foundations and solids*. Springer Science & Business Media, 2012.

[371] E. Atroshchenko and S. P. A. Bordas. "Fundamental solutions and dual boundary element methods for fracture in plane Cosserat elasticity." *Proceedings of the Royal Society A: Mathematical, Physical and Engineering Sciences* 471.2179 (2015), p. 20150216.

[372] S. Grbčić, A. Ibrahimbegović, and G. Jelenić. "Variational formulation of micropolar elasticity using 3D hexahedral finite-element interpolation with incompatible modes." *Computers & Structures* 205 (2018), pp. 1–14.

[373] E. Diegele, R. ElsÄßer, and C. Tsakmakis. "Linear micropolar elastic crack-tip fields under mixed mode loading conditions." *International journal of fracture* 129.4 (2004), pp. 309–339.

[374] Y.-D. Li and K. Y. Lee. "Fracture analysis in micropolar elasticity: mode-I crack." *International journal of fracture* 156.2 (2009), pp. 179–184.

[375] A Yavari, S Sarkani, and E. Moyer. "On fractal cracks in micropolar elastic solids." *Journal of Applied Mechanics* 69.1 (2002), pp. 45–54.

[376] R. Lakes and W. Drugan. "Bending of a Cosserat elastic bar of square cross section: theory and experiment." *Journal of Applied Mechanics* 82.9 (2015), p. 091002.

[377] D Bigoni and W. Drugan. "Analytical derivation of Cosserat moduli via homogenization of heterogeneous elastic materials." *Journal of Applied Mechanics* 74.4 (2007), pp. 741–753.

[378] P. Neff, J. Jeong, and A. Fischle. "Stable identification of linear isotropic Cosserat parameters: bounded stiffness in bending and torsion implies conformal invariance of curvature." *Acta Mechanica* 211.3-4 (2010), pp. 237–249.

[379] R. Mindlin and H. Tiersten. "Effects of couple-stresses in linear elasticity." *Archive for Rational Mechanics and analysis* 11.1 (1962), pp. 415–448.

[380] R. Mindlin. "Influence of couple-stresses on stress concentrations." *Experimental mechanics* 3.1 (1963), pp. 1–7.

[381] M McGregor and M. Wheel. "On the coupling number and characteristic length of micropolar media of differing topology." *Proceedings of the Royal Society A: Mathematical, Physical and Engineering Sciences* 470.2169 (2014), p. 20140150.

[382] J. Clayton and J Knap. "Phase field modeling of directional fracture in anisotropic polycrystals." *Computational Materials Science* 98 (2015), pp. 158–169.

[383] B. Bourdin, C. J. Larsen, and C. L. Richardson. “A time-discrete model for dynamic fracture based on crack regularization.” *International journal of fracture* 168.2 (2011), pp. 133–143.

[384] C. Miehe et al. “Phase field modeling of fracture in multi-physics problems. Part II. Coupled brittle-to-ductile failure criteria and crack propagation in thermo-elastic–plastic solids.” *Computer Methods in Applied Mechanics and Engineering* 294 (2015), pp. 486–522.

[385] E. Lorentz, S. Cuvilliez, and K. Kazymyrenko. “Modelling large crack propagation: From gradient damage to cohesive zone models.” *International Journal of Fracture*. 2012.

[386] E. Lorentz, S. Cuvilliez, and K. Kazymyrenko. “Convergence of a gradient damage model toward a cohesive zone model.” *Comptes Rendus Mécanique* 339.1 (2011), pp. 20–26.

[387] F. Cazes et al. “A cohesive zone model which is energetically equivalent to a gradient-enhanced coupled damage-plasticity model.” *European Journal of Mechanics-A/Solids* 29.6 (2010), pp. 976–989.

[388] J.-Y. Wu. “A geometrically regularized gradient-damage model with energetic equivalence.” *Computer Methods in Applied Mechanics and Engineering* 328 (2018), pp. 612–637.

[389] R. Larsson and Y. Zhang. “Homogenization of microsystem interconnects based on micropolar theory and discontinuous kinematics.” *Journal of the Mechanics and Physics of Solids* 55.4 (2007), pp. 819–841.

[390] Y. Zhang et al. “Interface modelling of microsystem interconnections using micropolar theory and discontinuous approximation.” *Computers & structures* 85.19-20 (2007), pp. 1500–1513.

[391] C. B. Hirschberger, N. Sukumar, and P. Steinmann. “Computational homogenization of material layers with micromorphic mesostructure.” *Philosophical Magazine* 88.30-32 (2008), pp. 3603–3631.

[392] C. V. Verhoosel and R. de Borst. “A phase-field model for cohesive fracture.” *International Journal for numerical methods in Engineering* 96.1 (2013), pp. 43–62.

[393] A. R. Ingraffea and M. Grigoriu. *Probabilistic fracture mechanics: a validation of predictive capability*. Tech. rep. CORNELL UNIV ITHACA NY DEPT OF STRUCTURAL ENGINEERING, 1990.

[394] R. Patil, B. Mishra, and I. Singh. “An adaptive multiscale phase field method for brittle fracture.” *Computer Methods in Applied Mechanics and Engineering* 329 (2018), pp. 254–288.